THE ROLE OF FRONT ELECTRODES AND INTERMEDIATE REFLECTORS IN THE OPTOELECTRONIC PROPERTIES OF HIGH-EFFICIENCY MICROMORPH SOLAR CELLS

Thèse présentée à la Faculté des Sciences
Institut de Microtechnique
Université de Neuchâtel

Pour l'obtention du grade de docteur ès sciences

Par

Didier Dominé

Acceptée sur proposition du jury :
Prof. C. Ballif, directeur de thèse,
Dr. A. Feltrin, rapporteur,
Prof. H. P. Herzig, rapporteur,
Dr. J. Meier, rapporteur,
Prof. M. Topic, rapporteur,

Soutenue le 20 mars 2009

Université de Neuchâtel

2009

Université de Neuchâtel unine

FACULTE DES SCIENCES
Secrétariat-Décanat de la faculté
- Rue Emile-Argand 11
- CP 158
- CH-2009 Neuchâtel

IMPRIMATUR POUR LA THESE

The Role of Front Electrodes and Intermediate Reflectors in the Optoelectronic Properties of High-Efficiency Micromorph Solar Cells

Didier DOMINE

UNIVERSITE DE NEUCHATEL

FACULTE DES SCIENCES

La Faculté des sciences de l'Université de Neuchâtel,
sur le rapport des membres du jury

MM. C. Ballif (directeur de thèse),
H.P. Herzig, A. Feltrin, M. Topic (Ljubljana, Slovenia)
Et J. Meier (Oerlikon Solar-Lab SA, Neuchâtel)

autorise l'impression de la présente thèse.

Neuchâtel, le 31 mars 2009

Le doyen :
F. Kessler

UNIVERSITE DE NEUCHATEL
FACULTE DES SCIENCES
Secrétariat - décanat de la faculté
Rue Emile-Argand 11 - CP 158
CH-2009 Neuchâtel
Felix Kessler

■ Téléphone : +41 32 718 21 00 ■ E-mail : secretariat.sciences@unine.ch ■ www.unine.ch/sciences

Mots-clés : cellules solaires en couches minces de silicium, silicium amorphe, silicium microcristallin, micromorphe, réflecteur intermédiaire, oxyde conducteur transparent, surfaces nano-texturées, piégeage de la lumière, théorie scalaire de la diffusion, microscopie à force atomique en conduction, microscopie à sonde de Kelvin

Keywords: silicon thin-film solar cells, amorphous silicon, microcrystalline silicon, micromorph, intermediate reflector, transparent conductive oxide, nano-textured surfaces, light trapping, scalar scattering theory, conductive atomic force microscopy, scanning Kelvin probe microscopy

Summary: On the road towards silicon thin-film photovoltaic modules with a conversion efficiency of 10%, the micromorph tandem solar cell is a promising candidate. Two ingredients are commonly used for light-management within the micromorph solar cell: (1) nano-textured interfaces and (2) insertion of an intermediate reflector in-between the two component cells of the tandem. The purpose of the nano-textures is to promote light scattering at the optical interfaces and therefore to increase the probability of absorption of red light in the amorphous silicon (a-Si:H) absorber of the top cell and of infrared light in the microcrystalline silicon (μc-Si:H) absorber of the bottom cell. For micromorph devices deposited on glass plates, these nano-textures are obtained by the deposition of the solar cell on a surface-textured transparent conductive front electrode. The function of the second ingredient, the intermediate reflector, is to increase the photo-current density within the a-Si:H top cell, thanks to reflections produced at the additional optical interface. This document study the interplay between those two ingredients within the optoelectronic system formed by the micromorph solar cell. In particular, the impact of the surface morphology of the front contact on the growth and performances of μc-Si:H solar cells is described. A study of the electronic transport within μc-Si:H cells is carried out using Scanning Kelvin probe microscopy and two original methods based on conductive atomic force microscopy. Also, the importance of the angular distribution of the light scattered by nano-textured front electrodes is demonstrated. Angular distributions for light scattered in-air and in a-Si:H are calculated from atomic force microscopy pictures of different front electrodes. The calculations are performed using phase screens and the scalar scattering theory. Theoretical results obtained with this approach are successfully confronted with experimental data obtained in-air. Besides, a quantitative comparison of the relative importance of a reduced free carrier absorption (FCA) in the front electrode and of an improvement of its light-trapping capability is presented. For the different types of front contacts used in this work, this comparison shows that the reduction of FCA produces more than 50% of the gains in photo-current density. Regarding the direct effect of the intermediate reflector, this work experimentally demonstrates that the gain obtained in the current density of the top cell is larger with nano-textured interfaces than with flat interfaces. An experimental gain up to 2.8 mA/cm^2 is achieved here. With respect to device optimization, the best initial conversion efficiency achieved in this work is 13.3% for a 1.2 cm^2 micromorph cell deposited on a glass plate with an anti-reflection (AR) coating, yielding the remarkably high value of 13.8 mA/cm^2 for the short-circuit current density. The best stabilized device achieved in this work yields 11.1% stabilized conversion efficiency (1.2 cm^2 and no AR coating).

Table of content

1 Introduction 11
1.1 Silicon thin-film photovoltaic solar cells 11
1.1.1 General context...11
1.1.2 Deposition techniques 11
1.1.3 Specific issues and past innovations 12
1.2 The micromorph solar cell 14
1.3 Aim and outline of this thesis..16
1.4 Contribution of this work to the research field...18
2 Deposition and characterization techniques 21
2.1 Micromorph cell fabrication..21
2.1.1 Zinc oxide layers deposited by the low pressure chemical vapor deposition (LPCVD) technique...21
2.1.2 Silicon deposition by the very high frequency plasma enhanced chemical vapor deposition (VHF-PECVD) technique...22
2.2 Characterization techniques 24
2.2.1 Illuminated current-voltage measurement (I-V) 24
2.2.2 External quantum efficiency (EQE)...24
2.2.3 Ultra-violet, visible, and near infrared spectroscopy 25
2.2.4 Angular resolved scattering measurement (ARS)...26
2.2.5 Conductive atomic force microscopy (C-AFM) 27
2.2.6 Scanning Kelvin probe microscopy (SKPM)..28
3 Modification of the surface morphology of LPCVD ZnO layers by means of plasma post-treatments...33
3.1 Introduction 33
3.2 Experimental 33
3.3 Comparison of plasma compositions: results and discussion 34
3.4 Evolution of the morphology with an increasing post-treatment time: result and discussion 35
3.5 Conclusion...36
4 Influence of the surface morphology of the front ZnO layer on the electrical performances of the device...39
4.1 Introduction 39
4.2 Experimental 39
4.3 Results 40
4.4 Discussion 45
4.5 Conclusion...46
5 Investigation of the electric-field distribution in μc-Si:H p-i-n solar cells by cross-sectional SKPM and planar C-AFM- based measurements..47
5.1 Introduction 47
5.2 Cross-sectional SKPM and comparison with TEM imaging 48
5.2.1 Experimental 48
5.2.2 Results 49

5.2.3 Discussion 54
5.3 'Near-V_{oc} planar C-AFM' and 'lock-in planar nanopotentiometry' 56
5.3.1 Experimental 56
5.3.2 Results 58
5.3.3 Discussion 60
5.4 Conclusions 64
5.4.1 Cross-sectional SKPM and TEM 64
5.4.2 Comparison of cross-sectional SKPM and electrical probing in the planar configuration 65
6 Scattering of the light transmitted through a rough nano-textured front contact ZnO layer.......67
6.1 Introduction: The Yablonovitch's $4n^2$ enhancement limit..67
6.2 Scalar scattering theory 73
6.2.1 Theoretical approaches and compatibility with our problem.......................................73
6.2.2 Usage of the scalar scattering theory for haze calculation 76
6.2.3 Non-paraxial scalar scattering theory..78
6.3 Diffuse transmittance through surface-textured LPCVD ZnO layers 84
6.3.1 Modeling of the ZnO layers 84
6.3.2 Comparison of measurements and calculations of the ARS in transmittance for different LPCVD ZnO layers 87
6.4 Conclusions 105
7. Intermediate reflector for high stable efficiency devices 107
7.1 Introduction 107
7.1.1 Motivation and related problems..107
7.1.2 Layout of the chapter..108
7.2 Effect of the current matching in micromorph tandem cells...109
7.2.1 Modeling 109
7.2.2 Results of calculations..112
7.2.3 Discussion 114
7.2.4 Conclusion..115
7.3 ZIR thickness series: experimental and optical modeling studies.....................................115
7.3.1 Experimental 115
7.3.2 Results of the ZIR thickness series 118
7.3.3 Discussion of the results..120
7.3.4 Conclusions on the ZIR thickness series..122
7.4 SOIR versus ZIR 122
7.4.1 Motivation 122
7.4.2 Experimental 124
7.4.3 SOIR versus ZIR: Results and discussion..127
7.4.4 SOIR versus ZIR: Conclusion..129
7.5 Interplay between the front TCO and the IRL 129
7.5.1 Motivation 129
7.5.2 Experimental 130
7.5.3 Results for the interplay between the front TCO and the IRL 132
7.5.4 Discussion of the results..141
7.5.5 Conclusions on the interplay between the front TCO and the IRL 144
7.6 Intermediate reflector for high stable efficiencies: Proof of concept...............................145
7.6.1 Motivation 145

7.6.2 Experimental 145
7.6.3 Results and discussion 145
7.6.4 Conclusion on the proof of concept 148
7.7 Conclusions 148
8 Anti-reflection effect and light absorption in rough nano-textured front contact ZnO layers 151
8.1 Experimental 151
8.2 Results and discussion 154
8.2.1 Reflectance measurement of glass/ZnO/a-Si:H structures 154
8.2.2 Front ZnO layer: effects of light trapping and FCA absorption 157
8.3 Conclusions 161
9 Conclusions and perspectives 163
9.1 Final conclusions 163
9.1.1 Device optimization 163
9.1.2 Study of the optoelectronic properties of the device: electronic 164
9.1.3 Study of the optoelectronic properties of the device: optics 164
9.2 Perspectives 165
References 167
List of publications 177
Acknowledgments 179

1 Introduction

This chapter introduces the context of silicon thin-film photovoltaic solar cells and motivation for this particular field of research in the more general context of thin-film solar cells. Then, the structure of the specific photovoltaic device discussed in this thesis is presented. Finally, the aim if this work and the outline of this document are described before summarizing the contributions of this thesis to its field of research.

1.1 Silicon thin-film photovoltaic solar cells

1.1.1 General context

Silicon (Si) thin-film (TF) silicon based photovoltaics (PV) is emerging as a promising technology because of the availability and environmental sustainability of the main raw materials (silane (SiH_4) and hydrogen (H_2)) used for the fabrication of solar cells and modules. These two criteria of availability and sustainability are unavoidable when considering solutions to energy issues on a long time scale and at a large fraction of the global energy mix. This technology requires the deposition of a very thin layer of silicon (typically 1-2 µm or less). In addition, the compatibility of TF PV with mass-production processes on rigid or flexible large area substrates provides immediate costs reduction potential. These reasons are at the origin of a tremendous industrial dynamism in the field of all TF PV technologies (Si, CdTe, CuIn(Ga)Se). An obvious example of this vitality is the result of recent synergies between PV researchers and large scale display production tools manufacturers [Shah 2006]. These companies, such OC Oerlikon and Applied Materials, provide now equipment for "low-cost" manufacturing of Si thin-film modules [Kroll 2007, Meier 2008, Kadam 2008, Klein 2008].

1.1.2 Deposition techniques

Silicon thin-films can be deposited in the amorphous phase and also in a microcrystalline phase [Vepreck 1968] which consists of crystallites of Si embedded in an amorphous Si tissue. In the following, we will consider hydrogenated amorphous silicon (a-Si:H) and hydrogenated microcrystalline silicon (µc-Si:H). The electronic quality of these materials is insured by a large amount of hydrogen atoms (more than 10 at.% for device-grade a-Si:H [Platz 1998]) which passivate dangling bonds in the twisted amorphous Si network and at the crystallites surfaces. Most of the deposition techniques for a-Si:H and µc-Si:H involve a chemical vapor deposition (CVD) process for the decomposition of a SiH_4 and H_2 gas-phase mixture. These techniques vary depending on the way the gas molecules are decomposed into precursors (neutral radicals and ions): a glow discharge sustained at radio frequency (rf, typically 13.56 MHz) or at very high frequency (VHF, 70-120 MHz) for the plasma enhanced CVD (PECVD) [Curtins 1987], a tungsten or

tantalum catalytic hot wire resistively heated for the hot-wire-assisted CVD (HWCVD) [Mahan 1991], and ultraviolet photons for the Photo-CVD [Sarkozy 1981] techniques.

At the Institute of Microtechnology of Neuchâtel (IMT), VHF-PECVD is used for deposition of a-Si:H and µc-Si:H. The advantage of increasing the plasma excitation frequency in the VHF technique is that the energy of ion-bombardment on the Si film on formation is reduced [Curtins 1987, Schwarzenbach 1995]. The microstructure of the Si thin-film depends primarily on the silane concentration (SC), defined by the gas flow ratio SC = $[SiH_4]/[SiH_4+H_2]$ used during deposition. With the variation of SC, all the microstructures ranging from purely amorphous Si to µc-Si:H layers with a crystalline volume fraction of more than 90% can be obtained.

1.1.3 Specific issues and past innovations

The solar cells studied in this work are constituted by a TF Si layer contacted by a transparent conductive oxide (TCO) on the front side and by a back conductive contact on the other side (which is here a TCO layer but could be a metallic contact). Sketches of the structure of typical amorphous Si and micromorph solar cells are given in Fig. 1.1.

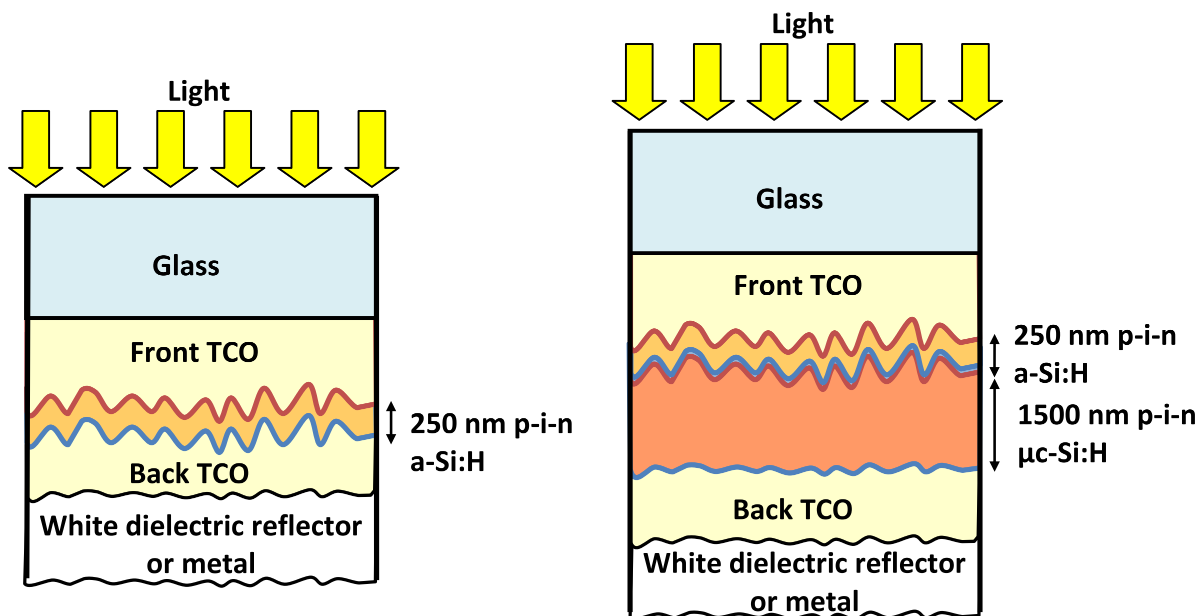

Fig. 1.1: Sketch of typical amorphous Si (left) and micromorph solar cell (right). They are built by depositing thin cells (300 nm amorphous Si, 1.5 microns microcrystalline Si) at low temperature (200°C) on a transparent conductive oxide.

We will see in chapter 6 that the thickness of the absorber of TF Si solar cells must be made much smaller than the absorption depth (see Fig. 1.2 later in the text) of red light for a-Si:H (several µm) and of near infrared light for µc-Si:H (several tenths of µm). Therefore, the probability of absorption of photons in the absorber layer of TF Si solar cells must be increased by means of an enhancement of the effective light path in the device. This is provided by scattering of the light transmitted in the absorber layer of the

solar cell and light trapping by total internal reflection. At IMT, for TF Si solar cells deposited in the pin configuration, the light-scattering is produced at the front TCO/silicon interface thanks to the use of as-grown surface-textured (as shown in Fig. 1) boron-doped zinc oxide (ZnO:B) layers obtained by the low-pressure chemical vapor deposition (LPCVD) technique [Fay 2000, Fay 2003].

The short diffusion lengths of charge carriers, resulting from the disordered lattice of a-Si:H and from non-passivated dangling bonds, make impossible the collection of carriers photo-generated through the whole thickness of the TF Si absorber by diffusion-assisted transport only. A drift of charge carriers must therefore be produced with the help of an electric-field. As doping of TF Si layers lead to a worsening of their electrical properties (dopant induce defects), doped layers are used only to "create" an internal configuration and build up the electric-field across the absorber. Eventually, devices are fabricated by deposition of TF Si solar cells in pin or nip configuration. This means that the device is composed of an intrinsic (i-) layer sandwiched between p-doped and n-doped layers. The pin (nip) configuration refers to the deposition sequence where the p-doped (n-doped) layer is first deposited on the substrate. The doped layers are obtained by addition, during the corresponding deposition step, of diborane (B_2H_6) or trimethylboron ($B(CH_3)_3$) for the p-type doping, and of phosphine (PH_3) for the n-type doping. It is preferable that light enters the p-type layer side first, because in a-Si:H, mobility of holes is smaller than mobility of electrons. Therefore, deposition of TF Si solar cells on opaque substrates must be done in the nip sequence. Whereas the pin sequence is used for devices in which light enters through the transparent substrate used for deposition. Noticeably, when only μc-Si:H cells are used, good results can also be achieved with n-layer as front layer [Huang 2008].

A well known issue in the field of TF Si PV is the light-induced degradation of the a-Si:H material (Staebler-Wronski effect) [Staebler 1977]. It is attributed to the creation of dangling-bonds by non-radiative recombination of free carriers [Stutzmann 1985]. This limits the stabilized energy conversion efficiency (η) of a-Si:H solar cells to values smaller than 10%. The present certified world record is held by IMT and was obtained in 2003 by Meier *et al.*, with a stabilized η of 9.5% for a single-junction a-Si:H solar cell deposited in the pin configuration [Meier 2003].

A way to mitigate the light-induced degradation is to reduce the probability of free carrier's recombination by increasing the electric-field in the device. This is done by sub-dividing the total thickness of a-Si:H material into two, or three, sub-cells. Therefore the individual cells are electrically and optically connected in series (see Fig. 1.1 for an example of tandem: two sub-cells).

The first efficient μc-Si:H solar cell device was deposited at IMT in 1994 by Meier *et al.* [Meier 1994]. This innovation, carried out first by "micro doping" and then thanks to successful deposition of true oxygen-free mid-gap intrinsic μc-Si:H material, opened the way towards higher stable efficiencies for TF Si solar cells. Indeed, depending on the

crystalline volume fraction of the photoactive layer [Meillaud 2005], these μc-Si:H solar cells do not suffer from the Staebler-Wronski effect [Meier 1994]. This innovation was the first step of the invention of the micromorph concept.

1.2 The micromorph solar cell

The invention, in 1996 by Meier *et al.*, of the micromorph solar cell device [Meier 1996] is an important consequence of the possibility to fabricate μc-Si:H solar cells. The micromorph is a tandem solar cell made of *micro*crystalline and a*morph*ous silicon, thus the name of this device. It consists of a serial optical and electrical connection of a high bandgap a-Si:H top cell and a low bandgap μc-Si:H bottom cell. The optical absorption spectra of a-Si:H, μc-Si:H and crystalline Si (c-Si) are plotted in Fig. 1.2. For wavelengths λ in the visible range of the spectrum, the optical absorption coefficient α of a-Si:H is about twice higher than for μc-Si:H. For $\lambda > 700$ nm, α of a-Si:H abruptly falls down. Thus, a-Si:H is transparent to photons with $\lambda > 800$ nm because their energy is smaller than its optical energy bandgap E_g (1.7 eV). On contrary, the E_g of μc-Si:H (which is a multiphase material) is lower and can be approximated by the energy bandgap of c-Si (1.12 eV). Therefore, the absorption band-edge of μc-Si:H corresponds to a wavelength of about 1100 nm. This makes μc-Si:H suitable to convert photons of the near infrared (NIR) part of the solar spectrum into photo-excited carriers. Therefore, in the micromorph device, the top cell absorbs photons in the visible part of the spectrum, whereas the bottom cell absorbs red and infrared photons.

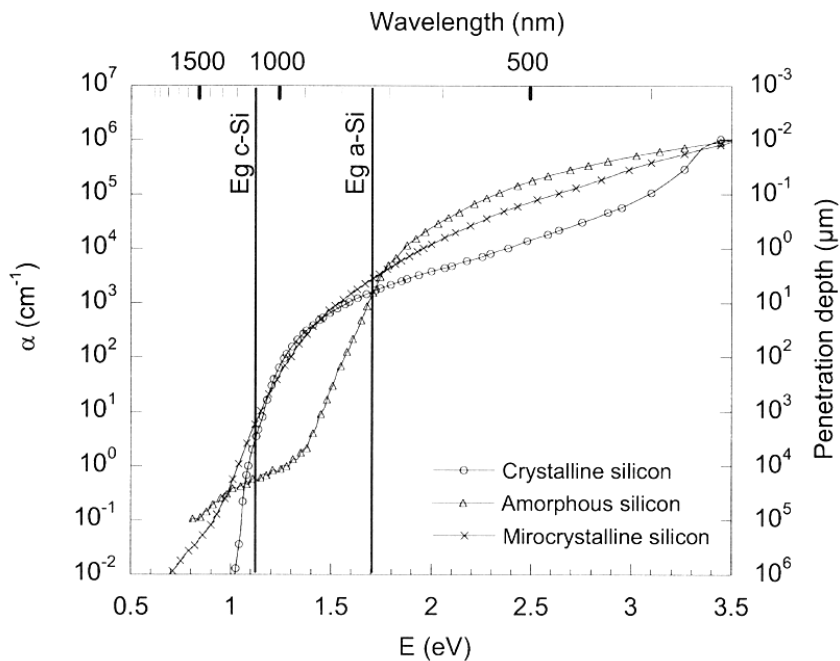

Fig. 1.2: Absorption spectra of amorphous, microcrystalline and crystalline silicon reproduced from [Shah 2004]. The values of the absorption coefficient α and the corresponding penetration depths are ported on the left and right axis, respectively. The vertical lines indicate the bandgap energies of amorphous silicon (E_g a-Si) and crystalline silicon (E_g c-Si).

We will see in chapter 7 that, to minimize Staebler-Wronski degradation in the top cell, the a-Si:H absorber should be thinner than typically 300 nm. As a consequence of the electrical series connection of the tandem device, this constraint considerably limits the photo-generated current density in the top cell and, as a result, the η of the whole device. A solution to this issue was proposed by Fisher *et al.* [Fischer 1996] and consists in introducing an intermediate reflector layer (IRL) between the top and bottom cell to preferentially increase the light intensity in the top cell, and, consequently, its photo-current. The IRL must be made of a low refractive index material, Fisher *et al.* used ZnO.

A schematic description of the micromorph cell device such as studied in this work and a cross-section of an actual device are given in Fig. 1.3.

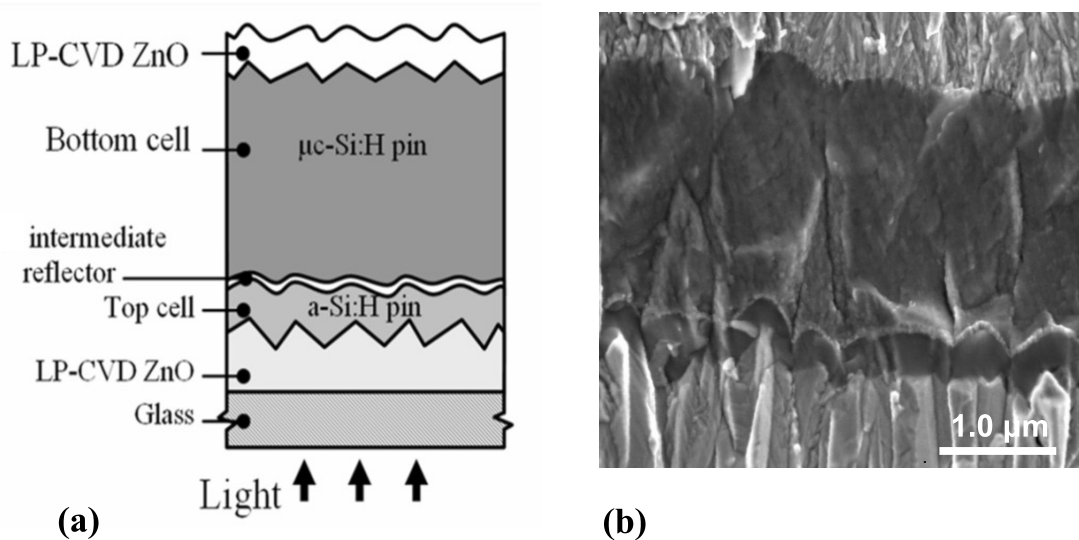

Fig. 1.3: (a) Structure of the micromorph solar cell device with intermediate reflector layer (IRL) and deposited on as-grown surface-textured ZnO:B layers deposited by the low-pressure chemical vapor deposition (LPCVD) technique. (b) Scanning electron microscopy micrograph of a cross-section of a micromorph solar cell with a ZnO IRL and two LPCVD ZnO layers for the front and back contacts.

The world record η for a micromorph device tabulated in the “Solar Cell Efficiency Tables” [Green 2009] is held by Kaneka Corp. for a micromorph mini-module (14.23 cm^2 of aperture area) with a stabilized η of 11.7%, obtained in 2003 by Yoshimi *et al.* [Yoshimi 2003]. Yamamoto *et al.* from the same company demonstrated, for devices incorporating an IRL (material of the reflector not disclosed), record initial values of η = 13.2% for a micromorph module with an aperture area of 910x455 mm^2 and 14.7% for a 1 cm^2 micromorph solar cell [Yamamoto 2003].

1.3 Aim and outline of this thesis

Basically, the aim of this work is to demonstrate high efficiency 1 cm^2 micromorph solar cells deposited in the laboratory scale VHF-PECVD reactors (substrate size: 8x8 cm^2) used at IMT. This thesis focuses on improvement of current density in the micromorph device dealing with current-matching issues. The strategy is to take profit of the versatility of the LPCVD technique for the fabrication of dedicated front TCO layers and to manage the photo-current density in each of the component cells of the micromorph with the insertion of an intermediate reflector.

Following this strategy, it becomes clear that the effects of the front TCO layer and of the IRL are optically and electrically coupled. The electrical coupling actually takes place via current matching of the tandem, but is also influenced by the quality of the μc-Si:H material grown on different substrate morphologies. Another aim of this work is therefore to provide insight on these different effects to ultimately draw guidelines for device development.

The following chapter 2 focuses on a description of the particular experimental techniques used in this work.

Chapter 3 describes a novel plasma post-treatment of the surface of our LPCVD ZnO:B layers. This chapter mainly focuses on the effects observed on the ZnO layer itself.

Chapter 4 focuses on the dramatic impact of this plasma post-treatment on the performances of single junction μc-Si:H solar cells and on the open-circuit voltage (V_{oc}) of single junction a-Si:H and micromorph solar cells. The role of nanoporosity (cracks) induced by the growth of the μc-Si:H material is emphasized in this chapter. Thanks to the plasma post-treatment, a new type of LPCVD ZnO layer can be used for solar cell deposition without impairing losses in V_{oc} and fill-factor (FF): a lightly doped layer with an increased thickness, larger grains and lower free carrier absorption (FCA).

Chapter 5 is dedicated to the analysis of single junction μc-Si:H solar cells by scanning electric-probe atomic force microscopy (AFM) –based methods. These measurements have been carried out during a stay in the Analytical Microscopy Group, leaded by Dr. M. M Al-Jassim, at the National Renewable Energy Laboratory, in Golden, Colorado. The techniques described here are scanning Kelvin probe microscopy (SKPM) and two original methods based on conductive-AFM measurements. The aim of these microscopic analyses is to study, at the nanometric scale, the distribution of the electric-field and of the local V_{oc} for μc-Si:H devices deposited on a surface-textured substrate. The main result is that differentiated electrical behaviors are evidenced for different μc-Si:H clusters. Therefore, a p-i-n μc-Si:H solar cell deposited on a LPCVD ZnO front contact can be thought as the parallel connection of the individual nanodiodes formed by the μc-Si:H clusters which are growing during the PECVD deposition on the top of each pyramid of the ZnO layer.

Chapter 6 is a theoretical and experimental study of the scattering of the light transmitted through a rough nano-textured front TCO layer. The chapter contains a review of the theoretical and experimental approaches used in the TF Si PV community to handle this complicated problem. In particular, the Yablonovitch's theoretical limit for the effective light path enhancement by means of Lambertian scattering is recalled. Then, a modified scalar scattering theory proposed by Harvey *et al.* is explained in details. After that an original approach, based on the scalar scattering theory as modified by Harvey *et al.*, and using random phase screens for the modeling of the front TCO layer, is presented. The calculation results obtained with this approach are successfully confronted to results of angular resolved scattering (ARS) measurements. Finally, the case of light scattering at the internal ZnO/Si interface is analyzed theoretically. The results are confronted to experimental external quantum efficiencies (EQE) of micromorph solar cells. This comparison demonstrates that ARS is the pertinent light scattering measurement, and not haze only, to assess the potential of a given surface morphology to produce an efficient light trapping of long wavelengths in silicon. However, this approach is not sufficient to successfully predict the behavior of light in the top cell of a micromorph tandem device with intermediate reflector.

Chapter 7 concerns the insertion, in the micromorph solar cell device, of different IRL made of ZnO (deposited *ex situ*) or silicon oxide based material (deposited *in situ*). The chapter starts with a theoretical analysis of the impact of current mismatch on the fill-factor (FF) of the cell. Then, experimental studies are carried out in order to extract rules on the effectiveness of the IRL in increasing the current density of the top cell ($J_{sc,top}$). Attention is paid to the interplay between the front contact morphology and the IRL. Two main results are obtained. (i) An experimental demonstration that for any thickness of the IRL, the gain in current density of the top cell ($\Delta J_{sc,top}$), when an IRL is introduced inside the device, is always larger in the incoherent case of nano-textured interfaces than in the coherent case of flat interfaces with an interferential (single layer) IRL; with a maximum gain of $\Delta J_{sc,top}$ = 2.8 mA/cm^2 achieved so far. (ii) The proposition of the concept that IRL actually promotes the light trapping capability of the front TCO layer in the 550-700 nm spectral range: the better this capability, the higher the gain $\Delta J_{sc,top}$. The chapter continues with the comparison of the V_{oc} of micromorph solar cells incorporating IRL layers with different in-plane conductivities. It ends with a proof of concept for the need of IRL to achieve large J_{sc} values (close to 14 mA/cm^2) in micromorph solar cells without impairing FF with a detrimentally thick a-Si:H top cell. Along different sections of this chapter 7, the best micromorph solar cells obtained at the time of carrying out the experiments are presented. The best initial η is 13.3% for a 1.2 cm^2 micromorph cell deposited on a glass plate with a broadband anti-reflection (AR) coating. The thicknesses of the top and bottom cells are 340 nm and 3.5 μm, respectively and a 150-nm-thick IRL is used. This yields a J_{sc} value of 13.8 mA/cm^2. The best stabilized device achieved in this work is a micromorph cell with 11.1% stabilized conversion efficiency (1.2 cm^2 and no AR

coating). The thicknesses of the top and bottom cells are 300 nm and 3.0 μm, respectively and a 150-nm-thick IRL is used.

Chapter 8 discusses first the anti-reflection effect produced by the rough front TCO/Si interface of our devices. It is demonstrated that on contrary to the intuition, refractive index grading effects play a minor role in decreasing the primary reflectance at this interface. The chapter continues with a comparison of the respective contributions of light trapping enhancement and reduction of free carrier absorption (FCA), in the increase of J_{sc} achieved in our micromorph solar cells when deposited on the thick, large grain, and lightly doped LPCVD ZnO:B layers. Results show that more than 50% of the gain in the total cell current density is produced by the decrease of free carrier absorption. Other calculations show that, the maximum effective light path enhancement obtained with the different LPCVD ZnO:B layers, once the effect of FCA is canceled, is around 22 paths with all these TCO. With n_{Si}~3.8, this factor is still ~2.5 times smaller compared to the theoretical Yablonovitch's upper limit of $4 \cdot n_{Si}^2$ and leaves room for further improvement.

A summary and the conclusions with perspectives for further studies and device efficiency improvement follow in chapter 9.

1.4 Contribution of this work to the research field

In the last years, the research on the micromorph solar cell has continued to be one of the major subjects in the TF Si PV research field. The topics of the intermediate reflector layer (IRL) and of light trapping by means of nano-textured front contacts have gained in importance. The topic of the change of the surface morphology of the substrate to make it suitable to the growth of μc-Si:H material without nanoporosity is just emerging. This PhD thesis has contributed to the research field with the following elements:

- Modification of the surface morphology of the front LPCVD ZnO layer to make it suitable to the growth of μc-Si:H material without nanoporosities (cracks) (see 4.3 and [Bailat 2006, Dominé 2006])
- For the first time, in our best knowledge, the angular distribution of the light scattered through a TCO used in TF PV technology is successfully calculated directly from the scalar scattering theory and AFM pictures of the surface considered (see 6.3)
- An experimental study on the effect of the insertion of an IRL proposes values for the gains and for the losses, per nm of IRL thickness, in the top and bottom cell current densities, respectively (see 7.3 and [Dominé 2005])
- Experimental observation of the relationship between the effectiveness of the IRL and the light trapping capabilities of the front TCO is given for the first time (see 7.5 and [Dominé 2006, Dominé 2008a, Dominé 2008b])

- SKPM measurement are carried out on cross-sections of working devices deposited on a rough substrate, with the possibility to change the bias-voltage at the terminals of the device during the analysis of the sample and original data are obtained (see 5.2.2 and [Dominé 2007])
- Experimental evidences are given, from scanning electric-probe AFM measurements, that the μc-Si:H clusters which are growing during the PECVD deposition on the top of each pyramid of a LPCVD ZnO layer, have a differentiated electrical behavior, once the back contact is removed (see 5.3 and 5.4)
- Micromorph solar cell with initial conversion efficiency of 13.3% and current density of 13.8 mA/cm^2 are obtained as well as devices with stable efficiency > 11% (see 7.5.3 and [Dominé 2008b]). The last value represents state-of-the-art value for cells > 1 cm^2 without anti-reflection coating and perspectives for further improvement are excellent.

2 Deposition and characterization techniques

In this chapter, we briefly describe the deposition process of our transparent conductive oxide layers and pin silicon thin-film solar cells. Then we describe the principle of particular characterization techniques used in this work. Experimental details on the experiments described in this thesis are given in the experimental section of the corresponding chapters.

2.1 Micromorph cell fabrication

2.1.1 Zinc oxide layers deposited by the low pressure chemical vapor deposition (LPCVD) technique

The transparent conductive oxide (TCO) electrodes used in this work are as-grown surface-textured boron-doped zinc oxide (ZnO:B) layers deposited by the low pressure chemical vapor deposition (LPCVD) technique. They are deposited on glass plates from diethylzinc (DEZ) and water vapors and from diborane (B_2H_6) used as the doping gas. Details of the process can be found in [Fay 2003] and [Steinhauser 2008b]. The thickness and the doping of the films are adapted to obtain layers with a sheet resistance of approximately 10 Ω/sq [Steinhauser 2005]. In this work, two thicknesses are mainly used for solar cell deposition: ZnO layers of about 1.8 and 4.5-µm-thick. This results in a small grain layer optimized for single junction a-Si:H solar cells (Type-A ZnO layer); and in a lightly doped, large grain layer (Type-B). A plasma post-treatment is usually applied to the surface of the Type-B LPCVD ZnO layer to obtain a Type-C layer, with possibly, different post-treatment durations. Typical scanning electron micrographs of these Type-A, -B and -C layers are presented in Fig. 2.1.

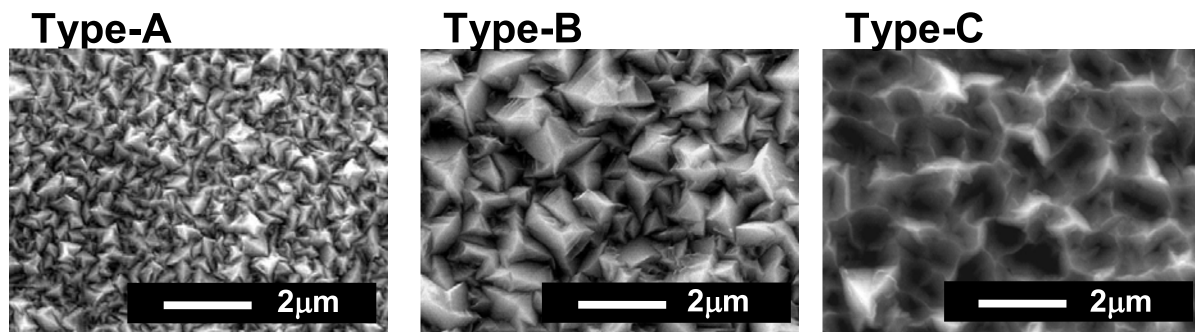

Fig. 2.1: Typical scanning electron micrographs of the Type-A, Type-B and Type-C ZnO layers used in this work. Type-A is the small feature sizes LPCVD ZnO layer optimized for a-Si:H solar cells, it has no or a short plasma post-treatment of its surface (< 5 min). Type-B is a thick, lightly doped, as-deposited large grain ZnO layer; and Type-C is a Type-B layer with a plasma post-treatment of its surface of typically 10 to 80-minute duration.

2.1.2 Silicon deposition by the very high frequency plasma enhanced chemical vapor deposition (VHF-PECVD) technique

The thin-film silicon layers fabricated in this work are deposited by very high frequency plasma enhanced chemical vapor deposition (VHF-PECVD) from the decomposition of silane, hydrogen and dopant gases [Curtins 1987]. Figure 2.2 illustrates very schematically the principle of operation of a PECVD reactor. It consists of a vacuum chamber with a gas mixture feed-in and a pumping unit which allow for process pressure regulation. Two parallel plate electrodes are mounted in the chamber. The substrate is charged in the upper grounded electrode (anode) while the second electrode (cathode) is powered by the VHF-source by means of a capacitive coupling. A glow discharge of the gas mixture in the chamber is then initiated and sustained by the VHF power. This leads to the decomposition of the species present in the gas phase into radicals and ions. These precursors in turn participate to the growth of a film. The unused gas are burned before the exhaust.

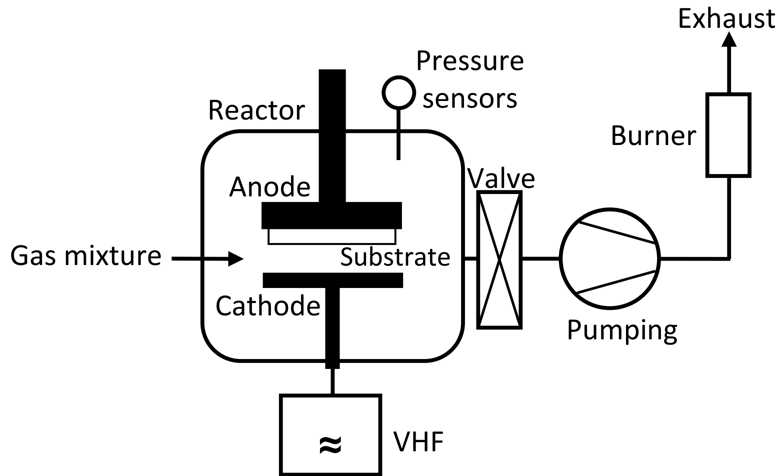

Fig. 2.2 from [Torres 1998]: Schematic representation of a VHF-PECVD reactor.

In this work, three different VHF-PECVD deposition systems have been used; they are listed in Table 2.1, with a brief description of the ranges of deposition parameters.

Table 2.1: VHF-PECVD deposition systems used in this work.

Description	system C	system B	KAI-S
Origin	in-house	in-house	Oerlikon Solar
Dual chamber	no	yes	no
Substrate size (cm^2)	8x8 cm^2	8x8 cm^2	35x45 cm^2
Excitation frequency (MHz)	70 MHz	110 MHz (doped layers) 120 MHz (intrinsic layers)	40 MHz
Deposition pressure (μbar)	300-600	300-700	-
Substrate temp. (°C)	200-250	200-250	-

The industrial system KAI-S was used for massive co-deposition of standard top cells for further thickness series of intermediate reflector layers (IRL) and/or IRL material comparisons. State-of-the-art a-Si:H top cells were first deposited in the single chamber system C while the bottom cells were deposited in the dual deposition chamber system B. In a second time, the entire micromorph tandem devices were deposited in the dual chamber system B.

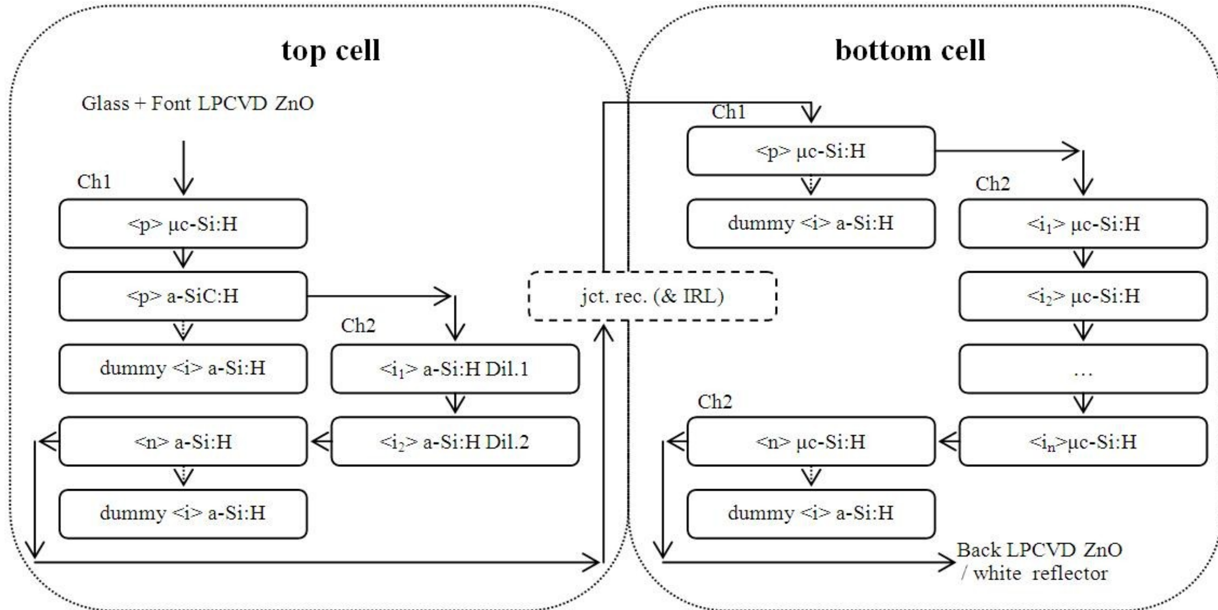

Fig. 2.3: Typical deposition sequence in a dual chamber deposition system (Ch1 and Ch2) for the fabrication of a micromorph solar cell with, our without, an intermediate reflector layer (IRL). After deposition of each doped layer in Ch1, this chamber is covered by a dummy a-Si:H layer. See text for details.

Figure 2.3 schematically explains the deposition sequence for a micromorph solar cell with or without an IRL in a dual chamber deposition system (system B: Ch1 and Ch2). The first silicon layer is a highly doped p-type μc-Si:H film. Thanks to its heavy doping, the narrow depletion width in this layer allows for tunneling at the Schottky barrier formed by the ZnO/Si interface. A large energy bandgap p-type amorphous silicon carbide alloy is then deposited to build the built-in potential while keeping low the absorptions losses in this window layer. The top cell absorber is deposited under high dilutions of silane in hydrogen, this, in order to minimize light-induced degradation. After deposition of the n-type layer, the process continues with deposition of a fully microcrystalline bottom cell. Before this, an intermediate reflector can be deposited (in-situ or ex-situ). For the problematic of the recombination junction between the top and the bottom cell, refer to the comprehensive study of Pellaton et al. in [Pellaton 1998]. The silane concentration SC is adapted during the deposition of the bottom cell absorber. This is to ensure that, growing conditions are maintained close to the transition between amorphous

and microcrystalline growth during the whole deposition of the intrinsic μc-Si:H layer. After deposition of each doped layer in Ch1, this chamber is covered by a dummy intrinsic a-Si:H layer. At the end of this PECVD process, the back ZnO electrode is deposited by LPCVD and a dielectric white reflector is applied to the cell.

2.2 Characterization techniques

2.2.1 Illuminated current-voltage measurement (I-V)

The current-voltage (I-V) characteristics of the illuminated solar cells are obtained under a class A steady-state dual lamp sun simulator (XS140s Wacom). The xenon lamp and the halogen lamp in the simulator reproduce the 1000 W/m^2 AM1.5g solar spectrum which corresponds to the sun energy incident normalized at 1000 W/m^2, at each wavelength, on a 37° sun-facing tilted surface relative to the horizontal under standard atmospheric conditions (see [IEC 2005] for a complete description of these standard conditions). The open-circuit voltage (V_{oc}), the fill factor (FF), and the short-circuit current (I_{sc}) are deduced from a four probe voltage sweep measurement operated with a Keithley 2700 sourcemeter. The room temperature is maintained at 25°C and a shutter allows illumination of the cell under measurement only during the few seconds needed for the I-V sweep.

2.2.2 External quantum efficiency (EQE)

External quantum efficiency (EQE) is a measure of the probability for an incident photon at a given wavelength to create an electron-hole pair that will contribute to the external current density of the solar cell. Experimentally, the solar cell under measurement is illuminated with a chopped light beam crossing a monochromator. At each wavelength, the photocurrent is measured and divided by the product of the elementary charge q and the incident flux of photons incident on the device. This flux is determined with a calibrated reference detector.

EQE can be performed under a voltage bias in order to superimpose an external electric-field onto the internal field of the solar cell. In reverse bias condition, the collection of the generated carriers increases (recombination losses become negligible) and all generated electron-hole pairs are collected. By comparing the EQE curves with and without the reverse bias, one can therefore distinguish between optical and collection losses.

Quantum efficiency measurement can also be used to evaluate the short-circuit current density (J_{sc}) of the solar cells by integration, over the wavelengths of the incident photons, of the product of EQE with the photon flux of AM1.5g spectrum. This method is more precise to determine J_{sc} than J-V measurement under a sun simulator with uncertainties of its spectrum, and when the area of the solar cell cannot be measured precisely.

Due to the series connection, the current of a multi-junction solar cell is limited by the sub-cell with the lowest photocurrent (limiting sub-cell). Therefore, for tandem solar cells, the EQE of the two component cells can be measured separately. The method was first proposed by Burdick et al. [Burdick 1986], and consists in the illumination of the tandem device by a colored bias light. When the tandem cell is illuminated with a blue bias light, the current photogenerated in the top cell absorber is much larger than in the bottom cell. Shining the low intensity chopped monochromatic light probe on the tandem, the current through the device will follow the photocurrent of the bottom cell, because it is the limiting one. Therefore with a blue bias-light, EQE of the bottom cell is measured. When a red bias light is used, the top cell becomes the limiting one and thus its EQE is measured.

2.2.3 Ultra-violet, visible, and near infrared spectroscopy

The total and diffuse transmittances spectra (T_{tot} and T_{dif}) of the LPCVD ZnO layers and the total reflectance spectrum (R_{tot}) of the silicon thin-film solar cells deposited in this work are measured with a Perkin Elmer dual beam UV/VIS/NIR Lambda 900 spectrometer equipped with an integrating sphere. The light sources are deuterium and halogen lamps. A monochromatic beam produced by a grating monochromator over the wavelength range from 320 nm to 2000 nm is directed on the sample trough the entrance port of the integrating sphere. A second monochromatic beam enters the sphere through another entrance port (the reference beam in Fig 2.4). Two detectors (a photomultiplier and a lead sulphide detector) are placed inside the integrating sphere and measure the intensities of these two beams, which are discriminated with a chopper technique. The change in reflectivity of the sphere due to the open port and the sample is deduced from the intensity of the reference beam. This change of reflectivity is used to correct the measured intensity of the "sample beam".

This equipment measures optical reflectance and transmittance of samples that diffuse the light. Before measurement of the sample, a calibration is performed by measuring a 100% background, with a 100% reflectance reference (Spectralon™) installed at the position "sample" in Fig. 2.4(b). Then, for transmittance measurements, the sample is placed at the entrance of the sphere (Fig. 2.4(a)); for reflectance measurement, it is placed at the rear side (Fig. 2.4(b)). To measure the diffuse part of the transmittance or reflectance the port at the opposite side of the sample must be opened (see Figs. 2.4(a) and (b)). With this setup, transmitted intensity diffused with a scattering angle larger than $\alpha = 5°$ is (arbitrary) considered as diffuse (see Fig. 2.4(a)).

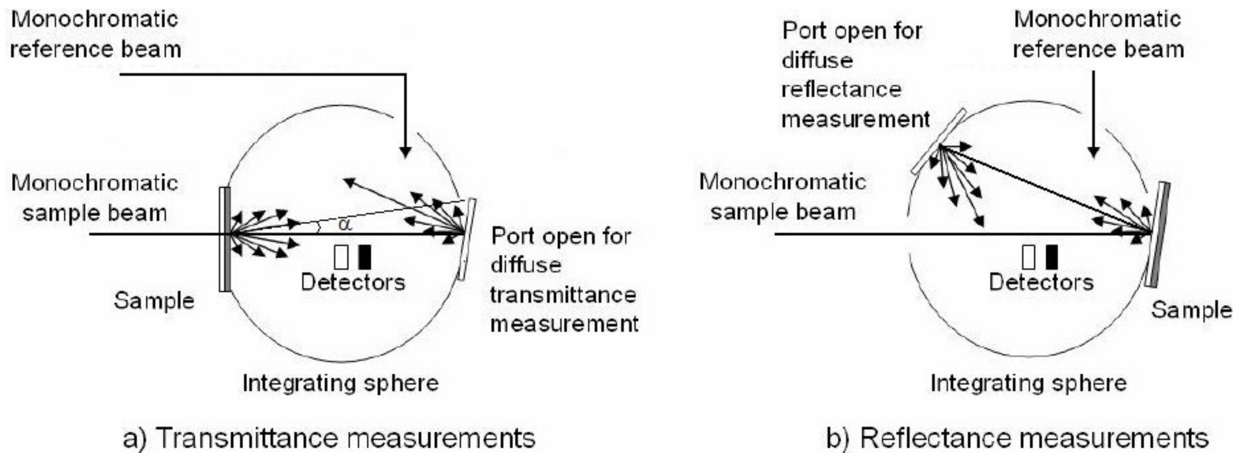

Fig. 2.4 adapted from [Steinhauser 2008b]: Schematic diagram of the configurations used to measure (a) the transmittance and (b) the reflectance spectra with an integrating sphere. The value of the angle α in (a) is 5°; it defines an arbitrary threshold of discrimination between specular and diffuse transmittance.

2.2.4 Angular resolved scattering measurement (ARS)

Angular resolved scattering measurements (ARS) are carried out with a set-up built at the IMT. In this work, measurements are performed with a laser beam (544 nm or 633 nm) normally incident on the glass side of glass/ZnO structures (see Fig. 2.5). The angular distribution of the intensity scattered in transmission is measured with a silicon photodetector mounted on a goniometric arm and rotating in a plane normal to the direction of incidence. The diameter of the laser beam is about 1.5 mm and the length of the arm of the photogoniometer is such that the radius of the observation hemisphere is 115 mm. Assuming an isotropic scattering over the azimuthal angle φ, only the polar angle θ is scanned. This is done with a stepper motor by increments of 1.44°, from -90° to +90°. The intensity diffused for each value of θ is measured with a lock-in detection technique using a Stanford Research instrument SR830 lock-in amplifier. ARS measurements can be represented in two ways:

(1) The normalized radiant intensity defined as $ARS(\theta) = I(\theta)/P_0 = \langle dP/d\Omega \rangle /P_0$ is plotted on a logarithmic scale versus the scattering angle θ; where $I(\theta) = \langle dP/d\Omega \rangle$ is the radiant intensity measured in units of watts per steradian with the photogoniometer, P_0 is the total incident power, and the brackets $\langle \cdot \rangle$ denote an average over the ensemble of realizations of a random process. When the illuminated surface area is much larger than the wavelength of the incident laser beam, this ensemble averaging is inherently contained in the experimental data [Elson 1980].

(2) The total intensity scattered at the angle θ is calculated by integration over the azimuthal angle φ and plotted versus θ [Stiebig 2000, Schulte 2007]. Considering an isotropic scattering over φ, the integration over φ yields a simple multiplication by a factor sin θ. The total intensity profile $ARS(\theta) \cdot |\sin\theta|$ is proportional to the probability density function

associated, in the scattering process, to the angular distribution function (ADF) of the possible values for θ [Krc 2002]. Therefore, the most probable scattering angle corresponds to the position of the maximum of the profile ARS(θ)·|sin θ|.

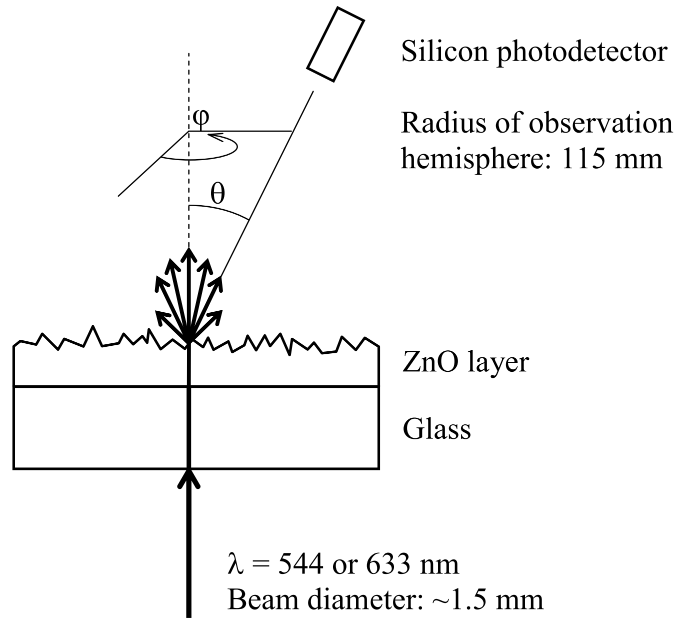

Fig. 2.5: Determination of the angular distribution of the intensity scattered in transmission trough glass/ZnO structures by angular resolved scattering measurement (ARS).

2.2.5 Conductive atomic force microscopy (C-AFM)

Conductive atomic force microscopy (C-AFM) measurements are performed in air with a Dimension 3100 scanning probe microscope from Digital Instruments operating in contact mode (see Fig. 5.8 in chapter 5). The cantilever spring constant is about 40 N/m, and the tip is made of phosphorus-doped Si coated with a doped diamond layer. The tip is connected to a current-voltage converter (trans-impedance amplifier). The polarization of the tip is maintained to the ground potential by the input of the trans-impedance amplifier while a bias voltage V_{bias} is applied to the front contact of the sample. This allows an electric current flowing through this contact and the tip via the probing point. While the tip is scanning on the surface of the sample, current maps and topography pictures are acquired.

2.2.6 Scanning Kelvin probe microscopy (SKPM)

The principle of operation of scanning Kelvin probe microscopy (SKPM) is based on the contact potential difference V_{CPD}, evidenced by Lord Kelvin, between any two faces of two metals with different work functions. V_{CPD} is given by the difference of the work functions, including changes due to adsorption layers on these surfaces [Nonnenmacher 1991]. If W is the unknown work function of a sample, and W' is the work function of a reference metallic probe, V_{CPD} is given by:

$$V_{CPD} = -1/q \cdot (W - W'), \quad (2.1)$$

where q is the (positive) elementary charge of the electron. Fig. 2.6 schematically explains the built-up of the potential difference V_{CPD} producing an electric-field in the region between two metallic surfaces, for the case without surface band-bending.

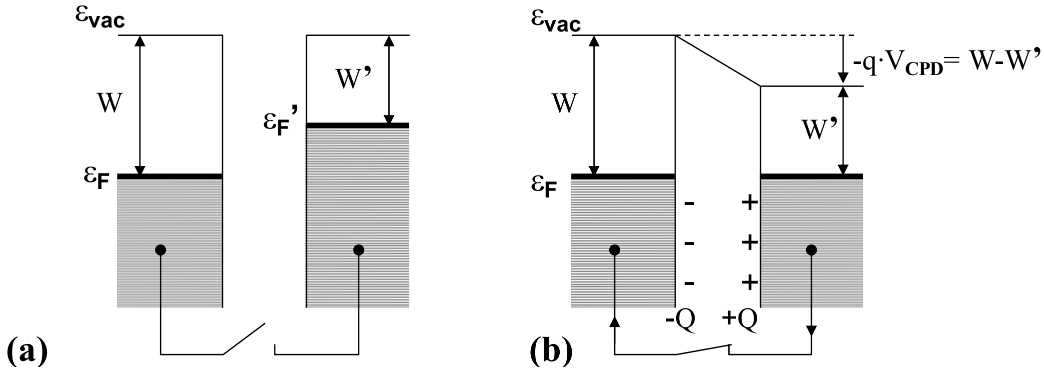

Fig. 2.6: Schematic energy band diagrams, without surface bend-bending, for two metallic samples with different work functions W and W' when the two samples are (a) electrically insulated and (b) in contact. ε_{vac} refers to the vacuum energy level. ε_F and ε_F' are the Fermi levels of the two samples, respectively. Once they are put into contact, an electrical current takes place until equilibrium is reached. The total charge transfer needed to reach equilibrium (i.e. to equals ε_F and ε_F') is noted Q and induces an electric-field between the two surface corresponding to the contact potential difference V_{CPD} =-1/q·(W – W'), where q is the (positive) elementary charge of the electron.

To determine the work function of a sample, Zisman proposed the vibrating capacitor method in 1932 where a vibrating reference metallic probe is placed just above the surface to be characterized. In this technique, an external DC voltage V_{ext} is applied between the reference probe and the sample. Because the probe is vibrating, the equivalent capacitance C(t) formed by the probe and the surface changes periodically. As the probe and the sample are electrically connected, the charge Q(t) transferred between them at the time t permanently accommodates. This maintains V_{CPD} constant and thus the equilibrium of the system:

$$Q(t) = C(t) \cdot (V_{CPD}+V_{ext}). \quad (2.2)$$

The resulting electrical current I(t) can be nullified by tuning V_{ext} to the value $-V_{CPD}$. This provides an indirect measurement of V_{CPD} between the reference probe and the surface of the sample:

$$I = dQ/dt$$
$$= dC/dt \cdot (V_{CPD}+V_{ext})$$
$$= 0 \text{ when } V_{ext} = -V_{CPD}. \quad (2.3)$$

With the aim to obtain maps of the local work function with a high lateral resolution, Nonnenmacher *et al.* invented, in 1991, the Kelvin probe force microscopy [Nonnenmacher 1991]. It consists to measure a force instead of a current, making usage of the tip of an atomic force microscope (AFM). On contrary to the Zisman's technique, in the Nonnenmacher's technique, the probe tip is not vibrating by means of a mechanical excitation. Instead, the bias voltage applied between the tip and the surface is formed by an ac component $V_{ac} \cdot \sin(\omega t)$ with circular frequency ω superposed to a dc component V_{dc}. This induces an electrostatic force between the tip and the surface, normal to its plane, given as a first approximation by (see e.g. [Ballif 2001]):

$$F = ½C'[V_{dc} + V_{ac} \sin(\omega t) – V_{CPD}]^2 = F_0 + F_1 \sin(\omega t) + F_2 \cos(2\omega t), \quad (2.4)$$

where C' derives from the tip-sample capacitance and where the amplitude of the ω component of the Coulomb force interaction between the tip and the sample is given by:

$$F_1 = -C'(V_{dc} – V_{CPD}). \quad (2.5)$$

If the dc voltage bias V_{dc} added to the tip equals and compensates V_{CPD}, then F_1 cancels and the corresponding vibration of the AFM microscope's cantilever at the circular frequency ω vanishes. The scanning Kelvin probe force microscopy, hereafter called a bit shortly scanning Kelvin probe microscopy (SKPM), consists in recording those values of V_{dc} needed to cancel F_1.

Figure 2.7 shows a schematic diagram of the SKPM set-up used in this work. The SKPM experiments are performed in air at the same time as non-contact AFM using a ThermoMicroscopes Autoprobe CP Research system. The Si probe has a small cantilever spring constant of about 2 N/m and is platinum-coated at the tip side. The first cantilever resonant frequency ($\omega_r/2\pi$) of about 70 kHz is used for the topographic imaging (AFM image). For the Kelvin probe, the frequency $\omega/2\pi$ of the ac voltage applied to the tip is about 20 kHz. The ω component of the vibration of the cantilever is sensed using a lock-in detection technique (SR830 DSP Lock-in Amplifier from Stanford Research). V_{dc} is produced and regulated by connecting a proportional-integral (PI) servo-controller (ECAP Interface Module from Park Scientific Instruments) between the output of the lock-in

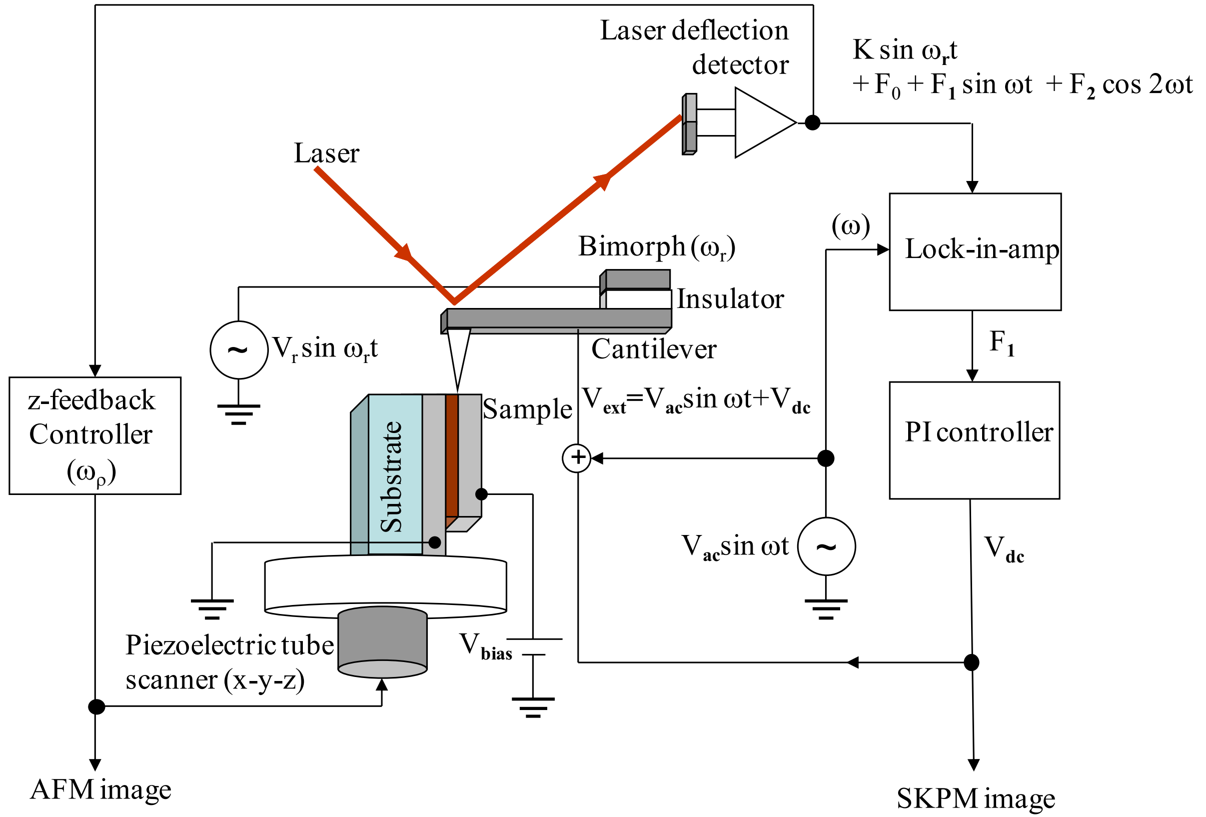

Fig. 2.7: Schematic diagram of the SKPM setup for simultaneous topographic (AFM image) and V_{CPD} (SKPM image) measurements, including an atomic force microscope (AFM) Autoprobe CP Research from ThermoMicroscopes, a lock-in amplifier SR830 DSP from Stanford Research and proportional-integral (PI) controller ECAP from Park Scientific Instruments. During the SKPM measurement, the sample can be biased with

amplifier and the tip. As the servo-controller contains an integrator, the absolute value of V_{dc} increases until its input signal, i.e. the ω component, cancels. Consequently, V_{dc} equals V_{CPD} and is thus recorded during the scan to produce the SKPM potential image. This image corresponds to the distribution of the electrochemical surface potential on the surface of the sample. A higher (smaller) value in the SKPM potential image corresponds to a smaller (higher) local work function on the surface of the sample. During the SKPM measurement, the sample can be biased with the voltage V_{bias}.

In our case, the tip probe is metallic (platinum-coated) and the sample is a semiconductor (μc-Si:H, see chapter 5). Therefore, the energy band diagram of the system tip-surface is complicated by the band bending of amplitude ψ produced at the surface of the semiconductor by filling of electronic surface states and possibly by surface contamination, oxidation, and water adsorption. This is illustrated in Fig. 2.8. From this figure we see that V_{CPD}, accessible by SKPM measurements, is given by:

$$V_{CPD} = -1/q \cdot [W_m - (\chi_{sc} + \Delta E_{Fn} + \psi)], \qquad (2.6)$$

where W_m is the wok function of the metallic tip, χ_{sc} the electron affinity of the semiconductor, ΔE_{Fn} the distance between the bottom of the conduction band and the Fermi level in the bulk of the semiconductor and ψ the amplitude of the band bending at the surface of the semi-conductor. Therefore, as ψ can change over the surface of the sample area, it is clear that the direct application of the SKPM technique cannot give without ambiguity information concerning the bulk of the semiconductor. This is the reason why in chapter 5, we will often consider *differences* of SKPM measurements induced by variations of the bias voltage V_{bias} applied to the sample.

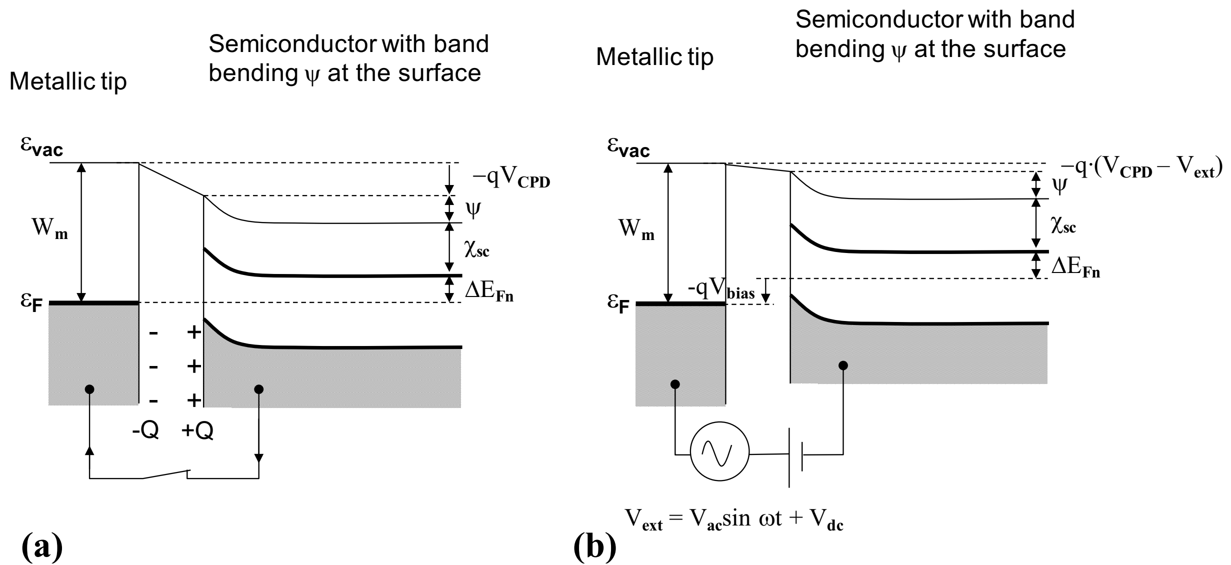

Fig. 2.8: Energy-band diagram of the system metallic tip–semiconductor, with a band-bending of amplitude ψ at the surface of the semi-conductor, (a) when the two surfaces are in contact and (b) when an external V_{ext} is applied between the tip and the sample (such as V_{ext} in Fig. 2.7). ε_{vac} refers to the vacuum energy level, ε_F to the Fermi level, W_m to the work-function at the surface of the metallic probe, χ_{sc} to the electron affinity of the semiconductor, ΔE_{Fn} to the distance between the bottom of the conduction band and the Fermi level in the bulk of the semiconductor.

3 Modification of the surface morphology of LPCVD ZnO layers by means of plasma post-treatments

In this chapter, modifications of the surface morphology of as-grown textured ZnO layers are demonstrated. The modification method consists in a plasma treatment, applied after deposition (post-treatment), to the surface of the layer. A motivation for a change of surface morphology is given in section 3.1. After a description of the experimental methods in section 3.2, we study the effect of different compositions of the plasma discharge in section 3.3. In section 3.4, we examine localy the progressive change of the surface morphology when the duration of the post-treatment is increased. In section 3.5, we summarize and comment on these results.

3.1 Introduction

The front transparent conductive oxide (TCO) layers used at IMT are ZnO:B films deposited by the low pressure chemical vapor deposition (LPCVD) technique. The surface of these layers is covered by pyramid-like features which provide an efficient light scattering for single-junction in amorphous silicon (a-Si:H) solar cells [Fay 2003, Meier 2003]. A decrease of the free carrier absorption (FCA) in the film can be achieved if it is lightly doped. Moreover an increase of the haze in transmission (fraction of the diffuse light intensity over the total transmitted intensity) produced by its rough surface texture is obtained if it is made of large grains. This can be obtained if thicker layers are deposited with a smaller gas phase doping ratio [Steinhauser 2005]. Using these thicker ZnO:B films as front TCO layer, an improvement of the short-circuit current density (J_{sc}) is found for single junction microcrystalline silicon (μc-Si:H) solar cells [Steinhauser 2005, Feitknecht 2005] and micromorph cells [Dominé 2005]. However, deposition of μc-Si:H solar cells on as-grown layers with larger grains systematically leads to a dramatic decrease of open-circuit voltage (V_{oc}) and fill-factor (FF) [Feitknecht 2005]. Previous findings concerning the apparition of cracks in μc-Si:H material near the valleys of surface-textured TCO layers [Nasuno 2001, Bailat 2003], suggest to change the morphology of the surface of the thick LPCVD ZnO:B layers. Following Nasuno et. al in [Nasuno 2001], the idea is to increase the opening angle of theses valleys. Here we suggest that increasing the radius of curvature near the bottom of the valleys is a less restrictive but still sufficient condition to mitigate the above mentioned decreases of V_{oc} and FF.

3.2 Experimental

The LPCVD ZnO:B layers are deposited on glass plates from diethylzinc (DEZ) and water vapors, and from diborane (B_2H_6) used as the doping gas. Details of the process can be found in [Fay 2003] and [Steinhauser 2008b]. The thickness of the layers is approximately 4.5 μm. The plasma treatments with discharges of argon (Ar), oxygen (O_2) or nitrogen (N_2) used to modify their surface morphology are performed in a reactive ion etching

(RIE) vacuum system, at a power density of 1 W/cm^2, pressure of 80 μbar and excitation frequency of 13.56 MHz. The resulting surface morphologies are characterized by scanning electron microscopy (SEM). Some ZnO layers are characterized by atomic force microscopy (AFM) performed in the non-contact mode. The root mean square (rms) value of their surface roughness (σ_{rms}) is calculated from the AFM data (256 x 256 data points on a 10 x 10 μm^2 surface area). Histograms of local angle vs. the normal to the plane of the substrate are also calculated from these data.

For analyzing the evolution of the surface morphology of the same region of interest, AFM microscopy is performed (i) just after deposition of the ZnO:B layer, (ii) after a plasma post-treatment of 40 minutes, and (iii) after an additional treatment of 40 minutes (i.e. after a cumulated duration of 80 minutes). Care is taken to perform the 3 scans (512 x 512 data points on a 5 x 5 μm^2 surface area) precisely at the same location. The final alignment is performed on the AFM pictures themselves by successive shifts and rotations in the x-y plane. The best alignment between two pictures F_1 and F_2 is achieved when their cross-correlation at the origin $F_1 * F_2(0,0) = \sum_m \sum_n F_1(m,n) \cdot F_2(m,n)$ is maximized.

3.3 Comparison of plasma compositions: results and discussion

Figures 3.1(a) to (d) show SEM micrographs of the surface of the ZnO layers as-deposited and after 60 minutes of post-treatment, with a plasma discharge of Ar, N_2, and O_2, respectively.

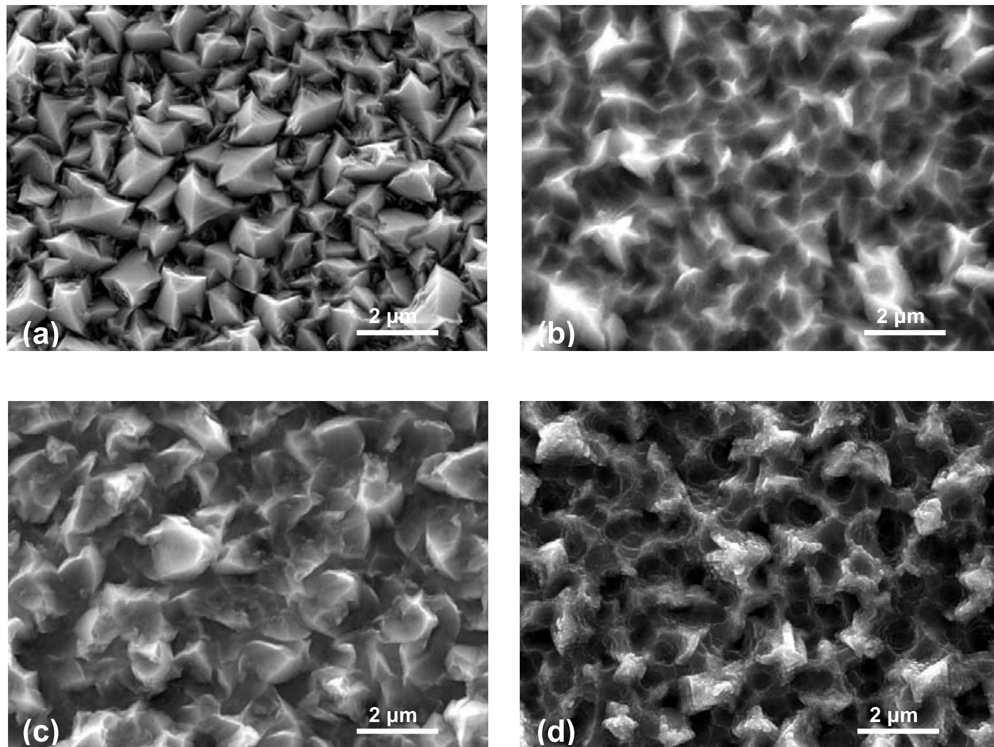

Fig. 3.1: SEM micrographs of LPCVD ZnO layers (a) as deposited, and after 60 minutes of post-treatment with a plasma discharge of (b) oxygen, (c) argon and (d) nitrogen. All the treatments are performed with a power density of 1 W/cm^2 at a pressure of 80 μbar.

For the different post-treatments shown in Fig. 3.1, the decreasing trends of the rms surface roughness (σ_{rms}) of the ZnO layer with increasing treatment times are plotted in Fig. 3.2.

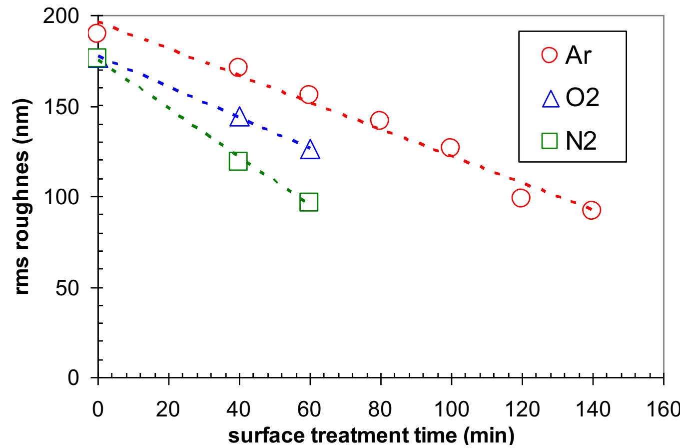

Fig. 3.2: Evolution of the rms surface roughness with argon, oxygen and nitrogen plasma discharge. All the treatments are performed with a power density of 1 W/cm^2 at a pressure of 80 μbar. The lines are the result of a linear fits. According to these fits, the rates of change of σ_{rms} are -74, -85 and -135 nm per 10 minutes of argon, oxygen and nitrogen plasma post-treatment, respectively.

The SEM micrographs in Fig. 3.1 qualitatively indicate that different types of morphologies are achieved if the surface treatment involves only physical etching or if it also includes chemical reactions with the surface, as it seems to be the case with O_2 and with N_2. Indeed, the rate of decrease of the rms roughness is 82% larger with the N_2-plasma compared to the post-treatment with the Ar-plasma. However, with N_2, the morphology does not seem to remain smooth as small asperities even seem to be created.

3.4 Evolution of the morphology with an increasing post-treatment time: result and discussion

For a plasma post-treatment with well chosen process parameters, Fig 3.3 shows AFM images and height profiles measured at exactly the same location of the ZnO layer, just after deposition, after 40 minutes of surface post-treatment, and after 40 additional minutes of treatment. It appears nicely in the height profiles of Fig. 3.3 (d-f) that the radii of curvature at the bottom of the valleys increase when the duration of the treatment is increased. Also, the profiles show (especially B-B') that tops and edges of the pyramids become sharper after the post-treatment. Note in Fig. 3.3 (e), at the position 1600 nm, that small corrugations at the bottom of the valleys are cleaned up after the first post-treatment.

Therefore, the post-treatment changes the V-shaped valleys between the pyramidal structures at the surface of the ZnO layer into broad U-shaped valleys. Moreover, small corrugations are cleaned up. We see also that, on the contrary to the case of the valleys, the radii of curvature along the edges of the pyramids become smaller.

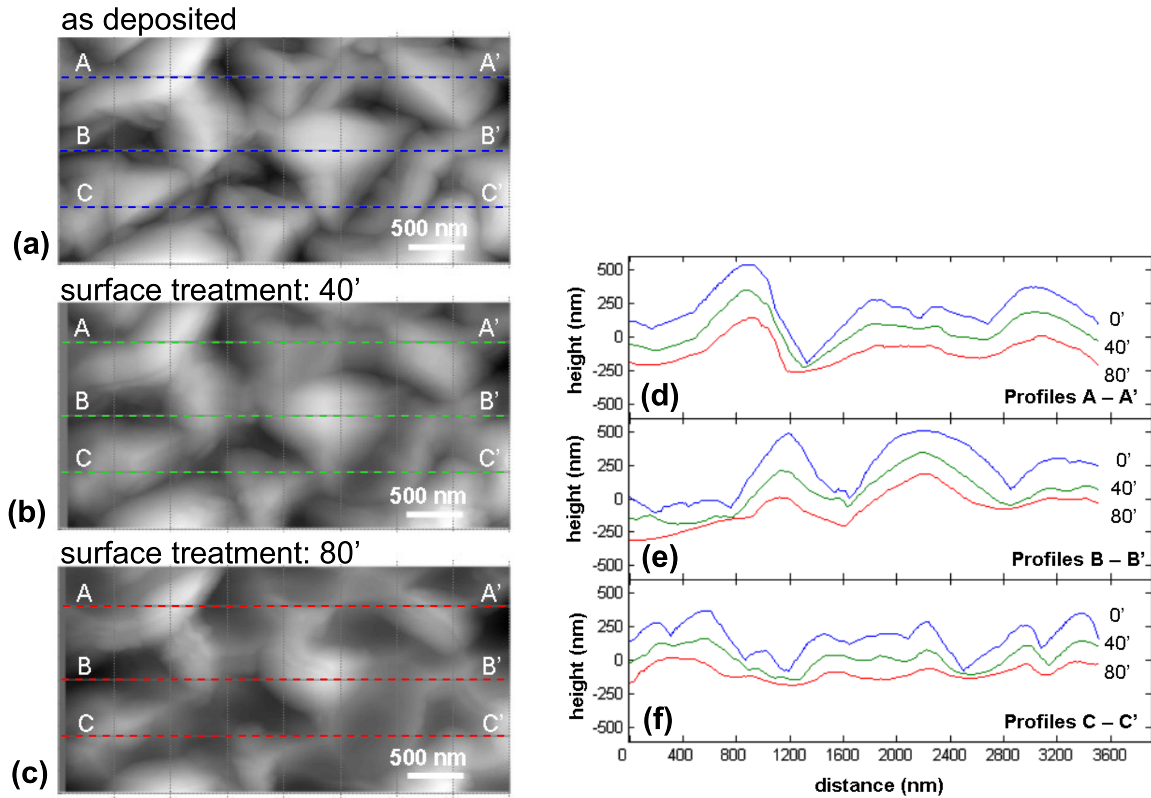

Fig. 3.3: (a)-(c) Atomic force microscopy images of the same region of interest (a) just after deposition of the ZnO:B layer, (b) after a post-deposition plasma treatment of 40 minutes and (c) after 40 additional minutes of plasma post-treatment (i.e. after a cumulated duration of 80 minutes. The horizontal lines in (a)-(c) indicate the position of the height profiles A-A', B-B' and C-C' plotted in (d), (e) and (f), respectively. In (d), (e) and (f), the evolution of the profile considered is plotted in the same graph.

For this plasma post-treatment, Fig. 3.4 shows SEM micrographs of ZnO samples after respective treatment durations of 0, 40, 80 and 140 minutes. In Fig. 3.5, the histograms of angle distribution vs. the plane of the substrate (local slope) are given for various treatment times. Even after prolonged treatment time (40 minutes), a high average angle, between 45° and 50°, is obtained. Whereas longer treatments (> 60 minutes) lead to a large fraction of flat areas (local angles smaller than typically 30°).

3.5 Conclusion

We demonstrated that changes of the surface morphology of LPCVD ZnO layers can be carried out by a variety of plasma post-treatments and quantified those changes. It is possible to change the sharp V-shaped valleys into broad U-shaped valleys by continuously increasing their radii of curvature. The choice of the optimal plasma parameters is actually not trivial because, ultimately, it requires the re-optimization of the solar cell processing parameters for each kind of substrate. However, we believe that a

qualitative judgment of the morphology from SEM micrographs or AFM images is already a good starting point.

We will see in chapter 4 the advantages, in terms of V_{oc} and FF of the solar cells, of the change of morphology presented in section 3.2 and 3.3. However, as these changes are accompanied by a linear decrease of the rms roughness of the surface we can expect a possibly detrimental decrease of the haze in transmission for layers with post-treatment. Moreover, the change of morphology also impacts the angular distribution of the light scattered by the rough surface. These optical considerations will be discussed all through chapter 6 and chapter 7.

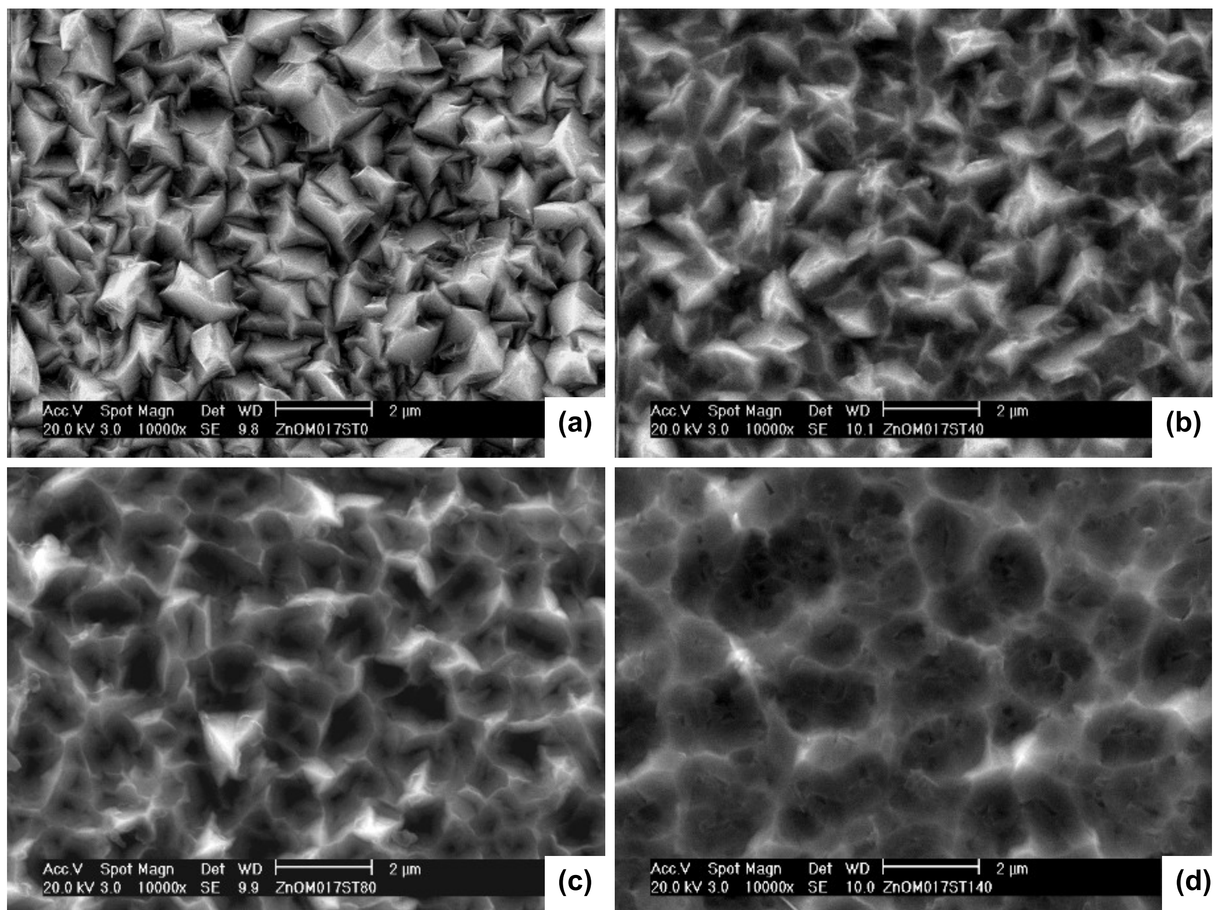

Fig. 3.4: SEM micrographs of LPCVD ZnO layers (a) as deposited, (b) after 40 minutes, (c) after 80 minutes and (d) after 140 minutes of the same plasma post-treatment as in Fig. 3.3.

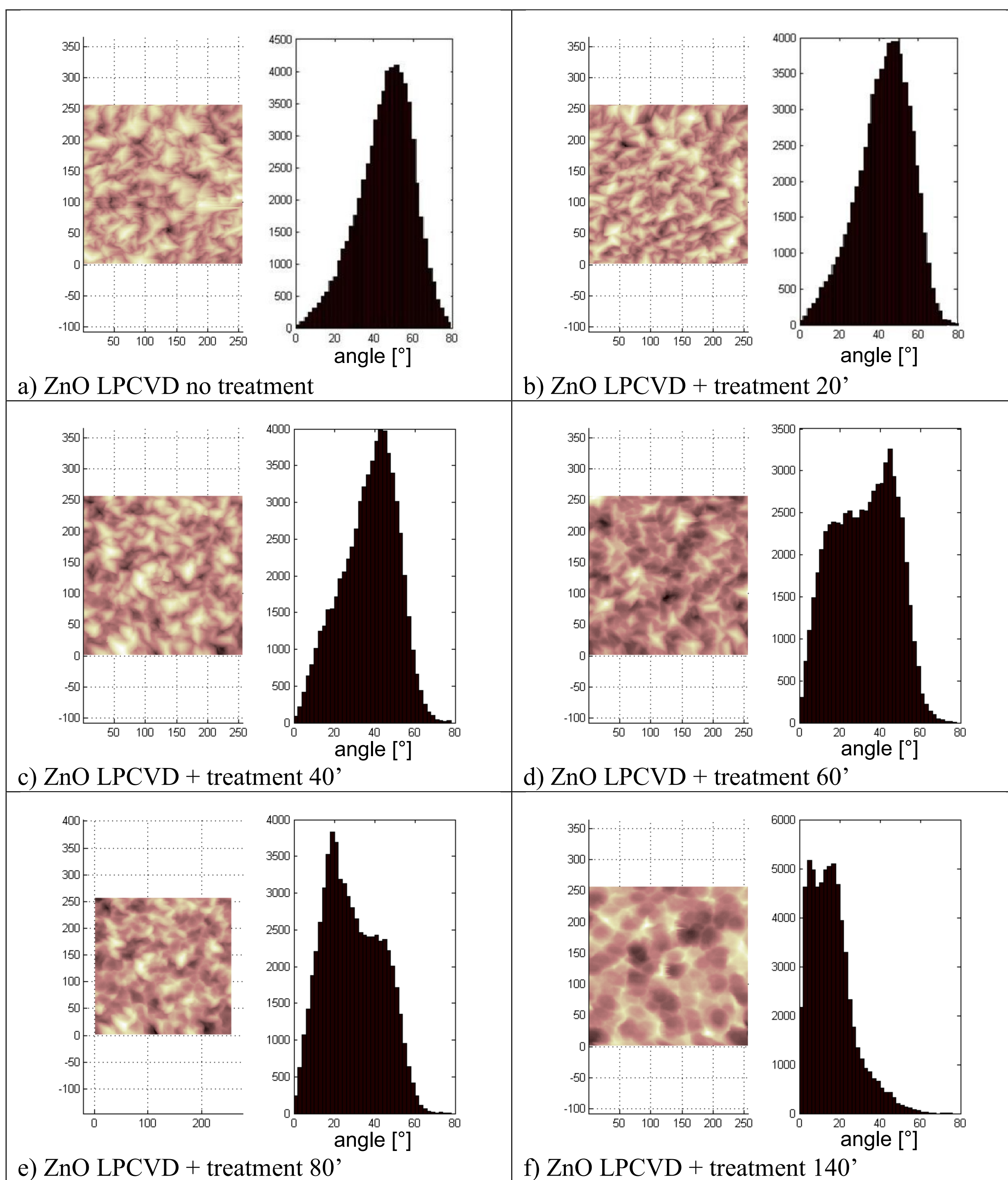

Fig. 3.5: AFM pictures of LPCVD ZnO layers (a) as deposited, (b) - (f) after 20, 40, 60, 80 and 140 minutes of the same plasma post-treatment as in Figs. 3.3 and 3.4. Next to each AFM picture, is shown the corresponding histogram of the local angle of the surface with respect to the plane of the layer.

4 Influence of the surface morphology of the front ZnO layer on the electrical performances of the device

The effects of a modification of the surface morphology of the transparent conductive oxide (TCO) layer used as substrate for deposition of silicon thin-film solar cells are demonstrated. For this purpose, the plasma post-treatments presented in chapter 3 are used to change steep V-shaped valleys on the surface of zinc oxide layers into broad U-shaped valleys. After a short historical review in section 4.1, experimental details are given in section 4.2. The effects of this modification of surface morphology on the growth of microcrystalline silicon are then presented in section 4.3. In that section, the influence of the plasma post-treatment on the electrical performances of silicon thin-film solar cells is also presented. In section 4.4, we discuss the physical origin of defective regions in silicon thin-films deposited on a substrate with V-shaped valleys. Conclusions follow in section 4.5.

4.1 Introduction

Sakai *et al*. first reported on the apparition of cracks in amorphous silicon (a-Si:H) near the valleys of the TCO layers used for deposition [Sakai 1990]. They reported that the white stripelike regions observed by transmission electron microscopy (TEM) near the valleys are defective. From dark current-voltage measurement of a-Si:H solar cells, they concluded that the defects act as recombination centers of carriers. For microcrystalline silicon (μc-Si:H) solar cells, Nasuno *et al*. proposed that the average slope of the surface morphology can be used to mitigate the harmful effect of grain boundaries [Nasuno 2001]. Bailat *et al*. observed by TEM the presence of cracks or nanoporosities in μc-Si:H material near the valleys formed by the surface morphology of ZnO layers deposited by the low pressure chemical vapor deposition (LPCVD) technique [Bailat 2003]. The systematic decrease of V_{oc} and FF observed by Feitknecht *et al*. when μc-Si:H solar cells are deposited on LPCVD ZnO layers with an increasingly large rms value of their surface roughness (σ_{rms}) [Feitknecht 2005] led to the modification of substrate morphology by means of a plasma post-treatment presented in chapter 3. In the present chapter we show the effect of this change of morphology on μc-Si:H material grown on modified LPCVD ZnO layers and on the performances of silicon thin-film solar cells deposited in the pin configuration. The results are also reported in [Bailat 2006] and in [Dominé 2006].

4.2 Experimental

The LPCVD ZnO layers used in this study are the same as those presented in chapter 3 (thickness and sheet resistance of approximately 4.5 μm and 10 Ω/sq, respectively. The plasma post-treatment (from 0 to 140 minutes), used to modify the surface morphology, is realized in a reactive-ion etching (RIE) vacuum system. The surface morphology of the layers is characterized by scanning electron microscopy (SEM) and the σ_{rms} value of their

surface roughness is determined from atomic force microscopy (AFM) measurements. The microcrystalline silicon solar cells are then deposited by very high frequency (VHF) plasma enhanced chemical vapor deposition (PECVD) as presented in section 2.1.2. Two deposition regimes are compared for the growth of the intrinsic μc-Si:H layer: "low pressure" deposition regime (lp) with a VHF power of 10 W injected in the plasma discharge and a pressure of 350 μbar during the process; and "high pressure" deposition regime (hp) with the same VHF power but pressure increased to 700 μbar. The silane concentration in the gas mixture is adapted to keep, in both cases, the deposition conditions close to the transition between growth of microcrystalline and amorphous material. The same deposition time is used for both regimes and the thickness of the resulting intrinsic layers is comprised between 1.4 and 1.8 μm. The rear contact consists of a ZnO layer covered with a white dielectric reflector. The cells area (~20 mm^2) is defined by lift-off of the back ZnO layer and SF_6 plasma etching of the silicon layers. The short-circuit current density (J_{sc}) is calculated from the measurement of the external quantum efficiency (EQE) curve. Note that because of the small cell area we are likely to underestimate the current with that method (light trapped in the glass). The current-voltage characteristics are measured under a WACOM solar simulator in standard test conditions (25°C, AM1.5g spectrum) and calibrated with the J_{sc} values obtained from the EQE measurements. For comparison, two samples are prepared by the tripod method [Benedict 1992] and analyzed by transmission electron microscopy (TEM) using a Philips CM200 microscope operated at 200 kV. For some samples, secondary ions mass spectroscopy (SIMS) is performed using a Cs^+ primary ion beam.

4.3 Results

The surface morphology of a ZnO layer is shown in Fig. 4.1(a). Pyramid-like surface objects appear separated by steep V-shaped valleys. Some small asperities and pyramids are randomly distributed between larger surface objects. By contrast, after 80 minutes of plasma post-treatment (Fig. 4.1(b), the smaller features in the bottom of the valleys have disappeared leaving only a network of salient edges. The flat facets of the pyramids become concave and the steep V-valleys change into broader U-valleys. In chapter 3 we showed that these modifications occur progressively with the duration of the surface treatment. The involved process likely consists in a sputtering and re-deposition process, as ZnO is found after the treatment on glass plates placed next to the ZnO coated substrate. This sputtering and re-deposition mechanism could also explain why the ZnO layer thickness does not change during the process.

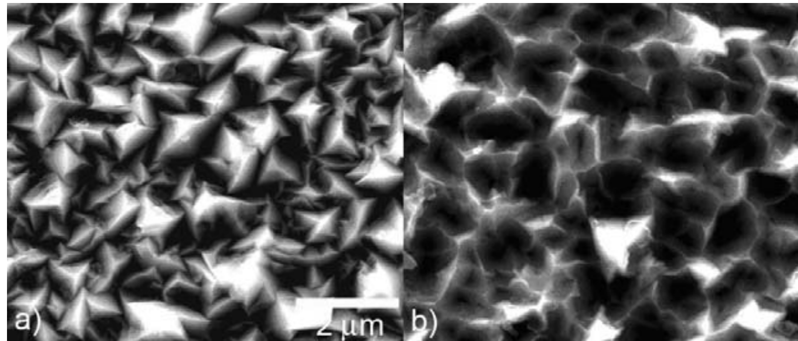

Fig. 4.1: SEM micrographs of the different surface morphologies of front LPCVD ZnO layers a) without treatment and b) with 80 minutes of plasma post-treatment.

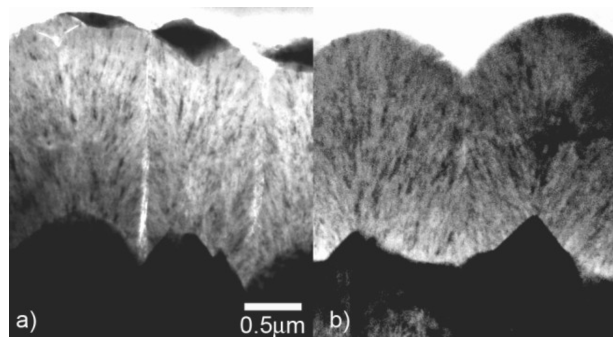

Fig 4.2: TEM micrographs of two typical cross-sections of pin microcrystalline silicon solar cells grown on rough LPCVD ZnO layer a) without treatment and b) with 80 minutes of plasma post-treatment. The rough ZnO layers appear in dark contrast at the bottom of the micrographs.

This surface treatment offers a unique opportunity to study the influence of different front TCO morphologies on the growth, microstructure and performances of microcrystalline silicon solar cells. In the TEM micrograph of the sample without plasma post-treatment (Fig 4.2(a)), long cracks and voids extend within the whole intrinsic layer from the bottom of most valleys towards the bottom of the cell (i.e. the top of the micrograph). On the contrary, no crack or void is visible in Fig. 4.2(b) for the sample with post-treatment.

Surprisingly, the presence of these much localized defective regions, occupying a small volume fraction of the μc-Si:H material, can be indirectly detected with a bulk analysis method. Indeed, Fig. 4.3 shows that the contamination of the bulk of the device by oxygen, measured by SIMS depth profiling, is three to nine times larger for a cell co-deposited on a ZnO layer with only 20 minutes of post-treatment, compared to 60 minutes. The deposition time of the intrinsic layer was kept constant with the two deposition regimes (lp and hp). The intrinsic layer is about 1.4-μm-thick when deposited in the hp regime and 1.7-μm-thick when deposited in the lp regime. We see directly in the SIMS profiles that, for the intrinsic layer with the lower deposition rate (hp regime), the oxygen contamination is reduced by a factor two to three. However this improvement

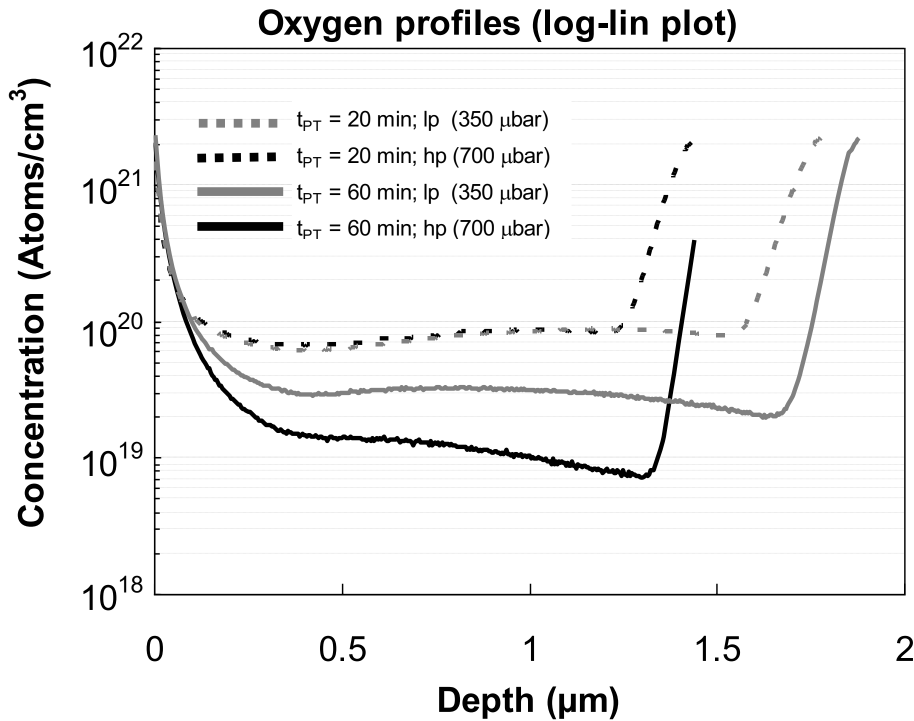

Fig. 4.3: SIMS depth-profiles of the oxygen content in pin µc-Si:H solar cells deposited on rough LPCVD ZnO layers with 20 minutes (dashed lines) or 60 minutes (continuous lines) of plasma post-treatment duration (t_{PT}). The clear (dark) lines correspond to the cell with an intrinsic layer deposited at 350 µbar (700 µbar). The back-contact of the devices is removed for the SIMS analysis. The left-hand side corresponds to the surface of the sample.

is effective for deposition on the substrate with the long post-treatment only. It is absolutely ineffective for µc-Si:H material grown on the substrate with the short post-treatment.

The preceding result gives an indication that the contamination by oxygen origins from air exposure of the sample. The physical mechanism involved could be water adsorption at the surface of the porous structures constituting the cracks [Finger 2005]. The slopes of the tails of oxygen contamination at the left-hand side in Fig. 4.3 support this hypothesis.

A direct evidence of contamination of the device from air-exposure is given in Fig. 4.4. This figure shows current-voltage characteristics of a pin µc-Si:H solar cell deposited on a moderately rough LPCVD ZnO (σ_{rms} < 60 nm) without post-treatment of its surface (therefore with V-shaped valleys). In this experiment, no encapsulation (e.g. by the white dielectric reflector) is used. After 14 days of exposure in-air, degradations of 6.2% and 14.3% of the V_{oc} and FF, respectively, occur. Note that this degradation is reversible under annealing of the sample for 90 minutes at 180°C. No degradation is observed when the sample is stored in vacuum (load-lock chamber of a deposition system) or when the cell is deposited on a LPCVD ZnO layer with a long enough plasma post-treatment (typically > 60 minutes).

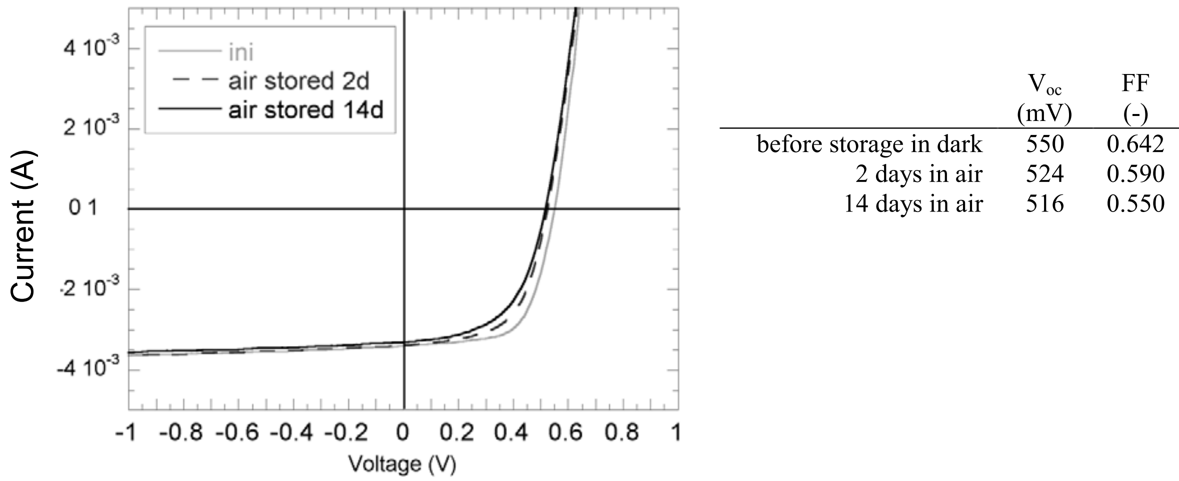

	V_{oc} (mV)	FF (-)
before storage in dark	550	0.642
2 days in air	524	0.590
14 days in air	516	0.550

Fig. 4.4: Degradation during storage in the dark, in contact with air, of a microcrystalline silicon solar cell deposited on a front LPCVD ZnO layer without plasma post-treatment. The current-voltage characteristics show that, after two days of storage in air, V_{oc} and FF degrade by 4.7% and 8.1%, respectively. After a total of 14 days the final losses are 6.2% and 14.3%, respectively. No degradation occurs in vacuum.

Figure 4.5 shows how the (initial) performances of pin μc-Si:H solar cells deposited on the rough LPCVD ZnO layers are improved by the change of surface morphology:

- after the first 20 minutes of plasma treatment, the open-circuit voltage (V_{oc}), fill-factor (FF) and short-circuit current density (J_{sc}) increase, as the largest cracks causing the shunting of the solar cells disappear,
- between 20 minutes and 40 minutes, J_{sc}, reaches a maximum whereas FF and V_{oc} keep improving,
- from 40 minutes to 140 minutes, J_{sc} decreases due to the flattening of the front TCO that reduces its light trapping capability. The simultaneous increase of V_{oc} and FF and decrease in J_{sc} result in an almost constant efficiency of 9.2% for treatment times above 40 minutes.

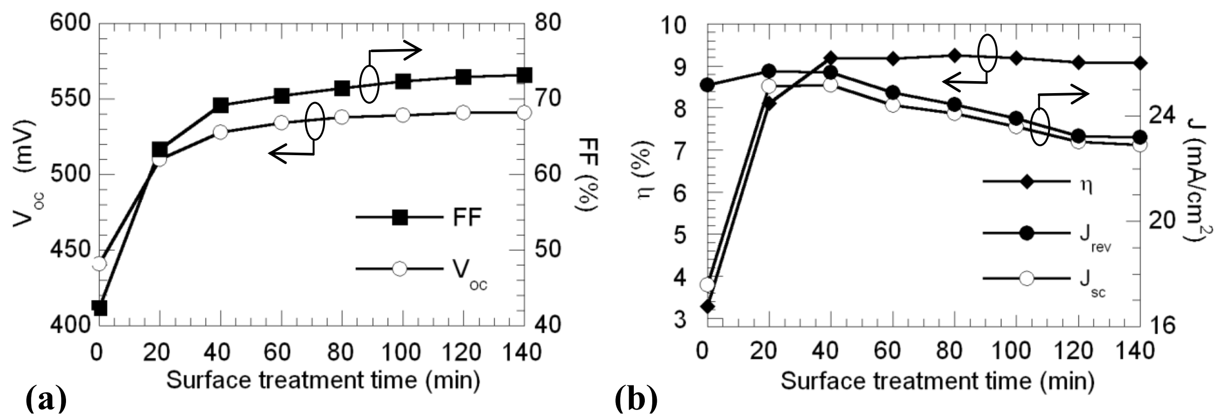

Fig. 4.5: Evolution of the electrical characteristics of the microcrystalline silicon solar cells in regards of the plasma post- treatment time: (a) V_{oc} and FF, (b) J_{sc}, J_{rev} (at -2V) and conversion efficiency η.

In Fig. 4.5(b), the current densities deduced from EQE measurements performed with a reverse polarization applied to the device (J_{rev}), indicate that the very poor J_{sc} value obtained for the cell deposited on the as-deposited substrate (without plasma post-treatment) is due to collection losses. The difference between J_{sc} and J_{rev} decreases when the duration of the post-treatment increases. This indicates a decrease of the rate of recombination of carriers in the bulk. In Fig. 4.6, we show the IV curve and EQE results obtained for the best µc-Si cells after process optimization. An efficiency of 9.9% is obtained with a J_{sc} of 24.7 mA/cm^2 and FF of 74.1%.

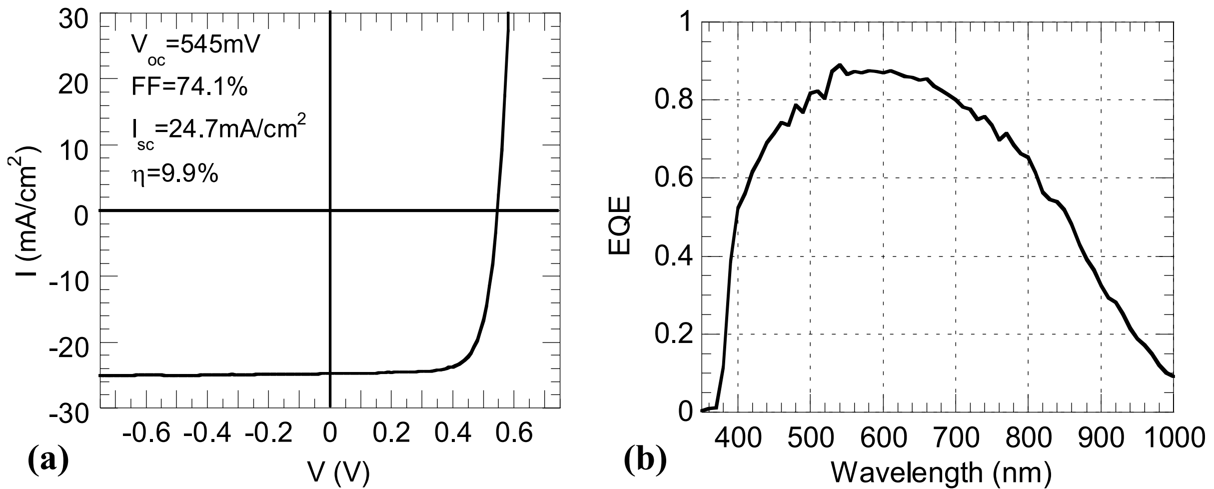

Fig. 4.6: (a) IV curve of optimized µc-Si:H solar cell on LPCVD ZnO with 60 minutes of surface post-treatment. (b) EQE of the same cell as in (a).

The plasma-post treatment of the front TCO is also effective for pin single-junction a-Si:H and micromorph solar cells, as shown in Table 4.1. Indeed, when applying a "standard" amorphous Si cell recipe, V_{oc} and FF of the a-Si:H cells improve with the duration of the treatment, while J_{sc} decreases. Without surface treatment, the values of V_{oc}, FF and J_{sc} are 868 mV, 72.3% and 15.18 mA/cm^2, respectively. By applying a 60 minute post-treatment to the front LPCVD ZnO layer, V_{oc} and FF increase to 927 mV and 75.1%, respectively, while J_{sc} decreases to 14.65 mA/cm^2. The initial conversion efficiency is thereby improved from 9.5% to 10.2% by the surface treatment of 60-minute duration.

Table 4.1: Electrical characteristics of single-junction a-Si:H solar cells and V_{oc} values of micromorph tandem cells with different durations of the plasma post-treatment used on the front LPCVD ZnO (0 minute stands for "no surface treatment").

Treatment time (min)	Single-junction a-Si:H FF (%)	V_{oc} (mV)	J_{sc} (mA/cm^2)	Eff (%)	Micromorph V_{oc} (mV)
0	72.3	868	15.2	9.54	1322
20	75.0	896	14.8	9.95	1392
30	-	-	-	-	1411
40	74.8	909	14.6	9.93	-
60	75.1	927	14.6	10.2	-

In the micromorph configuration, both the top and bottom cells benefit from the favorable surface morphology obtained on the front LPCVD ZnO layer. The surface treatment is, thus, efficient in increasing V_{oc} of micromorph tandem solar cells. Table 4.1 shows the evolution of the V_{oc} values of tandem cells with respect to the duration of the surface treatment. Indeed, 30 minutes treatment improves V_{oc} from 1.32 V to 1.41 V.

The surface treatment influences the tandem current densities: a decrease is observed for both the top and the bottom cell. These effects will be discussed in details in chapter 7.

4.4 Discussion

The better FF and V_{oc} with increasing treatment times are attributed to lower density of cracks within the intrinsic layer. The cracks indeed constitute a region where carrier recombination occurs. The nature of the cracks (indeed region of porous material) as well as their quantitative influence on the μc-Si cell properties are described in detail in the work of Python [Python 2006, Python 2008]. He showed that the cracks in μc-Si:H solar cells can be modeled by diode-like shunts, with a poor (large) reverse saturation current (J_0). Similar conclusions have been obtained recently by Li *et al*. [Li 2009] for nip devices.

If sufficiently large, these cracks could also act as conductive channels connecting the p- and n-layers causing thereby the shunting of the solar cells. In addition, the presence of cracks and voids within the intrinsic layer, favors the adsorption of water vapor from the atmosphere at the surface of the microcrystalline silicon grains which strongly degrades the quality of the intrinsic layer of the solar cells [Finger 2005]. We presume that the deposition regime lp, with a lower deposition rate, provides favorable conditions to the growth of a more compact μc-Si:H material. But we also presume that this favorable effect, is canceled by the presence of cracks.

The smaller crack density in microcrystalline silicon layers grown on ZnO layer processed with the surface treatment is attributed to the U-shaped valleys, as seen from the TEM picture. A first possible reason for this is likely the different local growth rates at the surface of the substrate which stems from shading effects. This explanation was also proposed for a-Si:H in [Sakai 1990]. For the growth of μc-Si:H on textured substrates, it has been successfully tested with numerical simulations by Python *et al*. [Python 2006]. The interpretation of these results is as follows. At pressures used for a-Si:H and μc-Si:H silicon deposition, the mean free path of the impinging species is 10-100 μm, which is larger than the dimensions of the objects constituting the surface (typically 1 μm). We assume here that the local deposition rate depends on the solid angle within which the impinging particles arrive onto the substrate: the larger is the solid angle the higher is the local deposition rate. This solid angle is reduced at the bottom of V-valleys as compared to the top of the pyramids and so is the local deposition rate. A lower deposition rate in turn inhibits the growth of the microcrystalline layer and produces cracks between microcrystalline grains. As a matter of fact, the cracks are predominantly observed at the bottom of V-shaped valleys rather than at the top of the pyramids – where no shading effects can possibly take place. Conversely, when one considers broad U-shaped valleys, the solid angle in the bottom is even larger than at the top of the pyramids. The local deposition rate is therefore higher at the bottom of the U-shaped valley, avoiding thereby

the formation of defective grain boundaries. An alternative way to view the crack formation is a collision of the "growth front".

In all cases, it appears that the radius of curvature of the valleys on a textured TCO is the relevant criterion to estimate if a substrate can be used for the growth of microcrystalline silicon solar cell. We estimate here that values from 50 nm and above are sufficient for this purpose.

This plasma post-treatment applied to SnO_2 coated glass substrates produces similar results as described above. These observations offer new possibilities for the optimization of solar cells on various types of substrates in pin or nip configurations.

We should note that other kind of substrates such as the sputtered-etched TCO developed by IPV Jülich (see e.g. [Beyer 2007]), offer naturally a texture favorable for the μc-Si growth. By applying our treatment we are able, with a different TCO and a different morphology to reach efficiencies close to state-of-the-art values for μc-Si solar cell efficiency (η = 10.3% reported for the sputtered-etched ZnO [Finger 2008], best certified efficiency of 10.1% as reported by Kaneka [Yamamoto 1998, Green 2009]).

Finally we should note that, when no or shorter treatment is applied, it is still possible to recover better efficiencies than the reported 4.5% of Fig. 4.5(b), by playing on the PECVD deposition parameters. In particular, we have shown in [Python 2009a] that fewer cracks are formed when the deposition temperature is raised. Additional parameter modification (pressure, dilution) also allow a recovery of the cell parameters, but not to the extent allowed by the texture modification. Also we should note that the case of the micromorph devices, for which the geometry of the substrates is modified by the a-Si:H cell deposition, is different from that the pure μc-Si:H case (as it is unlikely that μc-Si:H single junction modules will be produced).

4.5 Conclusion

We demonstrate here that shading effects caused by an inappropriate surface morphology of the substrate can provoke the growth of μc-Si:H with highly defective regions. These regions are detrimental to the electrical characteristics of the solar cells. This is still valid for a-Si.H but the effects in the electrical performances of pin a-Si:H solar cells is less dramatic than for μc-Si:H devices. A plasma surface treatment transforming the V-shaped valleys into U-shaped valleys allows demonstrating the effect of different surface morphologies on the growth of microcrystalline silicon. The obtained U-shaped valleys allow the removal of the cracks because less shading effects occur and allow the realization of state-of-the-art microcrystalline devices with efficiencies close to 10%.

In the next chapter, scanning electric-probe techniques, based on atomic force microscopy, will be used to investigate more about the defective regions produced in μc-Si:H when the layer is deposited on a substrate without, or with a short post-treatment.

5 Investigation of the electric-field distribution in µc-Si:H p-i-n solar cells by cross-sectional SKPM and planar C-AFM-based measurements

In this chapter we present scanning Kelvin probe microscopy (SKPM) and conductive-atomic force microscopy (C-AFM) analyses preformed on complete microcrystalline silicon (µc-Si:H) solar cells. The aim of these microscopic analyses, is to give more insight into the electronic transport in the complex multi-phase µc-Si:H material, particularly when deposited on a surface-textured substrate.

In section 5.1 we motivate the study of the electronic transport mechanisms in µc-Si:H at a nanometric scale and we situate the present work in the fields of the research in SKPM and C-AFM measurements on µc-Si:H material and solar cells. In section 5.2 we present and discuss cross-sectional SKPM analysis of µc-Si:H solar cells. To complete these measurements we present then, in section 5.3, two new planar C-AFM-based measurement techniques performed on the n-type layer of µc-Si:H p-i-n solar cells.

5.1 Introduction

The relative role of drift and diffusion mechanisms involved in the carrier transport in µc-Si:H solar cells is an open question [Meier 1994] [Wyrsch 1998a]. Previous voltage-capacitance and charge-collection (time of flight) experiments conducted by Wyrsch *et al.* suggested a drift controlled transport at the grain boundaries and a diffusion controlled transport inside the grains [Wyrsch 1998a,b]. Information about the electric-field distribution in the intrinsic layer is decisive for the comprehension and the optimization of the carrier collection efficiency of µc-Si:H solar cells. In this chapter, we present nanoscale measurements of surface potentials on cross-sections of µc-Si:H cells using scanning Kelvin probe microscopy (SKPM). Recently, this technique has been applied to the analysis of silicon thin-film solar cells deposited on flat substrates. Jiang *et al.* reported on SKPM measurements, with application of a bias voltage (V_{bias}) to the sample, on fractured cross-sections of a-Si:H n-i-p solar cells deposited on GaAs substrates [Jiang 2004]. Breymesser *et al.* reported on measurements, without V_{bias}, on polished cross-sections of µc-Si:H p-i-n cells deposited on a flat indium tin oxide layer [Breymesser 2001]. In the present work we go one step further and analyze, with a V_{bias} applied to the sample during the SKPM measurement, fractured and polished cross-sections of µc-Si:H p-i-n solar cells deposited on a surface-textured substrate. We also compare features in the SKPM pictures to features observed in transmission electron microscopy (TEM) micrographs.

Conductive atomic force microscopy (C-AFM) experiments have been carried out by several groups on µc-Si:H intrinsic layers (see [Kocka 2006] and [Cavallini 2007]) and, recently, on complete µc-Si:H solar cells deposited on rough Asahi U-type SnO_2 substrates [Shen 2007]. Because artifacts are very common when performing standard C-AFM

measurements (see for example [Kleider 2001] or [Shen 2007]), here we complete our cross-sectional SKPM measurements with two different planar C-AFM-based electrical probing methods performed on the n-type layer of p-i-n μc-Si:H solar cells. We call these two original methods *near-V_{oc} planar C-AFM* and *lock-in planar nanopotentiometry*.

Finally, we discuss our observations and emphasize the special role played by μc-Si:H cluster boundaries, where voids and cracks can take place, in the recombination mechanisms that can affect the performances of μc-Si:H solar cells deposited on surface-textured substrates.

5.2 Cross-sectional SKPM and comparison with TEM imaging

5.2.1 Experimental

The entirely μc-Si:H p-i-n solar cells are prepared using very high frequency plasma enhanced chemical vapor deposition (VHF-PECVD) in a dual chamber deposition system. The thickness of the intrinsic layer is 1.8 μm. The cells are grown on glass coated with a surface-textured front transparent conductive oxide (TCO). This front TCO is a zinc oxide (ZnO) layer deposited by low-pressure chemical vapor deposition (LPCVD). Prior to μc-Si:H deposition, the ZnO is exposed to a surface treatment in order to remove sharp pinches and therefore increase the V_{oc} and FF value of the solar cell [Bailat 2006]. The back contact is a LPCVD ZnO layer and the cell area is patterned by SF_6 plasma etching (0.25 cm^2). The current density-voltage curves are measured using a two-source AM1.5g sun simulator (Wacom). When grown on the suitable substrates, the cells have high efficiencies of 8-9%.

The cross-sections are either prepared by simple fracture of the samples using the procedure presented in [Ballif 2000] or by grinding and mechanical polishing. As schematically shown in Fig. 5.1, both the fractured and polished samples are electrically connected for the application of V_{bias}.

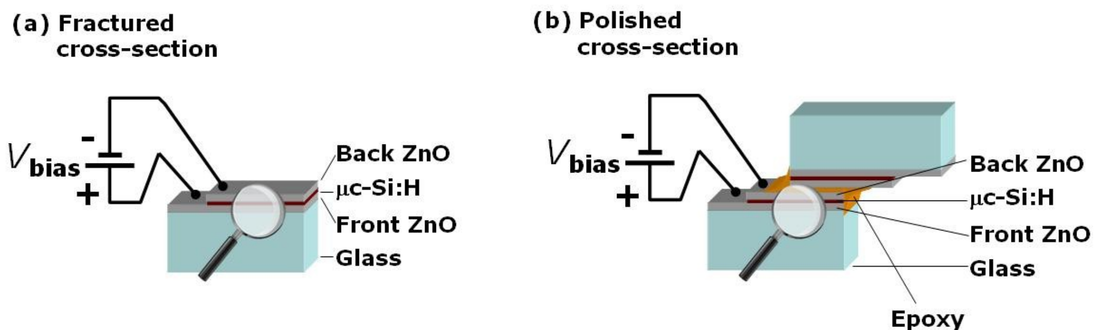

Fig. 5.1: Schematic drawings of (a) a fractured cross-section and (b) a polished cross-section of a p-i-n μc-Si:H cell ready for analysis by SKPM. Both types of preparation allow for the application of a bias voltage V_{bias} during SKPM measurement. In (b), two samples are glued together in a sandwich configuration before polishing.

Prior to mechanical polishing, two samples are glued in sandwich configuration with epoxy. This permits a homogeneous polishing, normal to the plane of the substrate over the whole cross-section. In order to allow the electrical connection of the front and back contacts, the two samples are laterally shifted before gluing (see Fig. 5.1(b)). The mechanical polishing is performed using diamond lapping films with particle sizes decreasing from 30 μm to 0.1 μm. To minimize the height of the step between the ZnO and the μc-Si:H layers, a final mechanical polishing using an aluminum oxide film with a grit size of 50 nm is performed, instead of the usual chemical-mechanical polishing with a suspension of colloidal silica particles.

The SKPM measurements are performed in air at the same time as non-contact atomic force microscopy topography imaging with a ThermoMicroscopes Autoprobe CP Research system. The topographic imaging is obtained using the first resonant frequency (~60 kHz) of the cantilever, while a 20 kHz ac voltage is applied to the tip for the SKPM potential measurement (see chapter 2 for details). The surface potential measured over the multilayer stacks depends on oxidation and water adsorption effects and on surface charge trapped at surface states; this may induce different surface Fermi level pinning for the different layers of the device [Ballif 2001], [Jiang 2004]. Therefore, assuming that the filling of the electronic surface states does not change with variations of the bias voltage (V_{bias}) applied between the front and back contacts, we can calculate the change of potential in the bulk as the difference of the surface potentials measured with V_{bias} and in short-circuit condition [Ballif 2001]. The V_{bias}-induced electric-field profiles are then calculated as the first derivative of this difference [Jiang 2004]. By convention, a positive (negative) V_{bias} value corresponds to a forward- (reverse-) bias of the sample.

For comparison of SKPM pictures and transmission electron microscopy (TEM) micrographs, μc-Si:H solar cells are prepared by the tripod method [Benedict 1992] and analyzed by TEM in bright-field using a Philips CM200 microscope operated at 200 kV.

5.2.2 Results

<u>SKPM on fractured cross-section</u>

Figures 5.2(a) and (b) show the AFM picture and the corresponding SKPM picture taken under reverse-bias condition, for a μc-Si:H solar cell, deposited on a highly surface-treated LPCVD ZnO layer, with an open-circuit voltage (V_{oc}) of 541 mV and a fill-factor (FF) of 72.2%. The fracture procedure produces a rough cross-section with a typical corrugation value of 200 nm. The SKPM picture suffers from convolution with the topography; however, the front ZnO, the μc-Si:H, and the back ZnO layers can clearly be distinguished. SKPM analysis is performed in short-circuit (V_{bias} = 0 V), forward-bias (V_{bias} = 0.5 V) and reverse-bias (V_{bias} = -1 V) conditions. The potential profiles measured on the dashed lines in Figs. 5.2(a) and (b) are plotted in Fig. 5.2(c), after averaging over 11 consecutive scan lines: The corresponding modifications of the electric-field are plotted in Fig. 5.2(d).

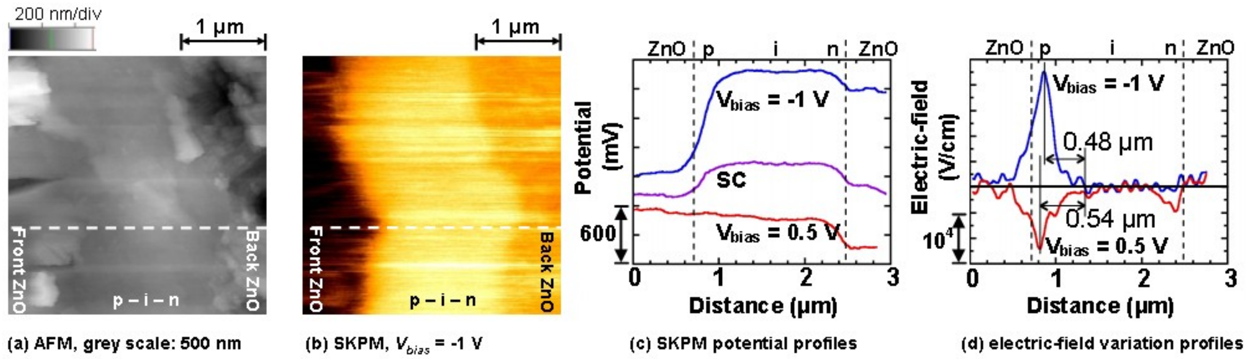

Fig. 5.2: (a) AFM picture and (b) the corresponding SKPM picture taken under reverse-bias conditions (V_{bias} = -1 V) on a fractured cross-section of a µc-Si:H p-i-n solar cell. (c) SKPM potential profiles measured on the dashed lines in (a) and (b), after averaging over 11 consecutive scan lines, under short-circuit (SC), forward-bias (V_{bias} = 0.5 V), and reverse-bias (V_{bias} = -1 V) conditions. (d) Corresponding increase and decrease in electric-field induced by V_{bias}.

Noise in the potential profiles is amplified by the derivative procedure and produces the ripple effect visible in the field profiles in Fig. 5.2(d). The electric-field induced by V_{bias} is confined to the first 500 nanometers after the p-i interface. At the electrical junction, the field is increased up to a maximum value of $2.3\cdot10^4$ V/cm for a V_{bias} value of -1 V (reverse-bias) and is decreased by a maximum value of $-1.2\cdot10^4$ V/cm for a V_{bias} value of 0.5 V (forward-bias). The position of the peak of the electric-field profile under the V_{bias} value of -1 V is shifted 60 nm toward the bulk of the intrinsic layer, compared to the position of the peak under the forward-bias condition.

The apparent extension of the electric-field into the front contact is most likely due to the low spatial resolution of this measurement on a rough cross-section, as already observed for a-Si:H solar cells [Jiang 2004].

SKPM on a polished cross-section

For a polished cross-section of a µc-Si:H solar cell deposited on a LPCVD ZnO layer with a short surface treatment (FF = 68.3% and V_{oc} = 528 mV), Fig. 5.3 shows the AFM picture and the corresponding SKPM pictures taken under short-circuit, forward-bias (V_{bias} = 0.8 V) and reverse-bias (V_{bias} = -0.8 V) conditions. The AFM picture shows that the mechanical polishing produces scratches with a typical depth of 2 to 5 nm. The SKPM pictures clearly demonstrate that the µc-Si:H layer is actually constituted of clusters growing from the peaks of the front TCO. SKPM potential profiles measured on the dashed lines in Fig. 5.3 and the corresponding variations in the electric-field distribution induced by V_{bias} are plotted in Fig. 5.4, after averaging over 11 consecutive scan lines. V_{bias}-induced variations of the electric-field profile are in the order of 10^4 V/cm and are

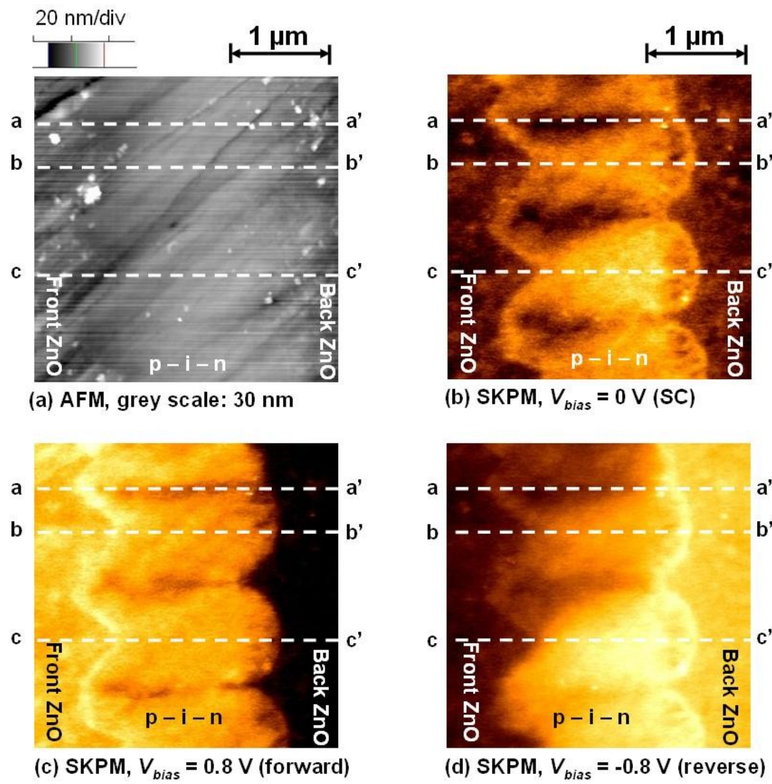

Fig. 5.3: (a) AFM picture and the corresponding SKPM pictures taken under (b) short-circuit (V_{bias} = 0 V), (c) forward-bias (V_{bias} = 0.8 V), and (d) reverse-bias (V_{bias} = -0.8V) conditions on a polished cross-section of a µc-Si:H p-i-n solar cell.

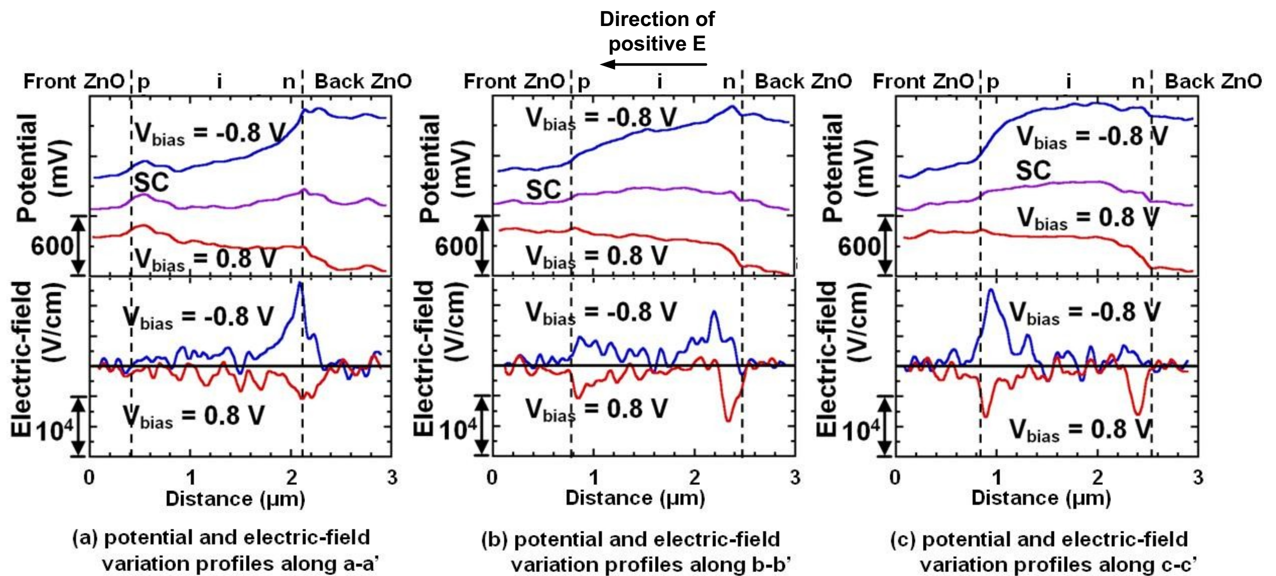

Fig. 5.4: SKPM potential profiles measured on the dashed lines in Fig. 5.3, after averaging over 11 consecutive scan lines, and the corresponding change in the electric-field profiles induced by V_{bias}.

mainly confined, depending on whether the measured profile is, near the p-i or near the i-n interface. As observed in the case of the fractured cross-section (Fig. 5.2), the position of the peak of the electric-field profile under reverse-bias is shifted toward the bulk of the intrinsic layer, compared to the peak position under the forward-bias condition.

For a larger area of the same cross-section, Fig. 5.5 shows the AFM picture and the corresponding SKPM pictures taken under short-circuit, forward-bias (V_{bias} = 0.8 V) and reverse-bias (V_{bias} = -0.8 V) conditions. The changes of the potential in the bulk for

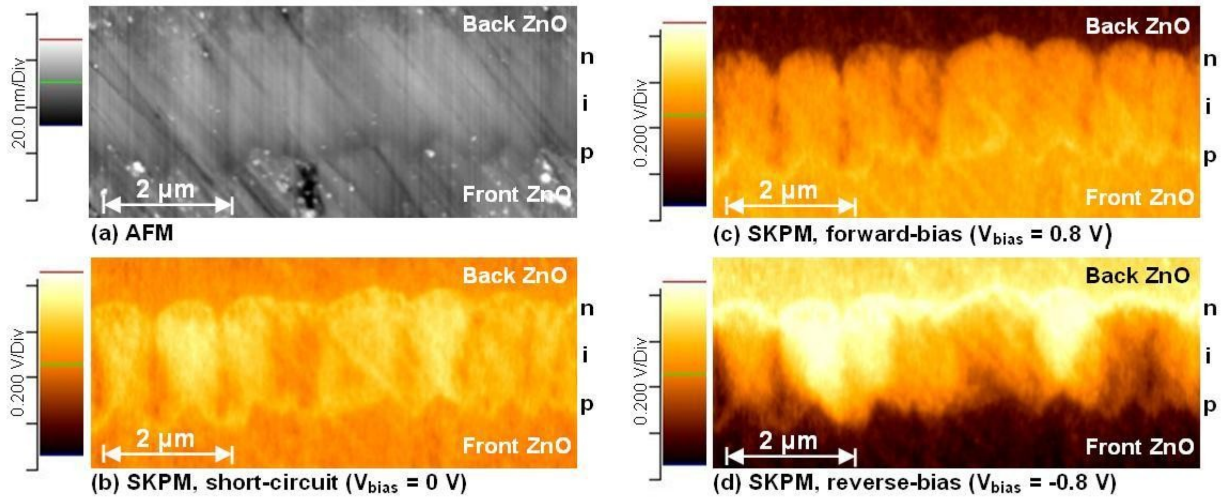

Fig.5.5: (a) AFM picture and the corresponding SKPM pictures taken under (b) short-circuit, (c) forward-bias, and (d) reverse-bias conditions on a polished cross-section of a µc-Si:H p-i-n solar cell.

different µc-Si:H clusters under forward- and reverse-bias conditions are highlighted in Fig. 5.6, where the SKPM picture taken under short-circuit (Fig. 5.5(b)) is subtracted from the pictures taken under forward-bias (Fig. 5.5(c)) and reverse-bias (Fig. 5.5(d)). Note that this subtraction procedure is carried out after careful alignment of the SKPM pictures, taking features in the AFM pictures as points of reference.

The first observation in Fig. 5.6 is that the cluster boundaries visible in Figs. 5.3 and 5.5 (drops of ~150 mV in the SKPM potential) are no longer visible after the subtraction procedure.

The gradient of the potential difference in Fig. 5.6 is equivalent to the V_{bias}-induced electric-field in the bulk beneath the surface of the cross-section. Under forward-bias (Fig. 5.6(a)), a gradient of the potential difference is visible at the p-i interface only near some peaks of the TCO and not near the valleys. Dashed lines drawn in Fig. 5.6(a) suggest this behavior is related to µc-Si:H clusters grown at the peak of the TCO. Under reverse-bias (Fig. 5.6(b)), the gradient induced by V_{bias} is located mainly at the p-i interface, except for the clusters with a potential gradient located at the i-n interface in forward-bias condition (marked with 'p' in Fig. 5.6). This suggests a p-type or n-type character for the different clusters, as indicated in Fig. 5.6.

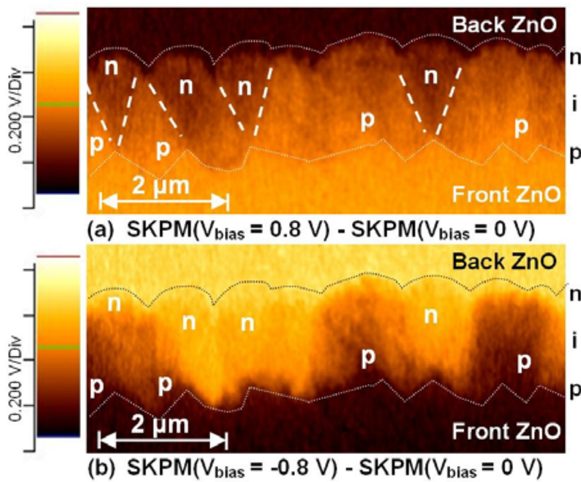

Fig. 5.6: Subtraction of the SKPM picture taken under short-circuit condition (Fig. 5.5(b)) from the SKPM pictures taken under (a) forward-bias (Fig. 5.5(c)), and (b) reverse-bias (Fig. 5.5(d)) conditions. The dotted lines indicate the position of the μc-Si:H/ZnO interfaces. The dashed lines suggest boundaries between clusters with p-type and n-type characters. The p- or n-type character for the different clusters is indicated.

The almost continuous dark stripe observed in Fig. 5.6(b) above the white dotted line (interface between the front ZnO and the p-type μc-Si:H layers) indicates that roughly the first 100 nanometers of the intrinsic μc-Si:H layer systematically presents a p-type character.

Cross-sectional TEM analysis

Figure 5.7 shows typical bright-field TEM micrographs of μc-Si:H solar cells deposited on LPCVD ZnO layers. These micrographs clearly show that, on a surface-textured TCO, the μc-Si:H layer is constituted of clusters containing columnar crystalline nanograins with lengths larger than 100 nm. Fig. 5.7(a) indicates that the clusters are either separated by cracks or by boundaries formed by the collision of columnar nanograins belonging to different clusters. Fig. 5.7(a) also shows that the μc-Si:H material grown on the valleys of the TCO is constituted by smaller, less-oriented nanograins; with a presumably smaller crystalline volume fraction.

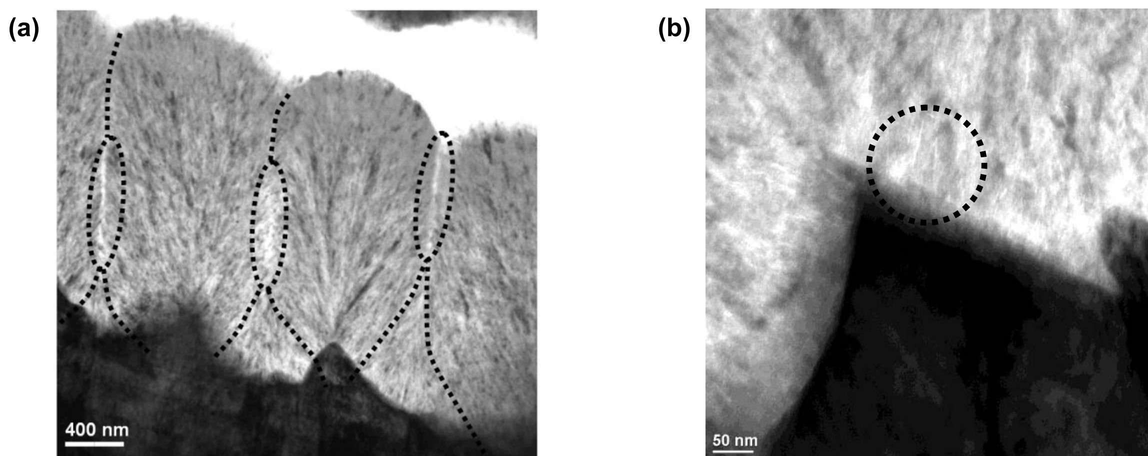

Fig. 5.7: Bright-field TEM micrograph of μc-Si:H p-i-n solar cells deposited on a LPCVD ZnO layer. (a) Enlarged view showing the front ZnO layer and clusters of μc-Si:H material containing elongated crystallites (with lengths greater than 100 nm) and separated by cluster boundaries with cracks. The μc-Si:H material on the valleys of the ZnO layer is formed by smaller crystallites. (b) Close-up view of the ZnO/μc-Si:H interface of another μc-Si:H p-i-n solar cell showing nano-cracks in the μc-Si:H on the side walls of the ZnO pyramids.

The micrograph shown in Fig. 5.7(b) indicates that not only large cracks at the cluster boundaries but also nano-cracks are present in the μc-Si:H material, some starting from the side walls of the ZnO pyramids, as highlighted in Fig. 5.7(b),.

5.2.3 Discussion

Fractured cross-section

Our results show that SKPM measurements can be performed on rough fractured cross-sections of p-i-n μc-Si:H solar cells deposited on surface-textured LPCVD ZnO. However, analysis of large areas is experimentally challenging due to the high corrugation of the fractured cross-section.

Moreover, due to variations of the capacitive coupling between the tip and the sample surface, the interpretation of SKPM pictures taken on rough cross-sections is complicated by a convolution of the measured potential with the topography. Nevertheless, this simple preparation method allows the measurement of the surface potential profile and the calculation of the electric-field profile on some chosen locations; where the SKPM signal does not exhibit doubtful transients, observable in Fig. 5.2(b) as bright lines parallel to the scan direction.

Despite a good collection efficiency of the carriers (FF = 72.2%), the calculated V_{bias}-induced electric-field profile is confined to the first 500 nanometers after the p-i interface (Fig. 5.2). This suggests that the intrinsic layer is slightly n-type, as observed in [Jiang 2005] for thick a-Si:H cells. This would also indicate that a strong diffusion of carriers is possible in μc-Si:H intrinsic layers. However, as we only measure the modification of the electric-field, we cannot evaluate the presence of an initial electric-field. Voltage drops at the p-i interface must then indicate a large interface defect density.

For a given V_{bias}, the peak positions of electric-field profiles correspond to the locations of the electrical junction, which is different from the p-i metallurgical junction. Under reverse-bias condition, the widening of the depletion region into the "intrinsic" layer (actually slightly n-type) shifts the electrical junction towards the bulk. This explains the shift of the peaks observed for the reverse-bias condition in Fig. 5.2(d) and in Fig. 5.4 for the polished cross-section (less clearly for Fig. 5.4(a)). This was also observed by Jiang et al. for a-Si:H solar cells [Jiang 2005].

Polished cross-section

Mechanical polishing produces a planar cross-section allowing the analysis of large areas, including many of the typical μc-Si:H clusters growing on surface-textured TCOs.

Both for the fractured and the polished sample, the SKPM potential profiles measured under short-circuit condition are essentially flat on the μc-Si:H layer. This indicates a Fermi level pinning at the surface of the cross-section for the whole thickness of the intrinsic layer, as previously observed for a-Si:H solar cells [Jiang 2005].

Although we cannot definitely exclude parasitic effects induced by the polishing procedure (e.g. heterogeneous oxide layer thickness or structure), our analysis of the SKPM potential profiles indicates that the amplitude of the electric-field modification induced by V_{bias} is heterogeneously distributed. It is mainly confined near the p-i interface for some cases and near the i-n interface for some others, strongly depending on the cluster considered. This gives rise to a concept of "isolated nanodiodes" with independent characteristics. We speculate that the n- or p-type character of a given cluster is conditioned by the surrounding cracks and cluster boundaries, which may have different electrical and structural characteristics. In a recent work, Python *et al.* indeed demonstrated that the effect of cracks can be modeled by diode-like shunts, with a high individual reverse saturation current, related to the length of the crack [Python 2008]. These micro-structural defects, determined to be regions of high nanoporosity, act likely as traps for various chemical impurities.

The lower SKPM potential observed at the cluster boundaries in Figs. 5.3 and 5.5, correspond to higher local work-function. This demonstrates a local upward band bending, due to negative charges located at the boundaries. On one hand, this negative charge could be the consequence of a difference in the surface states at these defective regions, which are structurally different with porosity and probably a lower crystalline fraction. On the other hand, Nasuno *et al.* reported on an enhanced diffusion of boron in the a-Si:H matrix during the deposition of μc-Si:H on textured ZnO [Nasuno 2002]. Consequently, the presence of activated boron could also explain the negative charge of the cluster boundaries.

The cluster boundaries visible in the surface potential pictures (Figs. 5.3 and 5.5) are not visible in the potential difference pictures (Fig. 5.6). This is most probably because the boundaries mainly induce surface effects. Indeed, the surface potential difference produced by the application of V_{bias} is affected by the average effect in the depth equal to the depletion width in the normal direction to the surface of the cross-section.

Comparison with TEM

Microstructure features highlighted in the TEM micrograph of Fig. 5.7(a) can directly be compared to the features of SKPM pictures presented in Figs. 5.3(c) and 5.6(a). This comparison demonstrates that cluster boundaries in the intrinsic μc-Si:H layer can be imaged by the SKPM technique. However, the distinction between cluster boundaries and cracks is not clear in the SKPM pictures. Note that Python *et al*. showed that for our μc-Si:H solar cells deposited on LPCVD ZnO, the cracks are not simply voids but are actually formed by porous μc-Si:H material [Python 2009a].

The region of μc-Si:H material grown on the valleys of the TCO, between the clusters, correspond in the SKPM picture of Fig. 5.6(a) to bright triangle areas, visible under forward-bias condition. These areas present a p-type character and therefore, due to their

supposed lower crystalline volume fraction, may be more contaminated by boron than the clusters themselves.

To explain a reduced EQE in the short wavelength range for µc-Si:H cells containing p-doped layers with a high crystalline fraction, Delli Veneri *et al*. point out that "[…] *diffusion of boron may occur, favored by the presence of cracks, giving rise to a thicker effective p-layer*" [Delli Veneri 2007]. This assumption is supported by the detection of nano-cracks starting from the side walls of the ZnO pyramids in the TEM micrograph of Fig. 5.7(b) and by the inference, from Fig. 5.6(b), of a p-type contamination of the first tens of nanometers of intrinsic µc-Si:H layer close to the p-i interface.

5.3 'Near-V_{oc} planar C-AFM' and 'lock-in planar nanopotentiometry'

5.3.1 Experimental

The C-AFM measurements are made in air with a Digital Instruments Dimension 3100 scanning probe microscope operating in contact mode. The scanning is performed over the n-type layer of a p-i-n µc-Si:H solar cell (after wet etching of the back ZnO with HNO_3) deposited on LPCVD ZnO without surface post-treatment. The cantilever spring constant is about 40 N/m, and the tip is made of phosphorus-doped Si coated with a doped diamond layer. The tip is connected to a current-voltage converter (trans-impedance amplifier). The polarization of the tip is maintained to the ground potential by the input of the trans-impedance amplifier while a positive bias potential V_{bias} is applied to the front-contact of the sample. This allows an electric current flowing through the front-contact and the tip via the probing point. While the tip is scanning on the cross-section, current maps and topography pictures are acquired. A small scanning frequency of 0.5 Hz is set to ensure a constant electrical contact between the tip and the surface of the sample. The

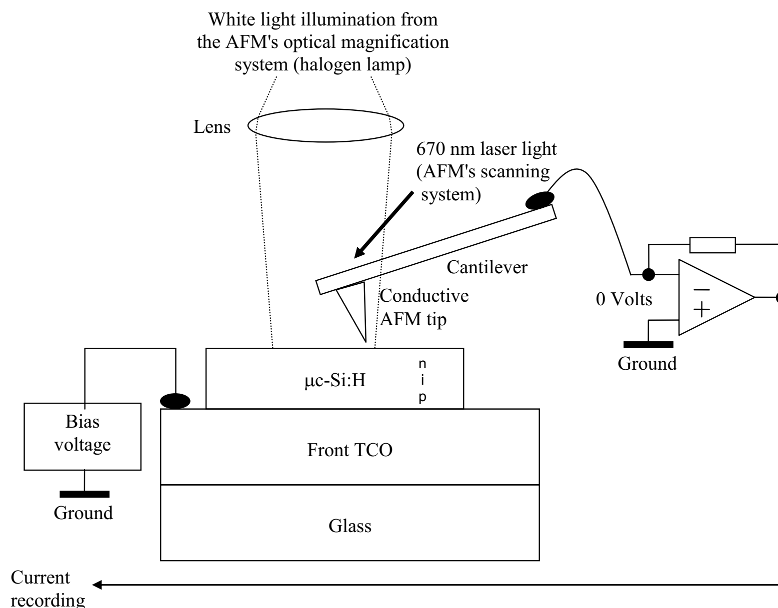

Fig. 5.8: Schematic near-Voc planar conductive-AFM (C-AFM) set-up used for the scanning over the n-type layer of p-i-n µc-Si:H solar cells in the present work, including a Dimension 3100 scanning probe microscope from Digital Instruments.

steadiness of this electrical contact is monitored by the comparison of the C-AFM current maps produced by recording the current flow through the tip in both the 'trace' and 'retrace' scanning directions. The speed of the scan and the force between the tip and the surface under analysis are adjusted until identical current maps are observed for these two scanning directions. Before picture acquisition, the potential V_{bias} on the front contact of the device (p-side) is adjusted in order to observe frequent changes of the direction of the current flowing through the tip, while, at the same time, the solar cell is illuminated from the n-side by the white light of the optical equipment of the C-AFM system (see Fig 5.8). When frequent changes of current flow direction are observed, it means that the section of the solar cell directly underneath the tip is polarized with a bias voltage close to the value of the local V_{oc}, averaged over the scanned area. Therefore, we call this measurement method *near-V_{oc} planar C-AFM*. Its benefit is to allow an increased sensitivity of the trans-impedance amplifier and therefore to permit current measurements in the +/-200 pA range.

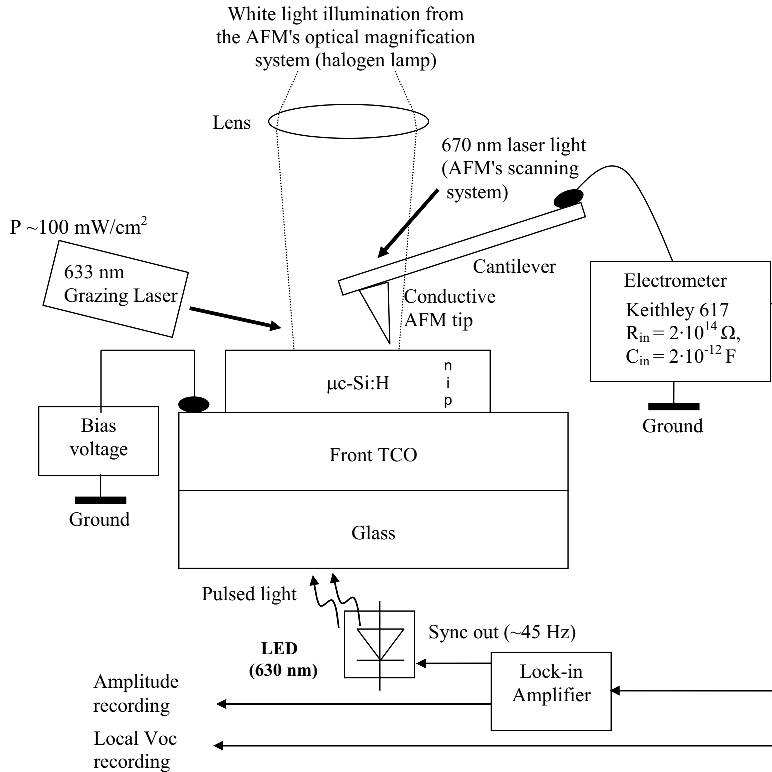

Fig. 5.9: Schematic planar nanopotentiometry set-up used for the scanning over the n-type layer of p-i-n μc-Si:H solar cells in the present work, including a Dimension 3100 scanning probe microscope from Digital Instruments, a Keithley 617 electrometer and a Stanford Research SR830 DSP lock-in amplifier.

To confirm results obtained with the *near-V_{oc} planar* C-AFM method described above, the C-AFM measurement set-up was modified in order to perform planar nanopotentiometry over the n-type layer of the same sample (see Fig. 5.9). This modification consists of the direct measurement of the local V_{oc} by connecting the tip to the input of an electrometer (Keithley 617, with an input impedance $>2 \cdot 10^{14}\Omega$). Because

the light from the laser diode of the AFM system bounces off the cantilever, it can produce uncontrolled illumination conditions on the n-side of the sample. Therefore, we add an illumination of the solar cell from the p-side with a pulsed light (~45 Hz) produced with a light emitting diode (LED) of red color (~630 nm). In addition to the direct measurement of the local V_{oc}, we measure the amplitude of the variation produced by this pulsed illumination with a lock-in detection technique. The scan frequency is decreased down to 0.1 Hz, which corresponds to a scan speed of 2 μm/s for the scan area considered here (10 x 10 μm^2). This very low scan frequency allows for a sufficient integration time of the signal applied to the input of the lock-in amplifier. To verify if uncontrolled illumination conditions of the n-side of the sample can change the features observed in the planar nanopotentiometry pictures, a laser light (633 nm) illumination can be added in grazing incidence on the n-side of the sample.

5.3.2 Results

The *near-V_{oc} planar C-AFM* method is performed on the n-type layer of a p-i-n μc-Si:H solar cell with the aim to investigate the defective areas of the cluster boundaries when the device is deposited on LPCVD ZnO without any surface post-treatment. Figure 5.10 shows the topographic pictures and the current map recorded during the scan in the 'trace' direction. Under the weakly controlled conditions of illumination provided by the white-light illumination system and by the unavoidable parasitic light from the laser diode of the scanning system of the AFM, a V_{bias} value of 350 mV is needed to reach the 'near-V_{oc}' condition. This provides local changes of about +/-100 pA in the current flowing through the tip. A comparison of the enhanced topographic picture (Fig 5.10(b)) with the current map (Fig 5.10(c)) clearly shows that the electrical behavior of different clusters is different even if they are direct neighbors. Another important observation is that no highly conductive paths are observed at the cluster boundaries. The mid-tone structures visible in the current map (0 pA) on each cluster correspond to locations where the electrical contact between the tip and the n-type layer is temporary lost.

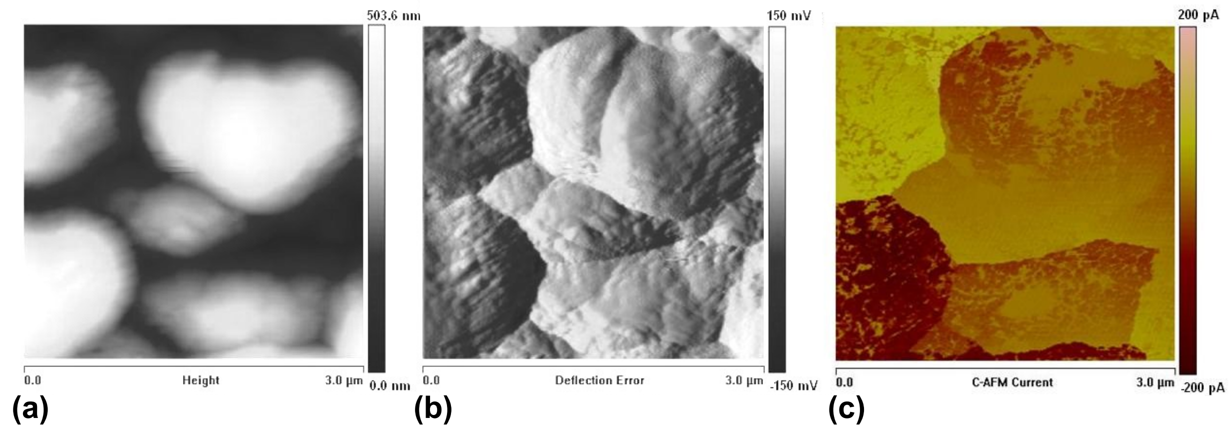

Fig. 5.10: 'Near-Voc planar C-AFM' results obtained by measurement on the n-type layer of a p-i-n μc-Si:H solar cell deposited on a LPCVD ZnO layer without surface post-treatment. The bias voltage V_{bias} is 350 mV and the scan speed is 3 μm/s. (a) AFM picture of the topography, (b) enhanced topographic picture (partial derivative of the AFM image in the trace direction), and (c) current-map recorded during the scan in the 'trace' direction (exactly the same picture was obtained for the 'retrace' direction).

Figures 5.11 and 5.12 show, over a 10 x 10 μm^2 area for the same sample, the topographic pictures and the voltage maps recorded during two consecutive *lock-in planar nanopotentiometry* measurements. The measurements are performed with (in Fig. 5.11), then without (in Fig. 5.12), the additional light in grazing incidence on the n-doped layer. The actual local V_{oc} values correspond to the V_{bias} potential applied to the front contact of the device minus the nanopotentiometric measurement reported in Figs. 5.11(b-c) and 5.12(b-c). The amplitude of the component of the local V_{oc} produced by the pulsed illumination of the solar cell from the p-side is reported in Figs. 5.11(e-f) and 5.12(e-f). During the first acquisition – with the additional grazing light (Fig. 5.11) – V_{bias} is set at 365 mV. This value corresponds to the local V_{oc} averaged over the entire scanned area. During the second acquisition – without grazing light (Fig. 5.12) – V_{bias} must be decreased to 290 mV. It can be seen in Fig. 5.12 that this second acquisition suffers from a deterioration of the electrical contact between the tip and the surface of the sample induced by the previous scan. This translates into more "frozen pixels" in Figs. 5.12(b-c) and "dark pixels" in Fig. 5.12(e-f). Once again, a comparison of the enhanced topographic pictures (Figs. 5.11(d) and 5.12(d)) with the voltage maps clearly shows that different clusters behave differently electrically, even if they are direct neighbors. The jumps observed for the local V_{oc} value when the tip scans over the boundary of some adjacent clusters is typically +/- 5mV. However, no systematic low values of the local V_{oc} are observed at the cluster boundaries.

In the local V_{oc} pictures of Fig. 5.11, the grazing laser light reveals some inversion of contrast and some other boundaries compared to the case without grazing light (cf. boundaries encircled in Figs. 5.11(b) and 5.12(b)). Gradients of local V_{oc} values are observed over the μc-Si:H clusters. The direction of these gradients is actually governed by the condition of illumination on the n-side of the sample, as shown by the arrows added in Figs. 5.11(c) and 5.12(c). On the contrary, and as expected, the measurement of the component of the local V_{oc} produced by the pulsed illumination incident on the p-side indicates identical features in Fig. 5.11(e-f) and in Fig. 5.12(e-f), with and without the grazing light on the n-side, respectively. Some boundaries not clearly visible in the local V_{oc} picture appear in the amplitude picture, and some boundaries visible in that local V_{oc} picture are not clearly visible in the amplitude picture.

To verify if there is a correlation between the features observed in the local V_{oc} maps (Figs. 5.11(b-c) and 5.12(b-c)) and the dark spots observed in the amplitude pictures (Figs. 5.11(e-f) and 5.12 (e-f)), we performed a scan over a large (50 x 50 μm^2) area. The resulting topography, local V_{oc} and amplitude pictures are shown in Fig. 5.13, where the circles indicate identical zones of interest. Indeed we observe that many dark spots in the amplitude picture (Fig. 13(c)) correspond to strongly contrasted cluster boundaries in the map of local V_{oc} (Fig. 13(b)).

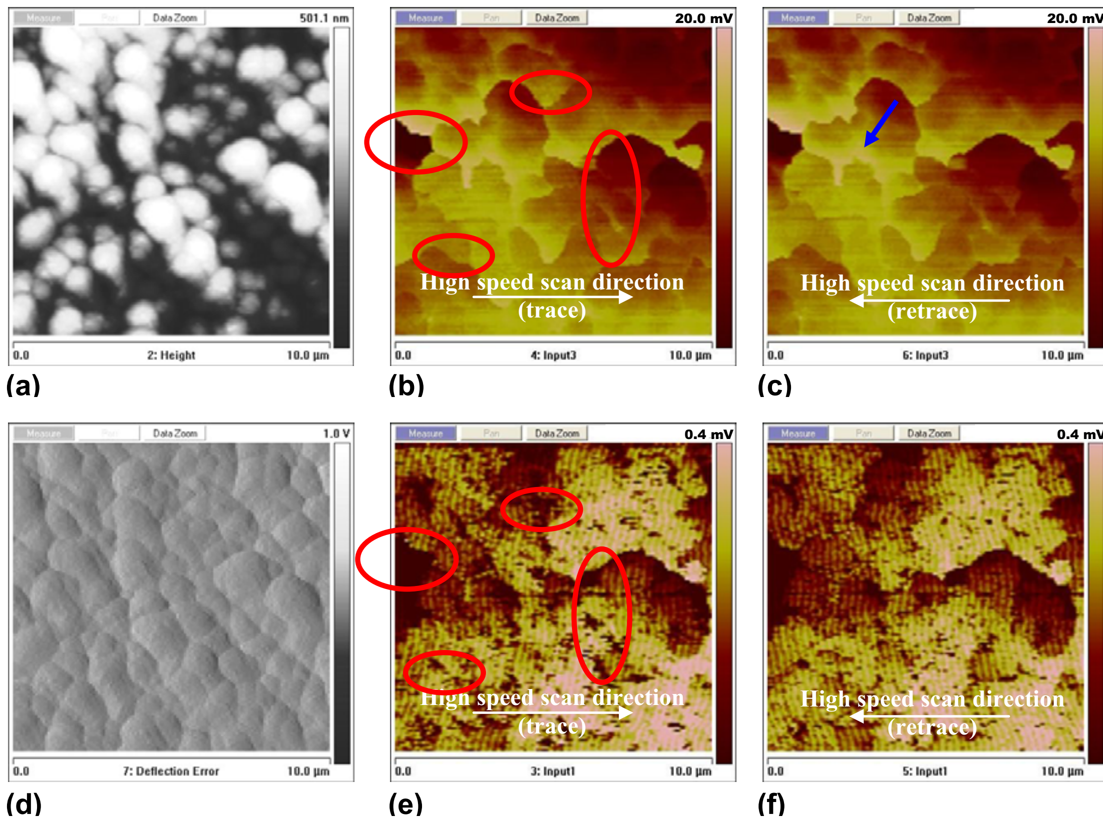

Fig. 5.11: 'Lock-in planar nanopotentiometry' results obtained with the additional laser light illumination added in grazing incidence (633 nm, from six o'clock) on the n-type layer of a p-i-n µc-Si:H solar cell deposited on a LPCVD ZnO layer without surface post-treatment. The bias voltage V_{bias} is 365 mV and the scan speed is 2 µm/s. (a) AFM picture of the topography, (b) map of the local V_{oc} recorded during the scan in the 'trace' and (c) in the 'retrace' direction, (d) enhanced topographic picture (error signal of the AFM's control loop), (e) map of the amplitude of the small-signal variation, produced by the pulsed illumination (630 nm) on the p-side, recorded during the scan in the 'trace' and (f) in the 'retrace' direction. The circles in (b) and (e) indicate cluster boundaries for comparison with Fig. 5.12. The arrow in (c) indicates the direction of the gradient of the local V_{oc} over the µc-Si:H clusters, which is governed by the condition of illumination on the n-side of the sample.

5.3.3 Discussion

First note that the electrical probing measurements performed in the planar configuration produce the same current and voltage maps when recorded during scans in both 'trace' and 'retrace' directions. This indicates that the relative variations recorded in these maps are reproducible and are not controlled by unwanted fluctuations in the contact force between the tip and the surface of the sample. Therefore, we believe that the patterns observed in the C-AFM current maps (Fig. 5.10(c)) and in the voltage maps (Figs. 5.11 and 5.12) must be attributed to the different electrical behaviors of the different µc-Si:H clusters visible in the enhanced topographic pictures. This also indicates that the conductivity of the n-doped layer is not high enough, or is low enough in the grain boundaries area, to ensure that voltage differences can develop between the clusters.

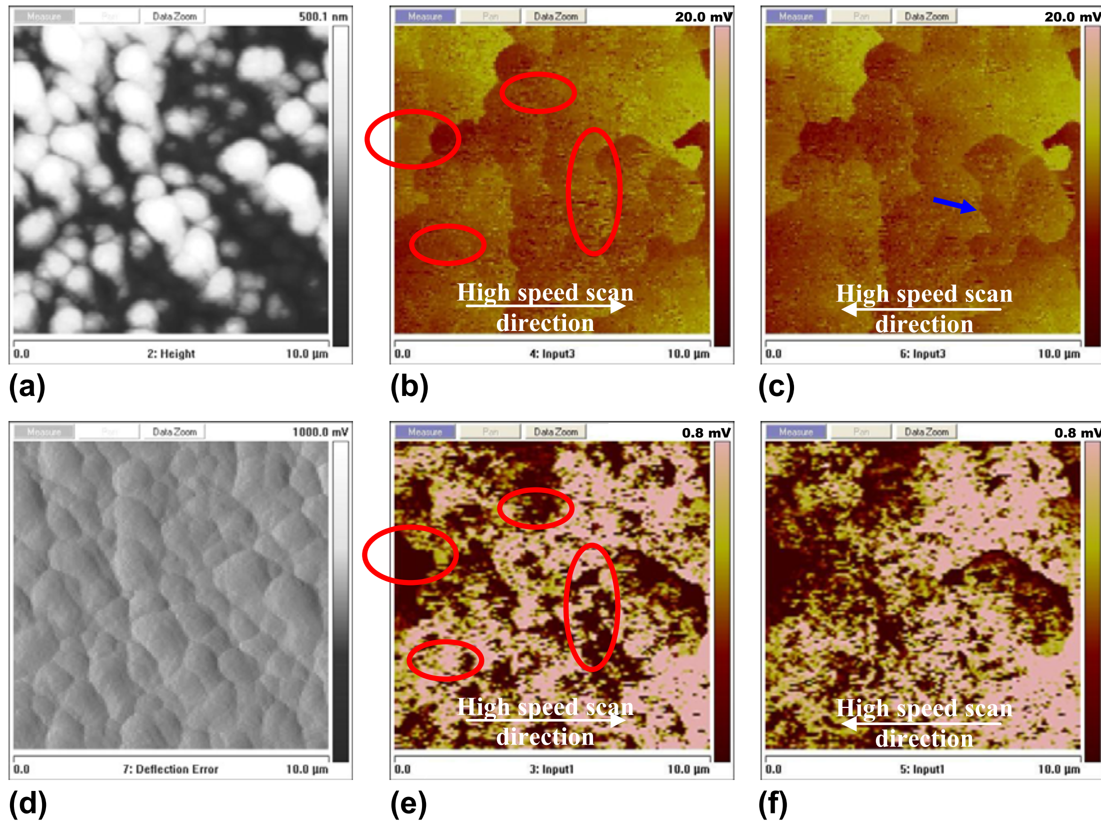

Fig. 5.12: 'Lock-in planar nanopotentiometry' results obtained without the additional laser light illumination on the same surface area as in Fig. 5.11 (second scan). The bias voltage V_{bias} is 290 mV and the scan speed is 2 µm/s. (a) AFM picture of the topography, (b) map of the local V_{oc} recorded during the scan in the 'trace' and (c) in the 'retrace' direction, (d) enhanced topographic picture (error signal of the AFM's control loop), (e) map of the amplitude of the small-signal variation, produced by the pulsed illumination (630 nm) on the p-side, recorded during the scan in the 'trace' and (f) in the 'retrace' direction. The circles in (b) and (e) indicate cluster boundaries for comparison with Fig. 5.11. The arrow in (c) indicates the direction of the gradient of the local V_{oc} over the µc-Si:H clusters, which is governed by the condition of illumination on the n-side of the sample.

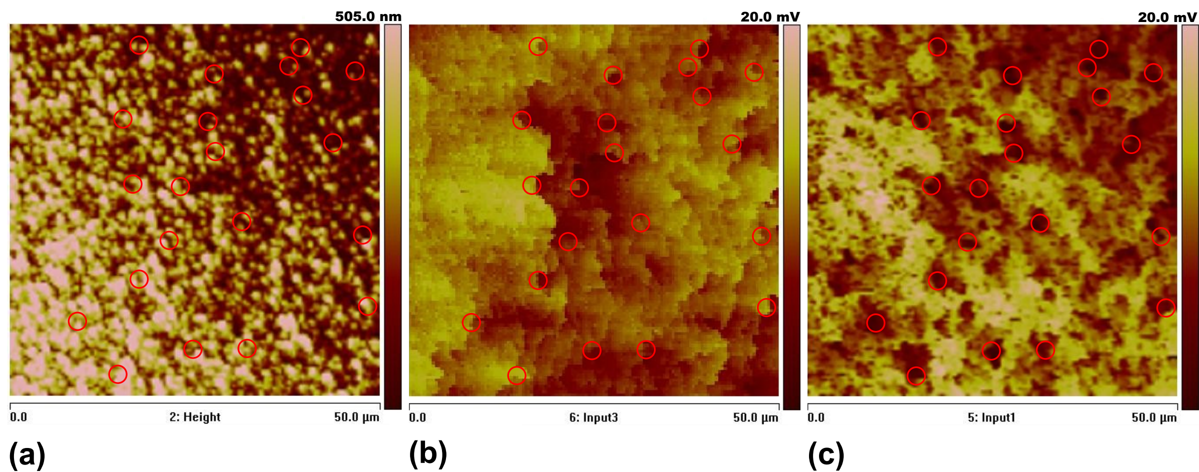

Fig. 5.13: 'Lock-in planar nanopotentiometry' results obtained on a large scan area of 50 x 50 µm^2 on the n-type layer of a p-i-n µc-Si:H solar cell deposited on a LPCVD ZnO layer without surface post-treatment. The bias voltage V_{bias} is 282 mV and the scan speed is 10 µm/s. (a) AFM picture of the topography, (b) map of the local V_{oc} recorded during the scan in the 'trace' direction and (c) map of the amplitude of the small-signal variation, produced by the pulsed illumination (630 nm) on the p-side, recorded during the scan in the 'trace' direction. The circles indicate dark spots in (c) corresponding to strongly contrasted cluster boundaries in (b).

The aging phenomenon in the electrical probing is systematically observed in our C-AFM and nanopotentiometry measurements, i.e. with and without an electrical current flowing through the conductive tip. It was reported for µc-Si:H layers by several authors (see e.g. [Kleider 2001] or [Shen 2007]). Our observations are coherent with the findings of Kleider *et al.*, who showed that the aging induced by the first scan is independent of the presence of an electrical current through the tip. They suggested that it is related to an enhanced oxidation due to a chemical change of the surface of the silicon layer induced by the contact with the tip [Kleider 2001].

Figure 5.14 schematically illustrates the principle of the *near-V_{oc} planar C-AFM* method. It shows how this measurement method discriminates between areas with high and low local V_{oc} and why dark and bright areas in Fig. 5.10(c) correspond to high and low local V_{oc}, respectively. This measurement method therefore demonstrates that if we remove the back contact of a p-i-n µc-Si:H solar cells deposited on a rough LPCVD ZnO layer, each µc-Si:H cluster behaves as an insolated nano-diode with its own V_{oc}, and that the lateral carrier transport between clusters in the same neighborhood does not influence the local V_{oc}. The difference in the V_{oc} values of different nano-diodes can be due to differences in the quality of the µc-Si:H material of different clusters and to inhomogeneous abruptness of the p-i (see Fig. 5.6(b)) or the i-n electrical junctions. But they can also be produced by different illumination conditions of the different clusters (e.g. strong light incoupling in one of the cluster), or even enhanced local shunting through the cracks. This is discussed below on the basis of the planar nanopotentiometry measurements.

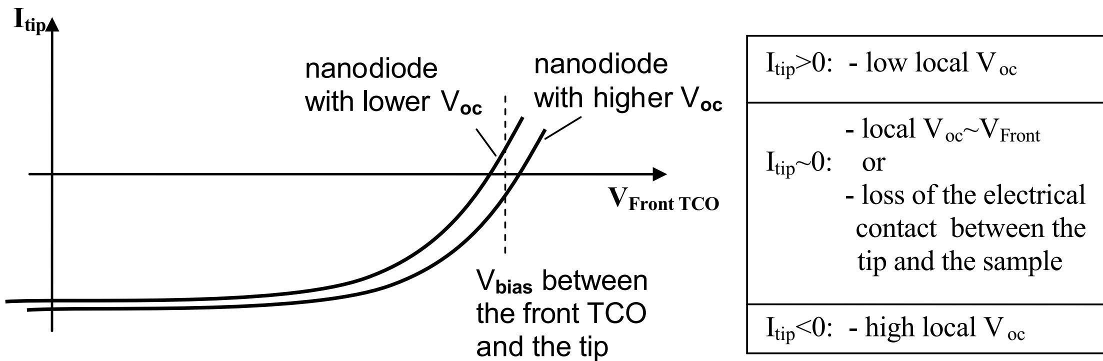

Fig. 5.14: Schematic of the principle of the 'near-V_{oc} planar C-AFM' method explaining that bright areas in Fig. 5.10(c) correspond to areas with a low local V_{oc}.

Before this, and to conclude with the discussion on the *near-V_{oc} planar C-AFM* results, we comment on the absence of highly conductive paths at the cluster boundaries in Fig. 5.10(c). Shen *et al*. reported on C-AFM measurements performed on µc-Si:H solar cells deposited on Asahi U-type SnO_2 layers. These measurements indicate higher leakage currents at the cluster boundaries [Shen 2007]. We know from TEM analysis [Python 2008] and

from a novel method based on SEM imaging for the counting of cracks over tenths of microns developed by Python *et al.* [Python 2009a], that a crack in the μc-Si:H material is present over each valley of the untreated LPCVD ZnO. Therefore, for the sample analyzed here, cracks are most probably present underneath the surface of the n-type layer along each cluster boundary. The absence of highly conductive paths indicates that cracks do not behave simply as shunts. Indeed, Python *et al.* recently showed, using a two-diode model, that the cracks in our p-i-n μc-Si:H cells deposited on LPCVD ZnO cannot be modeled by a simple shunt resistance but must be modeled by a bad diodes with high value of J_0 [Python 2008]. However, due to the high J_0 value of the bad diode associated with the cracks, we should observe areas with low local V_{oc} in Fig. 5.10(c) all around the μc-Si:H cluster. The question as to why we do not observe low V_{oc} areas localized at the cluster boundaries in Fig. 5.10(c*),* deserves further investigation. It could in part be attributed to a lowering of the conductivity of the n-layer at the cluster boundaries, whereas it is high enough on the top of the cluster to provide a minimum contrast change. Other interpretations are partly addressed in the following discussion on the planar nanopotentiometry measurements.

The planar nanopotentiometry measurements shown in Figs. 5.11(b-c) and 5.12(b-c) confirm that when the back contact is removed, each μc-Si:H cluster behave as an insulated nanodiode with typical variations of +/-5 mV for the value of the local V_{oc} of adjacent clusters. They also demonstrate that the illumination conditions on the n-side influence the local V_{oc}. Unfortunately, the uncontrolled illumination of this n-side by the laser diode of the AFM system is difficult to avoid. A solution to suppress this photo-perturbation could be the use of a special AFM cantilever with lateral wings, such as developed by Chang *et al.* [Chang 2005], which provides a shadow area that fully covers the scan region. The illumination from the p-side by a pulsed light and the lock-in detection technique, as described in Fig. 5.9, provides an alternative method to discriminate the effects produced by the photo-perturbation. The amplitude pictures showed in Figs. 5.11(e-f) and 5.12(e-f) confirms that the local V_{oc} depends on the μc-Si:H cluster considered. Compared to the local V_{oc} pictures in Figs. 5.11(b-c) and 5.12(b-c), these amplitude pictures reveal different cluster boundaries. This is most probably due to the fact that the light incident from the rough LPCVD ZnO front contact is scattered. Therefore, we believe that the boundaries observed in the amplitude pictures are mainly due the electrical behavior of the cluster and are no longer influenced by the illumination condition on the n-side. We attribute the low (non-zero) amplitude areas visible in the amplitude pictures to clusters with poor electrical characteristics. Moreover, the small dark spots in Figs. 5.11(e-f), 5.12(e-f) and 5.13(c) correspond to very poor material with almost no response to the pulsed illumination from the p-side. As it is highlighted in Fig. 5.13, all of these dark spots correspond to cluster boundaries and many of them correspond to a high contrast on the map of local V_{oc}. This most probably indicates that the dark spots correspond to the areas of very high J_0 value of the bad diode associated with the cracks, which were missing in the C-AFM picture of Fig. 5.10. Therefore, thanks

to the pulsed illumination from the p-side, the *lock-in planar nanopotentiometry* allows us to probe the photo-response of the μc-Si:H material close to the p-i interface, even if the electrical probing is performed on the n-side. The observation of a localized effect of cracks only in the amplitude picture provides an indication that cracks affect the p-i interface more severely than the bulk or the n-i interface of the device.

The poor electrical characteristics evidenced by the dark spots in the amplitude pictures can be due to (1) a low equivalent shunt resistance R_{shunt}, (2) a high reverse saturation current J_0 of the equivalent nanodiode, or (3) a high recombination current J_{rec} (which itself depends on the mobility-lifetime product $\mu_0\tau_0$ of the material). Although we cannot definitely exclude the presence of shunt current paths in our μc-Si:H material, as we already mentioned, we do not observe evidence of leakage paths in our *near-V_{oc} C-AFM* measurements and, in a two diodes model, an increased cracks density cannot be modeled by a simple linear R_{shunt} resistance. Considering that the dark current is thermally generated from mid-gap defects [Meillaud 2006], both J_0 and J_{rec} increase if the mid-gap defect density increases. The terms J_0 and J_{rec} also increase if the density of (not necessarily mid-gap) recombination centers increases. These can be lattice defects and contaminant atoms in the c-Si nanograins of the cluster. They can also be dangling bonds and contaminant atoms at the surface of the nanograins and in the surrounding a-Si:H tissue. In device-grade material, the diffusion length is sufficiently high so that a non negligible fraction of the carriers can recombine at the cluster boundaries.

If the drift component of the transport mechanism of the photogenerated carriers is weak, recombination at the cluster boundaries will even become dominant. This would be the case if the electric field profile in the intrinsic μc-Si:H layer is deformed by a shift of the Fermi level produced by the presence of e.g. oxygen, boron, or phosphorous contamination. The result of the cross-sectional SKPM analysis presented above in Fig. 5.6 supports the assumption of a heterogeneous distribution of the electric-field over the different clusters, albeit with this technique we cannot definitely exclude parasitic effects induced by the polishing procedure. The two electrical probing measurement methods performed in planar configuration, however, do not include polishing steps and show sharp contrast between cluster boundaries. Therefore they provide an additional indication of a heterogeneous distribution of the electric-field over the different clusters.

5.4 Conclusions

5.4.1 Cross-sectional SKPM and TEM

SKPM analysis can be performed on rough fractured cross-sections of μc-Si:H solar cells deposited on a surface-textured LPCVD ZnO. However, the measured surface potential is sensitive to convolution with the topography of the fractured cross-section; this may render difficult the interpretation of features observed in the SKPM pictures.

By providing a mechanical polishing of the cross-section, we show that the amplitude of the modification of the electric-field induced by the bias voltage is heterogeneously distributed over different μc-Si:H clusters. Each cluster behaves as an "isolated nanodiode", with the electric-field confined within about 500 nm in the intrinsic μc-Si:H layer either near the p-i or near the i-n interface. This supports the assumption of an important contribution of diffusion-assisted transport along the growth axis of the large crystalline nanograins observed by TEM in the μc-Si:H clusters.

On the SKPM pictures taken under short-circuit and forward-bias conditions, the cluster boundaries appear as areas with a low local surface potential, demonstrating a local negative charge. Possible explanations could be the presence of activated boron due to a selective contamination of the clusters boundaries or a difference in the filling of the electronic surface states at these defective regions.

A comparison of SKPM pictures with a TEM micrograph demonstrates that cluster boundaries in the intrinsic μc-Si:H layer can be imaged by the SKPM technique. Moreover, SKPM imaging seems to be able to show the effective thickness of the p-type layer in case of in-diffusion of boron caused by nano-cracks. This ability, which was not pointed-out a the time of the SKPM measurements, merits further in-depth investigations, and could become a simple method – compared to sample preparation for TEM analysis – to determine if nanocracks are present in the first part of the intrinsic μc-Si:H layer close to the p-i interface.

5.4.2 Comparison of cross-sectional SKPM and electrical probing in the planar configuration

The cross-sectional SKPM measurement and the two different planar C-AFM-based electrical probing methods presented in this chapter provide evidence of differentiated electrical behaviors for different μc-Si:H clusters. Consequently, we conclude that a p-i-n μc-Si:H solar cell deposited on a LPCVD ZnO front contact can be sought as a parallel connection of the individual nanodiodes formed by the μc-Si:H clusters which are growing during the PECVD deposition on the top of each pyramid of the ZnO layer. This way, each nanodiode has its own electrical characteristics (reverse saturation current density J_0, and recombination current density J_{rec}).

Our *lock-in planar nanopotentiometry* measurement technique provides the ability to image at the same time highly localized effects of cracks at the p-i interface (amplitude picture) and their averaged results on the n-side (map of local V_{oc}), which can affect groups of many μc-Si:H clusters. We suggest that the cluster boundaries affect in large part the values of the terms J_0 and J_{rec} of the equivalent nanodiode, which model a given μc-Si:H cluster. This is because during multiple scattering events, free carriers see an enhanced equivalent recombination center density, due to the presence of the highly defective material at the cluster boundaries. Moreover, this effect will be worsened by a weakening of the electric field depending on the degree of contamination of the different

clusters. This in turn explains how clusters, made of *a priori* the same μc-Si:H material, can present very dissimilar individual electrical characteristics, as evidenced in this work both for cross-sections, by SKPM measurements, and for samples analyzed in planar configuration, by C-AFM and nanopotentiometry-based measurement techniques.

6 Scattering of the light transmitted through a rough nano-textured front contact ZnO layer

The aim of this chapter is to provide insight into the mechanisms involved when light transmitted through the front contact zinc oxide (ZnO) layer of our p-i-n solar cells is scattered by its rough nano-textured surface.

In section 6.1 we explain our motivation for the use of light scattering in silicon (Si) thin-film photovoltaic (PV) solar cells by means of randomization. We give a short overview of the current status of the research in this field in the Si thin-film PV community, where far-field and near-field approaches are considered. In section 6.2 we introduce the principles of the Beckmann-Kirchhoff scalar scattering theory and we explain how J. E. Harvey *et al.* successfully showed that providing a slight modification, this theory is actually applicable in the non-paraxial case. In section 6.3 we describe how we model our surface-textured ZnO layers by random phase screens and we present the results of a study where we compare transmitted light scattering measurements with calculation results for different surface morphologies. We then calculate the light scattering produced in silicon for different surface morphologies and compare results with measurements of the external quantum efficiency of real solar cells. In section 6.4, we discuss the significance of light scattering measurements performed in air to predict effects in Si and we comment on the limitations of our calculation method and on its applicability in predicting the benefits of different real or hypothetical surface morphologies for the front contact of a complete p-i-n micromorph solar cell device.

6.1 Introduction: The Yablonovitch's $4n^2$ enhancement limit

For wavelengths λ larger than 700 nm, the optical absorption coefficient α of amorphous silicon (a-Si:H) and microcrystalline silicon (μc-Si:H) is lower than 10^4 cm^{-1}. Therefore, for light in normal incidence on these materials and in absence of any light scattering, layers significantly thicker than the corresponding penetration depth of 1 μm should be used to absorb photons from the near infrared part of the solar spectrum. For the spectral range of 800–1000 nm, this thickness is increased to the range of 10–100 μm for μc-Si:H whereas a-Si:H is transparent because of its higher energy bandgap. This is illustrated in Fig. 1.2 of chapter 1, which shows α(λ) for crystalline Si, a-Si:H and μc-Si:H.

Such layer thicknesses are highly undesirable because of the decreased electric-field, which would be produced in the drift assisted p-i-n solar cell device. This would, in turn, lead to high charge carrier collection losses. The thickness of the intrinsic layer of a a-Si:H solar cell should not exceed 300 nm [Platz 1998] because of its low mobility-lifetime

product in the degraded state (typically 10^{-7} V/cm^2) [Shah 2006]. For μc-Si:H solar cells using the gas purifier technique to ensure a true mid-gap intrinsic layer, thicknesses up to 3.6 μm have been demonstrated with only minimum collection losses [Meier 1996]. However, due to the rather low deposition rate (5-7 Å/s) achievable so far for state-of-the-art μc-Si:H in typical production lines [Kroll 2007, Klein 2008], such thicknesses are detrimental in terms of production costs.

A way to solve these issues is to increase the mean path length of the light inside the silicon layer. In 1965, St. John proposed to take advantage of total internal reflection and promote light trapping in a silicon photodiode [St John 1965]. In the mid-seventies Redfield was the first to demonstrate multiple-pass through a silicon thin-film solar cell using a grooved mirror [Redfield 1974]. Nowadays, the most common practical way to produce refraction and therefore oblique in-coupling of incident light in thin-films of silicon is to texture one or both sides of the layer. This can be done by deposition of silicon on a surface-textured (opaque) substrate – e.g. hot-silver [Terrazzoni 2006], polymer replications [Bailat 2005] and gratings [Haug 2008a] – or on a transparent rough superstrate – e.g. glass plates covered with tin oxide (SnO_2) by atmospheric-pressure chemical vapor deposition (APCVD) [Taneda 2007] or with ZnO deposited by the low-pressure chemical vapor deposition (LPCVD) technique [Meier 2002], textured glass plates [Isabella 2008].

In the case of full randomization of the incident light by a textured surface and in the weak absorption limit, Yablonovitch derived a superior limit of $4n^2$ for the possible enhancement of absorption by means of light trapping, where n is the refractive index of the medium considered [Yablonovitch 1982]. For the optical absorption in a-Si:H of the infrared part of the spectrum, this enhancement corresponds, with n~4, to a factor as large as 64. The derivation of Yablonovitch follows from the three steps 1), 2), and 3) explained as follows:

1a) Yablonovitch uses statistical mechanics arguments. He considers a transparent medium, and thus excludes inelastic events with absorption and reemission at another frequency. He also assumes a full randomization when the light is scattered by the rough interfaces of the medium considered (i.e. the system is supposed ergodic, which implies that even if the external-radiation field is not isotropic, the angular distribution of the light rays inside the medium will be perfectly isotropic). The spectral intensity I_{int} of the radiation at the frequency ω through the solid angle dΩ in the medium of volume V is obtained by multiplying its group velocity v_g and its electromagnetic energy density $u(\omega) = \langle E(\hbar\omega)\rangle \cdot N(\omega)/V$, where $\langle E(\hbar\omega)\rangle = \hbar\omega/(\exp[\hbar\omega/k_BT]-1)$ is the average energy of the corresponding ensemble of harmonic oscillators (with ħ the reduced Planck's constant, k_B the Boltzman's constant, and T the absolute temperature), and where and $N(\omega) = 2\cdot V\cdot d\Omega\cdot k^2 dk/(2\pi)^3$ is the number of photonic modes at the frequency ω comprised in the infinitesimal element of volume $d\Omega\cdot k^2 dk$ in the k-space (the factor 2 stands for the two possible polarizations). On one hand, the number of modes N(ω) in the medium is n^3 times larger than in the vacuum, because at a position x in the medium, the wave vector's

length is k = n(ω,x)·ω/c. On the other hand, the group velocity v_g = dω/dk = c/n of the radiation in the medium will be n times smaller than in the vacuum. Therefore, if the above conditions are fulfilled, the spectral intensity I_{int} will be n^2 times larger than the incident intensity I_{inc} in the surrounding of the medium:

$$\begin{aligned} I_{int}(\omega, x) &= v_g \cdot \langle E(\hbar\omega)\rangle \cdot 2 \cdot d\Omega \cdot k^2 dk/(2\pi)^3 \\ &= c/n \cdot \langle E(\hbar\omega)\rangle \cdot 2 \cdot d\Omega \cdot (n \cdot \omega/c)^2 (n/c) d\omega/(2\pi)^3 \\ &= n^2 \cdot \langle E(\hbar\omega)\rangle \cdot 2 \cdot d\Omega \cdot (\omega/c)^2/(2\pi)^3\, d\omega \\ &= n^2(\omega, x) \cdot I_{inc}(\omega). \end{aligned} \qquad (6.1a)$$

1b) When the shape of the medium is a layer, the relation (6.1a) can also be derived from geometrical optics, assuming perfect Lambertian scattering (see also [Goetzberger 1981]). In this case, the entire intensity incident on both sides of the layer is diffused with a cosine-dependence, independently of the direction of incidence. Moreover, the critical angle θ_c of total internal reflection, deduced from the Snell's law, is asin(1/n). Therefore, the fraction of intensity escaping through the solid angle subtended by the two escape cones of angular width $2\theta_c$ is, in the worst case of 100% transmittance through the cones:

$$\frac{I_{esc}}{I_{int}} = \frac{2 \times \int_0^{2\pi}\int_0^{\theta_c} L_{int} \cos\theta \cdot \sin\theta d\theta d\varphi}{2 \times \int_0^{2\pi}\int_0^{\pi/2} L_{int} \cos\theta \cdot \sin\theta d\theta d\varphi} = \sin^2\theta_c = \frac{1}{n^2} \ ,$$

where L_{int} is the radiance in the medium and the factors 2 indicate that the intensities are bidirectional. Applying the principle of detailed balancing, the medium being supposed perfectly transparent, the incident intensity I_{inc} is equal to the escaping intensity I_{esc}; therefore the result (6.1a) is found again:

$$I_{int} = n^2 I_{esc} = n^2 I_{inc}. \qquad (6.1b)$$

2) Until now, the layer was entirely surrounded by the external incident intensity I_{inc}. If at this point it is covered on the bottom side by a perfectly reflective mirror, only the escape cone towards the top direction remains active. But inside the layer the intensity is still bidirectional. The fraction of intensity escaping through the single cone becomes:

$$\frac{I_{esc}'}{I_{int}'} = \frac{1 \times \int_0^{2\pi}\int_0^{\theta_c} L_{int}' \cos\theta \cdot \sin\theta d\theta d\varphi}{2 \times \int_0^{2\pi}\int_0^{\pi/2} L_{int}' \cos\theta \cdot \sin\theta d\theta d\varphi} = \frac{1}{2}\sin^2\theta_c = \frac{1}{2n^2} \ .$$

According to the principle of detailed balance, I_{inc}' and I_{esc}' are equal. Thus with the back reflector, the intensity enhancement is twice:

$$I_{int}' = 2n^2 \cdot I_{inc}'. \qquad (6.2)$$

3) If the layer is weakly absorbing, the light intensity through its full thickness is approximately constant and therefore, because the radiation in the layer is Lambertian, the optical path in a layer of width d is twice the thickness of the layer (double-pass absorption formula). Moreover, according to (6.2), the effective coefficient of absorption α_{eff} is $2n^2$ times larger than α. Therefore, the double-pass absorption formula for the absorbance A of the layer becomes:

$$A = 1\text{-}\exp(-2\alpha_{eff}\, d) \approx 2d\cdot\alpha_{eff} = 2d\cdot 2n^2\alpha = 4n^2 d\cdot\alpha. \qquad (6.3)$$

The relation (6.3) indicates that the effective optical path d_{opt} induced by the light trapping is $4n^2$ times the average width d of the layer.

This Yablonovitch's upper limit of $4n^2$ for the absorption enhancement follows, at the points 1b) and 3) from the hypothesis of a Lambertian distribution. However 1b) is equivalent to 1a), which follows from statistical mechanical considerations. Therefore, we can state, for a homogeneous medium with a homogeneous distribution of photonic states in the k-phase space, that Lambertian scattering is optimum to uniformly fill this phase-space and make the relation (6.1) valid. This suggests that even if a "super Lambertian" distribution could produce a factor larger than 2 in the double-pass absorption formula used in (6.3), that better optical path enhancement would, however, have to compete with a weakening of the light intensity in the medium, because of a suboptimal (inhomogeneous) filling of the optical modes available with a given absorber geometry. Therefore, in recent works, Gee and others proposed to go beyond that $4n^2$ limit by engineering the photonic density of states g(ω) of the medium itself, making n(x) inhomogeneous by means of a photonic crystal. Gee proposed to increase g(ω) in the weak absorbing regions at the expense of well chosen other spectral bands (not absorbing) [Gee 2002]. He also notes that submicrometer diffractions gratings can be used to preferentially fill optical modes and that among different grating geometries, blazing structures couple more energy into the non-zero diffraction orders [Heine 1995, Zaidi 2000]. The perspectives opened by these photonic structure approaches are huge but are clearly outside of the framework of the present study, in which we deal with traditional thin-film technologies, i.e. with absorbing materials that are homogenous. Therefore, we follow the statement, that full randomization of the light by Lambertian scattering is optimum for light trapping with random surface textures. This statement is also followed by Vanecek *et al.* in [Vanecek 2003].

From the preceding, it becomes clear that for practical realizations of silicon thin-film solar cells, not only the amount of light scattered by the front contact but also the angular distribution of the scattered radiation are of primary importance for the performance of the device. The most common measurement technique to assess light scattering properties of a front transparent conductive oxide (TCO) layer is the haze measurement [Mizuhashi 1988] carried out with a spectrometer and an integrative sphere. This measurement technique provides the ratios H_T and H_R corresponding to the haze in transmission and in reflection, respectively:

$$H_T = T_{tot}/T_{dif} \text{ and}$$
$$H_R = R_{tot}/R_{dif}, \qquad (6.4)$$

where T_{tot} (T_{dif}) and R_{tot} (R_{dif}) are the total (diffuse) transmittance and reflectance, respectively. Here we consider that the diffuse component refers to light escaping at an angle > 5° from the specular direction (see section 2.2.3).

In addition to haze measurement, angular resolved scattering (ARS) measurement of front TCO layers is increasingly used in the thin-film PV community [Stiebig 2000, Krc 2002, Schulte 2007, Poruba 2008]. This measurement is performed by means of an incident laser beam and a photodetector mounted on a goniometric arm (see chapter 2). Attempts to model light scattering produced by different front TCO are currently under way in many groups, where far-field and near-field approaches are considered. In the near-field approach, the scattered electromagnetic field is considered down to distances, from the scattering surface, much smaller than the wavelength λ; whereas, in the far-field approach, the scattered field is considered only from distances much larger than λ from the scattering surface. Both of these approaches are based on characterization of the surface topography of the TCO layer by atomic force microscopy (AFM) measurements.

In the near-field approach, exact solving of the Maxwell's equations is carried out with finite element methods [Haase 2007, Rockstuhl 2007, Poruba 2008]. Haase *et al.* showed that, using idealized tridimensional periodic surfaces, a period of 0.7 to 1.2 µm is optimum for light trapping in µc-Si:H [Haase 2007]. For a sputtered-etched ZnO layer, Rockstuhl *et al.* demonstrated the validity of their finite-difference in time-domain (FDTD) calculations by comparing them with results of scanning near-field optical microscopy (SNOM) performed in-air above the surface of the ZnO layer [Rockstuhl 2007]. These authors also deduced that the absorption in a-Si:H films deposited on rough layers of sputtered-etched ZnO is maximized near the edges of the craters present on the surface of the TCO [Rockstuhl 2008]. Poruba *et al.* also used a FDTD calculation approach and a near-to-far-field conversion technique for the calculation of the angular distribution of light scattered by SnO_2 Asahi U-type, sputtered-etched ZnO and LPCVD ZnO layers [Poruba 2008]. The comparison with experimental ARS measurements indicated similarities with measurements, but a too large amount of light scattered in the large angles was

predicted by the calculations. They proposed to improve their results by increasing the size of the AFM's scan area (currently 10 x 10 μm^2), decreasing the meshgrid-size of their calculation and consequently increaseing the size of the memory of the computers involved in the calculation to several hundreds of gigabytes [Poruba 2008]. In the far-field approach, Schulte *et al.* [Schulte 2007] proposed to use a geometrical optics analysis by performing ray-tracing of light rays in models of sputtered-etched ZnO layers. In this method, the surface of the ZnO layer is also characterized by AFM. The comparison of calculation results with ARS measurements indicated that geometric optics can account for the main features of the behavior of light when transmitted through the ZnO layer. However, an effective medium approximation (EMA) and Mie scattering need to be included in the calculation to reproduce the value of the most probable scattering angle and the contribution of large scattering angles, respectively [Schulte 2007].

For the optical modeling of complete silicon thin-film solar cells, or more generally of any multi-layered thin-film device with nanorough interfaces, specific software have been developed by different groups (e.g. GENPRO [Zeman 1995], SunShine [Krc 2003], CELL [Springer 2004]). These softwares involve coherent modeling of the optical stack, which takes into account interferences, and modeling of the incoherent part of light intensity scattered by the rough interfaces. They include a particular result of the scalar scattering theory: the haze formulas that predict H_T and H_R for given values of σ_{rms} and λ (see section 6.2.2). Actually, they do not include more about scalar scattering theory. Indeed, the angular distributions functions (ADF) of light intensity scattered at the rough interfaces are left as parameters. Therefore, modeling of complex optical structures such the micromorph device with intermediate reflector, even with the help of these softwares, is not trivial. This is mainly because results depend strongly on the ADF functions related to reflection and transmission at the different interfaces [Krc 2003, Krc 2006] and, these ADF functions are difficult to know *a priori*. This will be the topic of section 6.3.2.

In the present work, we model our different surface-textured LPCVD ZnO layers by random phase screens, on the basis of AFM measurements, and we use a scalar scattering theory as modified by Harvey. The theoretical aspects of this approach are developed in the next section. Comparisons of our calculations with ARS measurements and with external quantum efficiency (EQE) measurements of solar cells deposited on different ZnO layers are presented afterwards. This approach is different with respect to what other authors in the field of thin-film PV propose, because we use the whole scalar scattering theory to completely calculate the angular distribution of the scattered field, and not simply the haze formula derived from this theory.

6.2 Scalar scattering theory

6.2.1 Theoretical approaches and compatibility with our problem

The theoretical treatment of scattering of electromagnetic waves by a random surface can be carried out by first order vector perturbation theories such as those developed by Rice [Rice 1951] or by Elson and Bennett [Elson 1979] or by scalar theories [Isakovich 1952, Beckmann 1963].

The advantages of the vector theories are that (1) they include polarization effects and (2) they are adapted to the case of large-angle scattering, i.e. they are not limited to directions making a small angle with the specular direction (no paraxial approximation). The drawback of such first-order perturbation models is that they are only valid within the limit of small surface roughness (σ) compared to the wavelength ($\sigma/\lambda \ll 1$) [Duparré 2006]. This constraint is unfortunately not compatible with our front ZnO layers because the root-mean-square (rms) values of their surface roughness (σ_{rms}) are typically comprised between 60 to 200 nm, whereas the effective wavelength ranges from 100 to 250 nm in a-Si:H with n~4 for our spectral range of interest (comprised between 400 and 1000 nm).

However, the Helmholtz scalar integral used in scalar theories is a solution of the Helmholtz equation of a scalar wave for any geometry and therefore also for very large σ. Using this integral with the appropriate Kirchhoff approximation, Beckmann and Spizzichino addressed the problem of the scattering of electromagnetic-waves from a perfectly conductive rough surface [Beckmann 1963]. The important benefit of this Beckmann-Kirchhoff (B-K) theory is that it is valid for any value of the ratio σ/λ. However, in addition to the fact that it does not directly include polarization effects, the B-K theory has major limitations:

A) The B-K theory deals only with reflection on a perfectly conductive surface and, therefore, does not include the effect of local variations of the Fresnel's coefficients of reflection due to variations of the local angle of incidence.

B) It does not include multiple scattering and shadowing effects.

C) It is valid only for surface with an autocorrelation length T much larger than the wavelength ($T \gg \lambda$).

D) A complete treatment is proposed only for the most common case where the vertical heights z of the rough surface ζ generated by the random process $z=\zeta(x,y)$, where the triplet (x,y,z) refers to a Cartesian coordinate system, are normally distributed (i.e. when the probability density function w(z) associated to the distribution of heights of the surface ζ is a Gaussian function).

Concerning the limitation A, a reformulation of the B-K theory extended to the case of the diffuse transmittance, but restricted to surfaces with small slopes ($\sigma/T \ll 1$) was proposed by Carniglia [Carniglia 1979]. Of course, the restriction to small slopes discards the problem of the variation of the reflectance with variations of the local angle of incidence

on the surface. Moreover, Carniglia only considered directions lying close to the axis of the specular direction, making a small angle ε with this axis. Note that within this restriction, the paraxial approximation is valid, i.e. sin(ε) and tan(ε) can be approximated by ε. Because Carniglia limited his calculations to small angles of scattering, he could only propose expressions for the haze in reflection and in transmission [Carniglia 1979] (but no result concerning the angular distribution of the scattered light). These two theoretical expressions, or empirical modifications of them, are used nowadays in the silicon thin-film PV community [Stiebig 2000, Zeman 2000, Poruba 2000, Krc 2002, Springer 2004]. The small slope restriction imposed by Carniglia and the inability of his theory to deal with the angular distribution has led to the misconception that scalar theories are not suitable for the study of large angle scattering (e.g. [Duparré 2006]). Following Harvey, we will show that scalar scattering theories are indeed perfectly valid outside any paraxial approximation, such as imposed e.g. in [Goodman 1968, section 4-2].

The limitation B validates the pertinence of the ray-tracing approaches proposed in [Schulte 2007] which seems especially designed to handle multiple-scattering and shadowing effects. Note that B can also be partially handled by sophisticated approaches. For example, the use of a second-order Kirchhoff approximation (iterative substitution of Kirchhoff solution into the integral equation) added to the use of propagation shadowing functions [Wang 2005].

The limitation C (T>>λ) is clearly not compatible with our ZnO layers because their typical lateral size is comprised between 0.4 and 0.8 µm. Three effects of the violation of the condition T>>λ are:

(a) Plenty of sharp edges and tips with radii of curvature r smaller or much smaller than λ will be present on the surface. AFM and SEM pictures throughout this thesis show that it is obviously the case for virtually all of our ZnO layers. Actually, the B-K theory is precisely restricted to surface with large correlation lengths because, in the resolution of the Helmoltz integral, the Kirchhoff approximation fails at points of the surface with radii of curvatures much smaller than λ [Beckmann 1963] (see Fig. 6.1). The consequence is that the B-K theory cannot predict near-field effects such as the lightning rod effect observed by Rockstuhl *et al*. at locations of high curvature in SNOM measurements and in FDTD calculation results [Rockstuhl 2007, Rockstuhl 2008]. We want to point out that such highly localized effects may correspond to a decrease of the ergodicity and, therefore, may be detrimental to reach the Yablonovitch's $4n^2$ limit discussed in the previous section.

(b) The local angles of the surface will be high (the ratio σ_{rms}/T is typical of the rms slope of the surface) and may vary significantly from place to place on the surface. Figure 6.7 shows the topography determined by AFM measurements for typical ZnO layers used in this work and the distribution of the local angles of

Kirchhof approximation
Electric-field E at a point P just above the surface:

$$E(P) = E_{inc}\,(1+R)$$

where E_{inc} is the electric-field of the incident radiation and R is the coefficient of reflection of the surface. Therefore this approximation consists to consider that the incident radiation is reflected from planes tangent to the points of the surface.

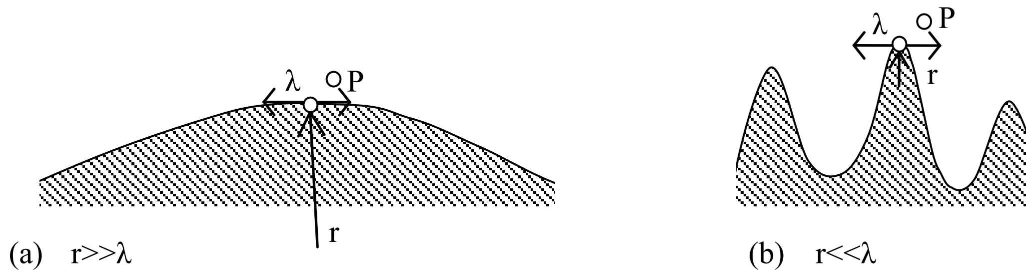

Fig. 6.1 Two reflective surfaces with (a) large and (b) small radii of curvatures r compared to the wavelength λ. In (b), r<<λ, and therefore the Kirchhof approximation completely fails. Figure adapted from [Beckmann 1963].

the surface with respect to the plane of the layer (presented later in the text). It clearly indicates that the range of significant values for the local angle is very large (from ~20° to ~60°). The consequence will be large local variations of the Fresnel's coefficients of reflection. For the case of a ZnO/air interface, the condition of total reflection will be reached on a large fraction of the surfaces (θ_c in air is 30° for n~2). Again this gives pertinence to the ray-tracing approach in [Schulte 2007]. Note that, no total internal reflectance will occur for light in transmission through a ZnO/Si interface.

(c) Twice the correlation length T used to describe random surfaces is the analog of the period Λ of periodic structures. Indeed, the random surface can be seen as a continuous superposition of its Fourier components. Therefore, if T>>λ is violated, according to the grating equation $\sin(\theta_q) = q\cdot\lambda/\Lambda$, higher orders of diffraction will become evanescent. In the case of a perfect dielectric/dielectric interface, the energy corresponding to evanescent orders is redistributed among the lower orders of diffraction (if they exist) and into the specular direction (order 0) (Wood's anomalies [Wood 1902]). Conversely, for a perfect dielectric/metallic interface, these evanescent modes will excite surface plasmons (see e.g. [Raether 1988] and [Haug 2008b]) and therefore will be absorbed.

(d) If T<λ or T<<λ, even the first order of diffraction becomes evanescent and a dielectric/metallic interface may become completely dark. In the case of a perfect dielectric/dielectric interface, all the incoming energy will be redistributed in the specular direction similarly to the case of very small roughness (σ<<λ). In addition, the use of the effective medium approximation (EMA) [Bruggeman 1935, Landauer 1952, Tinga 1973] will be needed to model the effective refractive index of the rough interfacial region [Springer 2004, Hagemann 2008], which will behave as an

index matching region, therefore decreasing the optical reflectance of the interface.

The last limitation D is actually not an issue, because Beckmann and Spizzichino proposed a method in their monography to apply the B-K theory to a surface with a different distribution of heights [Beckmann 1963]. Actually, by providing data of AFM measurements, numerical calculations can always be carried out without knowing the exact expressions for the autocorrelation function $C(\tau)$ of the surface $\zeta(x,y)$ and for its distribution of heights $w(z)$.

We will see following this chapter that the B-K theory gives good results despite all these limitations. However, it is important to keep them in mind when analyzing results.

6.2.2 Usage of the scalar scattering theory for haze calculation

The most well known result of the B-K theory concerns the spectral dependence of the ratio of the diffuse to the total reflected intensities in a medium of refractive index n_1 (namely the haze in reflection $H_R = R_{dif}/R_{tot}$). It is valid if the verticals heights $z = \zeta(x, y)$ of the reflecting surface ζ are normally distributed:

$$\text{if} \quad w(z) = (2\pi\sigma^2)^{-1/2}\exp[-z^2/2\sigma^2], \quad \text{then} \quad H_R(\lambda) = 1 - \exp[-(2\cdot 2\pi/\lambda\cdot\sigma\cdot n_1\cos\theta_1)^2]. \quad (6.5)$$

This result indicates that H_R is a function of the ratio σ/λ multiplied by $\cos\theta_1$, where σ^2 is the variance of the Gaussian probability density $w(z)$ and θ_1 the angle of incidence of the light with respect to the normal at the plane defined by the x and y axis. If $w(z)$ associated to the surface ζ is a Gaussian function, $\sigma = \sigma_{rms} = (1/N\cdot\sum_{i=1..N}(z_i - \langle z \rangle)^2)^{1/2}$ can be calculated from the N data points $z_i(x_i,y_i)$ obtained by AFM measurements. The physical interpretation of (6.5) is that the rough surface produces a reduction of the reflection in the specular direction by means of averaged interferences between outgoing waves, the later having experienced different phase shifts introduced by the local variation of the height of the surface. This is why in (6.5), H_R is only sensitive to the vertical variations of the surface $\zeta(x,y)$, projected onto the difference in wave vectors between the incident and the scattered waves. The factor 2 in the exponential in (6.5) comes from this difference.

This formula was extended to the case of diffuse transmittance by Carniglia with the limitation $\sigma/T \ll 1$ and the paraxial approximation discussed above. He approximated the projection on the z direction of the difference in wave vectors between the incident and the transmitted scattered waves by $k\cdot(n_1\cos\theta_1 - n_2\cos\theta_2)$ where θ_2 is the angle of specular transmission given by the Snell's law. Fig. 6.2 illustrates the geometry of the situation. For the haze in transmission (H_T) this yields [Carniglia 1979]:

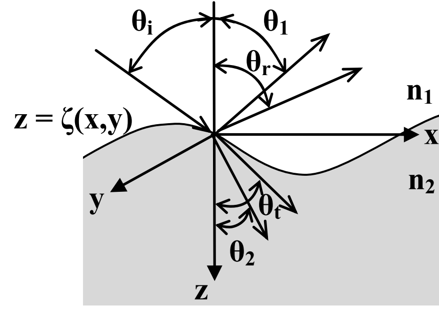

Fig. 6.2 Geometry of the light scattering by a rough surface ζ(x,y), in reflection and in transmission. The indexes i, r, t refer to incident, reflected, and transmitted waves, respectively. θ_1 and θ_2 are the angles of specular reflection and transmission given by $\theta_1 = \theta_i$ and by the Snell's law $n_1 \cdot \sin \theta_1 = n_2 \cdot \sin \theta_2$. In his calculations, Carniglia restricted the angles θ_r and θ_i two small deviations from θ_1 and θ_2, respectively.

$$H_T = 1 - \exp[- (2\pi/\lambda \cdot \sigma \cdot |n_1 \cos \theta_1 - n_2 \cos \theta_2|)^2]. \quad (6.6)$$

Defining an effective wavelength $\lambda_{eff,R}$ as $\lambda/(2n_1 \cos \theta_1)$ and $\lambda_{eff,T}$ as $\lambda/|n_1 \cos \theta_1 - n_2 \cos \theta_2|$, it follows from (6.5) and (6.6), that in the limit of long wavelengths ($\sigma/\lambda \ll 1$), the scalar scattering theory predicts a λ_{eff}^{-2} law for the diffuse scattering. However, Zeman *et al*. experimentally observed a λ_{eff}^{-3} dependence for the haze in transmission of Asahi U-type SnO_2 layers [Zeman 2000]. Therefore they proposed a modified scalar theory expression by replacing, in (6.5), the power factor 2 by a fitting parameter β_T:

$$H_T = 1 - \exp[- (2\pi/\lambda \cdot \sigma \cdot |n_1 \cos \theta_1 - n_2 \cos \theta_2|)^{\beta_T}]. \quad (6.7)$$

Note that Stiebig *et al*. mentioned power factors larger than 3 for ZnO:Al layers textured by post-etching in HCl [Stiebig 2000].

Krc *et al*. proposed to add two fitting parameters C_R~1 and C_T~0.5 in the expressions (6.6) and (6.7), respectively, and to make these fitting parameters dependent on λ:

$$H_R = 1 - \exp[- (4\pi/\lambda \cdot \sigma \cdot C_R(\lambda) \cdot n_1(\lambda) \cos \theta_1)^2], \quad (6.8)$$

$$H_T = 1 - \exp[- (4\pi/\lambda \cdot \sigma \cdot C_T(\lambda) \cdot |n_1(\lambda) \cos \theta_1 - n_2(\lambda) \cos \theta_2|)^{\beta_T}]. \quad (6.9)$$

This modification allowed these authors to perfectly fit experimental data obtained by measurement in air and to extrapolate them at the TCO/Si internal interfaces [Krc 2002].

This technique was used to carry out optical simulation of thin-film a-Si:H cells [Krc 2003] and the relation (6.8) and (6.9) implemented in the software SunShine of the University of Ljubljana.

6.2.3 Non-paraxial scalar scattering theory

In this section we conclude our theoretical overview on light scattering with a consistent presentation of how Harvey *et al*. use the scalar theory to calculate large angle light scattering by an arbitrary diffracting screen [Harvey 1979, Harvey 1989, Harvey 1999, Harvey 2007]. The main idea is that, if we consider *radiance* and not *intensity*, the use of the transfer function approach of linear systems theory is still possible in the case of non-paraxial diffraction. As Fourier transforms and convolutions are familiar in the framework of the paraxial approximation of image formation systems, this gives a powerful insight in the phenomenon of diffraction even under large angles (see also [Hopkins 1985, Hopkins 1991]). In the following we restrict the discussion to the case of diffuse transmittance; it can easily be adapted to the case of diffuse reflectance [Harvey 1989].

The *general* Rayleigh-Sommerfeld diffraction formula for the problem of diffraction by an arbitrary screen, valid down to the position z=0 of the plane P_0 of the screen, is:

$$U(x,y;z) = \iint_{-\infty}^{\infty} U_0(x',y';0)\frac{1}{2\pi}\left(\frac{1}{r_{10}} - ik\right)\frac{z}{r_{10}}\frac{e^{ikr_{10}}}{r_{10}}dx'dy' \quad , \tag{6.10}$$

where $k = \frac{2\pi}{\lambda}$ and $r_{10}^2 = (x-x')^2 + (y-y')^2 + z^2$.

It can be derived [Harvey 1979] with the only assumption of the existence of a Fourier transform of the initial disturbance $U_0(x,y;z=0)$ of the scalar field in the plane P_0, and, of course, the request that any monochromatic wave propagating through the free space satisfies the Helmoltz's time-independent wave equation.

In the following, the complex amplitude distribution emerging from the screen is given by $U_0(x,y;z=0) = U_{in}(x,y;z=0)\cdot t_S(x,y)$ where U_{in} is the scalar field before the screen and t_S is the complex amplitude transmittance of the screen. In addition, an observation hemisphere of radius r is centered on the diffracting screen. Moreover, the Cartesian coordinate system and all distances are renormalized in units of wavelength: $X = x/\lambda$, $Y = y/\lambda$, $Z = z/\lambda$, $R = r/\lambda$, $R_{10} = r_{10}/\lambda$. Therefore, the position vector of an arbitrary point of observation on the observation hemisphere is expressed by its direction cosines α, β, γ (see Fig. 6.3):

$$\alpha = X/R,\ \beta = Y/R,\ \gamma = Z/R \text{ with } R^2 = X^2+Y^2+Z^2. \tag{6.11}$$

The angular spectrum of plane waves can be written as the Fourier transform of the amplitude distribution emerging from the screen, using the direction cosines as the reciprocal variables in the Fourier space (see e.g. [Goodman 1968]). In the treatment of Harvey, the usage of the scaled coordinates system simplifies the mathematical expressions of the angular spectrum. After rewriting the quantity $r_{10}/\lambda = R_{10}$ in (6.10) as a function of R:

$$R_{10} = R(1+\varepsilon);\ \varepsilon = (R_{10} - R)/R, \tag{6.12}$$

the utilization of this scaled coordinate system and of the algebraic substitution (6.12) allow to rewrite the *usual* Rayleigh-Sommerfeld diffraction formula (valid at distances larger than many wavelengths from the diffracting screen: $R = r/\lambda >> 1$) as a Fourier transform integral, where the reciprocal variables in the Fourier space are the direction cosines (α, β):

$$U(\alpha,\beta;R) = \gamma \frac{e^{i2\pi R}}{iR} \iint_{-\infty}^{\infty} U_0'(X',Y';\alpha,\beta;R) \cdot e^{-i2\pi(\alpha X'+\beta Y')} dX'dY' . \qquad (6.13)$$

The function to be Fourier-transformed in (6.13):

$$U_0'(X',Y';\alpha,\beta;R) = U_{in}(X',Y';0) \cdot t_s(X',Y';0) \frac{1}{(1+\varepsilon)^2} e^{i2\pi W(R)} \qquad (6.14)$$

is a generalized pupil function [Harvey 1979]. It contains the transmittance t_s of the screen and a wave front aberration function W(R). This quantity W(R) contains the phase variations produced by the terms of the binomial expansion for R_{10}-R, except for the term used in the Fourier kernel. If all these terms are preserved in W(R), (6.13) is exact without restriction on the size of the aperture or on the diffraction angles we would consider. In the case of a planar aperture and a hemispherical observation plane, Harvey showed that W(R) takes the form of all the well known conventional aberrations for this geometrical configuration: defocus, astigmatism, coma, and spherical aberration.

Therefore, (6.13) establishes that the result on the observation hemisphere of the diffraction process produced by a plane wave in normal incidence on the screen is the Fourier transform of a generalized pupil function $t_s \cdot e^{i2\pi W(R)}/(1+\varepsilon)$ of the screen. This follows from the fact that the coordinates of the point of observation projected on the plane P_0 (the direction cosines) are the reciprocal variables in the Fourier space (see Fig. 6.3). Because the aberration effects contained in the quantity W(R) have well known expressions (tabulated in [Harvey 1979]), it can be discarded in (6.14). This is equivalent to the Fresnel's approximation in rectangular coordinates, but here, the difference with the actual diffraction pattern can still be calculated in terms of aberrations, for any aperture size, observation hemisphere radius and angle of diffraction. The relation (6.13) is also true for "quasi-near field" distances much smaller than the minimal distance imposed by the usual Fraunhofer's region $r >> \pi b^2/\lambda$, where b is the radius of the diffracting area. This is because the Rayleigh-Sommerfeld diffraction formula requests only distances larger than many wavelengths. If from now on we neglect the aberrations contained in the quantity W(R), and we suppose r >> b (i.e. ε negligible), the equation (6.13) reduces to:

$$U(\alpha, \beta; R) = \gamma \cdot e^{i2\pi R}/iR\ \mathcal{F}\{U_{in}(X,Y; 0) \cdot t_s(X, Y)\} = \gamma \cdot e^{i2\pi R}/iR\ \mathcal{F}\{U_0(X, Y; 0)\} \qquad (6.15)$$

where $\mathcal{F}\{\cdot\}$ denotes the Fourier transform operation.

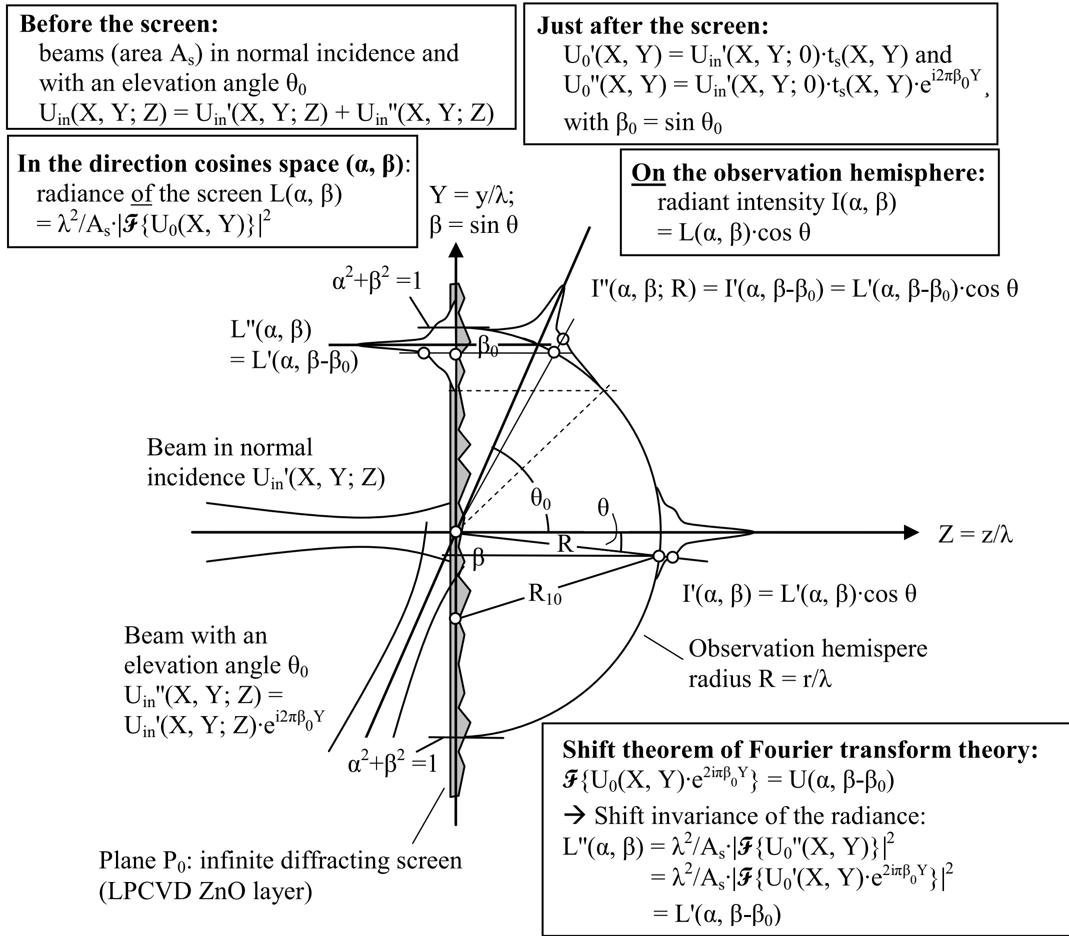

Fig. 6.3: Schematics of the radiance L(α, β) of an infinite diffracting screen (in watts per steradian and per units of projected area) and the corresponding radiant intensity I(α, β) on the observation hemisphere, when two beams of area A_s, one in normal incidence and one with an elevation angle θ_0, are diffracted. It follows from the shift theorem of the Fourier transform theory that even under a large angle of incidence, the radiance L(α, β) is shifted in the direction cosines space. But then, a significant amount of diffracted radiance may lie outside the unit-circle $\alpha^2+\beta^2=1$ and becomes evanescent. Figure adapted from [Harvey 1989].

Three points must be made before obtaining the final non-paraxial scalar diffraction theory [Harvey 1999] (1) the diffracted amplitude U(α,β) on the observation hemisphere must be converted into a diffracted *radiance* L(α,β); (2) a correction of L(α, β) must be performed to take into account the non-propagating evanescent waves; and (3) the corrected *radiance* L(α, β) must be converted into a diffracted *radiant intensity* I(α, β). These three points are developed below:

(1) The *irradiance* $dP/dA_c = |U(\alpha,\beta)|^2$ (in units of watts per units of the area A_c of the collector) is the squared modulus of the scalar amplitude at the observation point (α, β) on the hemisphere. If we observe that the surface dA_c on the hemisphere subtended by a solid angle dΩ is $dA_c = r^2 \cdot d\Omega = \lambda^2 R^2 \cdot d\Omega = \lambda^2 R^2 \sin\theta d\theta d\varphi = \lambda^2 R^2 d\alpha d\beta/\gamma$, we find that the *radiant*

intensity through $d\Omega$ (in units of watts per steradian but expressed in the direction cosines space) is $I(\alpha,\beta) = dP/d\Omega = \lambda^2R^2/\gamma\cdot|U(\alpha,\beta)|^2$. Therefore, for a source area A_S, the *radiance* $L(\alpha,\beta) = d^2P/(d\Omega\cdot\gamma dA_s)$ diffracted in the direction of the observation point on the hemisphere (in units of watts per steradian and per units of the *projected area* γA_s of the radiant surface on the plane normal to the observation direction) is, using (6.15):

$$L(\alpha,\beta) = \lambda^2R^2/(\gamma^2A_s)\cdot|U(\alpha, \beta; R)|^2 = \lambda^2/A_s\cdot|\mathcal{F}\{U_0(X,Y;0)\}|^2 , \qquad (6.16)$$

which is compatible with the relation (21) in [Harvey 1999].

(2) Each spectral component of the solution (6.13) must obey Helmoltz's equation. Therefore γ, which is the analog in the direction cosines space of the z component of the reduced wave-vector in the usual Fourier space, is given by:

$$\gamma = [1-\alpha^2-\beta^2]^{1/2}. \qquad (6.17)$$

Thus, only waves with γ real will propagate, whereas waves with imaginary γ are non-propagating evanescent ones. In other words, only the portion of the radiance-distribution function $L(\alpha,\beta)$ lying inside the unit-circle in the direction cosines space is real and contains radiant power (the angle of diffraction θ is $\leq\pi/2$), whereas the part of $L(\alpha,\beta)$ extending beyond this unit circle is imaginary and is therefore evanescent. Harvey proposed to discard the evanescent part $L(\alpha, \beta)|_{\alpha^2+\beta^2>1}$ and, in order to conserve the total energy, to renormalize the part $L(\alpha, \beta)|_{\alpha^2+\beta^2<=1}$ of the radiance distribution inside the unit-circle with a factor K defined as the ratio of total energy over the energy inside the circle:

$$L'(\alpha,\beta)|_{\alpha^2+\beta^2>1} = 0,$$

$$L'(\alpha,\beta)|_{\alpha^2+\beta^2<=1} = K\cdot L(\alpha,\beta). \qquad (6.18)$$

Harvey notes that this method of renormalization is consistent with Wood's anomalies [Wood 1902] observed in reflection for diffraction gratings [Harvey 1999]. In the case of non-normal incidence under a large elevation angle θ_0, a significant amount of diffracted radiance may lie outside of the unit-circle (see Fig. 6.3). This is because the radiance $L(\alpha,\beta)$ is shifted in the direction cosines space, according to the shift theorem of Fourier transform theory [Harvey 1999].

(3) When a comparison is made between an experimental result and a theoretical calculation, we must take into account the fact that the photogoniometer measures an *intensity* $I = dP/d\Omega$ (in watts per steradian), whereas both the scalar and vector theories

predict the *radiance* $L = d^2P/(d\Omega dA_S \cos\theta)$ of the source. Harvey proposed to convert the radiance L provided by the theory into an intensity $I(\theta)$ with a simple multiplication by the Lambert's factor $\gamma A_S = A_S \cdot \cos\theta$. This removes the discrepancies between the B-K theory and experimental results [Harvey 2007] observed by O'Donnel and Mendez [O'Donnel 1987]. Therefore, having assumed that the size of the diffractive area is much smaller than the radius of the observation hemisphere and having neglected the aberrations contained in the quantity W, if now we assume an isotropic radiation over the azimuthal angles, the final expression for the radiant intensity in the direction θ is finally:

$$I(\theta) = \gamma A_S L'(\alpha,\beta) = K \cdot \cos\theta \cdot \lambda^2 \cdot |\mathcal{F}\{U_0(X,Y;0)\}|^2, \quad \cos^2\theta = \gamma^2 = 1-(\alpha^2+\beta^2). \tag{6.19}$$

If the scalar field U_0 is randomly distributed, its Fourier transform cannot be calculated analytically. But according to the Wiener–Khinchin theorem, its power spectral density $|\mathcal{F}\{U_0(X,Y;0)\}|^2$ is equal to the Fourier transform of its autocorrelation function $C(U_0)$. Therefore, if an analytical expression of $C(U_0)$ is known (e.g. if a plane wave interacts, with a surface $\zeta(x, y)$ with a Gaussian distribution of heights [Harvey 1989]), an analytical solution can be written.

To conclude this section we summarize the advantages and the limitations of this new formulation of the B-K theory. The advantages are:

A) In contrast with the B-K theory, it is valid for reflection or transmission for all angles of incidence and all angles of diffraction; however the aberration effects contained in the quantity W for the non-paraxial conditions must be checked separately.

B) Identically to the B-K theory, there is no limitation for the ratio σ/λ.

C) Local fluctuations of the Fresnel's reflection coefficients due to variations of the local slopes of the surface can be included in the complex transmittance $t_s(X,Y)$ of the screen. But of course this can be done for only one given angle of incidence; multiple (back) scattering is thus not included.

D) If $T \sim \lambda$, the apparition of evanescent modes is included. But we need to choose, *a priori*, between redistribution in propagating modes (perfect dielectric) [Wood 1902] and plasmonic absorption (metallic interface) [Haug 2008b]. We believe that in most practical situations, the optical interface belongs to a class somewhere in-between those two extremes. In case of total dissipation of the energy transferred in evanescent modes, the factor K in (6.18) and (6.19) should be set to unity.

E) If $T \ll \lambda$, the transfer of the energy of the 1st order into the specular direction is of course also included. However the apparition of the index grading effect (which can be modeled by the EMA, see section 6.3.1) *seems* not to be included. Actually, all the evanescent modes lie outside of the unit-circle in the direction cosines space,

and then, the theory re-injects them in the specular direction weighted by the factor K (relation (6.18)). Therefore, we propose that the change of transmittance and reflectance, corresponding to the index grading effect modeled by the EMA, can be included in the quantity K. This corresponds to impose conservation of energy, considering at the same time transmittance and reflectance. We believe that this is in agreement with the underlying physical mechanism modeled by the index grading effect observed when $T<\lambda$ [Hagemann 2008]. Indeed, the evanescent mode *propagates* but only in the plane of the interface. Therefore, we presume that these modes have the possibility to probe both materials of the interface before being rejected in the specular direction, resulting in the averaging of the optical coefficients modeled by the EMA.

F) In contrast with the B-K theory, which is restricted to the Fraunhofer region, the relation (6.13) provides a "quasi-near field" theory, valid in the limit of the Rayleigh-Sommerfeld diffraction formula ($r>>\lambda$), with a practical applicability until about $r>3\lambda$ [Harvey 2002], [Harvey 2003]. As the largest effective wavelength of interest in μc-Si:H is ~1000/3.5 = 286 nm, with n~3.5, this means that scattered field at a distance of about 3·286 ~860 nm in a μc-Si:H solar cell could be considered using this theory.

However, two strong limitations remain:

A) Identically to the B-K theory, it does not include multiple scattering and shadowing effects, which typically occur when $\sigma>>\lambda$. However, simple shadowing effects can be included by zero values in the complex transmittance $t_s(X,Y)$ of the screen.

B) It is not a real "near field" theory. Therefore, distances equal or smaller than λ cannot be assessed. By the way, if $T<<\lambda$, high-field effects [Rockstuhl 2008] near high curvature regions of the surface cannot be studied with this theory.

Once the complex transfer function of the rough interface is known, the problem of diffraction can be numerically solved very effectively because this non-paraxial scattering theory requires the calculation of a single bi-dimensional Fourier transform. Therefore, even if it does not offer all the advantages of a rigorous calculation performed with a finite-element approach, its effectiveness and its natural interpretation in the framework of linear systems theory are appreciable. The next section is devoted to the determination of a transfer function for our ZnO layers and to the presentation of ARS calculation results. Our approach is original because it applies the complete scalar scattering theory, not the well known haze formulas which are results of the theory, to the case of very rough TCO layers used for thin-film PV devices, and uses a random phase screen for the modeling of the surface morphology.

6.3 Diffuse transmittance through surface-textured LPCVD ZnO layers

6.3.1 Modeling of the ZnO layers

The optical interface produced by the random surface ζ of a LPCVD ZnO layer is schematically illustrated in Fig. 6.4. The top part of the figure concerns surfaces with a large enough correlation length T, such that geometrical optics still applies (T>>lateral coherence length>λ). Following a ray tracing approach, it would be possible to calculate an equivalent angle of refraction θ_{Snell} for each pyramidal facet typical of our LPCVD ZnO layers. However, for these layers, T>>λ is violated, and diffraction effects must be considered. This will be managed with scalar scattering theory and the definition of appropriate complex amplitude transmittances $t_s(x, y)$ for diffracting screens equivalent to the ZnO layers. As these layers are reasonably transparent [Steinhauser 2007, Steinhauser 2008a], we choose to model $t_s(x, y)$ using a random-phase screen (RPS) [Goodman 1985]. We assume a plane wave in normal incidence on the rough surface, therefore the phase φ of the incident wave at the spatial coordinates $(x, y; z_{min})$ in Fig. 6.4(b) is constant (φ=0). In this figure, the coordinates z_{min} and z_{max} correspond to the minimum and maximum heights on the rough surface ζ. We model the phase change along the vertical path from the point $(x, y; z_{min})$ to the point $(x, y; z_{max})$ by:

$$\begin{aligned}\varphi(x, y; z_{max}) &= \varphi_0 + k\cdot z_1\cdot n_1 + k\cdot z_2\cdot n_2 \\ &= \varphi_0 + k\cdot(\zeta(x, y) - z_{min})\cdot n_1 + k\cdot(z_{max} - \zeta(x, y))\cdot n_2 \\ &= C + k\cdot\zeta(x, y)\cdot(n_1 - n_2), \end{aligned} \qquad (6.20)$$

where C is a constant, $k = 2\pi/\lambda$ is the wave-number of the incident light, and n_1, n_2 are the refractive indexes of ZnO and of the outgoing medium, respectively. By getting rid of the constant C, this model provides the following expression for the amplitude transmittance of the RPS:

$$t_s(x,y) = \exp[i2\pi/\lambda\cdot \zeta(x, y)\cdot(n_1-n_2)]. \qquad (6.21)$$

Note that t_s is only an approximation of an exact amplitude transmittance for the ZnO layer. Indeed, the model does not allow diffraction in the space between z_{min} and z_{max}, and therefore does not reproduce the exact wave-front propagation in the peak-to-valley height of the rough surface.

For the case of an infinite facet, the angle of refraction α_2 is related by Snell's law to the (local) angle of incidence α_1 of the wave on the facet:

$$\sin \alpha_2 = n_1/n_2\cdot\sin \alpha_1. \qquad (6.22)$$

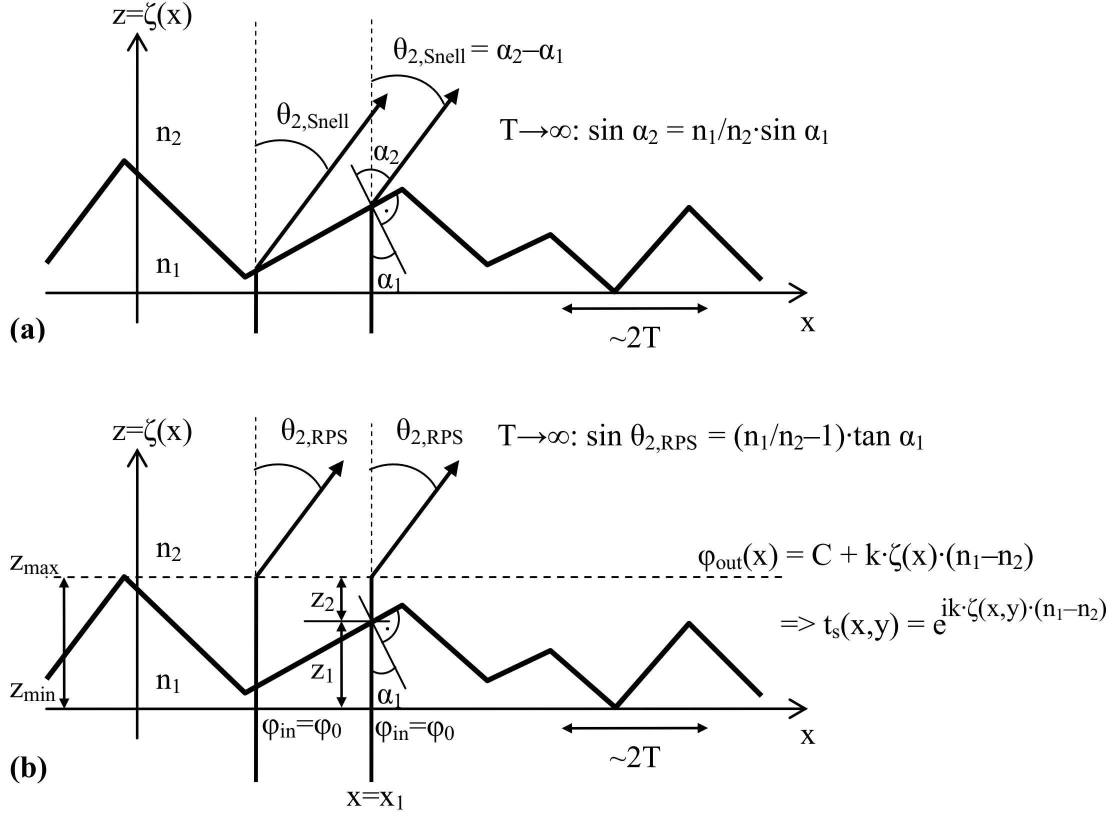

Fig. 6.4: Modeling of a random optical interface. (a) Ray optics approximation if the correlation length T is much larger than the wavelength. (b) Modeling by a random-phase screen (RPS) of complex amplitude transmittance $t_s(x,y)$.

As the wave is normally incident on the x-y plane, α_1 is also equal to the (local) angle of the facet with respect to the x-y plane. Because $\alpha_2 = \alpha_1 + \theta_{2,\mathrm{Snell}}$ (see Fig. 6.4), the relation (6.22) can be rewritten as:

$$\sin\theta_{2,\mathrm{Snell}} = (n_1/n_2 - \cos\theta_{2,\mathrm{Snell}})\cdot\tan\alpha_1. \tag{6.23}$$

When the infinite facet is modeled with the RPS, the amplitude transmittance (6.21) is periodic. Its period Λ in the direction of the gradient of $\zeta(x, y)$ on the facet is $\Lambda = 2\pi/(\tan\alpha_1\cdot k\cdot(n_1-n_2))$. The angle of diffraction $\theta_{2,\mathrm{RPS}}$ is therefore related to the local angle of incidence α_1 by the grating equation $\sin\theta_q = q\cdot\lambda/\Lambda$ at the 1st order:

$$\sin\theta_{2,\mathrm{RPS}} = (\lambda/n_2)/\Lambda = (n_1/n_2 - 1)\cdot\tan\alpha_1. \tag{6.24}$$

From comparison of (6.23) and (6.24), we see that the RPS model is valid for small angles of diffraction $\theta_{2,\mathrm{RPS}}$, i.e. for small local angles α_1 of the rough surface, but fails for

large angles of diffraction, predicting too large values of $\theta_{2,RPS}$ when $n_1/n_2>1$ and too small absolute values of $\theta_{2,RPS}$ for $n_1/n_2<1$ e.g. for a ZnO/a-Si:H interface. A quantitative comparison is given in Fig. 6.5, where $\theta_{2,RPS}$ and $\theta_{2,Snell}$ and their relative differences are plotted versus the angle α_1 of inclination of the infinite facet for the cases of a ZnO/air and a ZnO/a-Si:H interface. For the ZnO/air interface, $\theta_{2,RPS}$ is slightly underestimated, within an error <20% until $\alpha_1 = 27°$. However the critical angle of total internal reflection is too large: 45° instead of 30°. On the contrary, for the ZnO/a-Si:H interface, the model slightly overestimates $\theta_{2,RPS}$ with an error <20% until $\alpha_1 = 42°$. For facets with α_1 larger than 50° the error strongly diverges and for α_1=65°, the transmission wrongly becomes evanescent. Therefore, the concept of phase-screen fails in correctly encoding a large slope of the surface in $t_s(x, y)$. On the basis of Fig. 6.5 we roughly consider that the RPS is reasonably valid until α_1<30° for a ZnO/air interface and until α_1<45° for a ZnO/a-Si:H interface.

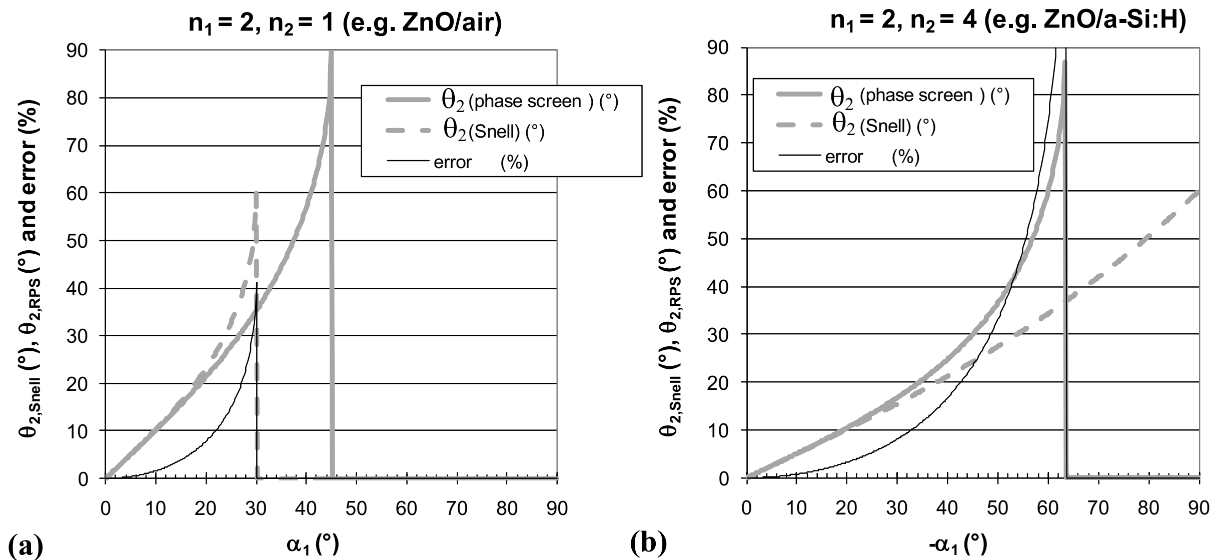

Fig. 6.5: Comparison of the angles of specular directions between a single pyramidal facet and its phase screen model. (a) ZnO/air interface, (b) ZnO/a-Si:H interface.

Note that these discrepancies relate to the *refraction* produced by a single facet. They will therefore be effective only in the limit T>>lateral coherence length>λ of geometrical optics. As the angular spectrum of the *diffraction* process is given by the spectral components of $t_s(x, y)$, i.e. its Fourier transform, we may expect that the number of pyramids per unit of area rather than the slope of some facets will dominate. The failure of our model for high slope values of the surface $\zeta(x, y)$ must be kept in mind when analyzing further results. This is particularly true for ZnO layers without or with a short surface post-treatment, where the most probable angles of local surface elements with the plane of the substrate is typically 50° (cf. Fig. 6.7).

6.3.2 Comparison of measurements and calculations of the ARS in transmitance for different LPCVD ZnO layers

Experimental

The front TCO layers used in this study are as-grown surface-textured ZnO films with two different doping levels obtained by low-pressure chemical vapor deposition (LPCVD) on AF45 borosilicate glass substrates from Schott. We will discuss three sets of ZnO samples as described in Tables 6.1 to 6.3. The topography ζ(x, y) of the surface of the layers and the root mean square value of their surface roughness (σ_{rms}) are determined by atomic force microscopy (AFM), on a 10 x 10 μm^2 surface area, with either 256 x 256 or 512 x 512 data points. The first set contains typical ZnO layers as optimized for our state-of-the-art single a-Si:H and micromorph tandem solar cells, further referred to as Set#1. The thickness of the layers of Set#1 is adjusted to obtain a sheet resistance of about 10 Ω/sq. Details on their characteristics are summarized in Table 6.1. The σ_{rms} values and the correlation lengths T of these surfaces are calculated on the basis of 10 x 10 μm^2 AFM pictures with 512 x 512 data points. Histograms of the local angle of the surface with respect to the plane of the substrate are calculated with a Matlab function written by J. Bailat and published in the annexes of [Fay 2003].

These surface characteristics depend on the thickness of the layers and on the duration of the plasma post-treatment applied to them. By increasing the duration of this post-treatment, the surface changes from V- to U- shaped morphology and σ_{rms} decreases.

Table 6.1: Thickness d, carrier concentration N [Steinhauser 2007], post-treatment time t_{PT}, surface roughness σ_{rms}, correlation length T and characteristic morphology of the valleys for the 1st set (Set#1) of front ZnO layers (Type-A1 to -D1). Type-B1 and -A1: no post-treatment.

Type of front ZnO (Set#1)	A1	B1	C1	D1
d (μm)	1.9	4.8	4.8	4.8
N (cm^{-3})	1.4x10^{20}	4x10^{19}	4x10^{19}	4x10^{19}
t_{PT} (min)	0	0	20	60
σ_{rms} (nm)	65	172	150	103
T (nm)	206	452	428	551
Morphology of valleys	V-shape	V-shape	U-shape	U-shape

Note that the type-A1 ZnO is our standard layer as optimized for a-Si:H solar cells. The type-B1 ZnO (without post-treatment), whose sharp V-shaped structures prevent good electrical properties of the micromorph device, is presented only for the sake of light scattering comparisons. The low doping level used for deposition of the thick, large grain, ZnO layers (type-B1, -C1 and -D1) provides high transparency in the near infrared (NIR) spectral range because of reduced free carrier absorption (FCA) [Steinhauser 2007].

The second set of ZnO layers, referred to as Set#2, is a thickness series of as-deposited (no post-treatment) undoped ZnO layers. Deposition times t_{dep} and thicknesses d, as well as σ_{rms} values and correlation lengths T (calculated on the basis of 10 x 10 μm^2 AFM pictures with 256 x 256 data points) are summarized in Table 6.2.

Table 6.2: Deposition time t_{dep}, thickness d, surface roughness σ_{rms}, and correlation length T for the ZnO layers of Set#2 (Type-A2 to -H2).

Type of front ZnO (Set#2)	A2	B2	C2	D2	E2	F2	G2
t_{dep} (min)	1	3	6	10	15	25	40
d (μm)	0.070	0.260	0.700	1.37	2.12	3.76	6.00
σ_{rms} (nm)	5	16	37	66	97	155	221
T (nm)	56	69	117	173	228	371	534

Finally, the third set of ZnO layers, referenced as Set#3, is a combination of double layers. The aim of these double layers is to assess if it is possible to add the respective advantages of the type-A1 ZnO layer (with small feature sizes) and of the type-C1 ZnO (with larger feature sizes). Indeed, these two types of front ZnO are, respectively, empirically optimal for the a-Si:H top cell and for the μc-Si:H bottom cell of a micromorph (cf. also chapter 7). Towards this purpose, we succeeded in producing layers with two different characteristic feature sizes on the same surface. This is done by the deposition of a thin (~5 nm) silicon oxide (SiO_x) layer on the first deposited ZnO layer, which prevents an epitaxial growth of the ZnO layer subsequently deposited. Scanning electron micrographs of this type of layer (Fig. 6.6) indicate that its surface morphology is indeed very similar to the surface of the SnO_2 layer with a double texture (W-texture) from Asahi, recently presented by Taneda *et al.* [Taneda 2007]. It is interesting to note that we independently developed a similar surface texture exactly at the same time as these authors. In this Set#3 of layers, the type-A3 ZnO is the first deposited and surface-treated layer, the type-B3 ZnO is the layer with the double-texture, the type-C3 is the layer co-deposited with type-B3, but without SiO_x in between the two ZnO films; and the type-D3 ZnO is the reference, equivalent to type-C1. The fabrication sequences, including plasma post-treatment steps, are summarized in Table 6.3, with the resulting individual and total thicknesses as well as the σ_{rms} values and correlation lengths T calculated on the basis of 10 x 10 μm^2 AFM pictures with 512 x 512 data points.

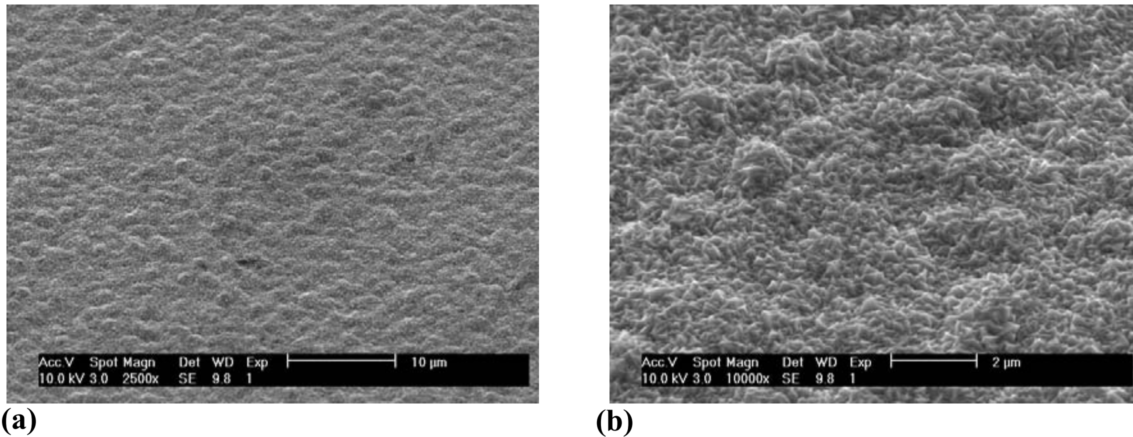

(a) **(b)**

Fig. 6.6: (a) 2'500x and (b) 10'000x scanning electron micrograph of a ZnO similar to the type-B3 ZnO discussed in the text. Note the similarity of the surface morphology with that of the SnO_2 layer with double-texture (W-texture) from Asahi, recently presented by Taneda et al. [Taneda 2007].

Table 6.3: Individual (d_1, d_2) and total (d_{tot}) thicknesses of the double-layer samples of Set#3 (type-A3 to -D3). The duration t_{PT1} and t_{PT2} of the possible plasma post-treatment introduced in the fabrication sequence are also indicated in addition to the surface roughness σ_{rms} and the correlation length T of the surface.

Type of front ZnO (Set#3)	A3	B3	C3	D3
d_1 (µm)	3.6	3.6	3.6	4.5
t_{PT1} (min)	20	20	20	20
SiO_x interlayer	-	yes	no	-
d_2 (µm)	-	1.1	1.1	-
t_{PT2} (min)	-	2	2	-
d_{tot} (µm)	3.6	4.7	4.7	4.5
σ_{rms} (nm)	100	102	152	159
T (nm)	370	683	430	531

The haze in transmission $H_T(\lambda)$ is calculated from total and diffuse optical transmittance measurements carried out with a Perkin-Elmer photo-spectrometer equipped with an integration-sphere. Angle-resolved scattering measurements (ARS) are performed with a laser beam (λ = 544 nm) normally incident on the glass side of the samples and a photodetector rotating in a plane normal to the direction of incidence. The diameter d of the laser beam is ~1.5 mm and the length of the arm of the photo-goniometer is such that the radius r of the observation hemisphere is 115 mm. We assume an isotropic scattering over the azimuthal angle, as demonstrated for LPCVD ZnO and other TCO layers in [Poruba 2008], therefore, we scan only the polar angle θ, but from -90° to +90° in order to verify the alignment of the experimental set-up. We present the ARS measurements in two different ways:

(1) The normalized radiant intensity $ARS(\theta) = I(\theta)/P_0 = \langle dP/d\Omega \rangle/P_0$ measured by the photogoniometer is plotted on a log scale, versus the scattering angle θ with respect to the direction of the incident laser beam; where P_0 is the total incident power and the brackets $\langle \cdot \rangle$ denotes an average over the ensemble of realizations of a random process. When the illuminated surface area is much larger than the wavelength of the incident laser beam, this ensemble averaging is inherently contained in the experimental data, whereas in theoretical calculations, it is implicitly contained in the spectral density function associated to the random rough surface [Elson 1980].

(2) The intensity measured at a scattering angle θ is integrated over the azimuthal angle φ, considering an isotropic scattering over φ. This second type of presentation provides the radiant intensity per unit of solid angle scattered at the angle θ [Stiebig 2000, Schulte 2007]. The integration over φ yields a simple multiplication of the intensity by a factor sin θ. We then obtain a *total intensity profile* $ARS(\theta)\cdot|\sin\theta|$ which is proportional to the *probability density function* associated, in the scattering process in a solid angle, to the angular distribution function (ADF) of the possible values for θ [Krc 2002]. Therefore, the most probable scattering angle corresponds to the position of the maximum of the profile $ARS(\theta)\cdot|\sin\theta|$.

The ZnO layers are modeled with a phase screen of complex amplitude transmittance $t_s(x, y)$ calculated with the relation (6.21) from the heights $\zeta(x, y)$ obtained from the AFM measurements. Assuming $U_{in}(X,Y;0)$ is the amplitude of a plane wave in normal incidence, the radiance $L(\alpha, \beta)$ is numerically evaluated from relation (6.16) using the fast Fourier transform (FFT) algorithm to perform the bi-dimensional Fourier transform integration. To reduce noise in the result, before determining the intensity $I(\theta)$ from (6.19), we average $L(\alpha, \beta)$ by integration over the azimuthal angle φ, taking advantage of the cylindrical symmetry of the diffraction process through our ZnO layers. For the sake of simplicity, we set the factor K to unity in (6.19). This corresponds to assuming that the energy reflected back by total internal reflectance is lost for transmittance, and that, under normal incidence, the energy transferred in evanescent modes is negligible.

Results and discussion for Set#1 samples

The AFM pictures of the topography for the ZnO layers of Set#1 described in Table 6.1, as well as the corresponding height histograms w(z) and local angle histograms, are presented in Fig. 6.7. The height distributions associated with the random surfaces are clearly not Gaussian. Indeed, without and with the short post-treatment (Type-A1 to -C1, $t_{PT} = 0$ min and $t_{PT} = 20$ min) the histograms indicate distributions with an asymmetric tail extending towards more positive values (positive skewness). For the long post-treatment (Type-D1, $t_{PT} = 60$ min) the height histogram is symmetrical, but has a triangular shape. Comparing the samples Type-B1 and Type-C1 in Fig. 6.7(b) and (c), we observe that the effect of the 20 min post-treatment is to decrease σ_{rms} from 172 to 150 nm and to slightly increase the amount of local area with a local angle of ~30°. For 60 minutes of surface

post-treatment, σ_{rms} decreases down to about 100 nm and the most recurrent local angle value dramatically changes from ~50° without post-treatment to only 26°.

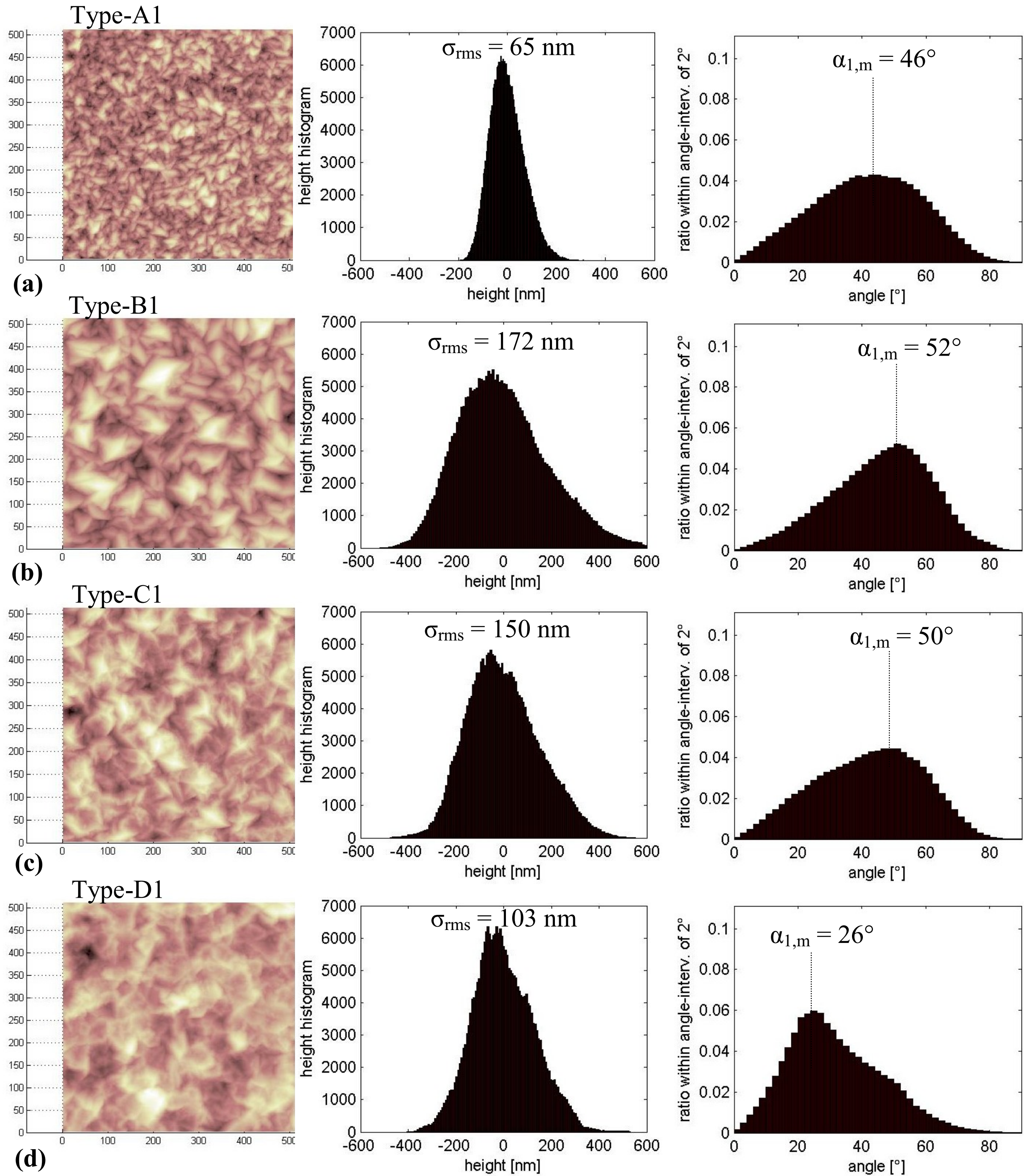

Fig. 6.7: (a)–(d) AFM pictures of the topography for the LPCVD ZnO layers of Type-A1 to D1 described in Table 6.1. Next to each AFM picture, are shown the histograms corresponding to the distribution of heights and to the distribution of local angles of the surface with respect to the plane of the layer. For each layer, the value of the most frequent local angle $\alpha_{1,m}$ is indicated.

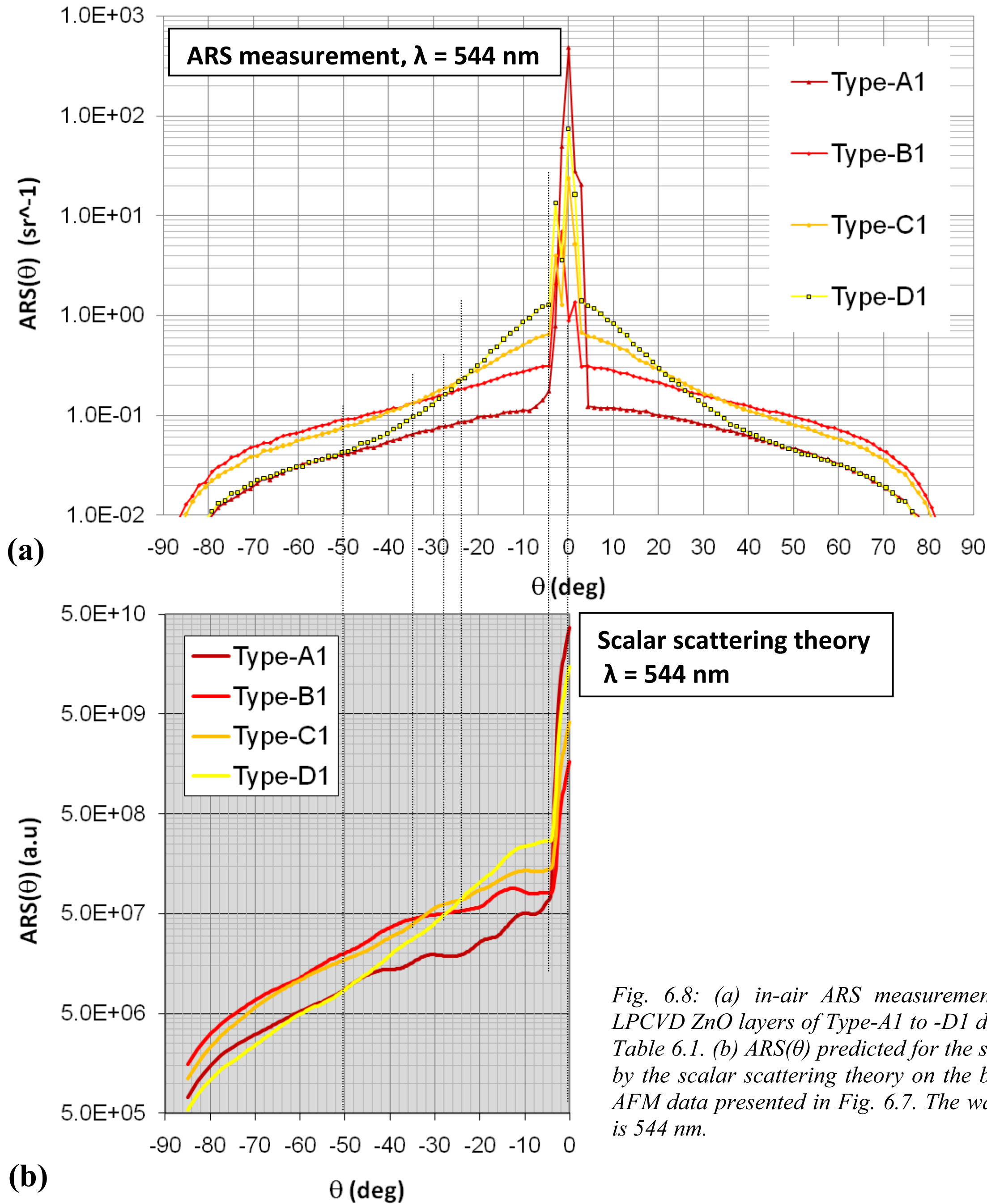

Fig. 6.8: (a) in-air ARS measurements for the LPCVD ZnO layers of Type-A1 to -D1 described in Table 6.1. (b) ARS(θ) predicted for the same layers by the scalar scattering theory on the basis of the AFM data presented in Fig. 6.7. The wavelength λ is 544 nm.

In Figs. 6.8(a) and (b) we compare ARS measurements and the corresponding total intensity profiles ARS(θ)·|sin θ| for the ZnO layers of this Set#1 of samples. For the thick ZnO layers (Type-B1 to D1), we observe in Fig. 6.8(a) that the effects of increasing the duration of the surface post-treatment is an increase of the intensity of the specular peak and a decrease of the intensity scattered into large angles (|θ| >30°) but also, in Fig. 6.9(a), a shift of the most probable angle of scattering from 33° for the layer without surface treatment (Type-B1) towards 16° and 11° for the layers with 20 min (Type-C1) and 60 min (Type-D1) surface treatment, respectively. Recalling that for a Lambertian diffuser,

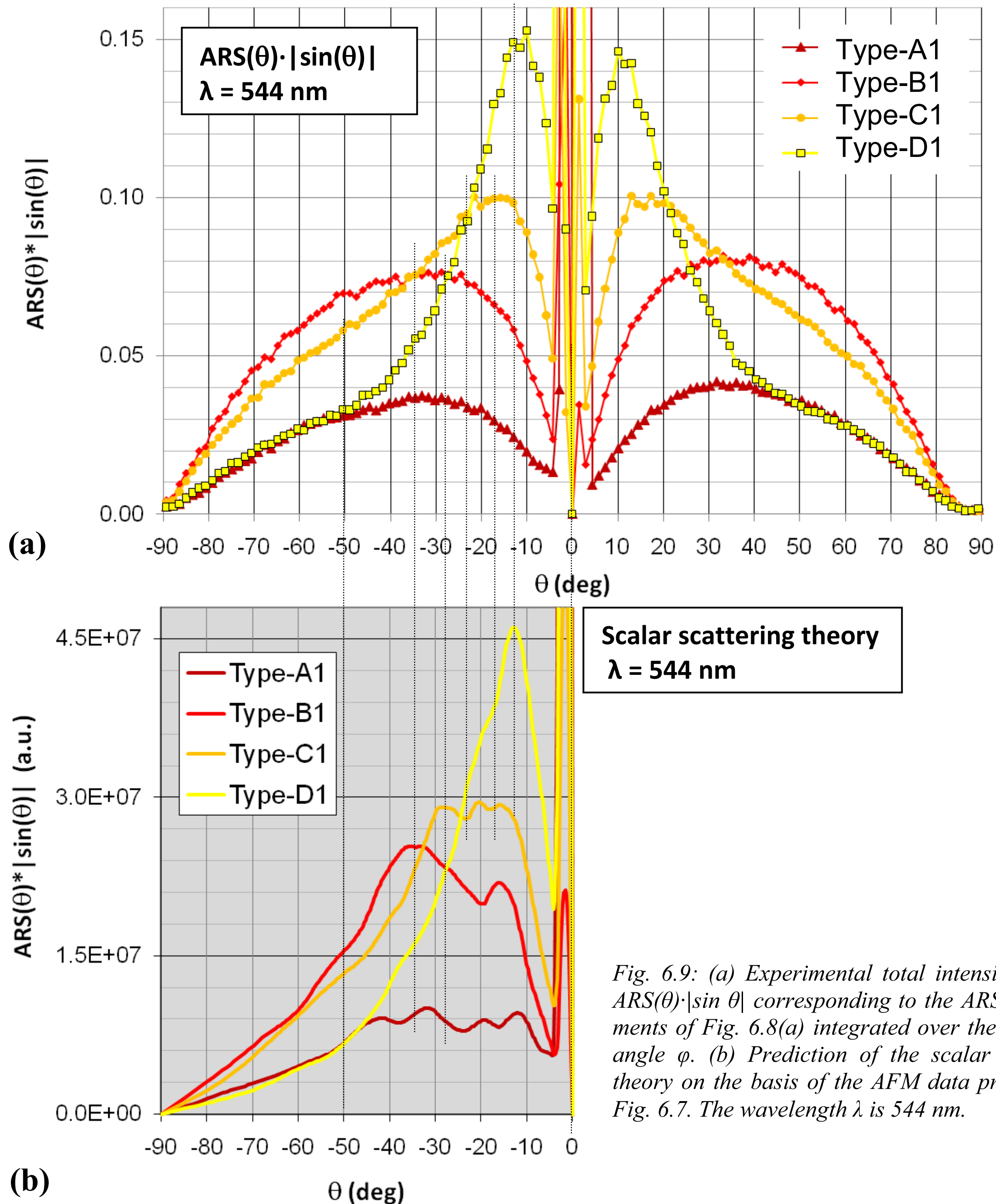

Fig. 6.9: (a) Experimental total intensity profiles ARS(θ)·|sin θ| corresponding to the ARS measurements of Fig. 6.8(a) integrated over the azimuthal angle φ. (b) Prediction of the scalar scattering theory on the basis of the AFM data presented in Fig. 6.7. The wavelength λ is 544 nm.

the most probable angle of scattering is 45°, this clearly demonstrates that the surface treatment increases the gap between our real front TCO layers and a perfect Lambertian diffuser. It is noticeable that the small change in the histogram of local angles induced by the 20 min surface treatment (Fig. 6.7 (c)) induces a substantial change in the ARS toward smaller scattering angles. For the thin ZnO layer with small feature sizes and no surface treatment (Type-A1), we observe a larger intensity in the specular direction and a smaller diffuse intensity (i.e. a smaller haze value). However, the angular distribution of light scattered by the latter (i.e. the ADF) is, with a most probable scattering angle of 33° also, comparable to the ADF of the Type-B1 sample.

In Figs. 6.8(a) and (b), we compare ARS measurements with the predictions of the non-paraxial scalar scattering theory. The same comparison is made in Figs. 6.9 (a) and (b) for the total intensity profiles ARS(θ)·|sin θ|. These comparisons show good agreement between ARS measurements and theoretical predictions based on the surface topography data obtained by AFM. Indeed, the scattering angles at which the diffuse intensities produced by the different layers intersect are almost the same between measured data and calculated results. However, the calculated curves ARS(θ) present ripples, which correspond to diffraction orders, not visible in the ARS measurements. This is because the size of the area scanned by AFM (10 x 10 μm^2) is less than one order of magnitude larger than the correlation lengths T of the surfaces and therefore, the ensemble averaging, which should be implicitly contained in the spectral density functions associated to the random rough surface, does not perfectly cancel any local periodicity. Whereas, for the ARS measurement, the diameter of the laser beam incident on the surface (~1.5 mm) is 3 orders of magnitude larger than T and therefore, the ensemble averaging performed when the light probes such a large surface area cancels all periodicity. Despite of these ripples, it is possible to compare the most probable scattering angles (position of the maxima of ARS(θ)·|sin θ|) for the different layers. We see, comparing Figs. 6.9 (a) and (b) that theoretical predictions and direct measurements are compatible. Another noticeable difference between theoretical predictions and direct measurements is the higher slope, in logarithmic scale, of ARS(θ) predicted for large scattering angles (compare Figs. 6.8(a) and (b)). Another difference is the shape of the curves ARS(θ)·|sin θ| for large scattering angles (|θ|>40°), which are concave in the theoretical predictions plotted in Fig. 6.9(b), whereas they are experimentally convex as seen in Fig. 6.9(a). Therefore, with the RPS models of the random rough surfaces, the scalar theory underestimates the scattering capability of our ZnO layers for large angles of diffraction. Schulte *et al*. made a similar observation with their ray-tracing approach applied to sputtered-etched ZnO samples and proposed to improve the accuracy of the theoretical predictions by adding Mie scattering [Schulte 2007], which describes scattering by features with a size comparable to the wavelength of the incident radiation. In our case, we could also explain the underestimation of the scattering capability of the ZnO/air interface for large angles of diffraction by looking back at Fig. 6.5(a). Indeed, we see in this figure that except for the narrow range of values of α_1 comprised between 40° and 45°, the RPS model actually underestimates the value of diffraction angles $\theta_{2,RPS}$ larger than 20°. Note that the total internal reflection predicted by geometrical optics in Fig. 6.5(a) for $\alpha_1 > \theta_c = 30°$ produces light trapping in the ZnO layer, which in turn produces a randomization of the angle of incidence at the ZnO/air interface and the escape of the light through the escape cone under angles with possible values as large as 90° (see section 6.1 and chapter 8).

Although some discrepancies exist, as discussed above, the qualitative and quantitative agreement between experiments and theory for the angular distribution of light transmitted through the different LPCVD ZnO layers is remarkable.*

* At the moment of publishing this thesis, an expression similar to (6.19) and (6.21) but derived from a different approach and leading, excepted for the specular part, to comparable results, has just been published by another group. See K. Jäger and M. Zeman, Appl. Phys. Lett. 95 (2009) 171108.

Results and discussion for Set#2 samples

The previous results with Set#1 samples demonstrate the ability of scalar scattering theory, used in conjunction with the RPS approach, to predict ARS(θ) for light transmitted in air through our LPCVD ZnO layers. Therefore, the question of how ARS(θ) changes, when the ZnO/air interface is replaced by a ZnO/Si internal interface, can be tackled by our calculation method, for any wavelength of the incident light.

Figures 6.10 and 6.11 show the predicted angular distributions of the light scattered in transmission by the Type-B2, -D2 and -F2 layers of Set#2 samples listed in Table 5.2, calculated for seven different wavelengths λ ranging from 400 to 1000 nm.

In order to compare only the effects of morphologies in the calculation, the refractive indexes of ZnO and a-Si:H are supposed constant for all wavelengths (n_{ZnO} = 2 and $n_{a\text{-}Si:H}$ = 3.8). The results for ZnO/air interfaces are presented in Figs. 6.10(a-c) for ARS(θ) plotted in logarithmic scale and in Figs. 6.10(d-f) for the total intensity profiles ARS(θ)·|sin θ|. The results for the case of scattering through internal ZnO/a-Si:H interfaces are presented in Figs. 6.11(a-c) for ARS(θ) and in Figs. 6.11(d-f) for ARS(θ)·|sin θ|. The comparison of the scattering through the ZnO/air interface, in Fig. 6.10, with the scattering through the internal ZnO/a-Si:H interface of a solar cell, in Fig. 6.11, indicates that:

(1) The slope, in logarithmic scale, of ARS(θ) is higher for the internal ZnO/a-Si:H interface than for the ZnO/air interface. This results in a dramatic shift of the total intensity profiles ARS(θ)·|sin θ| towards smaller angles, compared to in-air scattering.

(2) For the ZnO/air interface, the area under the total intensity profiles, i.e. the total diffuse transmittance $T_{dif} = \int_{5°}^{90°} ARS(\theta)\cdot\sin\theta d\theta$, almost systematically decreases when λ increases (except for the rougher Type-F2 sample, with σ_{rms} = 155 nm, when λ<633nm). In contrast, and in accordance with the haze values predicted in section 7.5.3 of chapter 7 for the internal ZnO/a-Si:H interface, T_{dif} almost does not decrease with increasing λ values for the Type-F2 sample (σ_{rms} = 155 nm) and also for the Type-D2 sample (σ_{rms} = 66 nm) when λ<633 nm.

(3) The positions of the maximum of the total intensity profiles ARS(θ)·|sin θ|, which correspond to the most probable scattering angle θ_M, shift in a somewhat, at first glance, complicated way, when λ increases. The analysis of this behavior for the ZnO/air interface is made more difficult due to the ripple in the scattering profiles. A closer look at the profiles concerning the ZnO/a-Si:H interfaces reveals the rules underlying this shift of θ_M: when the increase of λ produces a decrease of T_{dif}, θ_M shifts towards larger angles, whereas when the increase of λ does not change T_{dif} (i.e. the haze is constant) θ_M shifts towards smaller scattering angles. Therefore, these calculations indicate that, when λ increases, the scattering capability always decreases, either because T_{dif} (i.e. the haze) decreases, or because θ_M decreases although T_{dif} is constant.

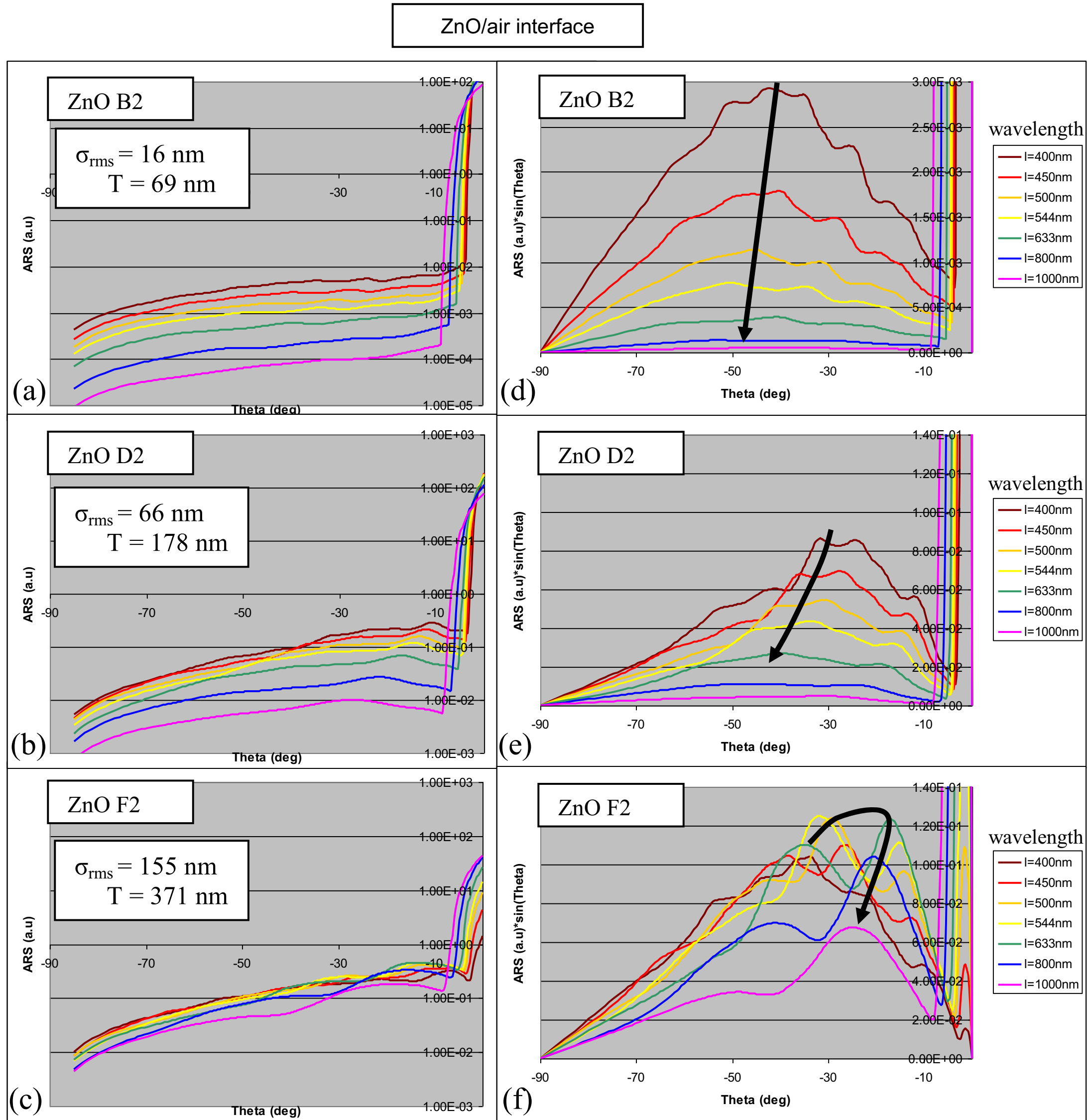

Fig. 6.10: (a)–(c) ARS (θ) and (d)–(f) ARS(θ)·|sin θ| profiles predicted by the scalar scattering theory for 7 values of the wavelength λ (400, 450, 500, 544, 633, 800 and 1000 nm) of the light transmitted through the ZnO/air interfaces formed by the ZnO layers of type B2, D2 and F2 listed in Table 6.2. The rms values of their surface roughness σ_{rms} and the correlation lengths T deduced from AFM measurements are indicated in (a)–(c). For each sample the arrows in (d)–(f) indicate how the most probable scattering angle shifts when λ is increasing.

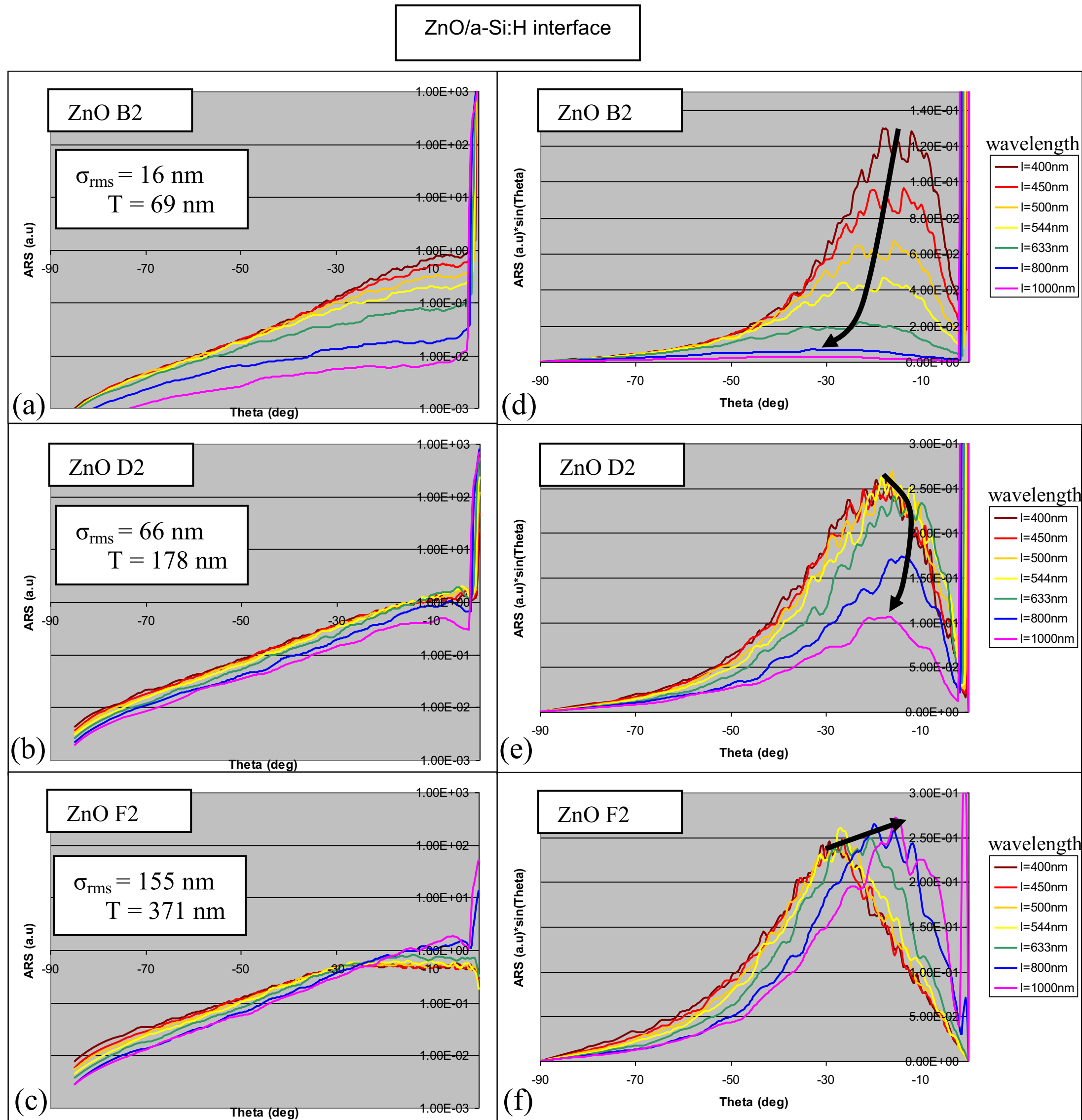

Fig. 6.11: (a)–(c) ARS (θ) and (d)–(f) ARS(θ)·|sin θ| profiles predicted by the scalar scattering theory for 7 values of the wavelength λ (400, 450, 500, 544, 633, 800 and 1000 nm) of the light transmitted through the ZnO/a-Si:H internal interfaces formed by the ZnO layers of type B2, D2 and F2 listed in Table 6.2. The rms values of their surface roughness σ_{rms} and the correlation lengths T, deduced from AFM measurements are indicated in (a)–(c). For each sample the arrows in (d)–(f) indicate how the most probable scattering angle shifts when λ is increasing.

For λ fixed to 633 nm and the seven ZnO layers of Set#2 samples, the total intensity profiles ARS(θ)·|sin θ| calculated for light transmitted trough ZnO/air and ZnO/a-Si:H interfaces are plotted in Fig. 6.12, after normalization to their maximum value. This normalization allows differences in haze to be discarded, which are huge for the range of σ_{rms} values of Set#2 samples, and only differences in the angular distributions to be considered. We observe that:

(1) The comparison of Fig. 6.12(a) with Fig. 6.12(b) again shows that in the case of the internal ZnO/a-Si:H interface, the angular distributions are dramatically shifted towards small angles compared to the case of in-air scattering.

(2) The position of θ_M is going back and forth when the feature sizes of the layers, characterized by the roughness σ_{rms} and the correlation length T, increase. Once again, due to the ripples in the scattering profiles, this behavior is more difficult to analyze in the case of the ZnO/air interface. However, for the case of the ZnO/a-Si:H interface in Fig. 6.12(b), the calculation clearly indicates that when θ_M is minimal, the intensity scattered under large angles (θ~50°) is also minimal while the intensity scattered under small (nearly specular) angles (θ~5°) is maximal. In the whole Set#2 of samples, for λ = 633 nm, the narrower total intensity profile ARS(θ)·|sin θ| would be the one produced by the Type-F2 ZnO layer (σ_{rms} = 155 nm and T = 371 nm) for the case of in-air scattering. However, for our case of interest, i.e. for the internal ZnO/a-Si:H interface, Fig. 6.12(b) indicates that the narrowest scattering profiles is produced for Type-D2 ZnO layer (σ_{rms} = 66 nm and T = 178 nm). This shows that what would be deduced from in-air ARS measurements is not obviously correct when considering scattering in silicon.

Those results for Set#2 samples can be understood considering the grating equation $\sin \theta_q = q \cdot \lambda / \Lambda$; recalling that 2T is the analog, for a random surface, of the period Λ of periodic structures, and that, for $T<\lambda/n_2$, the higher orders of diffraction become evanescent. Therefore, for $T<\lambda/n_2$, when λ increases, the increase of θ_q produces a widening of the specular peak (see Figs. 6.10(a-c)) and an increase of θ_M, accompanied by a loss of transmitted energy into evanescent modes which, in turn, produces the decrease of T_{dif} (the area under the total intensity profiles) observed in Figs. 6.10(d-f) and 6.11(d-e). However, for $T>\lambda/n_2$, the increase of θ_q does not produce losses into evanescent modes when λ increases, as seen in Figs. 6.10(f) and 6.11(e-f), but mainly a transfer of intensity from the specular peak to small angles of diffraction and therefore, the shift of θ_M towards smaller angles observed in Figs. 6.10(f) and 6.11(e-f).

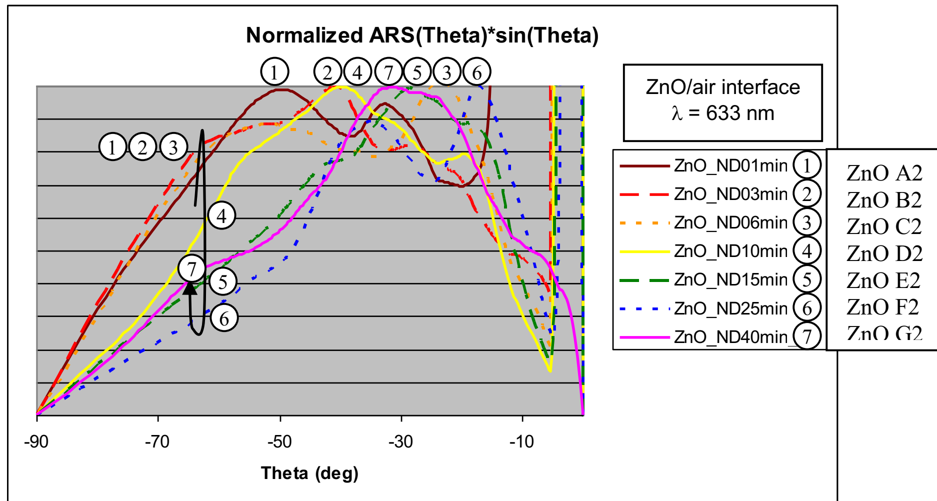

(a) ZnO/air interface

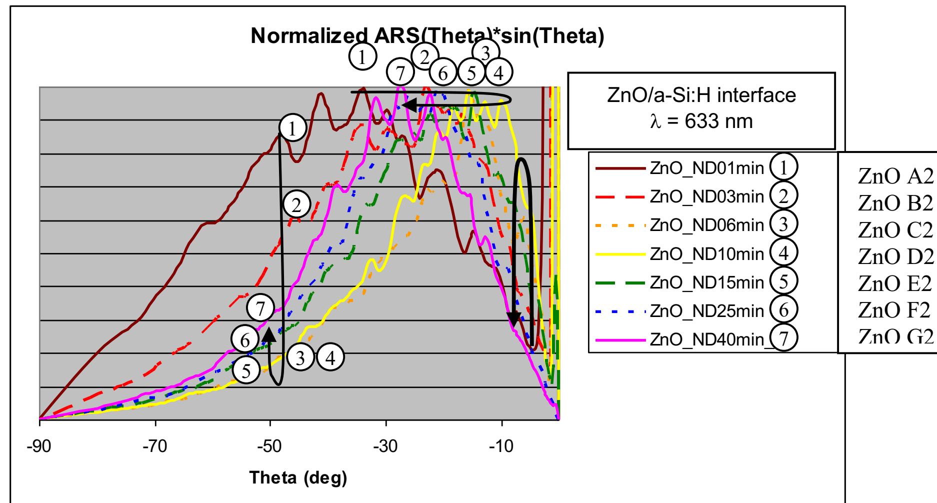

(b) ZnO/a-Si:H interface

Fig. 6.12: Normalized total intensity profiles ARS(θ)·|sin θ| predicted by the scalar scattering theory for the seven ZnO layers of Set#2 of samples described in Table 6.2, when light with a wavelength of 633 nm is transmitted through the layers. In (a) a ZnO/air interface and in (b) the internal ZnO/a-Si:H interface of a solar cell is considered.

The important conclusion that the angular distribution of light scattered at the internal ZnO/a-Si:H interface is narrower than for the experimentally accessible case of in-air scattering must be emphasized. This is because the RPS model actually overestimates the scattering angles in the case of the ZnO/a-Si:H interface, as deduced in Fig. 6.5. Therefore the actual angular distribution in a-Si:H may be even more dramatically shifted towards small scattering angles. Recalling that full randomization of the light by Lambertian scattering is a prerequisite to reach the Yablonovitch's $4n^2$ absorption enhancement limit, such a shift of the angular distribution is undesired.

Results and discussion for Set#3 samples

The AFM pictures of the topography, and the corresponding height and local angle histograms of the ZnO layers of Set#3 described in Table 6.3 are presented in Fig. 6.13. Once again we observe that the height distributions associated with the random surfaces are not Gaussian but present a positive skewness (asymmetric tail extending towards more positive values). For these 4 samples, the curves of haze measured in transmission ($H_T(\lambda)$) are shown in Fig. 6.14(a) and the result of ARS measurements are shown in Fig. 6.14(b). These experimental ARS results, performed with λ = 544nm, are compared to the total intensity profiles predicted by the scalar scattering theory for a ZnO/air interface and λ = 544 nm in Fig. 6.14(c); and for an internal ZnO/a-Si:H interface and λ = 800 nm in Fig. 6.14(d). Again, there is good agreement between the experimental and the predicted angular distributions, although the RPS models, as discussed above, introduce some ripples in the calculation and underestimate the in-air scattering capability of the ZnO layers for large angles of diffraction. Also, compared to in-air scattering, the angular distribution in a-Si:H is dramatically shifted towards small scattering angles.

Concerning the deposition of the second ZnO layer on a SiO_x film, for the Type-B3 sample, comparisons in Figs. 6.13 and 6.14 indicate that:

(1) A double-texture is clearly visible in the AFM picture of Fig. 6.13(b), whereas without SiO_x (Type-C3 sample, Fig. 6.13(c)) no double-texture appears.

(2) σ_{rms} increases from 100 nm for the Type-A3 sample in Fig. 6.13(a) to only 102 nm for the Type-B3 sample (with SiO_x) in Fig. 6.13(a) and to 152 nm for the Type-C3 sample (without SiO_x) in Fig. 6.13(c). Therefore, when the SiO_x layer is present, the deposition of the second ZnO layer almost does not increase the value of σ_{rms}.

(3) When the SiO_x layer is present, the deposition of the second ZnO layer almost does not induce any increase of $H_T(\lambda)$ in Fig. 6.14(a) for the Type-B3 sample, compared to the single ZnO layer (Type-A3 sample). Whereas, without SiO_x, H_T at λ = 800nm increases from about 0.45 for the single ZnO layer to about 0.70 for the Type-C3 sample.

(4) In the histograms of local angle, we observe that the amount of local area with a large (~55°) local angle follows an increasing trend when considering the Type-B3, -A3, -D3 and -C3 samples, respectively.

(5) Although H_T produced by Type-A3 and Type-B3 samples are comparable, the shape of the total intensity profiles $ARS(\theta)\cdot|\sin\theta|$ in Figs. 6.14(b-d) indicates that, if the second ZnO layer is deposited on a SiO_x layer (Type-B3 sample in Figs. 6.14(b-d)), T_{dif} is almost unchanged but the angular distribution is shifted towards small scattering angles, compared to the single ZnO layer (Type-A3 sample). Whereas, if the second ZnO layer is deposited without the thin intermediate SiO_x layer (Type-C3 sample in Figs. 6.14(b-d)), T_{dif} increases and

the angular distribution shifts towards larger scattering angles, compared to the single ZnO layer.

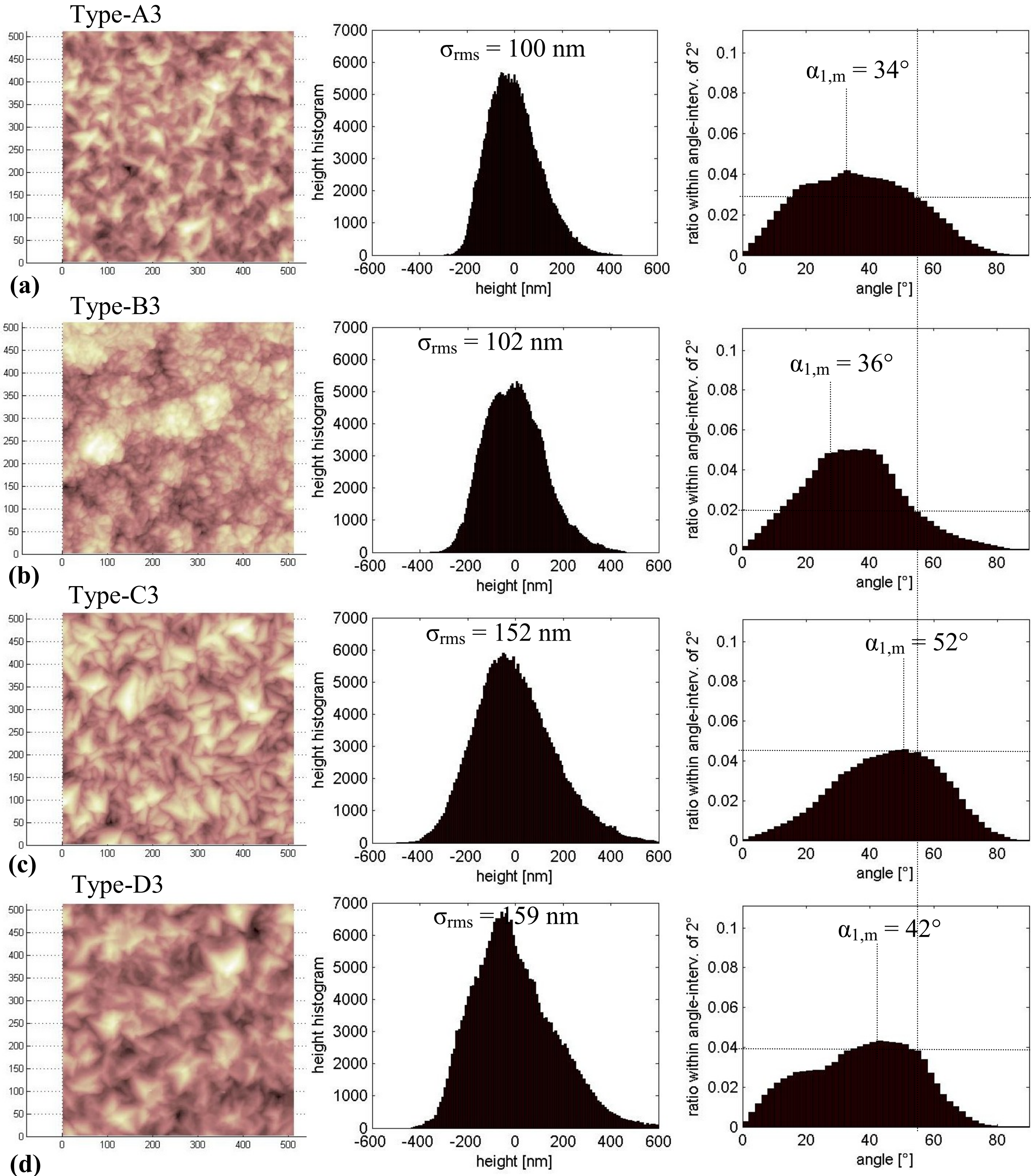

Fig. 6.13: (a)–(d) AFM pictures of the topography for the LPCVD ZnO layers of Type-A3 to D3 described in Table 6.3. Next to each AFM picture, are shown the histograms corresponding to the distribution of heights and to the distribution of local angles of the surface with respect to the plane of the layer. For each layer, the value of the most frequent local angle $\alpha_{1,m}$ is indicated. The horizontal lines allow for a comparison of the amount of local area with a large (~55°) local angle.

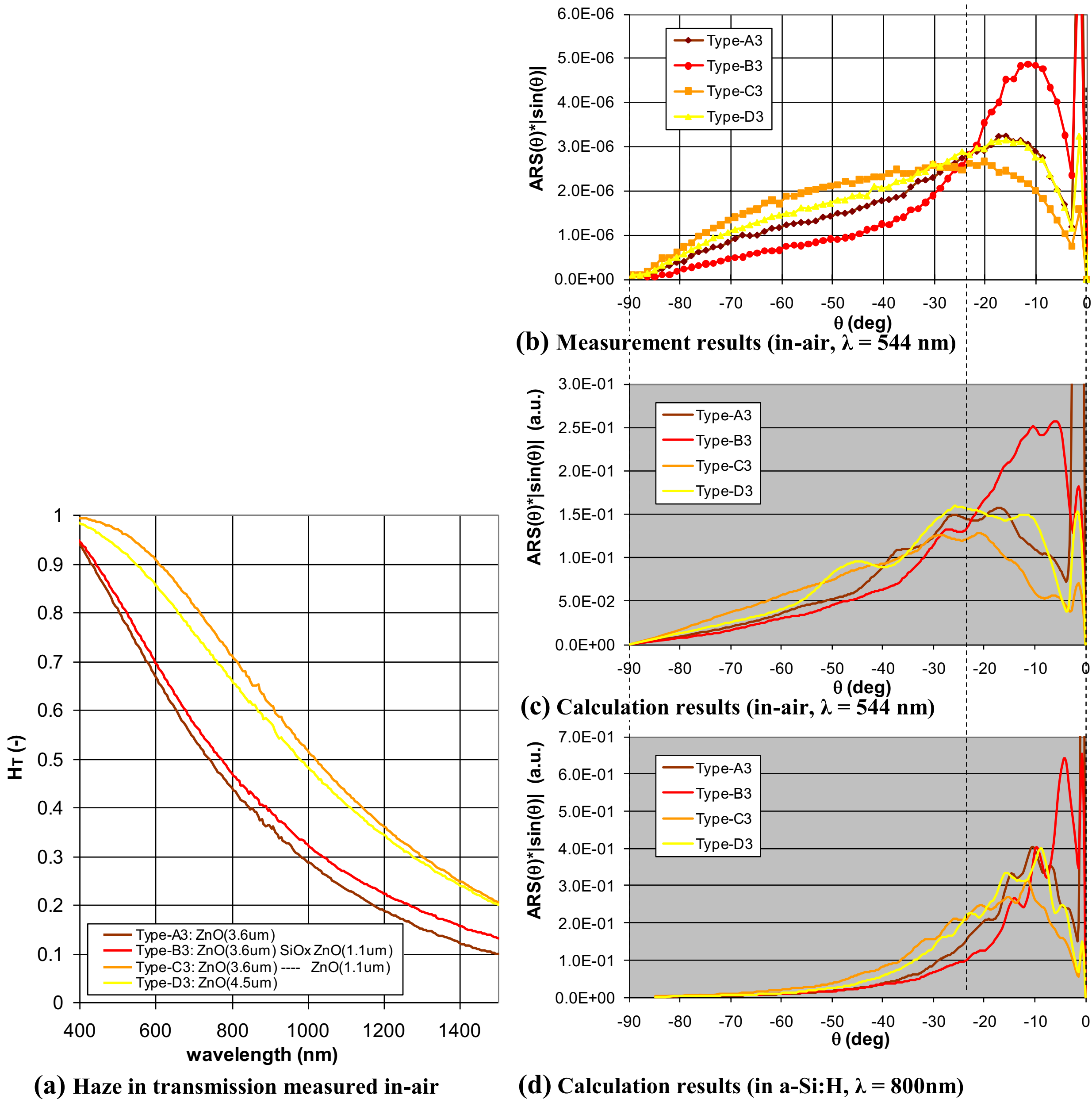

Fig. 6.14: (a) Haze in transmission $H_T(\lambda)$ measured in-air for the LPCVD ZnO layers of Type-A3 to -D3 described in Table 6.3. (b) Total intensity profiles $ARS(\theta)\cdot|\sin\theta|$ integrated over the azimuthal angle φ measured in-air with λ = 544 nm. Profiles predicted by the scalar scattering theory (c) in-air for λ = 544 nm and (d) in a-Si:H for λ = 800 nm, from the AFM data presented in Fig. 6.13.

We know from the relation (6.9) that the haze is controlled by σ_{rms}. Therefore, the observation (2) of a very small increase of σ_{rms} explains the observation (3) of a very small increase of $H_T(\lambda)$. Fig. 6.14(b) and the observation (4) concerning the local slope of the different ZnO surfaces give a coarse, empirical, relationship between surface morphology and angular distribution of the light scattered in air: the larger the proportion of the ZnO surface with slope>50°, the larger the scattering angles. This gives a possible explanation of why the scattering angles are shifted towards small angles for the Type-B3 samples: the deposition of the second ZnO layer on the thin SiO_x layers produce a noticeable decrease in the amount of local angles with α>50°. A complementary explanation can be deduced from Fig. 6.15, where the RPS functions $t_s(x,y)$ given by the relation (6.21) in the case of a ZnO/a-Si:H interface and with λ = 633 nm are plotted in bi-dimensional maps, for the four ZnO samples. The phase produced by the RPS function $t_s(x,y)$ for the Type-B3 sample is almost constant over large connected areas (green and pink areas in Fig. 6.15(b)). Therefore, these areas of almost constant phase will not contribute to enhance the spectral components of $t_s(x,y)$ with high spatial frequencies (i.e. they will not contribute to $\mathcal{F}\{t_s\}$ for large values of the direction cosines (α, β) in the relation (6.16)). This leads to a narrow angular spectrum of the diffracted waves. We conclude that large local slope is not a sufficient condition to obtain a broad angular spectrum. Actually, the size of the projected area of a facet on the x-y plane must be large enough to allow $t_s(x,y)$ to change of at least 2π radians over this facet. Therefore, *large slopes* and *sufficient facets area* must both be provided by the nano-textured surface to achieve large scattering angles.

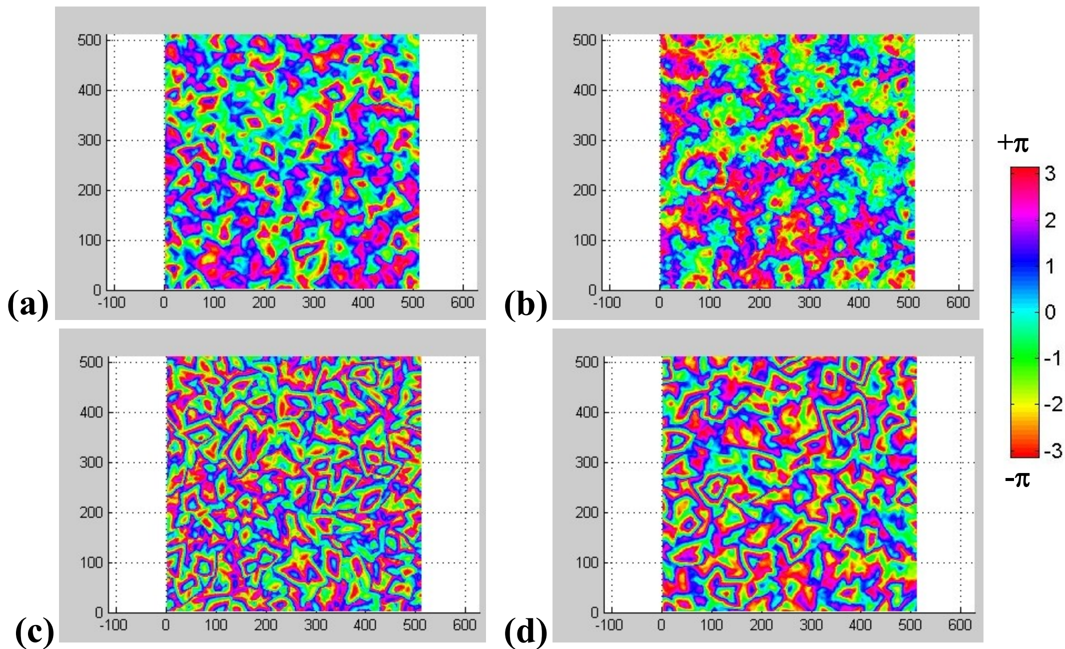

Fig. 6.15: (a)–(d) Random phase screens (RPS) for the LPCVD ZnO layers of Type-A3 to D3 described in Table 6.3 and for scattering in a-Si:H (n_2 = 3.8) and λ = 633 nm.

The experimental external quantum efficiency (EQE) of state-of-the-art micromorph solar cells (all incorporating an intermediate reflector, as detailed in chapter 7) deposited onto the four ZnO layers of Set#3 samples are plotted in Fig. 6.16. The consequence of the poor angular distribution provided by the Type-B3 ZnO layer with the double-texture is observed in Fig. 6.16 for λ>700 nm. Indeed, the EQE curve for the bottom component cell of the micromorph (EQE_{bot}) clearly drops when the front TCO is the ZnO layer with the double-texture (EQE_{bot}(900nm) = 0.40). Interestingly, with all the three other front TCO layers, EQE_{bot} for λ > 800nm is identically higher (EQE_{bot}(900nm) = 0.45), this despite of the fact that the smaller H_T measured in air is obtained with one of them (the Type-A3 ZnO layer, see Fig. 6.14(a)). We suggest this is because the angular distribution actually dominates the light scattering in the device (see also chapter 7, section 7.5), as H_T in Si is always larger than H_T in air, according to the relation (6.9), and as seen on the scales of ARS(θ)·|sin θ| of the plots for the ZnO/Si interface, larger than for the ZnO/air interface (e.g. Fig. 6.14(d) vs Fig. 6.14(c)).

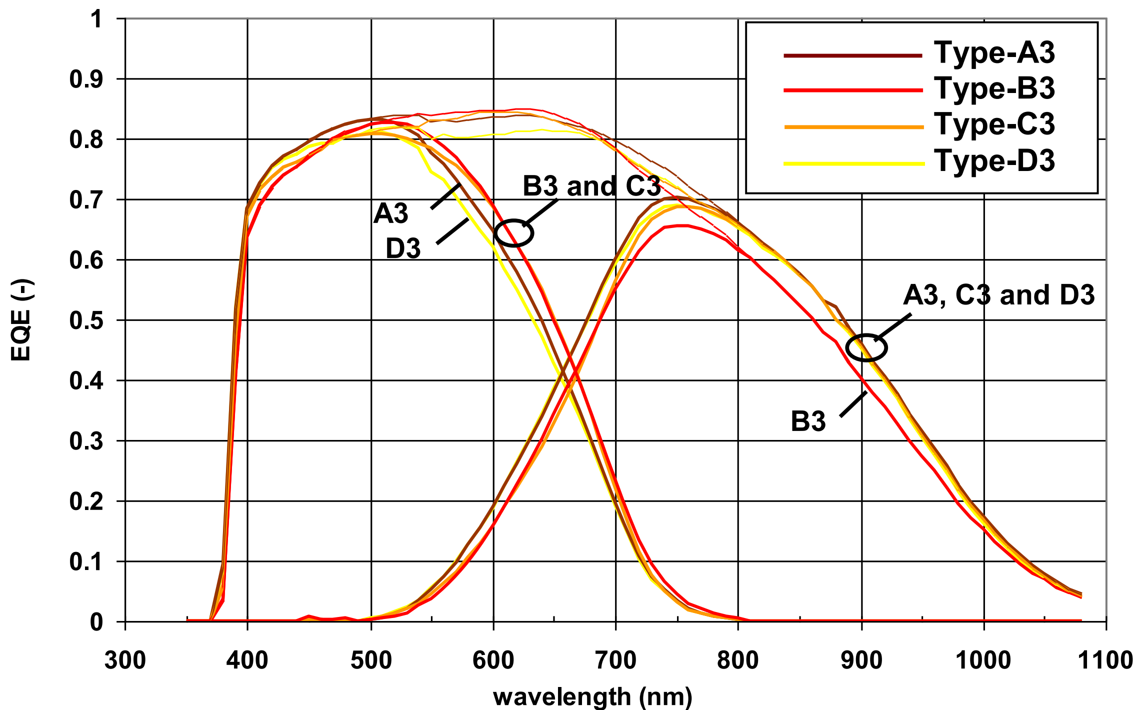

Fig. 6.16: External quantum efficiency (EQE) curves of micromorph solar cells deposited onto the LPCVD ZnO layers of Type-A3 to D3 described in Table 6.3. The thick curves at the left- (right-) hand side are the EQE curves of the top (bottom) component cells of the tandems: EQE_{top} and EQE_{bot}. The thin curves correspond to the sum of the corresponding EQE_{top} and EQE_{bot} curves.

For the EQE curve of the top component cells (EQE_{top}), we observe in Fig. 6.16 that EQE_{top} for 550nm<λ<700nm is higher when the cells are deposited on the double ZnO layers (Type-B3 and Type-C3 samples) than when they are deposited on the single ZnO layers (Type-A3 and Tye-D3). Because no common characteristic appears in Fig. 6.14 between the Type-B3 and Type-C3 samples, this experimental observation is difficult to explain on the basis of our haze and ARS measurements and calculations. We believe that the pertinent common characteristic between these two samples is that the plasma treatment of the ZnO surface after the deposition layer is only 2 minutes, whereas it is 20 minutes for the Type-A3 and Type-D3 samples. We suggest that sharp structures beneficial to the light trapping in the 550–700 nm wavelengths range of interest for the top cell are not smoothed in the case of a short surface treatment. However, we are not able to exhibit these features, neither in the AFM data of Fig. 6.13, neither in the RPS model or ARS data presented in Figs. 6.14 and 6.15. Therefore, this point merits further investigations. As the top cell thickness is typically 300 nm, a near-field approach would be better adapted to this task.

In chapter 8, we will also consider the effect of absorption in the TCO, which leads to a reduction of the EQE, and we will correct the EQE to estimate the effective light path enhancement provided by our different light trapping structures. We will find that in the best cases a factor 23 is found, still a factor ~2.5 below the ideal Yablonovitch's limit of $4 \cdot n_{Si}^2$ (with n_{Si}~3.8).

6.4 Conclusions

In this chapter, we have shown that the angular distribution of the diffuse light transmitted through different rough nano-textured LPCVD ZnO layers can be predicted by the scalar scattering theory as modified by Harvey *et al.*, using random phase screen functions. Our calculations suggest that the angular distribution of light scattered at the internal ZnO/a-Si:H interface is narrower than for the experimentally accessible case of in-air scattering. As an introduction to this chapter, we have recalled the importance of Lambertian scattering to maximize light trapping, according to Yablonovitch's theoretical derivation. In agreement with this, we have experimentally demonstrated that ARS is the pertinent light scattering measurement, and not haze, when we want to assess the potential of a given surface morphology to produce an efficient light trapping for long wavelengths in the bottom cell of micromorph devices. These results show that our calculation method, although it is based on an approximated random phase screen function, can be a valuable tool to predict the light trapping capability in silicon of an arbitrary surface morphology for the long wavelength range (700-1100 nm). In particular we find that for ZnO layers with a narrow angular distribution, the EQE of the bottom component cell of a micromorph is lower in the NIR part of the spectrum than for micromorph devices deposited on a ZnO layer with a broad ARS. Therefore, with a new type of TCO layer, ARS measurement is the most valuable tool to assess its long-wavelength light trapping

capability in the device. Whereas our calculation method may provides a quick and efficient method to design “ideal” surface morphologies.

However, this approach, which does not deal with reflection and near-field effects, does not explain details of light trapping in the top cell of micromorph devices with an intermediate reflector.

The next chapter (chapter 7) is devoted to the study of the intermediate reflector in micromorph solar cells, where the relationship between the surface morphology of the front contact and the effects of the intermediate reflector are discussed. Anti-reflection effects and absorption losses produced by the front contact will finally be discussed in chapter 8.

7 Intermediate reflector for high stable efficiency devices

In this chapter we discuss the electrical and optical effects of the insertion of an intermediate reflector layer (IRL) in-between the component cells of the micromorph solar cell device.

After a motivation for the concept of IRL, given in section 7.1, we discuss the effects of current matching in section 7.2. Thickness series of IRL made of zinc oxide are presented in section 7.3. In section 7.4, we compare zinc oxide versus silicon oxide based materials when they are deposited as IRL. The interplay between the front contact surface morphology and the IRL is discussed in section 7.5 where we also present our best devices. Before concluding, we give, in section 7.6, an experimental proof of concept for the need of IRL to achieve high stable efficiencies.

7.1 Introduction

7.1.1 Motivation and related problems

As a consequence of the electrical series connection of the individual a-Si:H top and μc-Si:H bottom cells of the micromorph device, the short-circuit current density (J_{sc}) of the whole tandem is limited by the absorber with the lower current generation capability. To mitigate the well known Staebler-Wronski light-induced degradation effect [Staebler 1977], the thickness of the a-Si:H top absorber should not exceed 300 nm, typically [Platz 1998]. This constraint considerably limits the J_{sc} on the top cell and, hence, the efficiency of the whole device. Triple-junction devices, such as a-Si:H/a-Si:Ge:H/μc-Si:H or a-Si:H/μc-Si:H/μc-Si:H structures [Yan 2006] lift this constraint, allowing smaller currents in each sub-cell for comparable efficiencies. However, these more complex structures require either scarce Ge, or increased deposition times for μc-Si:H absorbers. Thus, to retain the simplicity of the micromorph approach, an intermediate reflecting layer (IRL) between the individual cells must be introduced to increase the current in the a-Si:H absorber [Fisher 1996, Yamamoto 2000, Yamamoto 2004, Lambertz 2007, Buehlmann 2007].

The concept of IRL was introduced by IMT in 1996 [Fisher 1996] and allowed the demonstration by Meier *et al*. of high stability (over 1300h of light-soaking) for a bottom-limited micromorph tandems with a thin (<0.2 μm) a-Si:H top cell [Meier 2003]. It was also applied by Yamamoto *et al*. who demonstrated an initial module efficiency of 13.5% [Yamamoto 2005].

Another benefit of the IRL concept is to allow the current balance to be tuned between given individual cells of the tandem [Dominé 2006]. It is well known that the J_{sc} but also the fill-factor (FF) of a tandem solar cell depend on the current matching between its two component cells [Platz 1997a, Nakijama 2004, Repmann 2003]. Whether a micromorph tandem cell

should be bottom-limited or top-limited is still being debated. On one hand, Platz *et al*. calculated, on the basis of a simple optical and electrical model, that slightly bottom-limited conditions after degradation are needed to maximize the stabilized efficiency of the micromorph tandem [Platz 1997b]. In [Platz1997b] this is attributed to the fact that only the top a-Si:H cell is subject to degradation and that it provides 2/3 of the output power thanks to its higher open-circuit voltage (V_{oc}). Indeed, if the bottom μc-Si:H cell is stable, we can expect no degradation of the J_{sc} value for a micromorph tandem under a slightly bottom-limited condition after light-soaking. This stability of J_{sc} was experimentally demonstrated with Kaneka's HYBRID modules by Nakajima *et al*. [Nakajima 2004]. On the other hand, these authors point out in [Nakajima 2004] that the outdoor behavior of top-limited Kaneka's HYBRID modules exhibits higher performances – in terms of power output normalized by the power measured under standard test conditions (STC) – than bottom-limited ones, but they do not comment on absolute values of the energy yield.

7.1.2 Layout of the chapter

In section 7.2, we calculate theoretical current density-voltage (J-V) curves of micromorph cells under initial and light-soaked conditions. We show that the relationship between the fill-factor (FF) and the current matching explains why the conversion efficiency (η) under STC of this tandem device is maximized if it is slightly bottom-limited.

In section 7.3 the gain in $J_{sc,top}$ ($\Delta J_{sc,top}$) and the loss in $J_{sc,bot}$ ($\Delta J_{sc,bot}$) produced by the insertion of a zinc oxide (ZnO) intermediate reflector (ZIR) are studied experimentally and by optical simulation. With the help of an optical model, we discuss the saturation of the gain $\Delta J_{sc,top}$ and loss $\Delta J_{sc,bot}$ experimentally observed when the thickness of the ZIR is increased. In this section we also open the discussion to the influence of the surface morphology of the front transparent conductive oxide (TCO) layer on the effectiveness of the IRL.

In section 7.4 we compare the insertion of a silicon oxide based IRL (SOIR) and a ZIR in micromorph solar cells deposited on two substrates with different surface roughness and lateral feature size. We also show experimentally that the lateral conductivity of the IRL plays a major role in the V_{oc} of the tandem.

Section 7.5 is a study of the interplay between the front TCO layer and the IRL and its impact on fill factor and current matching conditions. We highlight the key role of the angular distribution of the light scattered by the front TCO layer for the gain $\Delta J_{sc,top}$. In this section we exhibit the best efficiencies achieved so far, by depositing thick micromorph cells on glasses coated with a broadband anti-reflection coating.

Finally, in section 7.6 we provide experimental proof of concept of the need of an IRL for micromorph solar cells with high and stable value of J_{sc}, before drawing general conclusions about IRL in section 7.7.

7.2 Effect of the current matching in micromorph tandem cells

7.2.1 Modeling

We calculate the J-V curve of the micromorph cells using an equivalent network model comparable to the network presented in [Repmann 2003]. In our model, the J-V characteristics of the top and bottom cells under illumination, $J(V_{top})$ and $J(V_{bot})$, respectively, are described by the following equations:

$$J(V_{top}') = J_{ph,top} \cdot \chi(V_{top}') + J_{01,top}\left(e^{\frac{qV_{top}'}{n_{1,top}k_B T}} - 1 \right) + \frac{V_{top}'}{R_{p,top}} \quad , \qquad (7.1)$$

$$J(V_{bot}') = J_{ph,bot} \cdot \chi(V_{bot}') + J_{01,bot}\left(e^{\frac{qV_{bot}'}{n_{1,bot}k_B T}} - 1 \right) + J_{02,bot}\left(e^{\frac{qV_{bot}'}{n_{2,bot}k_B T}} - 1 \right) + \frac{V_{bot}'}{R_{p,bot}} \quad , \qquad (7.2)$$

$$V_{top}'(J) = V_{top} - J \cdot R_{s,top} \qquad (7.3a) \qquad \text{and} \quad V_{bot}'(J) = V_{bot} - J \cdot R_{s,bot} \, , \quad (7.3b)$$

where $J_{01,top}$ and $J_{01,bot}$, $J_{02,bot}$ are the reverse saturation currents and $n_{1,top}$ and $n_{1,bot}$, $n_{2,bot}$ the ideality factors of the one diode model of the a-Si:H top cell and of the two diode model of the µc-Si:H bottom cell, respectively. In (7.1) and (7.2), $R_{p,top}$ ($R_{p,bot}$) and $R_{s,top}$ ($R_{s,bot}$) are the shunt and series resistances and $J_{ph,top}$ ($J_{ph,bot}$) is the photogenerated current density of the top (bottom) cell, q is the elementary charge of the electron, k_B the Boltzmann's constant and T the absolute temperature. The photo-generated current-recombination terms $J_{ph,top} \cdot \chi_{top}(V_{top}')$ and $J_{ph,top} \cdot \chi_{top}(V_{top}')$ in (7.1) and (7.2) can be written in terms of the Hubin's collection function [Hubin 1995, Hof 1999]:

$$\chi(V') = \frac{1}{1 + L / l_s} \quad . \qquad (7.4)$$

In the relation (7.4), L is the thickness of the intrinsic layer and l_s is an effective drift length expressed by:

$$l_s = (\mu\tau)_{eff} \frac{V_{bi} - V'}{\varphi(V')L} \, , \qquad (7.5)$$

where $(\mu\tau)_{eff}$ is the effective mobility-lifetime product, $\varphi(V')$ the electric field deformation factor, considered here as constant [Hof 1999], and V_{bi} the built-in potential. Note that $(V_{bi} - V)/\varphi L$ is the averaged electric-field in the intrinsic layer normalized by the

deformation factor φ. This form factor φ equals unity if the field is constant across the intrinsic layer, while φ>1 if the field is deformed, e.g. by a shift of the Fermi level in the intrinsic layer due to contamination [Shah 2006]. Note also that if $L/l_s << 1$, the Hubin's collection function can be expressed by the Merten's collection function [Merten 1998, Hof 1999]:

$$\chi = 1 - L / l_S \,. \tag{7.6}$$

With this first order approximation of the collection function (7.4), we can draw the equivalent network model for the micromorph tandem presented in Fig. 7.1. We calculate the J-V curve of the corresponding micromorph cell by simply summing, for each value of J, the corresponding voltages of the individual cells of the tandem:

$$V(J) = V_{top}(J) + V_{bot}(J) \,. \tag{7.7}$$

In our calculations, for simplicity, the total photocurrent density $J_{ph,sum} = J_{ph,top}+J_{ph,bot}$ is fixed at a constant value. The individual photocurrent densities for the top and the bottom cells are calculated according to:

$$J_{ph,bot} = J_{ph,sum} \cdot G_b / G_t \cdot D \quad \text{and} \tag{7.8}$$

$$J_{ph,top} = J_{ph,sum}(1 - G_b / G_t \cdot D), \tag{7.9}$$

where G_b/G_t is defined as the ratio of the irradiance that would be measured by top and bottom reference cells with spectral responses such as $G_b/G_t = 1$ under AM1.5 spectral irradiance [Nakajima 2004]. Therefore, the actual spectral irradiance is "blue-rich" when $G_b/G_t < 1$ and "red rich" if $G_b/G_t > 1$. The factor D in (7.8) and (7.9) gives the intentional (designed) current mismatch of the tandem ($0 < D < 1$). Therefore, with this definition, a micromorph cell designed with $D = 0.5$ will be current-matched under AM1.5 spectral irradiance.

The values of the model parameters used for the calculation of the J-V curves of an idealized micromorph cell in the initial and in the light-soaked states are listed in Table 7.1. These values are chosen to reproduce, for a given value of $J_{ph,sum}$, realistic initial efficiencies achievable with intrinsic a-Si:H and µc-Si:H characteristics in the same order of magnitude than values measured at IMT for layers deposited on glass (see [Beck 1997]), and to demonstrate the effect of a significant degradation of the top cell.

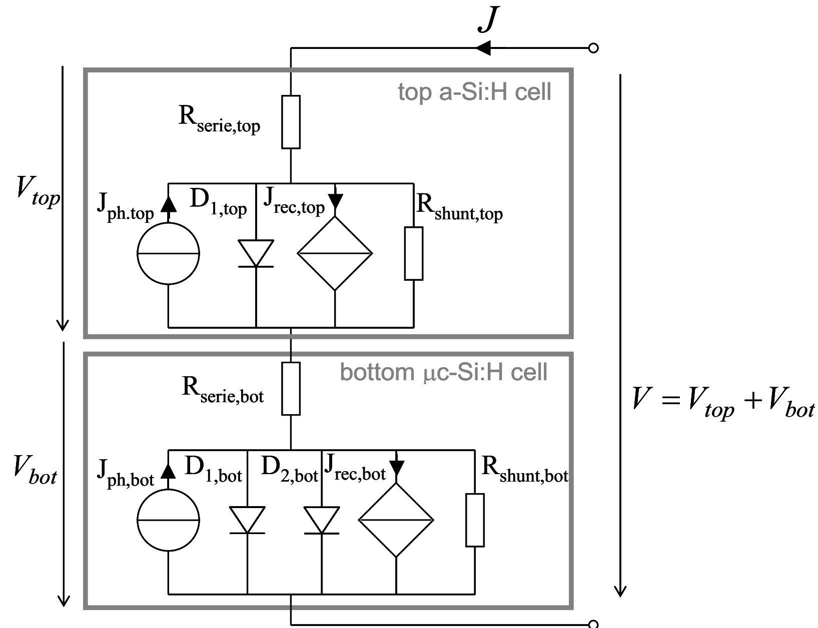

Fig. 7.1: Equivalent network model for a micromorph cell using a two-diode model for the bottom μc-Si:H cell and Merten's collection function in the generated-recombination terms for the top a-Si:H and the bottom μc-Si:H cells [Merten 1998].

Table 7.1: Values for the parameters, introduced in the relations (7.1) to (7.7), of the model for the micromorph tandem.

Model parameter	Value used in the calculation	Unit
T	300	(K)
L_{top}	$3\cdot10^{-5}$	(cm)
$V_{bi,top}$	1.1	(V)
φ_{top}	3	(-)
$(\mu\tau)_{eff,top}$	$5\cdot10^{-8}$ (initial) / $2.5\cdot10^{-8}$ (degraded)	(cm^2/V)
$J_{01,top}$	$2.5\cdot10^{-9}$ (initial) / $8.0\cdot10^{-8}$ (degraded)	(mA/cm^2)
$n_{1,top}$	1.55 (initial) / 1.80 (degraded)	(-)
$R_{p,top}$	$5\cdot10^{2}$	$(k\Omega\cdot cm^2)$
$R_{s,top}$	$6\cdot10^{-4}$	$(k\Omega\cdot cm^2)$
L_{bot}	$1.5\cdot10^{-4}$	(cm)
$V_{bi,bot}$	1.0	(V)
φ_{bot}	1	(-)
$(\mu\tau)_{eff,bot}$	$6\cdot10^{-7}$	(cm^2/V)
$J_{01,bot}$	$1.25\cdot10^{-5}$	(mA/cm^2)
$n_{1,bot}$	1.48	(-)
$J_{02,bot}$	$2\cdot10^{-4}$	(mA/cm^2)
$n_{2,bot}$	2	(-)
$R_{p,bot}$	$4\cdot10^{3}$	$(k\Omega\cdot cm^2)$
$R_{s,bot}$	$3\cdot10^{-4}$	$(k\Omega\cdot cm^2)$

7.2.2 Results of calculations

J-V curves, under AM1.5 illumination spectrum, of the micromorph and its individual cells in the initial and degraded state modeled with the values listed in Table 7.1 are plotted in Fig. 7.2. The corresponding J-V parameters are listed in Table 7.2. In these calculations $J_{ph,sum}$ is fixed to 26 mA/cm^2 and D = 0.5, i.e. the tandem is designed to be matched in the initial state (negligible recombination).

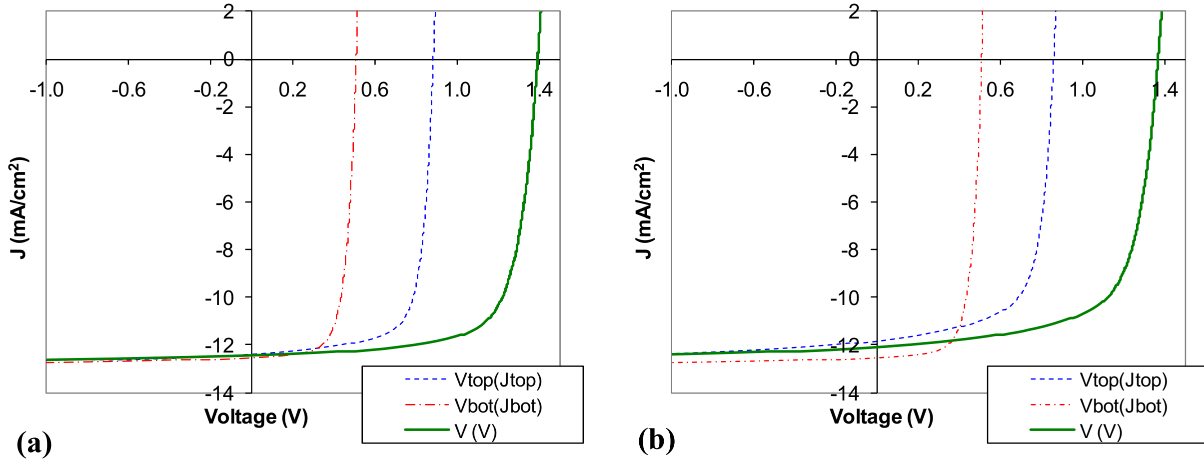

Fig. 7.2: *Calculated J-V curves of the individual cells and of the corresponding micromorph cell in (a) initial and (b) degraded state, for the model parameters listed in Table 7.1.*

Table 7.2: J-V parameters of the calculated curves plotted in Fig. 7.2.

J-V parameter	top cell	bottom cell	micromorph cell	Unit
initial state:				
J_{sc}	12.39	12.53	12.45	(mA/cm^2)
V_{oc}	0.885	0.509	1.395	(V)
FF	73.9	70.7	72.6	(-)
η	8.10	4.51	12.60	(%)
degraded state:				
J_{sc}	11.83	12.53	12.08	(mA/cm^2)
V_{oc}	0.860	0.509	1.369	(V)
FF	68.0	70.7	68.0	(-)
η	6.92	4.51	11.25	(%)

The J-V parameters of the micromorph cell will change if the spectral irradiance changes. For the micromorph cell with D = 0.50 and for a second micromorph with D tuned in order to obtain a matched tandem in the degraded state (D = 0.49), the behavior of the J-V parameters with respect to variations of the spectrum of the illumination ($0.9 < G_b/G_t < 1.1$) are plotted in Fig 7.3. As expected, this figure indicates that V_{oc} is almost insensitive to the current mismatch and that, when the tandems are in the current-matched condition, J_{sc} is maximized whereas FF is minimized. A more striking

observation is that in Fig. 7.3(c), the increase in FF is steeper when G_b/G_t changes towards "blue-rich" than when it changes towards "red-rich" spectral irradiance. Moreover, our calculation shows that this asymmetry in the increase of FF with current-mismatch is more pronounced for the micromorph cell in the degraded state (see Fig. 7.3(c)). Together with the symmetrical behavior of J_{sc}, the strong asymmetry for FF shifts the maximum of η towards "blue-rich" spectral irradiance (see the position of maxima in Fig. 7.3(d)).

The J-V parameters of the micromorph cell will change if the spectral irradiance changes. For the micromorph cell with D = 0.50 and for a second micromorph with *D* tuned in order to obtain a matched tandem in the degraded state (D = 0.49), the behavior of the J-V parameters with respect to variations of the spectrum of the illumination ($0.9 < G_b/G_t < 1.1$) are plotted in Fig 7.3. As expected, this figure indicates that V_{oc} is almost insensitive to the current mismatch and that, when the tandems are in the current-matched condition, J_{sc} is maximized whereas FF is minimized. A more striking observation is that in Fig. 7.3(c), the increase in FF is steeper when G_b/G_t changes towards "blue-rich" than when it changes towards "red-rich" spectral irradiance. Moreover, our calculation shows that this asymmetry in the increase of FF with current-mismatch is more pronounced for the micromorph cell in the degraded state (see Fig. 7.3(c)). Together with the symmetrical behavior of J_{sc}, the strong asymmetry for FF shifts the maximum of η towards "blue-rich" spectral irradiance (see the position of maxima in Fig. 7.3(d)).

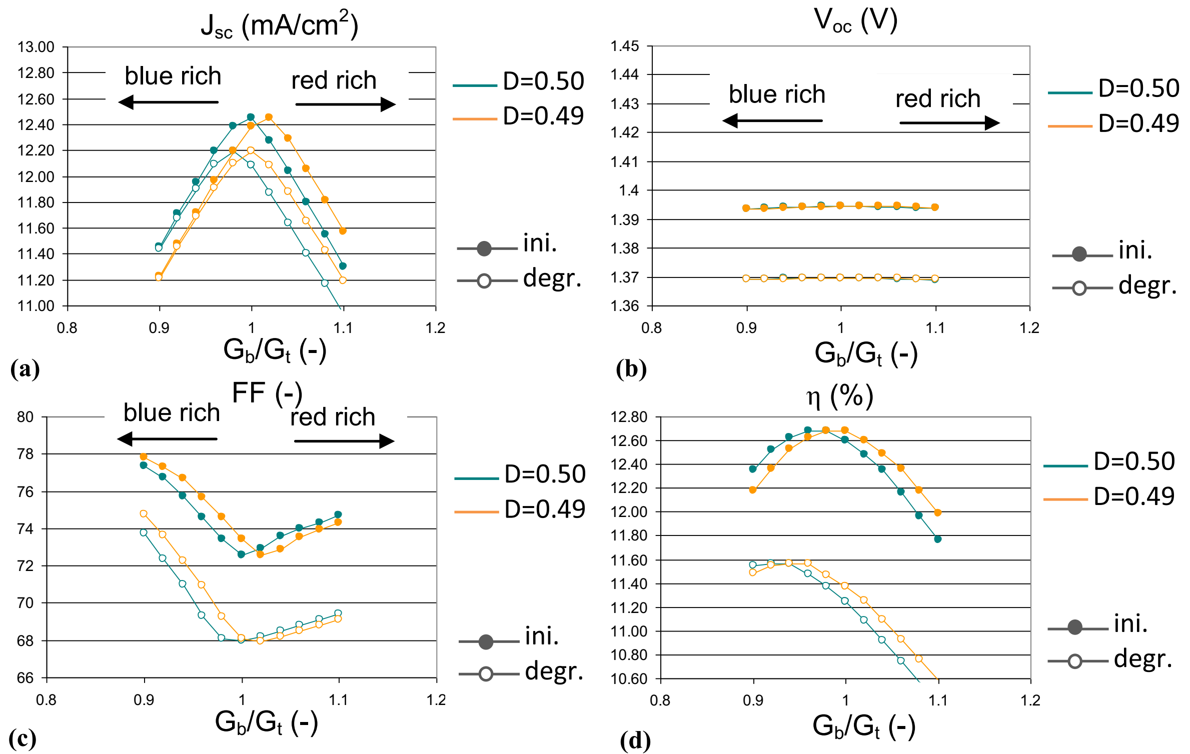

Fig. 7.3: Variation of (a) J_{sc}, (b) V_{oc}, (c) FF and (d) η with respect to the modification of the spectral mismatch G_b/G_t, for a micromorph cell matched under AM1.5 in the initia state (D = 0.50, green) and a second micromorph cell matched under AM1.5 but in the degraded state (D =0.49, orange). The plain (empty) symbols correspond to the initial (degraded) state.

7.2.3 Discussion

Fig. 7.2(b) shows that, for the micromorph cell, the slope of the J-V curve at the point of short-circuit $R_{sc}^{-1} = \partial J/\partial V|_{V=0V}$ is controlled by R_{sc}^{-1} of the limiting sub-cell. This can be better understood with the help of Fig. 7.4 where we show graphically that, as expected from (7.7), the voltage $V_{mimo}(J)$ between the terminals of the micromorph is equal to the sum of V_{top} and V_{bot}. It follows that close to the point of J_{sc} indicated in Fig. 7.4(a), the rate of change of $V_{mimo}(J)$ depends mainly on R_{sc}^{-1} of the component cell that is limiting (the top cell in Fig. 7.4).

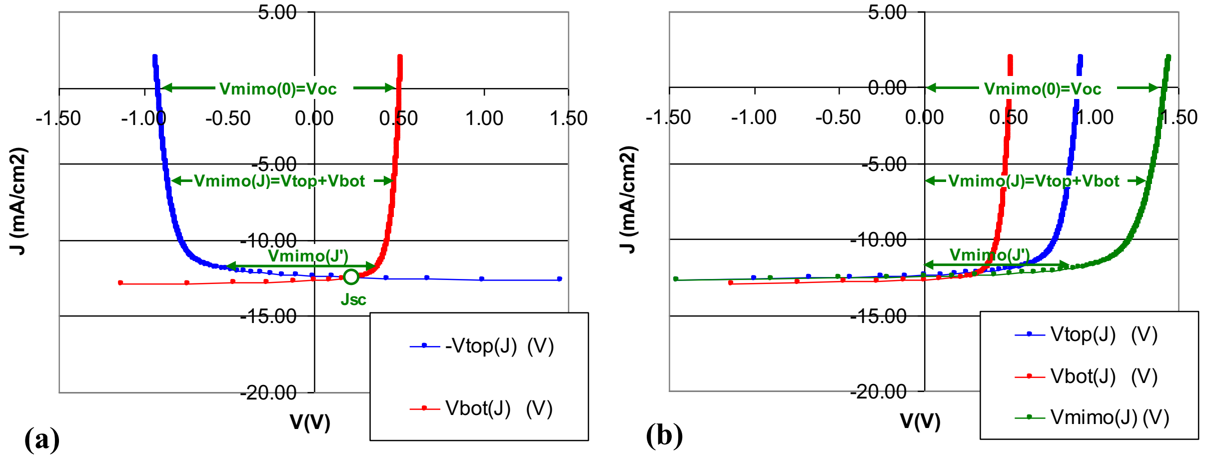

Fig. 7.4: Construction of the J-V curve of a micromorph cell from the J-V curves of the component top and bottom cells of the tandem: $V_{mimo}(J) = V_{top}(J)+V_{bot}(J)$. V_{bot} and $-V_{top}$ are reported in (a) where $V_{mimo}(J)$ graphically corresponds to the horizontal distance between V_{bot} and $-V_{top}$. The resulting J-V curve of the micromorph tandem is reported in (b). The point of J_{sc} is easily identified in (a) as the crossing point of $V_{bot}(J)$ and $-V_{top}(J)$. The reciprocal slopes R(V) of the J-V curves of the top and bottom cells add to give: $R_{mimo} = R_{top}+ R_{bot}$. Therefore, because the knee of the J-V curve of the non-limiting cell is close to the point of J_{sc}, the rate of change of $V_{mimo}(J)$, when J increases from J_{sc}, depends mainly on the reciprocal slope of the J-V curve of the limiting cell (the top cell here): $R_{bot}(J >\approx J_{sc}) << R_{top}(J >\approx J_{sc})$, thus $R_{mimo}^{-1}(J >\approx J_{sc}) \cong R_{top}^{-1}(J >\approx J_{sc})$.

The control of R_{sc}^{-1} of the current-limiting sub-cell on R_{sc}^{-1} of the micromorph cell explains the asymmetrical behavior of FF in Fig. 7.3: in "red-rich" illumination conditions, R_{sc}^{-1} of the micromorph cell is controlled by the limiting a-Si:H top cell with a poorer R_{sc}^{-1} than the μc:Si:H bottom cell. Therefore, FF of the micromorph under a top-limited condition is always smaller than for the same degree of mismatch but towards bottom-limitation. This control on R_{sc}^{-1} by the top a-S:H cell also explains the higher asymmetry observed in Fig. 7.3(c) for the cell in the light-soaked state. This is because light-induced defects decrease $(\mu\tau)_{eff,top}$ in (7.5). Therefore, R_{sc}^{-1} of the top cell increases due to a subsequent decrease of the collection function (7.6).

For a micromorph cell that is matched under AM1.5 in the degraded state, the consequence of the asymmetric behavior of FF is that η is maximized if the spectral irradiance is not AM1.5-like but slightly shifted towards a "blue-rich" spectrum (see Fig. 7.3(d)). Identically, for a micromorph cell evaluated under AM1.5, η will be maximized if the tandem is designed such that, in the degraded states, it is slightly bottom-limited.

The asymmetric behavior of FF under variation of the spectral irradiance is actually evident in experimental data published in [Nakajima 2004] for Kanecka's Hybrid modules. However, this asymmetry is not commented on by these authors. Instead, they focus on the fact that under real outdoor conditions, at noon and in summer, the spectral irradiance periodically changes towards "blue-rich" conditions at the same time as the temperature increases. They observe therefore that the relative performance of a top limited HYBRID module exceeds its performance under STC by 10% and conclude that, top limitation is more favorable than bottom limitation. We emphasize that they do not exhibit energy yields but the output power normalized by the power under STC and that their result depends on the geographical location of the experiment. Top limitation (relatively to AM1.5) will indeed be beneficial, in terms of energy yield, if “blue-rich” conditions shift the working point at the left of the maximum in Fig. 7.3(d) sufficiently often during the year. This may be not the case in northern European countries. Therefore, energy rating studies of micromorph modules, such as presented in [Nikolaeva 2007], still have to be conducted in different geographical locations to clarify the question of top versus bottom limitation for micromorph solar modules.

7.2.4 Conclusion

We showed that under STC and for a given value of the total photocurrent density $J_{ph,sum}$, the efficiency of a bottom-limited micromorph cell is higher than for top-limited or matched ones. This is due to the control of R_{sc}^{-1} of the micromorph by the limiting sub-cell of the tandem. Indeed, the increase of FF is higher when the current mismatch changes towards bottom-limitation than when it changes towards top limitation, because R_{sc}^{-1} of the top a-Si:H cell in the light-soaked state is always poorer than R_{sc}^{-1} of the μc-Si:H bottom cell. The consequence is that, for a micromorph cell matched in the degraded state, η is maximized if the spectral irradiance is not AM1.5-like but slightly shifted towards the "blue-rich" spectrum. Identically, for a micromorph cell evaluated under AM1.5, η will be maximized if the design of the tandem is such that in the degraded states, it is slightly bottom-limited. For the energy yield of a micromorph module under real natural conditions, the question of top versus bottom limitation depends on the geographical location considered and would deserve dedicated energy rating studies.

7.3 ZIR thickness series: experimental and optical modeling studies

7.3.1 Experimental

Fabrication and characterization of the micromorph cells

The solar cells are deposited on AF45 glass plates covered by as-grown surface-textured TCO layers. These front TCO layers are ZnO:B films deposited by the low-pressure chemical vapor deposition (LPCVD) technique. The precursor gases used for deposition of these LPCVD ZnO:B films are diethylzinc (DEZ) and water vapors, and

diborane (B_2H_6) as the doping gas. Details of the process can be found in [Fay 2003] and [Steinhauser 2008b]. The surface roughness of the different front TCO layers used in this work is varied by changing the film thickness. Their sheet resistance is kept constant at approximately 10 Ω/sq by adapting the gas phase doping ratio for each film thickness [Steinhauser 2005]. The root-mean-square (rms) value of their surface roughness (σ_{rms}) and the lateral feature size of their surface morphology are determined by atomic force microscopy (AFM) measurements performed in the non-contact mode.

The ZIR layers deposited here have thickness values ranging from 16 nm to 330 nm and are ZnO:Al layers deposited by RF-magnetron-sputtering (13.56 MHz) of a ZnO:Al target in an argon plasma. The RF power density and argon pressure were 1.6 W/cm^2 and $8\cdot10^{-3}$ mbar, respectively. The measured (coplanar) conductivity values for the 35 nm to 330-nm-thick ZIR layers are comprised between 10^2 and 10^3 S/cm. In order to precisely evaluate the influence of the ZIR layer, half of the 4 x 4 cm^2 freshly deposited a-Si:H layers of the top cell was masked by an AF45 glass plate during ZIR deposition. This permits the comparison of closely spaced micromorph cells with and without ZIR layer and therefore the minimization of the errors due to inhomogeneous a-Si:H and μc-Si:H films deposition. The co-deposited ZnO films on AF45 glass substrates (i.e. on the masks) permitted us to determine the thickness of the ZIR layers with a stylus surface profiler Alpha Step 200 from Tencor Instruments.

The top and bottom p-i-n cells were deposited by very-high frequency plasma enhanced chemical vapor deposition (VHF-PECVD). The a-Si:H top cells were deposited in a single chamber reactor with a plasma excitation frequency of 70 MHz (system C, see section 2.3) and the μc-Si:H bottom cells were deposited at 122 MHz in a dual chamber deposition system (system B, see section 2.3). The back contact consists of a LPCVD ZnO:B layer covered with a dielectric back reflector. The back reflector is not employed for the samples used in the ZIR thickness series. For the ZIR thickness series, the cell area (25 mm^2) was patterned by laser scribing (532 nm). For the best cells presented at the end of section 7.3, it was patterned by lift-off of the back LPCVD ZnO layer and SF_6 plasma etching of the silicon layers (~20 mm^2). In this case, an intermediate wet etching step in HNO_3 must be completed to pattern the ZIR layer.

The external quantum efficiencies (EQE) of the top and bottom cells (EQE_{top} and EQE_{bot}) are measured under red and blue bias-light illumination, respectively. Short-circuit current densities for top and bottom cells ($J_{sc,top}$ and $J_{sc,bot}$) are calculated from the EQE curves, by integrating, over the wavelength range, the product of EQE times the spectral density of the photon flux of AM1.5g solar spectrum. The current density-voltage (J-V) curves are measured using a dual lamp (Xe and Ha) sun simulator (Wacom) in standard test conditions (25°C, AM1.5g spectrum, 100 mW/cm^2) and normalized with the J_{sc} value deduced from the EQE measurements (see section 2.3).

Optical modeling

Optical effects of ZIR are studied by means of optical modeling and by calculation of the optical absorption of the various layers within the device. The computer program used is Cell7 and is written by J. Springer. It includes coherent calculation, scalar scattering theory (relations 6.8 and 6.9 of chapter 6) and Monte Carlo tracing of scattered photons [Springer 2004] as well as experimentally determined wavelength-dependent optical constants [Poruba 2000]. Under the assumption of 100% collection efficiency, the optical absorption in the top and bottom absorbers permits us to determine the projected increase and decrease in $J_{sc,top}$ and $J_{sc,bot}$, respectively, as caused by ZIR insertion (designated as $\Delta J_{sc,top}$ and $\Delta J_{sc,bot}$, respectively).

For the textured interfaces, a one-layer effective media approximation (EMA) is used [Springer 2004]. For a ZIR layer with a thickness value $d < \sigma_{rms}$, a three-layer EMA is used: the a-Si:H/ZIR/μc-Si:H region is subdivided into three zones (1), (2) and (3) of thicknesses d, $\sigma_{rms} - d$ and d, respectively. The volume of zone (1) is occupied by a-Si:H and ZnO, the volume of zone (2) is a mix of the 3 materials and the volume of zone (3) is occupied by ZnO and μc-Si:H. The corresponding effective refractive indexes $\tilde{n}_1$, $\tilde{n}_2$ and $\tilde{n}_3$, are calculated as the weighted sum of the refractive indexes of a-Si:H, ZnO, and μc-Si:H. This is schematically illustrated in Fig. 7.5 The weighting coefficients α_{ij} are calculated as the volume fractions of these materials in zones (1), (2), and (3), supposing homogenous coverage of the surface by the same pyramidal structures.

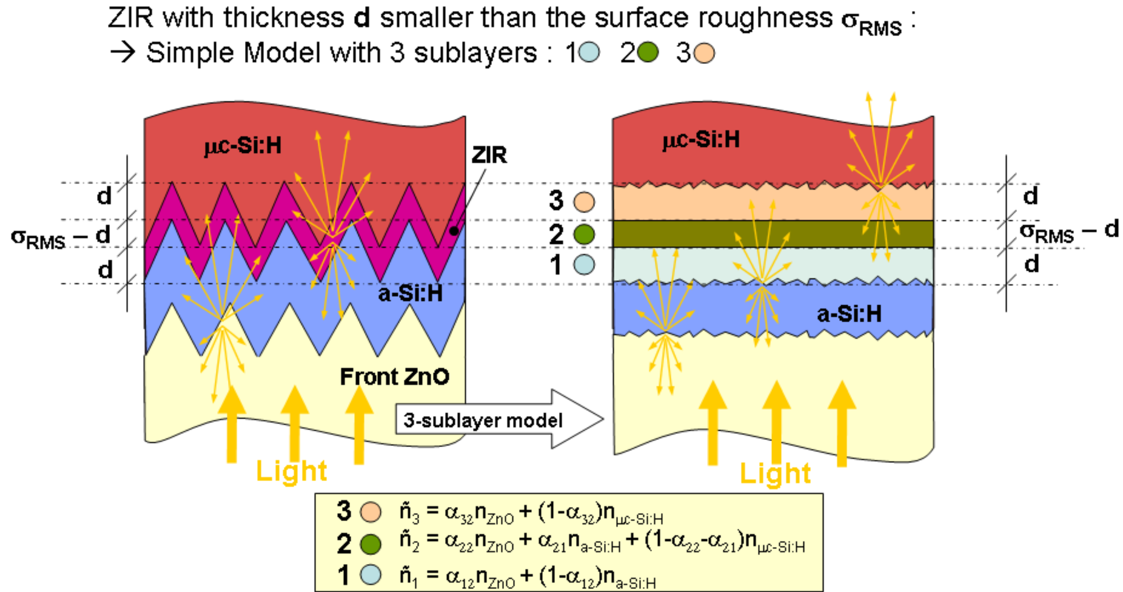

Fig. 7.5: Schematic illustration of the modeling of the rough intermediate reflector region, when the intermediate reflector is thin, by an effective media approximation (EMA) with 3 sublayers. The weighting coefficients α_{ij} used in the calculation of the effective refractive index $\tilde{n}_i$ is calculated as the volume fraction in zone (i) of a-Si:H (j=1), ZnO (j=2) and μc-Si:H (j=3), supposing homogenous coverage of the surface by identical pyramids. Light scattering at the a-Si:H/ZIR and ZIR/μSi:H interfaces is modeled by the scalar scattering theory formulas (relations (6.8) and (6.9) in chapter 6, with $C_R = 1$, $C_T = 0.5$ and $\beta_T = 3$) and by the fit $ADF(\theta) = \sin(\theta)\cdot(8.296\text{-}23.886\cdot\theta+29.696\cdot\theta^2\text{-}16.788\cdot\theta^3+3.453\cdot\theta^4)$, provided in the software Cell7, of the experimental angular distribution function presented in [Springer 2004].

7.3.2 Results of the ZIR thickness series

ZIR thickness-effect for a given type of front ZnO

The ZIR thickness d was varied from 16 nm to 327 nm inside the tandem cells deposited on our standard front LPCVD ZnO layer, optimized for a-Si:H cells, with a surface roughness σ_{rms} of approximately 80 nm and no plasma post-treatment of their surface. The experimental difference in J_{sc} values obtained with and without the ZIR layer (designated here as $\Delta J_{sc,top}$ and $\Delta J_{sc,bot}$ for the top and bottom cells, respectively) are compared with simulated results in Fig. 7.6.

The experimental gain $\Delta J_{sc,top}$ increases with a slope of approximately 0.3 mA/cm^2 per 10 nm of ZIR thickness. The maximum gain obtained is 2.8 mA/cm^2 for d = 110 nm. For higher d values, $\Delta J_{sc,top}$ remains in the range of 1.8 to 2.8 mA/cm^2. The experimental loss $\Delta J_{sc,bot}$ continuously decreases when d increases. Assuming a linear approximation for this trend for d < 100 nm, its slope is approximately -0.4 mA/cm^2 per 10 nm of ZIR thickness.

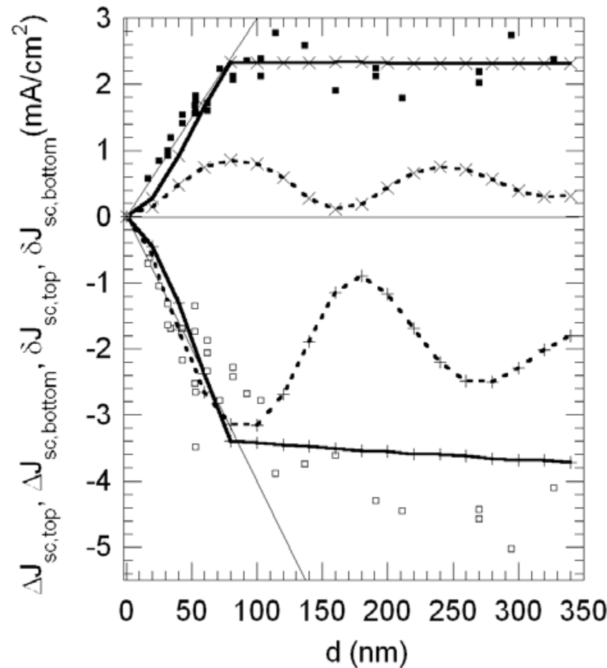

Fig. 7.6: Experimental gain $\Delta J_{sc,top}$ (closed squares) and loss $\Delta J_{sc,bot}$ (open squares) in the current densities of top (180 nm) and bottom (1.8 µm) cells, respectively, as a function of ZIR thickness d. The solid lines correspond to the simulated gain $\delta J_{sc,top}$ (x) and loss $\delta J_{sc,bot}$ (+) for rough interfaces and the dashed lines correspond to the simulated results for the case of the flat interfaces. The two continuous hairlines indicate the slopes (0.3 mA/cm^2 and -0.4 mA/cm^2 per 10 nm of ZIR thickness) observed experimentally for small values of d.

Optical modeling

When d increases, the simulated gain $\delta J_{sc,top}$ in the top cell increases up to 2.3 mA/cm^2, followed by a saturation for d > σ_{rms} (80 nm). Reversely, the simulated loss $\delta J_{sc,bot}$ in the bottom cell decreases rapidly down to -3.4 mA/cm^2 for d = 80 nm and then continues to decrease less steeply (continuous lines in Fig. 7.6).

One may compare these results with those obtained for flat interfaces (verified experimentally in [Pellaton 1998b]), which demonstrate the interferential behavior of a flat ZIR but with a gain $\delta J_{sc,top}$ always smaller than the one obtained for rough interfaces (dashed lines in Fig. 7.6).

Roughness and feature size effect

With our novel surface treatment for LPCVD ZnO layers [Bailat 2006] it is now possible to successfully deposit micromorph tandem cells on rougher front TCO layers, without incurring dramatic losses in open-circuit voltage (V_{oc}) and fill-factor (FF) reported in [Feitknecht 2005]. In Fig. 7.7 we compare EQE curves of micromorph tandems and a-Si:H single junction solar cells deposited on 2 strongly different front LPCVD ZnO layers with σ_{rms} values of 69 nm and 276 nm and lateral feature sizes of 360 nm and 1.05 µm, respectively (i.e. correlation lengths of about 180 nm and 500 nm, respectively). The post-treatment time of the surface of the very rough ZnO layer is 30 minutes. For the micromorph cells a 90 nm thick ZIR layer is inserted and a back reflector is used, whereas no back reflector is used for the single a-Si:H cell. When the tandem is deposited onto the highly-textured front TCO, $J_{sc,top}$ decreases from 12.4 to 10.7 mA/cm^2 (-14%) and the sum of the J_{sc} values of top and bottom cells increases from 22.1 mA/cm^2 to 23.2 mA/cm^2 (+5%), as compared to the less textured substrate (Fig. 7.7(a)). Note that J_{sc} of the single a-Si:H cell decreases by 5%, from 13.5 mA/cm^2 to 12.8 mA/cm^2, when the cell is deposited on this TCO (Fig. 7.7(b)) with a ZnO back contact and no back reflector. The reduction in $J_{sc,top}$ corresponds to a decrease in the top cell EQE in the 500-750 nm spectral range (Fig. 7.7(a)). Whereas, when the single a-Si:H cell is deposited on the very rough TCO, a decrease of EQE is observed in the narrower range comprised between 550 and 700 nm (see Fig. 7.7(b)).

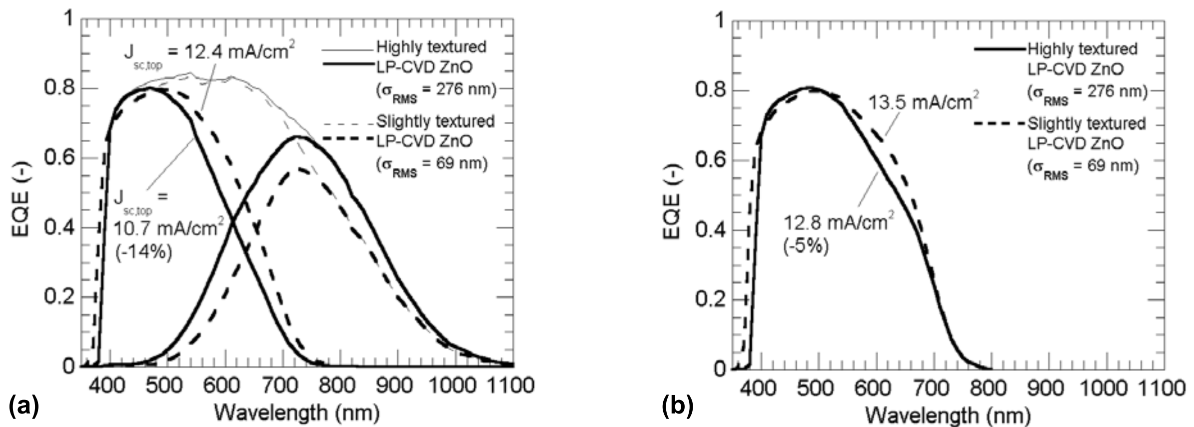

Fig. 7.7: (a) Comparison of EQE curves of devices deposited on two different front TCO layers, with σ_{rms} values of 69 nm and 276 nm. (a) EQE of a-Si:H top (180 nm) and µc-Si:H bottom (1.8 µm) cells of micromorph tandems with a 90 nm thick ZIR layer and a back reflector. (b) EQE of a-Si:H single junction cells (180 nm) without back reflector. In (a) the sums of the EQE curves of the component cells of the tandems are also plotted. One finds, for the micromorph cell: $J_{sc,top}$=12.4 mA/cm^2, $J_{sc,bot}$=9.7 mA/cm^2 for the slightly-textured TCO and $J_{sc,top}$=10.7 mA/cm^2, $J_{sc,bot}$=12.5 mA/cm^2 for the highly-textured TCO, thus $J_{sc,bot}$ increases by 29% and $J_{sc,top}$ decreases by 14% when the highly TCO is used. For the single a-Si:H cell: J_{sc} decreases by (5%), from 13.5 mA/cm^2 to 12.8 mA/cm^2, when the cell is deposited on this TCO.

Cell optimization

The linear dependence of $\Delta J_{sc,top}$ and $\Delta J_{sc,bot}$ on ZIR thickness has been experimentally observed for ZIR layers thinner than 100 nm and for front TCO layers with σ_{rms} values between 60 and 110 nm. It can be used as a design tool to determine the ZIR thickness required to obtain slightly bottom-limited micromorph tandem cells. Recall that we showed, in section 7.2, that slight bottom-limitation increases the efficiency, due to the asymmetric behavior of FF under variation of the current mismatch between the top and bottom cells.

With our standard front LPCVD ZnO layer (σ_{rms} = 80 nm) optimized for a-Si:H solar cells and with top and bottom cell thicknesses of 180 nm and 1.8 μm, respectively, we obtained, by the insertion of a 50 nm thick ZIR, a bottom-limited tandem with J_{sc} = 12.1 mA/cm^2, V_{oc} = 1315 mV and FF = 73.2%, yielding an initial conversion efficiency of 11.6%. The sum of the J_{sc} values of this tandem is 24.5 mA/cm^2.

With the new front LPCVD ZnO layers developed for μc-Si:H solar cells, the decrease in $J_{sc,top}$ has to be taken into account. Therefore, the top and bottom cell thicknesses were increased to 290 nm and 3.0 μm, respectively, and a short 10 minute surface treatment was applied to the front LPCVD ZnO. We obtained, with the 50 nm thick ZIR, a bottom-limited tandem cell with J_{sc} = 12.8 mA/cm^2 (top cell 13.2 mA/cm^2), V_{oc} = 1315 mV and FF = 70.2%, yielding an initial conversion efficiency of 11.8%. The EQE and J-V curves of the cell are presented in Fig. 7.8.

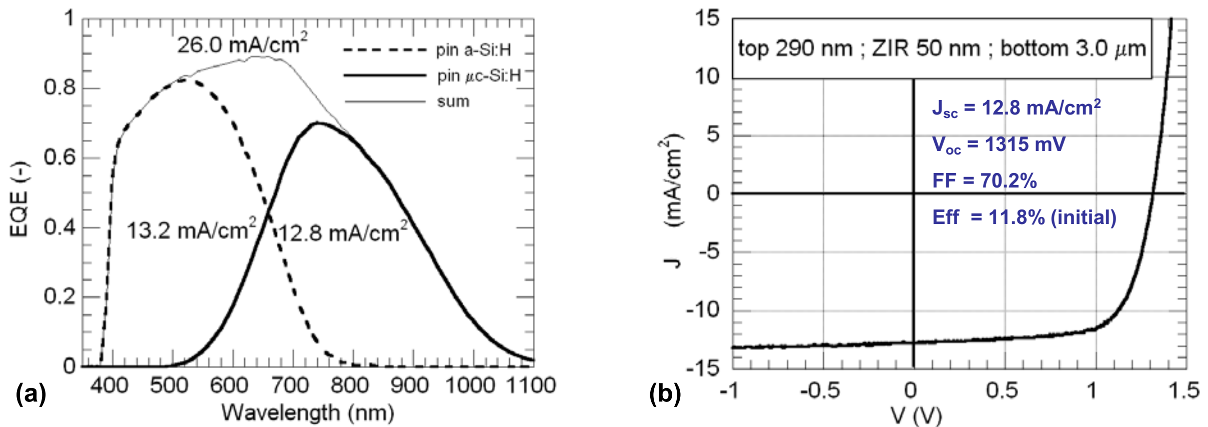

Fig. 7.8: (a) EQE curves of the top (290 nm) and bottom (3.0 μm) cells of a micromorph tandem solar cell optimized on the new front LPCVD ZnO. (b) I-V curve of the same micromorph cell as in (a).

7.3.3 Discussion of the results

ZIR thickness-effect for a given type of front ZnO

For ZIR thicknesses d<100 nm, we observed that the slopes of the linear trends for $\Delta J_{sc,top}$ and $\Delta J_{sc,bot}$ are 0.3 mA/cm^2 and -0.4 mA/cm^2, respectively, per 10 nm of ZIR thickness. These values are useful for the prediction of the top and bottom current

densities when varying d. A ZIR thickness larger than 100 nm may not be favorable as the loss $\Delta J_{sc,bot}$ then gets continuously larger.

Optical modeling

The three-layer EMA model for thin ZIR succeeds in predicting a gradual change in $\delta J_{sc,top}$ and $\delta J_{sc,bot}$ when d increases up to the σ_{rms} value of the interfaces. This is because $\tilde{n}_2$, the effective refractive indexes of zone (2) of the a-Si:H/ZIR/μc-Si:H region, continuously decrease when d increases. The discontinuity obtained when the value of d reaches the value of σ_{rms} is obviously produced by a discontinuity in the model, since $\tilde{n}_2$ reaches its minimum value and stops changing at this point.

A wavelength-dependent EMA model may be better suited to addressing the situation arising with rougher interfaces, with very large σ_{rms} and lateral feature size values (see next section).

Roughness and feature size effect

The gain of 5% obtained for the sum of the J_{sc} values of the tandem with rougher front ZnO surfaces (see Fig. 7.7(a)) is the consequence of enhanced light-scattering effects in the infrared part of the spectrum (relations (6.8) and (6.9) in chapter 6) but also of a decreased free carrier absorption (FCA) of the front TCO in the near infrared (NIR) part of the spectrum. This shows the substantial advantage of using the new very rough front TCO for μc-Si:H and micromorph solar cells. The relative roles of light-scattering and FCA reduction will be discussed in chapter 8. The challenge here is to overcome the reduction observed for $J_{sc,top}$ (14%) implied by the very strong increase of surface texture (σ_{rms} = 276 nm and 1.05 μm of lateral feature size).

For comparison, single-junction a-Si:H solar cells present a J_{sc} loss of only 5% when deposited on this highly-textured ZnO layer. This 5% loss corresponds to a decrease in EQE in the 550-700 nm spectral range, as shown in Fig. 7.7(b). This decrease in EQE may be caused by (i) a decrease in the effective intrinsic absorber thickness when deposited onto a very rough front TCO and (ii) a decrease of the light trapping capability in this 550-700 nm wavelength when the front TCO has very large lateral feature sizes.

In addition to (i) and (ii), another cause must be involved in the 14% reduction observed for $J_{sc,top}$ of the micromorph cell. As for the tandems deposited on both TCO the sums of EQE of the component cells are almost the same in the 500-650 nm range of wavelengths (Fig. 7.7(a)), the reduction in $J_{sc,top}$ could be linked to a decrease in the ZIR effectiveness for large values of σ_{rms} and lateral feature size. This will be experimentally investigated in section 7.5.

Note that the difference of EQE near λ = 350 nm observed in Figs. 7.7(a) and (b) is due to the Burstein-Moss shift effect in the ZnO layer: the higher the charge-carrier density in a degenerated semiconductor, the larger its optical energy gap [Burstein 1954].

Cell optimization

With the novel front LPCVD ZnO layers developed for μc-Si:H solar cells, the sum of the top and bottom cell J_{sc} values is 26 mA/cm^2, which corresponds to an improvement of 6% compared to 24.5 mA/cm^2 obtained with the thinner tandem deposited onto the front TCO layer optimized for a-Si:H cells. Matched current density of 13 mA/cm^2 is then directly achievable with the new TCO. The value of 26 mA/cm^2 was, at present, achieved with a short treatment time (10 minutes) applied to the LPCVD ZnO layer. Further increase in treatment time may possibly further improve the V_{oc} and FF values but of course will decrease J_{sc}. This is the topic of section 7.5.

7.3.4 Conclusions on the ZIR thickness series

The insertion of a ZIR layer provides a controlled gain in the current density of the top cell within a micromorph tandem. For any thickness of the ZIR layer, this gain is always larger in the case of nano-textured interfaces than in the case of flat interfaces. The maximum gain is almost 3 mA/cm^2. For a micromorph tandem with a thin a-Si:H top cell (180 nm) and a 1.8 μm thick μc-Si:H bottom cell, the insertion of the ZIR layer allowed us to achieve a J_{sc} value of 12.1 mA/cm^2.

Using our "novel" front LPCVD ZnO optimized for μc-Si:H cells, we obtained a J_{sc} value of 12.8 mA/cm^2 with a top cell thickness of 290 nm and a bottom cell thickness of 3.0 μm. This yielded an initial conversion efficiency of 11.8%, with a total current density of 26 mA/cm^2.

7.4 SOIR versus ZIR

7.4.1 Motivation

Three issues are related to the use of ZnO for the IRL:

(a) Its large in-plane conductivity ($\sigma_{//,ZIR}$) may often be large enough to induce a reduction of the V_{oc} and FF of the micromorph cell. Indeed, for the ZIR with d<300nm deposited by RF-sputtering, $\sigma_{//,ZIR} = 10^2$ S/cm, typically. According to [Okada 2007], the decrease of V_{oc} is related to the presence of shunts in the bottom cell. They provide current paths for electrons, which recombine with holes in the p layer of the bottom cell. The benefit of decreasing the in-plane conductivity of the IRL is schematically illustrated in Fig. 7.9.

(b) For micromorph module fabrication, the large in-plane conductivity of the ZIR involves a shunting of the bottom cell if the standard 3 groove laser patterning is used. Therefore, Meier *et al.* proposed the introduction of a fourth laser groove in order to use the μc-Si:H material of the bottom cell to electrically insolate the ZIR layer from the back electrode [Meier 2002]. This is illustrated in Fig. 7.10. This solution, however, decreases the active area of the module.

(c) Device fabrication processes including ZIR layer deposition are more complicated because the sample must be moved from the PECVD reactor to a LPCVD reactor or a RF-sputtering chamber for ZIR deposition and then put back in the PECVD reactor.

To solve these issues, Buehlmann *et al*. developed, at IMT, a silicon oxide based intermediate reflector (SOIR), with low in-plane conductivity [Buehlmann 2007]. Another significant advantage of this layer is that it is deposited *in situ* in the same PECVD reactor as the doped layers of the micromorph device (chamber 1 of system B, see chapter 2, section 2.1).

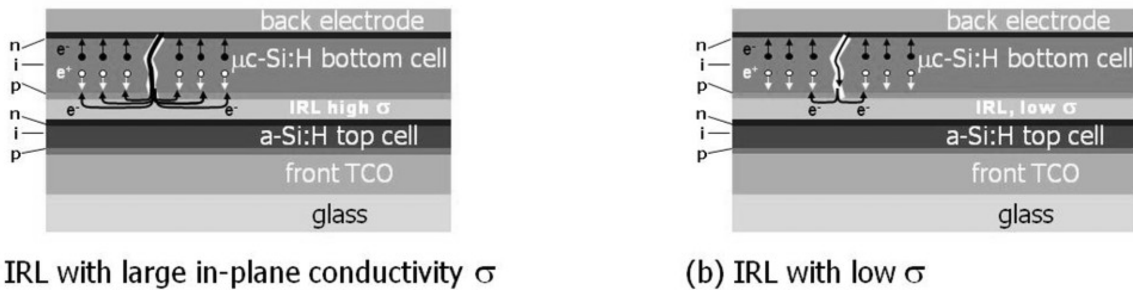

Fig. 7.9: Schematic explanation of the decrease of V_{oc} in micromorph cells with intermediate reflector (IRL). The decrease of V_{oc} follows from the presence of shunts in the bottom cell, which provide current paths for electrons (e^-) for recombination with holes (e^+) in the p-type layer of the bottom cell. The current flow of e^- through one shunt is higher in (a) than in (b) because the equivalent resistance of the shunt is smaller if the in-plane conductivity of the IRL (σ_{IRL}) allows for interaction of those e^- with a larger surface area of the p-type layer. Therefore, V_{oc} decreases less in (b) than in (a) because the smaller σ_{IRL}, the lower the rate of recombination of e^+ arrived in the p-layer with e^- arrived in the IRL from the shunt. Note that the front TCO may have the same detrimental effect as the IRL in case of shunts in the top cell. Note also that on the contrary to the case of n-i-p micromorph cells, in the case of p-i-n micromorph cells, the detrimental effect of a large σ_{IRL} could be mitigated if the shunt of the bottom cell are cured by means of selective electro-chemical etching, oxidation or reduction of the back electrode, as described e.g. in [Nath 1988]. Figure adapted from [Okada 2007].

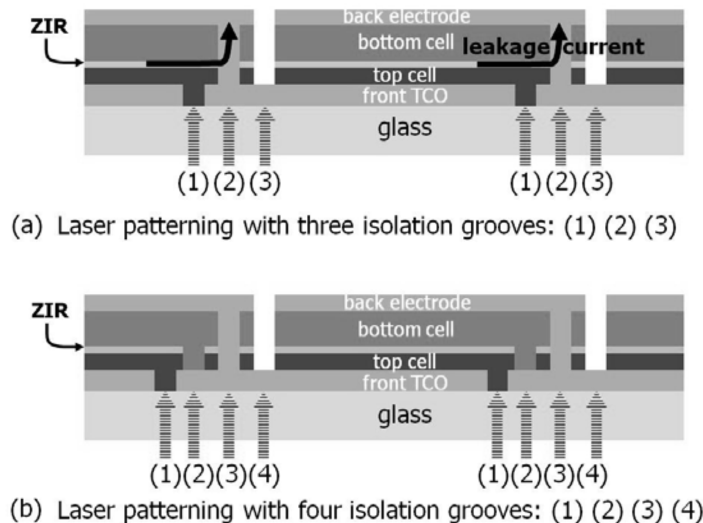

Fig. 7.10: Monolithic series interconnection of micromorph modules with ZIR. (a) Module, with a standard 3 groove interconnection, which suffers from the current leakage path between the ZIR layer and the back electrode. (b) Solution proposed by Meier et al. [Meier 2002] where 4 grooves are used: the groove (2) insulates the ZIR layer from the back electrode.

In this section, we present the results of two experiments, carried out in two deposition runs. Firstly we compare the insertion of a SOIR layer, deposited *in situ* by VHF-PECVD, versus a ZIR layer deposited by LPCVD, for two substrate morphologies. Secondly, we compare the effect of the SOIR layer and of two different ZIR layers, with medium and low in-plane conductivity, on the V_{oc} of the micromorph cell.

7.4.2 Experimental

The two deposition runs are summarized in Tables 7.3 and 7.4, in which *co-depositions* were carried out on AF45 borosilicate glass plates from Schott. The back contact of the solar cells consists of a LPCVD ZnO layer covered with a dielectric back reflector. The cell area was patterned by lift-off of the back LPCVD ZnO layer and SF_6 plasma etching of the silicon and SOIR layers (1.2 cm^2). For the cells with ZIR, an intermediate wet etching step in HNO_3 must be completed to pattern the ZIR layer. Note that in our case the IRL is n-type and does not belong to the recombination junction of the tandem. The measurement of the EQE and J-V curves is described in sub-section 7.3.2.

Front TCO layers

The front TCO layers used for deposition of the micromorph cells with ZIR and SOIR are the LPCVD ZnO:B films of Type-A and Type-C described in detail in the sub-section 7.5.2.

IRL layers

The ZIR layers are ZnO films deposited by LPCVD with DEZ and H_2O vapors as precursor gases and no addition of any doping gas, in order to keep their in-plane conductivity $\sigma_{//,ZIR}$ low (deduced from the thickness of the films and a four-point resistance measurement). The thickness of ZIR layers ranges from 57 nm to 4 µm. Two deposition temperatures are used in order to compare ZIR layers with different values of $\sigma_{//,ZIR}$. With the standard deposition temperature (around 170°C), $\sigma_{//,ZIR}$ = 1 S/cm for a 300-nm-thick ZIR layer. By adapting the temperature of deposition, $\sigma_{//,ZIR}$ is decreased down to 10^{-6} S/cm for this thickness.

The SOIR layers were deposited by VHF-PECVD, with a plasma excitation frequency of 110 MHz, from a mixture of SiH_4, CO_2 and PH_3. The index of refraction of the SOIR is tuned by adjusting the CO_2/SiH_4 gas flows ratio, while at the same time the *transverse* conductivity of the film is maintained to a sufficiently high value for electronic transport through its thickness (experimentally deduced from the threshold of working devices), by increasing the PH_3 content in the gas mixture. This transverse conductivity is most probably carried by nano-crystallites of silicon imbedded in an amorphous SiO_x tissue [Buehlmann 2008]. The corresponding in-plane conductivity ($\sigma_{//,SOIR}$), measured on glass, is approximately 10^{-9} S/cm [Buehlmann 2007]. The thickness of the SOIR layers ranges from 50 to 300 nm.

Table 7.3: Summary of the co-deposition run for the 1st comparison of SOIR versus ZIR, with different thicknesses d_{IRL} of the intermediate reflector layer (IRL) and two different front LPCVD ZnO layers. The in-plane conductivity $\sigma_{//}$ of the corresponding IRL is indicated. The thicknesses d_{front} and d_{back}, the carrier concentrations N [Steinhauser 2007], and the surface roughness σ_{rms} of the front and back LPCVD ZnO layers are also indicated, as well as the thicknesses d_{top} and d_{bot}, and the deposition reactor and plasma excitation frequency for the top and bottom cells.

Characteristic		**Value**					
Front LPCVD ZnO	Type	Type-A			Type-C		
	d_{front} (µm)	1.9			4.8		
	N (cm^{-3})	1.4x10^{20}			4x10^{19}		
	σ_{rms} (nm)	66			165		
Top cell	Reactor	KAI-S			KAI-S		
	Excitation freq.	40 MHz			40 MHz		
	d_{top} (nm)	180			180		
IRL	Type	SOIR	ZIR	no IRL	SOIR	ZIR	no IRL
	Dep. technique	VHF-PECVD	LPCVD	--	VHF-PECVD	LPCVD	--
	Excitation freq.	110 MHz	--	--	110 MHz	--	--
	$\sigma_{//}$ (S/cm)	10^{-9}	1	--	10^{-9}	1	--
	d_{IRL} (nm)	50, 75,	57, 85,	--	50, 75,	57, 85,	--
		120, 200,	145, 202,	--	120, 200,	145, 202,	--
		300	4000	--	300	4000	--
Bottom cell	Reactor	KAI-S			KAI-S		
	Excitation freq.	40 MHz			40 MHz		
	d_{bot} (µm)	1.8			1.8		
Back contact	d_{back} (µm)	1.9			1.9		
	N (cm^{-3})	1.4x10^{20}			1.4x10^{20}		
	White reflector	yes			yes		

Table 7.4: Summary of the co-deposition run for the 2nd comparison of SOIR versus ZIR comparison, with different in-plane conductivity $\sigma_{//}$. The corresponding d_{IRL} of the intermediate reflector layer (IRL) is indicated. The thicknesses d_{front} and d_{back}, the carrier concentrations N [Steinhauser 2007], and the surface roughness σ_{rms} of the front and back LPCVD ZnO layers are also indicated, as well as the thicknesses d_{top} and d_{bot}, and the deposition reactor and plasma excitation frequency for the top and bottom cells

	Characteristic	**Value**			
Front LPCVD ZnO	Type	Type-A			
	d_{front} (µm)	1.9			
	N (cm^{-3})	1.4×10^{20}			
	σ_{rms} (nm)	66			
Top cell	Reactor	Syst. B			
	Excitation freq.	70 MHz (a-Si:H layers) and 110 MHz (doped µc-Si:H layers)			
	d_{top} (nm)	300			
IRL	Type	no IRL	SOIR	ZIR	ZIR
	Dep. Technique	--	VHF-PECVD	LPCVD	LPCVD
	Excitation freq.	--	110 MHz	--	--
	$\sigma_{//}$ (S/cm)	--	10^{-9}	10^{-6}	1
	d_{IRL} (nm)	--	230	352	316
Bottom cell	Reactor	Syst. B			
	Excitation freq.	110 MHz (doped µc-Si:H layers) and 122 MHz (intr. µc-Si:H layer)			
	d_{bot} (µm)	3.0			
Back contact	d_{back} (µm)	4.8			
	N (cm^{-3})	4×10^{19}			
	White reflector	yes			

Optical reflectance and transmittance of SOIR and ZIR layers are measured with a Perkin-Elmer Lambda900 UV/VIS/NIR spectrometer, within a spectral range from 320 to 2000 nm. The refractive index n and the absorption coefficient α are estimated by fitting the transmittance and reflectance spectra with the software FTIR from ECN, Netherlands [Biebericher 2004].

7.4.3 SOIR versus ZIR: Results and discussion

Fitted refractive index and absorption spectra of SOIR and ZIR materials, used in the 1st experiment, are compared in Fig. 7.11. The thickness of the SOIR and ZIR layers used for characterization is 250 and 202 nm, respectively. We observe that for $\lambda = 600$ nm (a typical wavelength of interest for back-reflection in the a-Si:H top cell) the refractive index is 1.88 and 2.02 for the SOIR and the ZIR layer, respectively. At the same wavelength the absorption curves just cross, the SOIR layer becoming more transparent to red and infrared photons than the ZIR layer. However the SOIR layer is yellowish and therefore absorbs more light in the visible range of the spectrum than the ZIR.

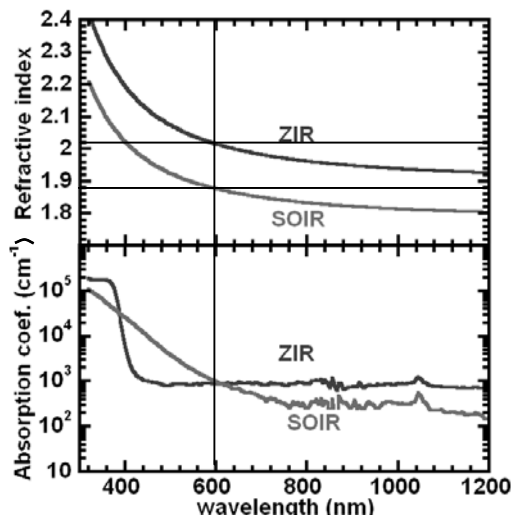

Fig. 7.11: Fitted refractive index and absorption spectra for SOIR and ZIR layers with thicknesses of 250 and 203 nm, respectively. The fit is performed from reflectance and transmittance spectra measurements with the help of the software FTIR from ECN, Netherlands [Bieberícher 2004].

The gains $\Delta J_{sc,top}$ obtained for the current density of the top cell, when IRL of different thicknesses are introduced in micromorph cells deposited on the Type-A ZnO:B layer with small feature size and on the Type-C ZnO:B layer with large feature size are exhibited in Fig. 7.12(a), for SOIR layers and in Fig. 7.12(b) for ZIR layers. Unfortunately, during this run, pressure regulation problems impaired the co-deposition of the µc-Si:H bottom cells and no reliable EQE_{bot} curves are measurable. Therefore we cannot compare the losses $\Delta J_{sc,bott}$. For the gains $\Delta J_{sc,top}$ we observe:

(1) for both types of IRL, $\Delta J_{sc,top}$ reaches a plateau,

(2) for both IRL, the maximum gain in the top cell is $\Delta J_{sc,top} = 2.4$ mA/cm^2,

(3) for both IRL, $\Delta J_{sc,top}$ is ~0.5 mA/cm^2 smaller with the rough substrate (Type-C ZnO).

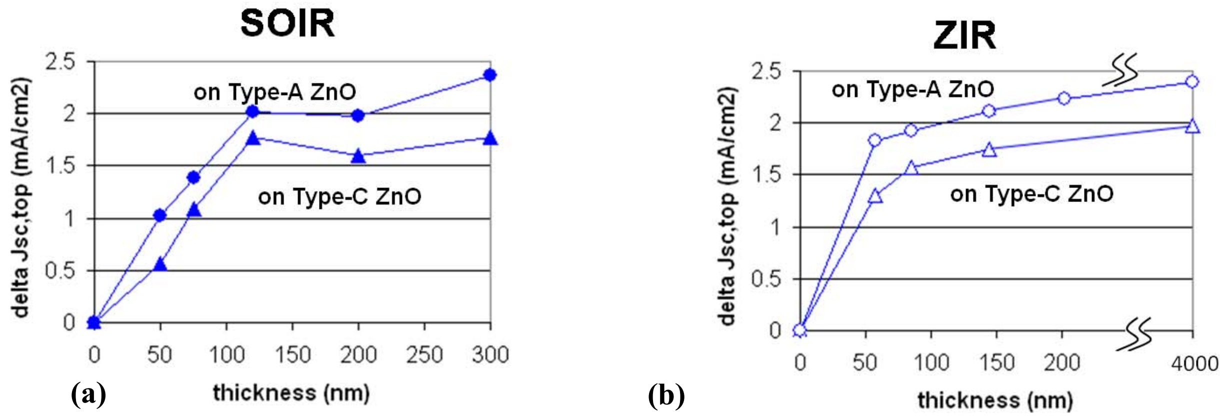

Fig. 7.12: Result of the co-deposition run, described in Table 7.3, for the 1st comparison of SOIR versus ZIR, with different thicknesses d_{IRL} of the intermediate reflector layer (IRL) and two different front LPCVD ZnO layers: $\Delta J_{sc,top}$ obtained by the insertion of (a) a SOIR and (b) a ZIR layer, when the device is deposited on a ZnO of Type-A or Type-C (see also Table 7.5). Lines are guides for the eye.

Therefore, despite of the lower refractive index of the SOIR material, when compared to ZIR, no evidence of a better effectiveness in increasing $J_{sc,top}$ is found for the SOIR layer. Observation (3) confirms the reduced effectiveness of the IRL when the surface roughness of the interfaces increases, as observed in section 7.3. This is further investigated in section 7.5.

The V_{oc} and FF of the micromorph cells co-deposited during the 2nd experiment are plotted in Fig. 7.13, where we compare devices without IRL, with a SOIR layer ($\sigma_{//,SOIR}$ = 10^{-9} S/cm), with a low conductivity ZIR layer ($\sigma_{//,ZIR}$ = 10^{-6} S/cm) and with a standard ZIR layer ($\sigma_{//,ZIR}$ = 1 S/cm). It appears that the V_{oc} of the micromorph cells without IRL, with a SOIR layer and with a highly resistive ZIR are statistically identical. However, when a standard ZIR with higher in-plane conductivity is introduced in the micromorph device, the V_{oc} is reduced by about 15 to 20 mV. We also observe that with both types of ZIR layers, the FF values are spread over a much wider range than when no IRL is inserted or when a SOIR layer deposited *in situ* is used. We suggest that the low values of FF and V_{oc} with ZIR layers are due to shunts, most probably induced by particle contamination of the sample during handling and ZIR deposition. Indeed, these lower V_{oc} and FF values correlate with smaller R_{sc} values measured under low illumination. The high FF values obtained for some cells on the sample with the highly resistive ZIR are obtained due to the fortunate absence of shunt and to the stronger bottom limitation resulting from a thicker IRL ($J_{sc,top}$ = 13.4 mA/cm^2 and $J_{sc,bot}$ = 11.6 mA/cm^2). We explain the identical FF values for the samples without IRL and with the SOIR by the fact that, when inserting the SOIR layer, the micromorph device moves from a strongly top-limited tandem ($J_{sc,top}$ = 11.2 mA/cm^2 and $J_{sc,bot}$ = 14.8 mA/cm^2) to a more moderate bottom limitation ($J_{sc,top}$ = 13.2 mA/cm^2 and $J_{sc,bot}$ = 12.0 mA/cm^2).

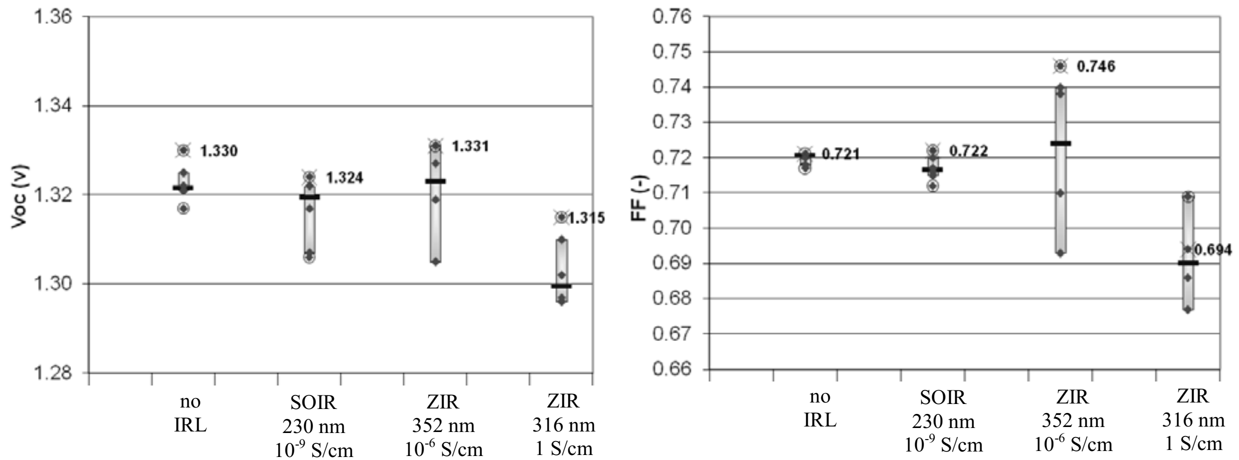

Fig. 7.13: Result of the co-deposition run, described in Table 7.4, for the 2nd comparison of SOIR versus ZIR: comparison of (a) V_{oc} and (b) FF of the co-deposited micromorph cells, without, and with, the insertion of an IRL (SOIR or ZIR with in-plane conductivity of 10^{-6} or 1 S/cm). For each of the 4 configurations, there is one substrate with 6 cells of 1.2 cm^2 surface area. The graphs display the results of the measurements in the form of "box-plots". For each set of 6 cells, the horizontal line is the median and the ends of the box are the first and third quartile of the set of data. For the cell with the best V_{oc} on each substrate, the numerical values of V_{oc} and FF are indicated.

7.4.4 SOIR versus ZIR: Conclusion

Despite of the lower refractive index of the silicon oxide based material used for SOIR deposition, no optical enhancement has been demonstrated so far in favor of SOIR, in the comparison with ZIR.

The low in-plane conductivity of the SOIR constitutes an intrinsic advantage of this layer, allowing the preservation of V_{oc} and FF if the bottom cell is moderately shunted. However, we have shown in this section that deposition of ZnO layers with low conductivity can provide the same performance, in terms of V_{oc} and best FF value.

Nevertheless, SOIR has a definitive advantage over ZIR: it is deposited *in situ* and, probably, in particle-free deposition conditions. The resulting improvement of yield is of course an advantage for industrial scale production, but also at the laboratory scale, where time saved, yield, reproducibility, and thus confidence in the results are tremendously increased when performing experiments with SOIR instead of ZIR.

7.5 Interplay between the front TCO and the IRL

7.5.1 Motivation

According to chapter 5 the electrical characteristics of the bottom cell are affected by the microstructure of the intrinsic μc-Si:H material. This microstructure depends on the plasma deposition conditions and shows that the formation of cracks and voids induced by the surface morphology of the substrate can occur during the growth [Bailat 2006, Python 2008]. We have seen in chapter 3 and in section 7.3 of the present chapter that we can

solve this issue by a change of the surface morphology of the front ZnO layer, from V- to U-shaped valleys, with a plasma post-treatment [Bailat 2006]. But we know from chapter 6 that with this post-treatment, the angular distribution function of the light transmitted through the layer will be narrower than without post-treatment. Krc *et al*. have shown by optical simulation that the angular distribution function (ADF) of light scattered at the rough interfaces of the micromorph device with IRL significantly influence $J_{sc,top}$ and $J_{sc,bot}$ and the balance between them [Krc 2006]. The plasma post-treatment of the ZnO layer can be used as a tool to change the ADF. In this section, we will therefore use this tool to experimentally study the situation.

We first analyze the light-scattering properties of different nano-textured TCO layers used as front electrodes for our p-i-n micromorph cells, incorporating a silicon oxide based IRL (SOIR) developed by P. Buehlmann [Buehlmann 2007]. Photocurrents in individual state-of-the-art cells are then compared for front TCOs with different surface morphologies. The interplay of the front TCO and IRL on the fill-factor (FF) and open-circuit voltage (V_{oc}) of the micromorph device is also discussed. Finally, we present the latest results obtained at IMT for state-of-the-art micromorph tandem cells.

7.5.2 Experimental

Front TCO layers

The front TCO layers used in this study are LPCVD ZnO:B films with two different doping levels deposited on AF45 borosilicate glass plates from Schott. The thickness of the resulting layers is adjusted to obtain a sheet resistance of about 10 Ω/sq. Their σ_{rms} values are determined by AFM in the non-contact mode. These characteristics, summarized in Tables 7.5 and 7.6 for the two sets of front ZnO layers used in this study, depend on the thickness of the layers and on the duration of the plasma post-treatment applied to their surface. By increasing the post-treatment time, the surface changes from V- to U- shaped morphology and σ_{rms} decreases.

Table 7.5: Thickness d, carrier concentration N [Steinhauser 2007], post-treatment time t_{PT}, and surface roughness σrms for the 1st set of front ZnO layers (Type-A, -B, -C).

Type of front ZnO	A	B	C
d (µm)	1.9	4.8	4.8
N (cm^{-3})	$1.4x10^{20}$	$4x10^{19}$	$4x10^{19}$
t_{PT} (min)	0	0	20
σ_{rms} (nm)	66	178	165

Table 7.6: Same as Table 7.5 for the 2nd set of Type-C (lightly-doped) front ZnO layers.

Type of front ZnO	C1	C2	C3	C4
d (μm)	4.8	4.8	4.8	4.8
N (cm^{-3})	$4x10^{19}$	$4x10^{19}$	$4x10^{19}$	$4x10^{19}$
t_{PT} (min)	60	30	20	10
σ_{rms} (nm)	122	160	169	175

Note that the Type-B ZnO (without post-treatment), whose sharp V-shaped structures prevent good electrical properties of the device, is presented only for haze measurement comparisons. The low doping level used for deposition of the thick, large grain, ZnO layers (Type-B and -C) provides high transparency in the near infrared (NIR) spectral range because of reduced free carrier absorption (FCA) [Steinhauser 2005, Steinhauser 2007].

The diffuse transmittance in-air of the different TCO layers, when light is normally incident to the glass side, is investigated by means of their haze factor H_T and by angular resolved scattering (ARS) measurements. $H_T = T_{dif}/T_{tot}$ is calculated from total and diffuse optical transmittance measurements (T_{tot} and T_{dif}) carried out with a dual-beam Perkin-Elmer Lambda 900 UV/VIS/NIR spectrometer equipped with an integration-sphere. The experimental H_T is then compared with the prediction of the scalar scattering theory (relation 6.9 of chapter 6) [Carniglia 1979]. ARS is performed with a red laser beam (633 nm) and a rotating photodetector. As in chapter 6, the intensity measured at a scattering angle θ with respect to the direction of the incident laser beam is integrated over the azimuthal angle φ, considering an isotropic scattering over φ. This provides the profile of the total transmitted intensity scattered at the angle θ per unit of solid angle [Stiebig 2000, Schulte 2007].

Fabrication and characterization of the micromorph cells

P-i-n micromorph cells and SOIR layers were deposited by VHF-PECVD. The top a-Si:H cells of the tandems presented in the first part of this study were deposited with a plasma excitation frequency of 40 MHz in a KAI-S deposition reactor from OC Oerlikon. The SOIR layers and the bottom μc-Si:H cells were deposited in a laboratory scale dual chamber deposition system (system B, see section 2.1). The VHF-PECVD process of the state-of-the-art micromorph cells was fully completed in this deposition system. One chamber is dedicated to the deposition of the SOIR and doped silicon layers at 110 MHz, whereas the a-Si:H and μc-Si:H intrinsic silicon layers are deposited in the other chamber at 70 MHz and 122 MHz, respectively. Note that the IRL is n-type and does not belong to the recombination junction of the tandem.

The last cell presented in section 7.5 was deposited on AF45 glass plates with one side covered with a broadband anti-reflection (AR) coating from Schott. A measurement of the reflectance of the AR coated glass (not shown here) indicates that the reflectivity at the

air-glass interface is smaller than 1.2% in the 400–970 nm spectral range. In agreement with this result a comparison of two micromorph cells co-deposited on AF45 glass plates with and without AR coating showed a relative increase of 3% for the sum of the J_{sc} values of the individual cells for the device deposited on the glass with this AR coating.

The back contact of the cells consists of a LPCVD ZnO layer covered with a dielectric back reflector [Meier 2005]. The cell area (~1.2 cm^2) is patterned by lift-off of the back LPCVD ZnO layer and SF_6 plasma etching of the μc-Si:H, SOIR and a-Si:H layers.

The measurement of the EQE and J-V curves is described in section 7.3.2. Curves of total reflectance (R_{tot}) of the solar cells with respect to the wavelength λ of the incident light are measured with the Lambda 900 spectrometer equipped with the integrating sphere.

7.5.3 Results for the interplay between the front TCO and the IRL

Light scattering properties of the front ZnO layers

For the TCOs presented in Table 7.5, typical SEM pictures are shown in Fig. 7.14(a) and the experimental haze factors H_T are plotted in Fig. 7.14(b) as a function of the wavelength λ of the transmitted light.

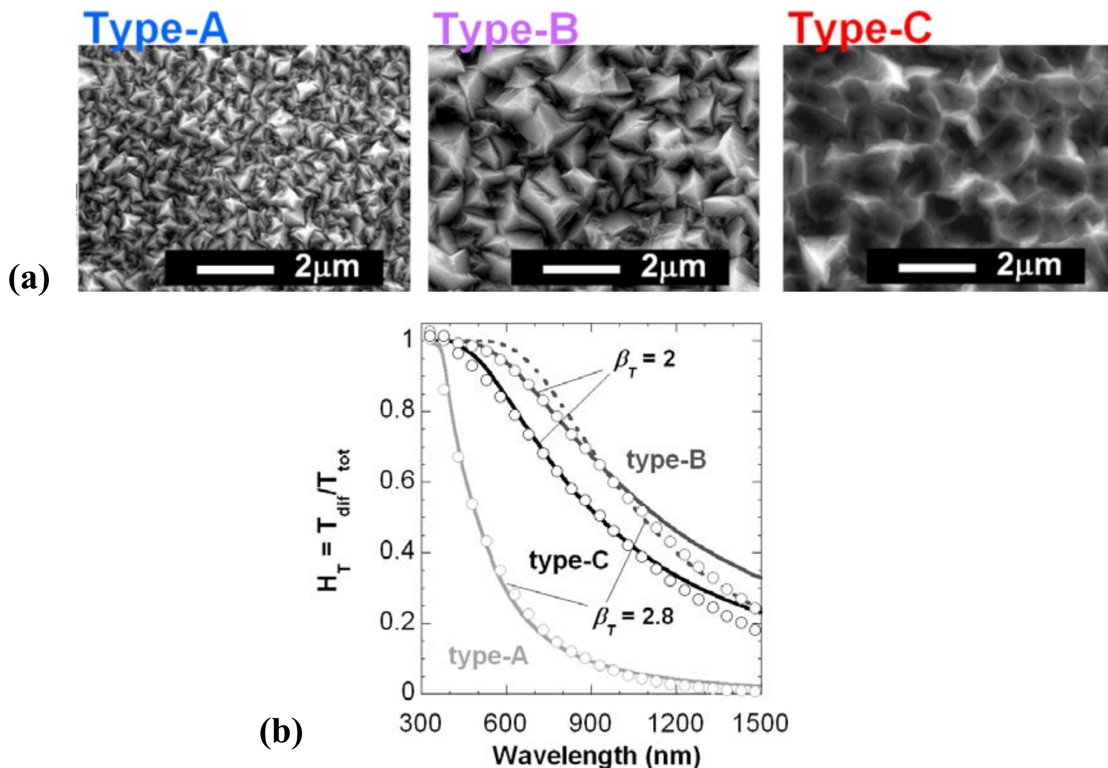

Fig. 7.14: (a) Typical SEM pictures of Type-A, -B, and -C ZnO layers presented in Table 7.5. (b) Experimental (symbols) and calculated (lines) haze, for transmission in air, through the Type-A, -B and -C front ZnO layers. The values of the fitting parameter β_T used for the calculation are also shown.

The experimental data can be fitted by the following function (the relation (6.9) already presented in chapter 6), which relates H_T to the surface roughness σ_{rms} [Stiebig 2000] [Zeman 2000]:

$$H_T(\lambda) = 1 - \exp[-(4\pi \cdot \sigma_{rms} \cdot C_T \cdot |n_1 - n_2| / \lambda)^{\beta_T}] \quad (7.1)$$

where n_1 and n_2 are the refractive indices of the incident and transmission media, respectively, and C_T, β_T are fitting parameters. The fits obtained with constant C_T values, comprised between 0.42 and 0.53 depending on the ZnO layer, are plotted in Fig. 7.14 for two values of β_T, together with the experimental results. Defining λ_{eff} as $\lambda/|n_1 - n_2|$, an almost cubic dependence ($\beta_T = 2.8$) on the factor $\sigma_{rms}/\lambda_{eff}$ in the exponential is found for the Type-A ZnO (small feature size). This is in agreement with Zeman *et al*. who found a cubic dependence on $\sigma_{rms}/\lambda_{eff}$ for H_T of Asahi U-type SnO_2:F layers (similar to Type-A ZnO) [Zeman 2000] and with Stiebig *et al*. who mentioned power factors larger than 3 for ZnO:Al layers textured by post-etching in HCl [Stiebig 2000], whereas a square dependence and $C_T = 0.5$ are predicted by the scalar scattering theory [Carniglia 1979]. For Type-B and Type-C ZnO layers (large feature size), H_T is described by a square dependence on $\sigma_{rms}/\lambda_{eff}$ for $\lambda < 900$ nm, as predicted by theory. But for larger λ, there is again an almost cubic dependence.

The spectral dependence of H_T at the internal ZnO/Si interface, as calculated from eq. (7.1) using $n_2 = 4$ for Si and the values deduced from the measurements in air for C_T and β_T, are plotted in Fig. 7.15(a). This indicates that, in a device, more than 65 %, 95 % and 100% of the light with $\lambda < 900$ nm would be diffused by ZnO of Type-A, -C and -B, respectively. For $\lambda < 700$ nm this ratio increases to 85% for the Type-A ZnO.

Angular distribution profiles (normalized to their maximum values [Schulte 2007]) of the diffuse light ($\lambda = 633$ nm) transmitted in air through Type-A, -B and -C ZnO layers are plotted in Fig. 7.15(b). This figure shows a narrower angular distribution for the light scattered by the Type-C ZnO layer, with the most probable scattering angle equal to 15°. This value is significantly smaller than with the Type-A ZnO (~40°).

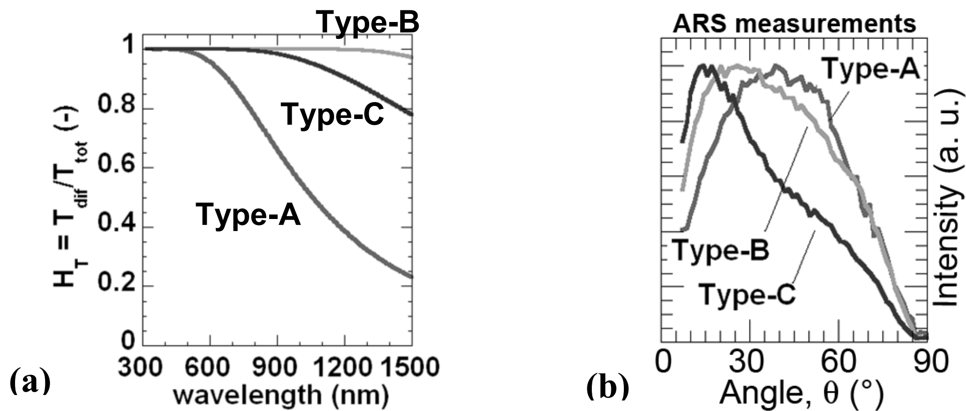

Fig. 7.15: (a) Calculated haze in transmission at the ZnO/Si internal interface for Type-A and Type-C front ZnO layers, with the values of C_T and β_T used in Fig. 7.14 for the fits. (b) Experimental angular distribution profiles of light ($\lambda = 633$ nm) diffused and transmitted in air by these TCO layers.

Optical interplay between the front ZnO and the IRL

EQEs of micromorph tandems deposited on Type-A and Type-C ZnO layers, with top cell, SOIR, and bottom cell thicknesses of 290 nm, 150 nm, and 3.0 µm, respectively, are plotted in Fig. 7.16. The sum of the J_{sc} values of the individual cells is increased by 7% from 25.0 to 26.8 mA/cm^2 when the tandem is deposited on the lightly-doped, large grain, thick ZnO layer. This is mainly produced by a relative gain in EQE in the red and NIR parts of the spectrum. However, $J_{sc,top}$ is smaller for the micromorph cell deposited on this thicker ZnO layer. This drawback, already observed with a ZIR layer, will be discussed in the sub-section 7.5.4, on the basis of the following comparison.

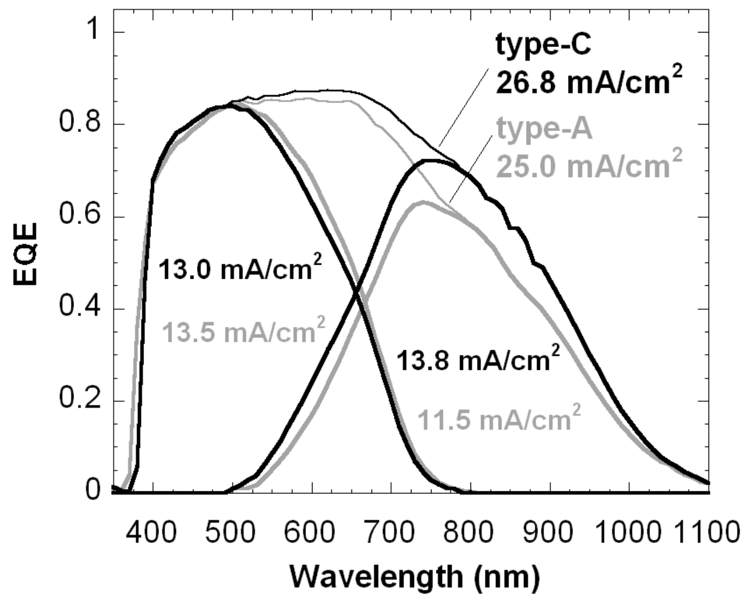

Fig. 7.16: EQEs of micromorph cells with 150 nm thick SOIR layers deposited on Type-A and Type-C front ZnO.

To explain why $J_{sc,top}$ is smaller when the Type-C ZnO layer with larger feature sizes is used as front TCO, we deposited four micromorph cells. Two cells were deposited with the insertion of a 150 nm thick SOIR layer and two cells were deposited without IRL. The deposition of these two types of device was carried out on Type-A and Type-C front ZnO layers. The EQE curves of these micromorph cells are plotted in Fig. 7.17. The striking point is that, for the two devices without IRL, the EQE curves for the top cells are almost identical. However the gain in $J_{sc,top}$ ($\Delta J_{sc,top}$) obtained by insertion of the IRL is larger when the tandem is deposited on the Type-A ZnO layer with the smaller feature size (2.6 instead of 2.1 mA/cm^2).

The influence of the SOIR thickness on $J_{sc,top}$ and $J_{sc,bot}$ is plotted in Fig. 7.18(a). The overall loss is illustrated in Fig.7.18(b), where the average of $J_{sc,top}$ and $J_{sc,bot}$, ($J_{sum}/2$), which corresponds to the maximum J_{sc} achievable for a current matched tandem, shows a decreasing trend when the thickness of the SOIR layer increases.

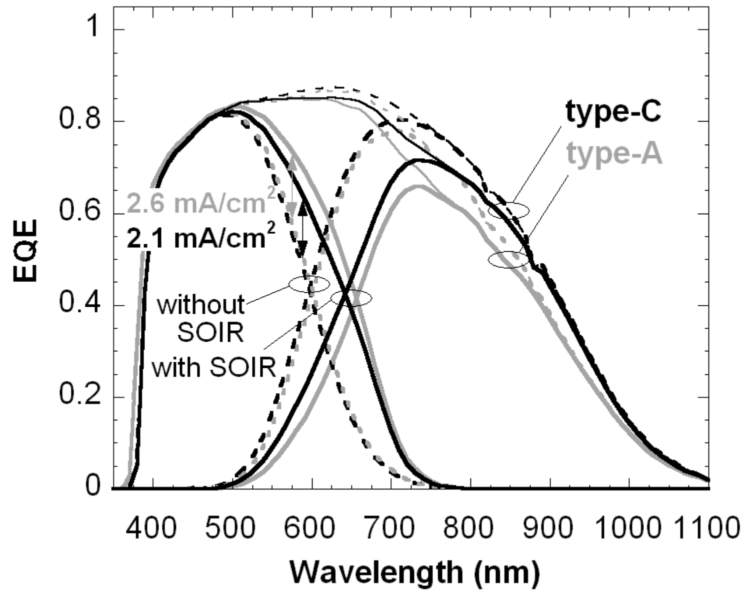

Fig. 7.17: EQEs of micromorph cells on Type-A and Type-C front ZnO with/without a 150 nm thick SOIR.

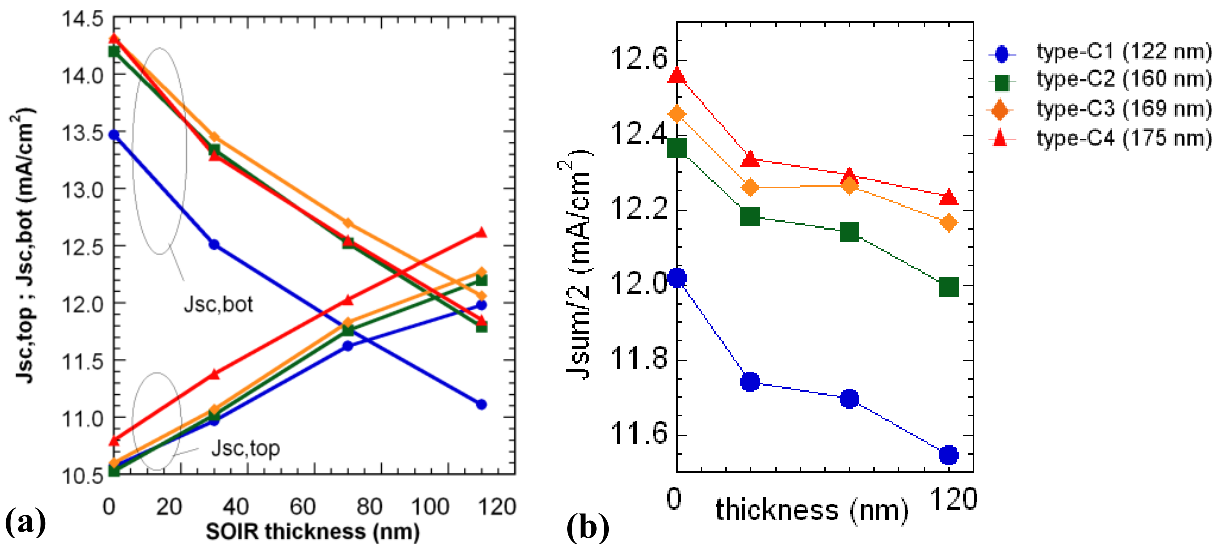

Figure 7.18: Dependence of (a) $J_{sc,top}$ and $J_{sc,bot}$ and (b) the average of $J_{sc,bot}$ and $J_{sc,top}$ on the thickness of the SOIR layer (0 nm stands for "no SOIR layer"), for micromorph cells deposited on front ZnO layers of Types-C1 to -C4 listed in Table 7.6.

We also observe, in Fig. 7.18(b), that $J_{sum}/2$ monotonically decreases when σ_{rms} of the front TCO decreases (i.e. when the post-treatment duration of the ZnO layer is increased). This follows from a monotonic (and somewhat steady) decrease of $J_{sc,top}$ and from a sudden decrease of $J_{sc,bott}$ for the longer post-treatment (see Fig. 7.18(a)).

Figures 7.19(a) and (b) show the curves of EQE_{top} and EQE_{bot}, with their sum, as well as the total absorbance ($1 - R_{tot}$) for the micromorph solar cells deposited on the Type-C1

and on the Type-C3 ZnO layers. R_{tot} is the total reflectance of the device. The corresponding gain $\Delta J_{sc,top}$ and loss $\Delta J_{sc,bot}$ in the J_{sc} of the top and bottom component cells are plotted in Fig. 7.19(c) and (d) versus the thickness d of the SOIR layer. In these figures, the origin of $\Delta J_{sc,bot}$ is divided into 3 parts: (i) the transfer of J_{sc} from the bottom to the top cell ($-\Delta J_{sc,top}$); (2) the loss by increased total reflectance R_{tot}, calculated as the difference of current density ΔJ_{Rtot}, by integration over the wavelength range, of the product of the difference of total reflectance, times the spectral density of the photon flux of AM1.5g solar spectrum; and (3) the increase of optical absorption in the doped Si layers, in the front and back TCO layers and in the IRL, calculated as the difference between $\Delta J_{sc,bott}$ and $(-\Delta J_{sc,top}+\Delta J_{Rtot})$.

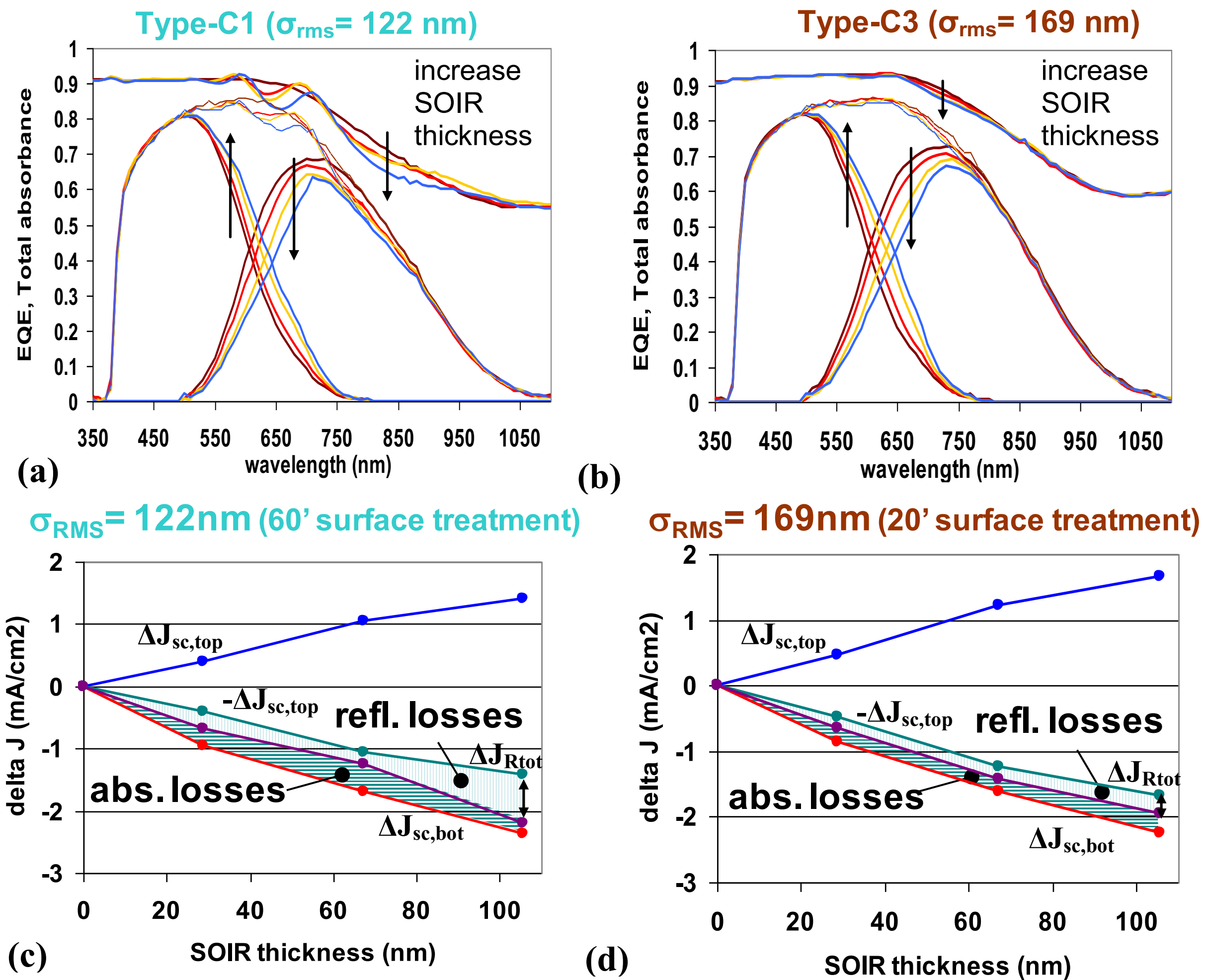

Fig. 7.19: EQE curves and total absorbance ($1-R_{tot}$) spectra for a SOIR thickness series of micromorph cells deposited on (a) Type-C1 (σ_{rms} = 122 nm) and (b) Type-C3 (σ_{rms} = 169 nm) front ZnO layers.(c) and (d) show the corresponding experimental gain $\Delta J_{sc,top}$ (blue points) and loss $\Delta J_{sc,bot}$ (red points) in the current densities of top and bottom cells, respectively, as a function of SOIR thicknes. A zero SOIR thickness stands for "no SOIR". In addition, $-\Delta J_{sc,top}$ and the loss by increased total reflectance ΔJ_{Rtot} are indicated in (c) and (d). This is for the evaluation of the loss by increased optical absorption, which corresponds to the distance between $\Delta J_{sc,bot}$ and ($-\Delta J_{sc,top}+\Delta J_{Rtot}$). The lines are guides for the eyes.

Concerning R_{tot} in Figs 7.19(a) and (b), we make two observations:

(1) The presence of the IRL produces bumps in R_{tot}, which increase in amplitude and are "red-shifted" when its thickness d increases.

(2) These bumps are significantly reduced for large σ_{rms} of the front ZnO layer (i.e. for short post-treatment of its surface).

We observe in Figs. 7.19(c) and (d) that the losses by optical absorption and by increased reflectance get larger when the thickness d increases. For the thicker IRL, these two effects contribute roughly equally to the total loss induced by the insertion of the IRL. This is the case for any thickness d and for both types of front TCO.

Curves of EQE_{top} and EQE_{bot} and of total absorbance (1 – R_{tot}) are plotted in Fig. 7.20(a), for the solar cells deposited on the Type-C1, -C2 and -C4 ZnO layers without and with the 70 nm thick IRL. These curves allow us to analyze the origin of the decrease of $J_{sc,top}$ and $J_{sc,bot}$ when the duration of the post-treatment of the ZnO layers increases.

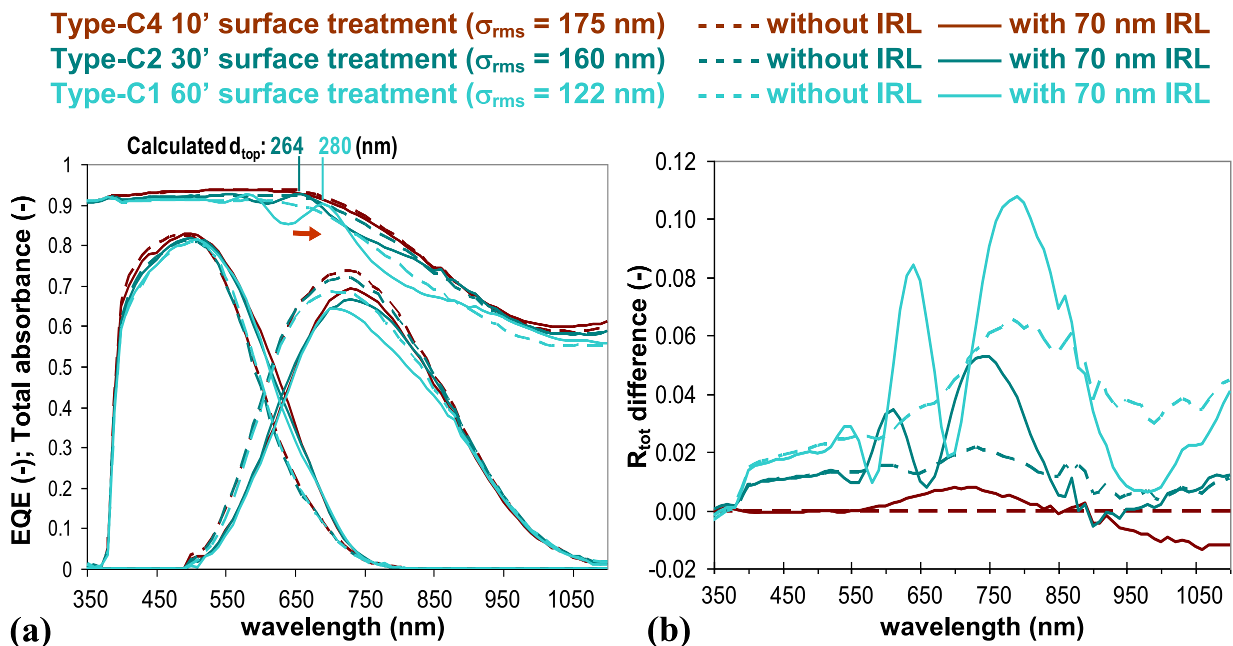

Fig. 7.20: (a) EQE curves and total absorbance (1 – R_{tot}) spectra for micromorph cells, without and with a 70 nm thick SOIR layer, deposited on Type-C1 (σ_{rms} = 122 nm), -C2 (σ_{rms} = 160 nm) and -C4 (σ_{rms} = 175 nm) front ZnO layers. (b) change of R_{tot} when compared to R_{tot} of the cell without IRL and deposited on the rougher (Type-C4) front ZnO layer. The arrow and numbers in (a) indicate a change of effective optical thickness of the top cell when it is deposited on different ZnO layers.

We draw 4 observations concerning R_{tot}, with the help of the curves (1 – R_{tot}) and of Fig. 7.20(b), on which are plotted the change of R_{tot} when compared to R_{tot} of the cell without IRL and deposited on the rougher (Type-C4) front TCO:

(a1) The increase of the post-treatment duration produces an increase of R_{tot}, which explains the decrease of $J_{sum}/2$.

(a2) For 400 nm < λ < 500 nm, this increase of R_{tot} is independent of the presence of the IRL and almost independent of λ. This points out an increase of the reflectance of the ZnO/Si interface when it gets smoother by means of surface post-treatment of the front ZnO layer.

(a3) For λ > 500 nm, the presence of the IRL produces interferential bumps in R_{tot}, which increase in amplitude and are subject to a "red-shift" when the duration of the post-treatment increases. Note that for the smoother ZnO layer, we identify 3 bumps: the first, very small, centered at λ ~550 nm; the second centered at λ ~640 nm; and the third broad one, centered at λ ~800 nm, which shifts R_{tot} by more than 10%.

(a4) For λ > 600 nm, R_{tot} of the cells deposited on the ZnO with the longer post-treatment is shifted by a further offset, independently of the presence of an IRL, which reach about +6% at λ = 800 nm.

On the basis of the above observations, we note, concerning EQE_{top} and EQE_{bot}:

(b1) The decrease of EQE_{top} for 420 nm < λ < 480 nm can be attributed in part to (a2) but absorption in the front ZnO layer and/or in the p-type layer of the top cell must contribute to the remainder of the loss of EQE_{top} in this wavelength range.

(b2) The small drops in EQE_{top} and EQE_{bot} around λ = 650 nm for the cells with IRL are produced by the second bump of R_{tot} pointed out in (a3)

(b3) The large drops in EQE_{bot} near λ = 800 nm must be attributed to (a4) and additionally to the bumps in R_{tot} (a3) for the case of cells with IRL.

Pellaton *et al*. showed in the case of flat interfaces that when an IRL is inserted in the micromorph device, the top cell behaves as a half-wavelength plate (it is indeed surrounded by material with lower refractive indexes) and, therefore, that the spectral position of the bumps of reflection is significantly influenced by the thickness of the top cell, and not only by the thickness of the IRL [Pellaton 1998a]. This would provide an explanation of the "red-shifts" of the bumps of reflectance observed in Figs. 7.19 and 7.20. Also, this provides a method to assess the effective optical thickness of the top cell when it is deposited on different ZnO layers. Considering, in Fig. 7.20, the anti-reflection effect produced by the top cell (half-wave plate) we calculate a decrease of the effective optical thickness of the top cell (300 nm nominal) from 280 nm to 264 nm when σ_{rms} increases from 122 nm to 160 nm.

Influences of the front TCO and IRL on the electrical properties of the device

The 2nd set of Type-C, lightly-doped, front ZnO layers (described in Table 7.6) with different post-treatment durations was used for deposition of micromorph cells without and with a SOIR layer with different thicknesses.

Figures 7.21(a) and 7.21(c) illustrate the influence of the surface roughness of the front ZnO on the V_{oc} and FF of micromorph cells without and with a 70 nm thick SOIR layer. Note that the same PECVD deposition conditions were used, and no specific recipe improvement was implemented that could compensate in part the observed losses for FF and V_{oc}. Figures 7.21(b) and 7.21(d) illustrate the change in V_{oc} and FF when SOIR layers of increasing thicknesses are introduced in the device.

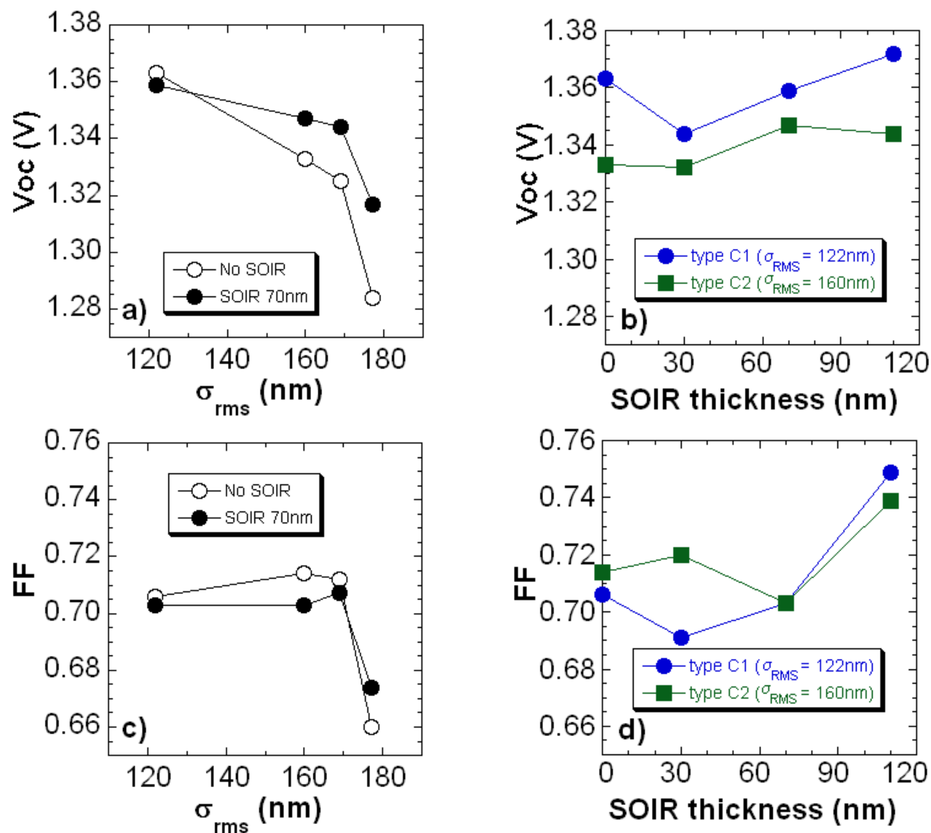

Fig. 7.21: Dependence of V_{oc} and FF (a, c) on the surface roughness (i.e. on the post-treatment time) and (b, d) on the SOIR thickness (0 nm stands for "no SOIR layer") for Type-C ZnO layers described in Table 7.6.

The results indicate that the V_{oc} drastically decreases when σ_{rms} increases (80 mV for a 55 nm increase of σ_{rms} for the cell without SOIR) but is not influenced by the presence of the SOIR layer (no trend in Fig. 7.21(b)). In both cases, optimums values of σ_{rms} (i. e. optimums post-treatment times) maximize the FF (Fig. 7.21(c)). Figure 7.21(d) indicates that, when the thickness of the SOIR layers increases, the FF value of the micromorph cells suddenly increases from about 70% to 74-75%.

Micromorph cell optimization

Further optimization of our state-of-the-art micromorph device consists of choosing the best post-treatment for the lightly-doped front ZnO in terms of high V_{oc} and good $J_{sc,bot}$ values and, for a given 300 nm thick top cell, possibly adapting the thicknesses of the SOIR layer and bottom absorber to obtain a bottom-limited tandem with J_{sc} close to 13 mA/cm^2. The J-V characteristics of our best light-soaked micromorph cell in the initial state and after 1000 h of light-soaking at 50 °C are plotted in Fig. 7.22. It was deposited on AF45 glass plates (without AR coating) covered by a Type-C2 front ZnO layer. The bottom absorber and the SOIR layer thicknesses are 3.0 µm and 150 nm, respectively, providing a bottom-limited tandem ($J_{sc,top}$=13.3 mA/cm^2) with a J_{sc} value of 12.7 mA/cm^2. The initial conversion efficiency of this cell was 12.6%. After light-soaking it stabilized at 11.1%.

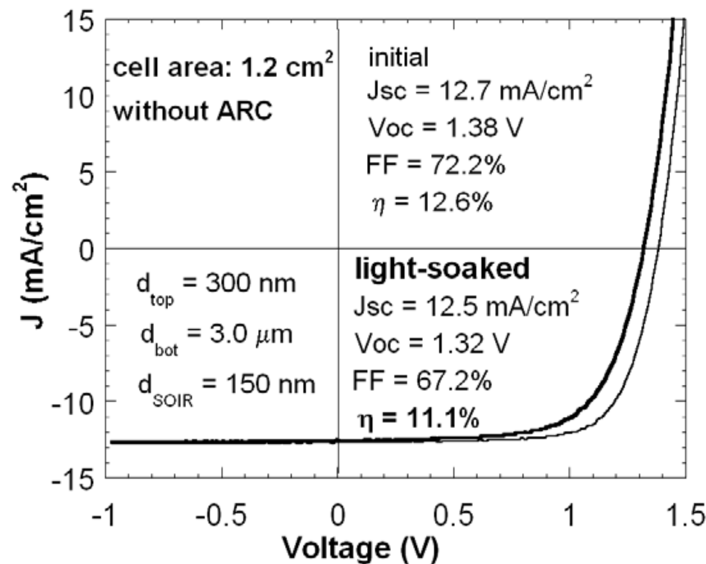

Fig. 7.22: J-V curves of a micromorph cell deposited on a lightly-doped, large grain, thick LPCVD ZnO layer in the initial state and after 1000 h of light soaking.

To reach initial conversion efficiencies close to 14% a further increase of J_{sc} towards 14 mA/cm^2 is needed. Therefore we deposited our device on AF45 glass plates covered with the broadband AR coating from Schott. Together with an increase of the bottom cell thickness to 3.5 µm, this permitted an increase in the sum of the J_{sc} of the component cells from 26.0 mA/cm^2 to 27.7 mA/cm^2 (+6.5%). The current matching was obtained with a top cell thickness increased to 340 nm. The J-V and EQE curves of the resultant micromorph cell are plotted in Fig. 7.23. This tandem is slightly top limited with a remarkably high value of 13.8 mA/cm^2 for J_{sc} ($J_{sc,bot}$=13.9 mA/cm^2) and yields an initial conversion efficiency of 13.3% (V_{oc}=1.36 V, FF=70.8%).

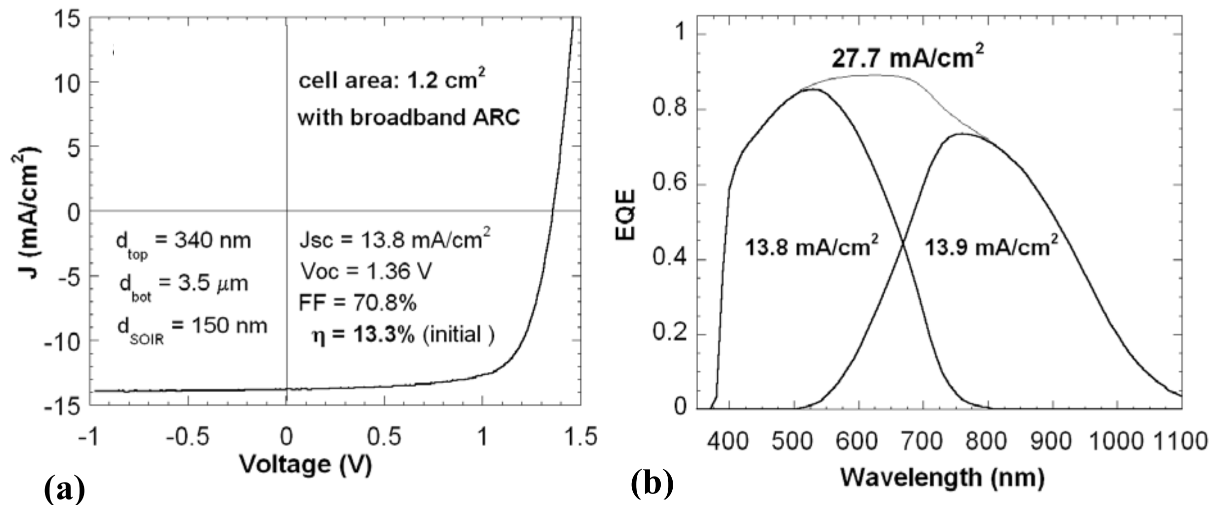

Fig. 7.23: (a) J-V curve of IMT's most recent micromorph cell deposited on a glass substrate with antireflection coating (ARC). (b) EQE curves of the top and bottom cells of the same micromorph cell as in a).

7.5.4 Discussion of the results

Light scattering properties of the front ZnO layers

Assuming that ARS in air is relevant to predict the ZnO/Si internal interface behavior [Krc 2002], the broader angular distribution produced by the Type-A ZnO, compared to Type-C (Fig. 7.15(b)) offsets the slightly lower H_T value at an internal ZnO/Si interface for $\lambda < 700$ nm (Fig. 7.15(a)). We showed in chapter 6 that ARS is the pertinent measurement method to predict the effectiveness of the light scattering produced in Si by different front TCO layers. Our calculations indicated that ARS trends at a semi-infinite ZnO/Si interface can be compared to ARS measurements performed in air, keeping in mind that the ARS profiles in silicon are actually shifted towards smaller scattering angles (compare Figs. 6.13(b) and (d) in chapter 6). This explains why the less diffusive Type-A ZnO is actually more suited for light trapping in a-Si:H single junction solar cells than the Type-C ZnO, as observed for similar ZnO layers in section 7.3, for the 550-700 nm spectral range.

Optical interplay between the front TCO and the IRL

Likewise for the micromorph cells with ZIR presented in section 7.3, the gain of EQE obtained in the red and NIR parts of the spectrum when micromorph cells are deposited on Type-C ZnO is the consequence of the lower FCA and of the larger H_T for long wavelengths of the thick and lightly-doped ZnO layer. The relative roles of the larger H_T and lower FCA will be discussed in chapter 8. It was shown in chapter 3 that ARS profiles are more relevant than H_T measurements to assess the light-scattering capability

of a front TCO. As the ARS profile is narrower for the Type-C than for the Type-A ZnO (Fig. 7.15(b)) a major contribution by the FCA is suspected.

When an IRL is inserted, losses due to an increased total reflectance of the cell occur, as indicated by the sum of EQE_{top} and EQE_{bot} curves in Figs. 7.16 and 7.19(a,b) and by the decrease of $J_{sum}/2$ in Fig. 7.18(b). If the device is deposited on a rougher substrate, we see in Fig. 7.19(b) that these losses can be mitigated. It is worth emphasizing that the position of the peaks of reflectance can be tuned by changing the thickness of the top cell [Okada 2003].

A change in the optical reflection at the ZnO/Si interface, partly by means of index grading, is observed in Fig. 7.20 for different post-treatment durations of the surface of the front TCO, as reported by Buehlmann *et al*. in [Buehlman 2007]. This anti-reflection effect will be discussed in chapter 8.

The striking point in the comparison of EQE curves plotted in Fig. 7.17 is that the EQE_{top} curves for the two devices without IRL are almost identical, despite of the very different light-scattering properties measured in air for the ZnO layers of Type-A and Type-C (see Figs. 7.14 and 7.15(b)). We suggest the following explanation. When no IRL is inserted, the fraction of light in the 550-700 nm spectral range not absorbed in the top cell during the first pass, travels only once through the micromorph cell because of absorption in the thick bottom cell. This makes ineffective a possibly better light scattering capability of the front TCO in this wavelength range, because even if the critical angle of total internal reflection is reached, no light trapping will be promoted in the top cell. Therefore, for micromorph cells without IRL, light absorption in the top cell is not strongly linked to differences in the surface morphology of the different front TCO layers used in this study. Conversely, there is an improvement shown in Figs. 7.16 and 7.17, of EQE_{top} in the 550-700 nm spectral range when a micromorph cell with IRL is deposited onto the Type-A ZnO layer. It is accounted for by the sufficient H_T (>85%) for wavelengths shorter than 700 nm combined with a broader angular distribution of the transmitted light scattered at this ZnO/Si interface. This enhances the light trapping promoted by the IRL in the top cell and, in turn, produces the improvement of the IRL effectiveness observed in Fig. 7.17. In other words, the IRL *promotes* the light trapping capability of the front TCO in the top cell.

Note that in the experiments and calculations on front ZnO layers with double-texture presented in chapter 6, no link was found between ARS and EQE_{top} of a micromorph cell with IRL. So far we identify only one common technological characteristic shared by the micromorph cells with an improved effectiveness of the IRL and therefore an improved EQE_{top}: *no or very short (<5 min) surface post-treatment was applied on the surface of their front ZnO layer*. As already stated in chapter 6, we expect that sharp structures beneficial to the light trapping in the 550–700 nm wavelength range of interest for the top cell are not smoothed in case of very short post-treatment of the surface of the ZnO. In other words, we believe that when an IRL is introduced in the micromorph tandem, this is

actually the "near-field ARS" in the top a-Si:H cell, which is significant for an efficient light trapping in the top cell. We expect that a broad "far-field ARS", as experimentally observed in-air for the Type-A ZnO discussed in this chapter, will produce a decent "near-field ARS" in the top cell. But a narrow "far-field ARS" measured in air may also produce a broad "far-field ARS" in the top cell, as it seems to be the case with the ZnO layer with double-texture presented in chapter 6.

Influences of the front TCO and IRL on the electrical properties of the device

The drastic decrease observed for V_{oc} when σ_{rms} increases (i.e. when the duration of the post-treatment of the front ZnO layer is reduced) can be related to a decrease of the V_{oc} of the individual cells of the tandem [Dominé 2006]. For the behavior of V_{oc} with the insertion of SOIR layers with different thicknesses, no influence can be deduced from Fig. 7.21(b).

The complicated behavior of FF with the variation of σ_{rms} in Fig. 7.21(c) is produced by competing influences of electrical quality for the bottom μc-Si:H cell and of current matching in the tandem. Indeed, when σ_{rms} decreases with increasing post-treatment time of the front ZnO, the FF tends to be enhanced by the improved quality of the μc-Si:H material, whereas it tends to be decreased when the current mismatch in the tandem decreases (see J_{sc} values in Fig. 7.18(a)).

Likewise, we suggest that the dramatic increase of FF observed in Fig. 7.21(d) with the thicker SOIR layers is caused by the current mismatch in the tandems going from top-limited to bottom-limited conditions (see J_{sc} values in Fig. 7.18(a)). Indeed, we calculated in section 7.2 that the increase in FF is larger in case of current-mismatch towards bottom-limitation.

Micromorph cell optimization

After light-soaking, the relative reduction of the performance of the bottom-limited micromorph cell with a top cell thickness of 300 nm is 12%. Since micromorph cells with stable V_{oc} under light-induced degradation have been demonstrated [Meier 2003], the relative decrease of 4% for the V_{oc} observed in this study should be avoidable. It is not fully understood yet and is briefly discussed later.

Note that for the top limited micromorph cell with a 13.3% initial efficiency, we have to be careful, due to the increased thickness of the a-Si:H absorber (340 nm), of an expected light-induced degradation higher than 12%.

The remarkably high J_{sc} value (13.8 mA/cm^2) achieved for this tandem demonstrates, however, the excellent collection efficiency of the carriers photogenerated in our relatively thick (3.5 μm) intrinsic μc-Si:H absorber. This result gets us a step closer to obtain J_{sc} values above 14 mA/cm^2, a prerequisite towards 14% micromorph cells.

7.5.5 Conclusions on the interplay between the front TCO and the IRL

In summary, we showed that an intermediate reflector layer is essential in micromorph cells to take fully advantage of the light scattering capabilities of front TCO layers in the 550-700 nm spectral range. We demonstrated a gain in $J_{sc,top}$ of 2.6 mA/cm^2 with a SOIR layer deposited *in situ*. This gain is comparable to previous results with an *ex situ* ZnO layer (2.8 mA/cm^2, see section 7.3). The gain is slightly larger for micromorph cells deposited on front ZnO layers with small feature size and short post-treatment of the surface, because of the broader angular distribution of the light scattered by this diffuser. However, when lightly doped, thick front ZnO layers with large feature size are used as front TCOs, higher $J_{sc,bot}$ values are achieved. This is due to the low FCA and large haze in the NIR of these TCOs. With a 3.0 µm thick µc-Si:H absorber and without any AR coating, $J_{sc,top} + J_{sc,bot} = 26.8$ mA/cm^2 has been obtained.

This study also highlights a complicated interplay between morphology of the front TCO and thickness of the SOIR layer in determining FF value and current matching conditions in micromorph cells. Post-treatment for the front ZnO allowed us to optimize these parameters and the best device (1.2 cm^2 and no AR coating) is a bottom-limited micromorph cell with 11.1% stabilized conversion efficiency.

By increasing the bottom cell thickness to 3.5 µm and using glass substrates with a broadband AR coating, a J_{sc} value of 13.8 mA/cm^2 is achieved. This remarkably high current density yields 13.3% initial conversion efficiency and makes an important contribution in paving the road towards 14% micromorph cells.

7.6 Intermediate reflector for high stable efficiencies: Proof of concept

7.6.1 Motivation

In our quest for micromorph tandem cells with J_{sc} values close to 14 mA/cm^2, we have made use of an IRL to keep the thickness of the top cell reasonably thin and therefore mitigate the Staebler-Wronski effect. However, as shown in section 7.5, the introduction of the IRL induces losses by additional absorption and an increase of R_{tot}. Therefore, it has to be proven that if an IRL is introduced in the device, the benefits of a thinner top cell balance the losses in $J_{sum}/2$. For this purpose, we compare two “high J_{sc}” micromorph cells in initial and light-soaked states: one without and one with an IRL. To make sense, this comparison involves micromorph cells with similar initial J_{sc} values.

7.6.2 Experimental

The micromorph cell with IRL is the device with 13.3% initial conversion efficiency presented in section 7.5, deposited on a AF-45 glass plate with broadband AR coating and a Type-C2 front ZnO layer. The IRL is a 150 nm thick SOIR. The cell without IRL is deposited on the same substrate and the thickness of its top cell is adapted in order to achieve similar J_{sc} values. For this, it was necessary to double that thickness from 340 to 680 nm. The bottom cells of both tandems are co-deposited in the same deposition run. The thickness of the component cells and the IRL are given for comparison in Table 7.7. J-V and EQE curves are measured before and after 955 h of light-soaking at 50 °C.

Table 7.7: Thicknesses d_{top}, d_{SOIR} and d_{bot} for the two micromorph cells with/without IRL compared in section 7.6.

Type of front ZnO	thin top, with SOIR	thick top, no SOIR
d_{top} (nm)	340	680
d_{SOIR} (nm)	150	-
d_{bot} (µm)	3.5	3.5

7.6.3 Results and discussion

In Fig. 7.24(a) we compare the EQE curves of the two micromorph cells in their initial state. The EQE curves in the initial and in the degraded state are compared in Figs. 7.24(b) and 7.24(c), for the device with a thick top cell and no SOIR and for the device with a thin top cell and a SOIR, respectively. The corresponding J_{sc} values for the top and bottom cells, deduced from the EQE measurements, are compiled in the tables next to the EQE curves, together with the J-V curves parameters of the micromorph devices .

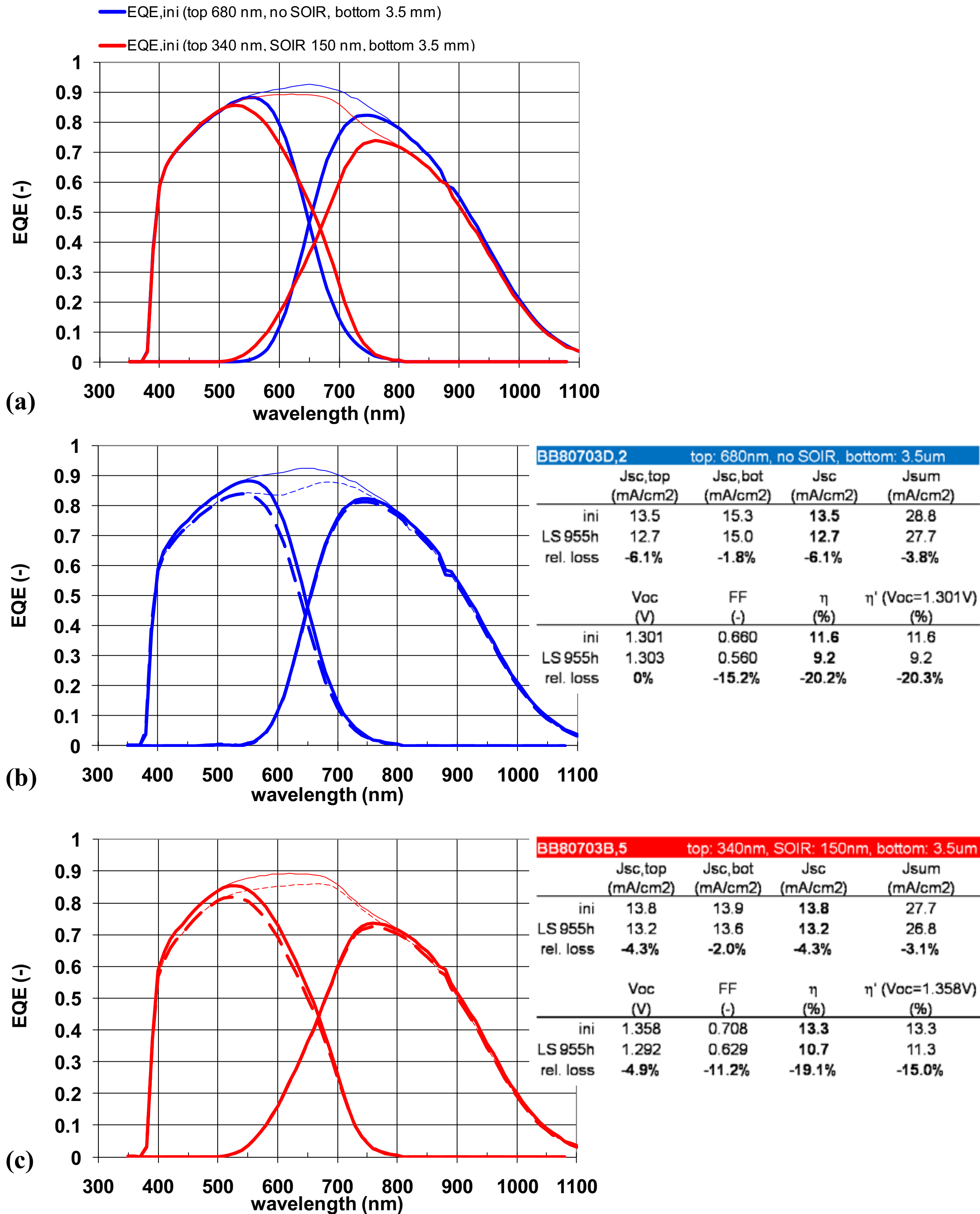

	Jsc,top (mA/cm2)	Jsc,bot (mA/cm2)	Jsc (mA/cm2)	Jsum (mA/cm2)
ini	13.5	15.3	13.5	28.8
LS 955h	12.7	15.0	12.7	27.7
rel. loss	-6.1%	-1.8%	-6.1%	-3.8%

	Voc (V)	FF (-)	η (%)	η' (Voc=1.301V) (%)
ini	1.301	0.660	11.6	11.6
LS 955h	1.303	0.560	9.2	9.2
rel. loss	0%	-15.2%	-20.2%	-20.3%

	Jsc,top (mA/cm2)	Jsc,bot (mA/cm2)	Jsc (mA/cm2)	Jsum (mA/cm2)
ini	13.8	13.9	13.8	27.7
LS 955h	13.2	13.6	13.2	26.8
rel. loss	-4.3%	-2.0%	-4.3%	-3.1%

	Voc (V)	FF (-)	η (%)	η' (Voc=1.358V) (%)
ini	1.358	0.708	13.3	13.3
LS 955h	1.292	0.629	10.7	11.3
rel. loss	-4.9%	-11.2%	-19.1%	-15.0%

Fig. 7.24: Comparison of external quantum efficiency (EQE) curves of micromorph solar cells without (with) SOIR and a thick (thin) top a-Si:H cell in the initial state and after 955h of light soaking (LS). (a) Comparison of EQE curves of the two micromorph devices in the initial state. (b-c) Comparison of the EQE curves before (lines) and after LS (dashed lines) for (b) the micromorph without SOIR and a thick (680 nm) top cell; and (c) for the micromorph with a SOIR and a thin (340 nm) top cell. In the tables, the corresponding current densities ($J_{sc,top}$ for the top cells, $J_{sc,bot}$ for the bottom cells, J_{sc} for the micromorph devices and J_{sum} = $J_{sc,top}$+$J_{sc,bot}$) are indicated with their relative degradations. Additionally, V_{oc}, FF and η are indicated, with their relative degradations. The hypothetical efficiency η' which would be obtained if a stable V_{oc} was achieved is indicated for comparison.

The initial values of $J_{sc,top}$ for the cells without and with SOIR are 13.5 and 13.8 mA/cm^2, respectively, hence they are fairly comparable, with a relative difference of only 2%. It is interesting to note, in Fig. 7.24(a), the differences in the shape of the curves EQE_{top}. They start to depart from each other for $\lambda > 510$ nm because with the thin top cell and the SOIR, a fraction of the photons with a wavelength larger than 510 nm are transmitted and absorbed into the bottom cell, whereas the totality of photons with $\lambda < 550$ nm are absorbed within the 680-nm-thick top cell. The effect of the SOIR is to decrease the rate at which EQE_{top} drop off when λ increases in the spectral range of weak absorption of a-Si:H. Without SOIR, the sum of $J_{sc,top}$ and $J_{sc,bot}$, is 28.8 mA/cm^2. Therefore, a micromorph with J_{sc} = 14.4 mA/cm^2 could in principle be achieved with a further (but not recommended) increase of the thickness of the top cell. With the SOIR, this sum of J_{sc} is reduced by 1.1 mA/cm^2 to 27.7 mA/cm^2. Thus, a relative loss of 4% is induced by the additional total reflectance and the absorption discussed in section 7.5. It mainly occurs in the 550–950 nm spectral range, as seen in Fig. 7.24(a).

Compared to the device with the thin top cell, the tandem with the thick top cell has a very low initial FF value (FF = 0.660). This is mainly due to collection losses because of the weaker electric-field in such a thick (680 nm) top cell. Therefore, also for devices in the initial state, the IRL is compulsory to achieve “high J_{sc}” micromorph cells with decent FF values. The initial efficiency is only 11.6% when no SOIR is used whereas it is 13.3% when a SOIR is used. This represents an improvement of 15% of the initial conversion efficiency.

After degradation, the decrease of the collection efficiency χ of the top cell (eq. (7.6)) induces a drop in EQE_{top} which is more obvious in the sum of EQE curves, as observed in Figs. 7.24(a) and (b). Therefore, J_{sc} decreases by -6.1% and by -4.3% for the thick and the thin top cell, respectively. For the corresponding micromorph cells, the relative losses of FF and V_{oc} are -15.2% and -11.2%; and 0% and -4.9%, respectively. These values lead to stabilized conversion efficiencies of 9.2% for the cell without SOIR and 10.7% for the cell with SOIR. This corresponds to a relative degradation of 20.3% and 19.3%, respectively.

For the device with a thick top cell and without SOIR, the V_{oc} is stable under light soaking. This indicates that the loss of V_{oc} after degradation observed here in the cell with a thin top cell and in section 7.5 is indeed due to the presence of the SOIR layer. This degradation of V_{oc} will have to be examined in detail in the future. At the moment of writing this thesis, we can only state we observed that: (1) it is not light-induced but happens also in the dark; and (2) it is influenced by the surface texture of the front TCO. We suggest that contamination through nano-cracks at the p-i interface of the bottom μc-Si:H cells, such as inferred for single junction μc-Si:H cells from the Figs. 5.6(b) and 5.7(b) of chapter 5, may produce this degradation of V_{oc}. A stable V_{oc} under light soaking is demonstrated for the micromorph cell without SOIR and was also demonstrated in [Meier 2003]. For the sake of discussion, a column is added in a Table 7.9 referring to the

cell with SOIR, where we show a hypothetical efficiency η', which would be obtained in the case of stable V_{oc}. In this case the stabilized conversion efficiency would be 11.3%, corresponding to a relative degradation of -15%, to be compared to the -20% relative degradation observed for the micromorph cell without IRL.

7.6.4 Conclusion on the proof of concept

With the experiment described in this section we show that when considering high-efficiency micromorph solar cells i.e. tandems with J_{sc} value close to 14 mA/cm^2, the thickness of the top cell of a device without IRL must be increased towards very detrimental large values. Here we needed to use a top cell thickness of 680 nm to achieve an initial J_{sc} value of 13.5 mA/cm^2.

Therefore, the insertion of an IRL is not only useful to mitigate the light-induced degradation (a reduction of the relative degradation from 20% to 15% is in principle achievable with the devices presented here) but also to avoid the poor initial FF, and therefore the low initial efficiency, due to an increase of the recombination losses by reduction of the electric-field in such a thick a-Si:H top cell.

Without IRL, the initial conversion efficiency with J_{sc} = 13.5 mA/cm^2 is 11.6% and stabilizes to 9.2%. With IRL, J_{sc} is 13.8 mA/cm^2 and yields a conversion efficiency of 13.3%. It stabilizes to the rather low value of 10.7% because of an unresolved V_{oc} degradation in presence of the SOIR layer. Anyway, the initial and light soaked conversion efficiencies, as well as the relative degradation are improved in the case of the thin (340 nm) top cell with insertion of the intermediate reflector.

7.7 Conclusions

In this chapter we tried to bring out different electrical and optical aspects linked to the introduction of an intermediate reflector layer (IRL) in the micromorph tandem solar cell. When deposited on a nano-textured substrate, the optical system constituted by this device becomes extremely complex. We have chosen an experimental approach to gain more insight on its behavior when changing the IRL thickness and the surface morphology of the front transparent conductive oxide (TCO) electrode. Our main conclusions are:

(1) We *experimentally* demonstrated that for any thickness d of the IRL (d_{IRL}), the gain in current density of the top cell ($\Delta J_{sc,top}$), when an IRL is introduced in the device, is always larger in the incoherent case of nano-textured interfaces than in the coherent case of flat interfaces with an interferential (single layer) IRL. The maximum gain achieved so far is $\Delta J_{sc,top}$ = 2.8 mA/cm^2 for a ZnO IRL (ZIR).

(2) The gain $\Delta J_{sc,top}$, increases linearly with d_{IRL} and saturates when d_{IRL} reaches a value comparable to the surface roughness of the interfaces.

(3) Conclusion (1) follows from the fact that *the IRL actually promotes the light trapping capability of the front TCO layer in the 550-700 nm spectral range*: the better this capability, the higher the gain $\Delta J_{sc,top}$.

(4) It follows from (3) that a broad angular distribution function (ADF) of the light scattered in silicon by the front TCO, as experimentally verifiable by angle resolved scattering (ARS) measurements performed in-air, will be linked to a large gain $\Delta J_{sc,top}$. However, the converse may not be true: we believe that a TCO producing a poor (narrow) in-air ARS measurement result may produce a broad near-field ADF in silicon and in turn a large gain $\Delta J_{sc,top}$ (see chapter 6, section 6.3.2).

(5) It follows from (4) that LPCVD-ZnO layers with very large surface roughness are detrimental for the effectiveness of the IRL because, to make them suitable for deposition of μc-Si:H material, we need to apply to them a post-treatment on their surface, which leads to a narrowing of the ADF of the transmitted light in silicon (see chapter 6, section 6.3.2).

Except for (1), these conclusions are, to our best knowledge, original in this field of research. We hope they will stimulate further research in the field: experimental determination of the thickness d_{IRL} at which $\Delta J_{sc,top}$ saturates for different front TCO, refinement of fundamental understanding by means of optical modeling of near-field effects, …

The electrical influence of the IRL is twofold:

(1) It influences the balance of the photocurrent between the component cells of the tandem and thus, this strongly influences the fill factor (FF) of the device, as demonstrated in section 7.2.

(2) The in-plane conductivity of the IRL can reduce Voc and FF by means of recombination of holes in the p layer of the bottom cell with electrons flowing though shunts in the bottom cell. Note that our IRL is n-type and does not belong to the recombination junction of the tandem.

Comparison of ZnO IRL (ZIR) and silicon oxide based IRL (SOIR) layers showed that providing deposition conditions to obtain a ZIR with low in-plane conductivity (10^{-6} S/cm), no fundamental evidence of an advantage of SOIR over ZIR is found. However, the practical benefit provided by the *in situ* PECVD deposition of the SOIR layer makes SOIR by far preferable to ZIR.

In this chapter we have shown that IRL is mandatory to achieve large J_{sc} values (close to 14 mA/cm^2) in micromorph solar cells without impairing FF with a detrimentally thick a-Si:H top cell. With a bottom cell thickness of 3.5 μm and using glass plates with a broadband anti-reflection (AR) coating, a J_{sc} value of 13.8 mA/cm^2 is indeed achieved. This remarkably high current density yields 13.3% initial conversion efficiency and makes an important contribution in paving the road towards 14% micromorph cells.

However the conversion efficiency of this cell stabilized to the rather low value of 10.7%. This is because the thickness of the a-Si:H absorber of this device is relatively large (340 nm) and also because the cell suffers from a degradation of the V_{oc}, induced by the presence of the IRL, but not yet fully understood. So far, the best stabilized device (1.2 cm^2 and no AR coating) is a bottom-limited micromorph cell with 11.1% stabilized conversion efficiency, including a SOIR. We expect that with proper mastering of SOIR induced degradation and further device optimization, stable efficiency above 12% should be reached soon.

8 Anti-reflection effect and light absorption in rough nano-textured front contact ZnO layers

In this chapter, we will discuss two aspects of the rough transparent conductive oxide (TCO) layers used as front electrodes in our solar cell devices: (1) the anti-reflecting effect provided by the nano-texture of its surface and (2) the losses by optical absorption in this layer.

Doing so, we will discriminate the relative roles of the increase of haze (related to the increase of the root-mean-square (rms) value of the surface roughness (σ_{rms})) and of the reduction of free carrier absorption (FCA) in the enhancement of external quantum efficiency (EQE) observed in the red and near infrared (NIR) parts of the spectrum for micromorph cells deposited on the lightly-doped, large grain, thick ZnO layer (Type-C) presented in the previous chapters of this thesis. The enhancement of EQE produces an increase of the current density (J) photogenerated in the absorber of the bottom cell of the device.

Finally we will assess the degree of enhancement of optical absorption for our devices by means of light trapping from the Yablonovitch's upper limit of $4n^2$ (chapter 6).

8.1 Experimental

<u>Samples and measurements</u>

The two sets of front TCO layers discussed in this chapter are LPCVD ZnO:B films deposited on AF45 glass plates already presented in chapters 6 and 7. For convenience, we recall their characteristics in Table 8.1 and Table 8.2. The morphology of the surface of some of these layers has been modified with the plasma post-treatment presented in chapter 3. AFM pictures of the 1st set of ZnO layers can be found in Fig. 6.7 of chapter 6.

Table 8.1: Thickness d, carrier concentration N [Steinhauser 2007], post-treatment time t_{PT}, surface roughness σ_{rms}, and characteristic morphology of the valleys for the 1st set of front ZnO layers discussed in this chapter (Type-A1 to -D1: same layers as in chapter 6). Type-A1 and -B1: no post-treatment.

Type of front ZnO	A1	B1	C1	D1
d (µm)	1.9	4.8	4.8	4.8
N (cm^{-3})	1.4×10^{20}	4×10^{19}	4×10^{19}	4×10^{19}
t_{PT} (min)	0	0	20	60
σ_{rms} (nm)	65	172	150	103
Morphology of valleys	V-shape	V-shape	U-shape	U-shape

Table 8.2: Thickness d, carrier concentration N [Steinhauser 2007], post-treatment time t_{PT}, surface roughness σ_{rms}, and characteristic morphology of the valleys for the 2nd set of front ZnO layers discussed in this chapter (Type-A2 and Type-C2: same as Type-A and Type-C discussed in chapter 7).

Type of front ZnO	A2	A3	C2	C3
d (µm)	1.9	1.9	4.8	4.8
N (cm^{-3})	$1.4x10^{20}$	$1.4x10^{20}$	$4x10^{19}$	$4x10^{19}$
t_{PT} (min)	2	10	20	40
σ_{rms} (nm)	66	n.a.	165	n.a.
Morphology of valleys	V-shape	U-shape	U-shape	U-shape

Let us recall that the low doping level used for deposition of the thick, large grain, ZnO layers provides high transparency in the NIR spectral range because of reduced FCA, even at a similar sheet resistance [Steinhauser 2005].

A 300-nm-thick a-Si:H film is deposited on the ZnO layers of the 1st set of samples (Type-A1 to -D1). Total reflectance (R_{tot}) and diffuse reflectance (R_{dif}) spectra of these samples, when light is incident on the glass side, are measured with a Perkin-Elmer Lambda 900 spectrometer equipped with an integration-sphere. The specular reflectance $R_{spec} = R_{tot} - R_{dif}$ is deduced from these experimental spectra. For the micromorph solar cells with intermediate reflector co-deposited (300-nm-thick top cell, SOIR 150 nm and 3-µm-thick bottom cell) on the 2nd set of samples (Type-A2, A3 and Type-C2, C3), R_{tot} spectra are also measured with the Perkin-Elmer spectrometer and the integration sphere.

Calculation methods

The internal quantum efficiency is defined by:

$$IQE = EQE/(1 - R_{tot}). \quad (8.1)$$

We will compare two TCOs, namely TCO' and TCO''. To evaluate the role of light trapping in the increase of current density when TCO'' is used for deposition of a solar cell instead of TCO', we calculate what the IQE will be if the absorptions losses (in the TCO) are exactly identical for the two devices deposited on those TCOs. If these absorption losses are equal, then the internal quantum efficiency IQE'' should be equal to IQE'. Therefore, from this equality and from (8.1), we can calculate what should be the external quantum efficiency EQE'' of the solar cell deposited on the TCO'':

$$EQE'' = EQE' \cdot (1 - R_{tot}'')/(1 - R_{tot}''), \quad (8.2)$$

where R_{tot}' and R_{tot}'' are the total reflectance of the devices deposited on TCO' and TCO'', respectively. In case equation (8.2) is not satisfied for two TCOs, the difference should hence be linked to a change of absorption losses in the TCO. Thus, from EQE and R_{tot} measurements, it is possible to calculate separately the contribution the enhancement of the light trapping capability to the increase of J_{sc} observed when a solar cell is deposited on the lightly-doped, large grain, thick ZnO layer (Type-C). This is done by integration over the spectral range of interest of the photon flux of the AM1.5g spectrum with the actual EQE of the cell deposited on the TCO'' and with the calculated EQE''. This gives the actual J_{sc} and the calculated J_{sc}'', which corresponds to the case of a change of light trapping capability without any change of the absorption losses. This method allows a quantitative assessment of the relative benefits of low FCA and light trapping enhancement.

The EQE and R_{tot} measurements also allow, neglecting the absorption in doped layers, the assessment of the absorbance A_{TCO} in the front and back TCO layers:

$$A_{TCO}(\lambda > 600\ \text{nm}) = 1 - R_{tot}(\lambda) - EQE(\lambda). \tag{8.3}$$

To calculate the effective light path enhancement obtained with our different ZnO layers, we will proceed in the same way as Berginski *et al*. who found an enhancement factor of 16 in μc-Si:H single junction solar cells deposited on sputtered-etched ZnO:Al front TCO layers [Berginski 2007]. On each path, part of the light trapped in the device is also absorbed in the TCO layers (and not only in silicon). Light absorbed in the TCO is lost for generation of carriers. The effect on EQE can be taken into account by the following correction [Berginski 2007, Python 2009b]:

$$EQE_{cor} = EQE/(1 - A_{TCO}), \tag{8.4}$$

which represents, in first approximation, the value the EQE would take if the TCO layers were perfectly transparent. For any wavelength λ, the light path enhancement factor m, is defined by:

$$EQE_{cor} = 1 - \exp[-m\cdot\alpha d], \tag{8.5}$$

which yields [Berginski 2007]:

$$m = -\ln(1 - EQE_{corr})/\alpha d. \tag{8.6}$$

The range of validy of (8.6) needs to be taken care of, as will be seen later.

8.2 Results and discussion

8.2.1 Reflectance measurement of glass/ZnO/a-Si:H structures

The reflectance spectra R_{tot}, R_{spec} and R_{dif} of the glass/ZnO/a-Si:H structures are plotted in Figs. 8.1(a), (b) and (c), respectively. The inset in Fig. 8.1(b) is a zoom for R_{spec} in the range of wavelengths λ comprised between 400 and 500 nm. For $\lambda > 550$ nm, the reflectance of the structure is increasing because, due to the vanishing of the coefficient of absorption α of silicon, light transmitted in the thin (300 nm) a-Si:H film is reflected back at the a-Si:H/air interface and transmitted out of the front surface of the sample. The corresponding increase in R_{tot} is exclusively related to an increase in R_{dif}. This indicates that the fraction of light intensity in the a-Si:H film which finally escapes out of the sample is totally diffuse. The interferences observed in the spectra R_{tot} and R_{spec} for the structure deposited on the Type-A1 ZnO are exclusively related to specular reflectance and are due to the smaller thickness of the ZnO layer. For photons of energy smaller than the optical bandgap of ZnO and with $\lambda < 550$ nm, the reflectance spectra relates to primary reflection and to light intensity in the ZnO layer, which finally escapes from the structure but not to light intensity transmitted to the a-Si:H film (because fully absorbed within the first light pass through the 300-nm-thick a-Si:H film). The striking observations concerning this spectral range are:

(1) For the samples without plasma post-treatment of the ZnO layer (Type-A1 with $\sigma_{rms} = 65$ nm and Type-B1 with $\sigma_{rms} = 172$ nm), a quasi negligible difference of reflectance is observed despite the very different surface roughness.

(2) This very little difference in R_{tot} is exclusively related to an increase in R_{spec} (+0.15%) for the samples with thick ZnO layers.

(3) The change of R_{tot} (2.4%) is almost exclusively related to a change of R_{dif}: the longer the post-treatment of the surface of the ZnO layer, the larger the increase of *diffuse* reflectance.

(4) A bump of reflectance is observed at $\lambda = 580$ nm for the sample with the longer post-treatment, this bump is exclusively related to T_{dif} and not to T_{spec}.

We believe that the slight change of R_{spec} noted in (2) between the Type-A1 and the other samples (+0.15%) is due to a refractive index grading effect, as modeled by the effective media approximation (EMA) [Bruggeman 1935, Landauer 1952, Tinga 1973] when the correlation length of the random surface is smaller than λ. In the wavelength range considered, light in-coupling by means of refractive index grading is slightly more effective for the Type-A1 ZnO, because of its small lateral feature size compared to the thick layers with large pyramids.

However (3) proves that, *index grading effects are not involved in the change of R_{tot} when σ_{rms} changes by means of the post-treatment of the surface of the ZnO layers.*

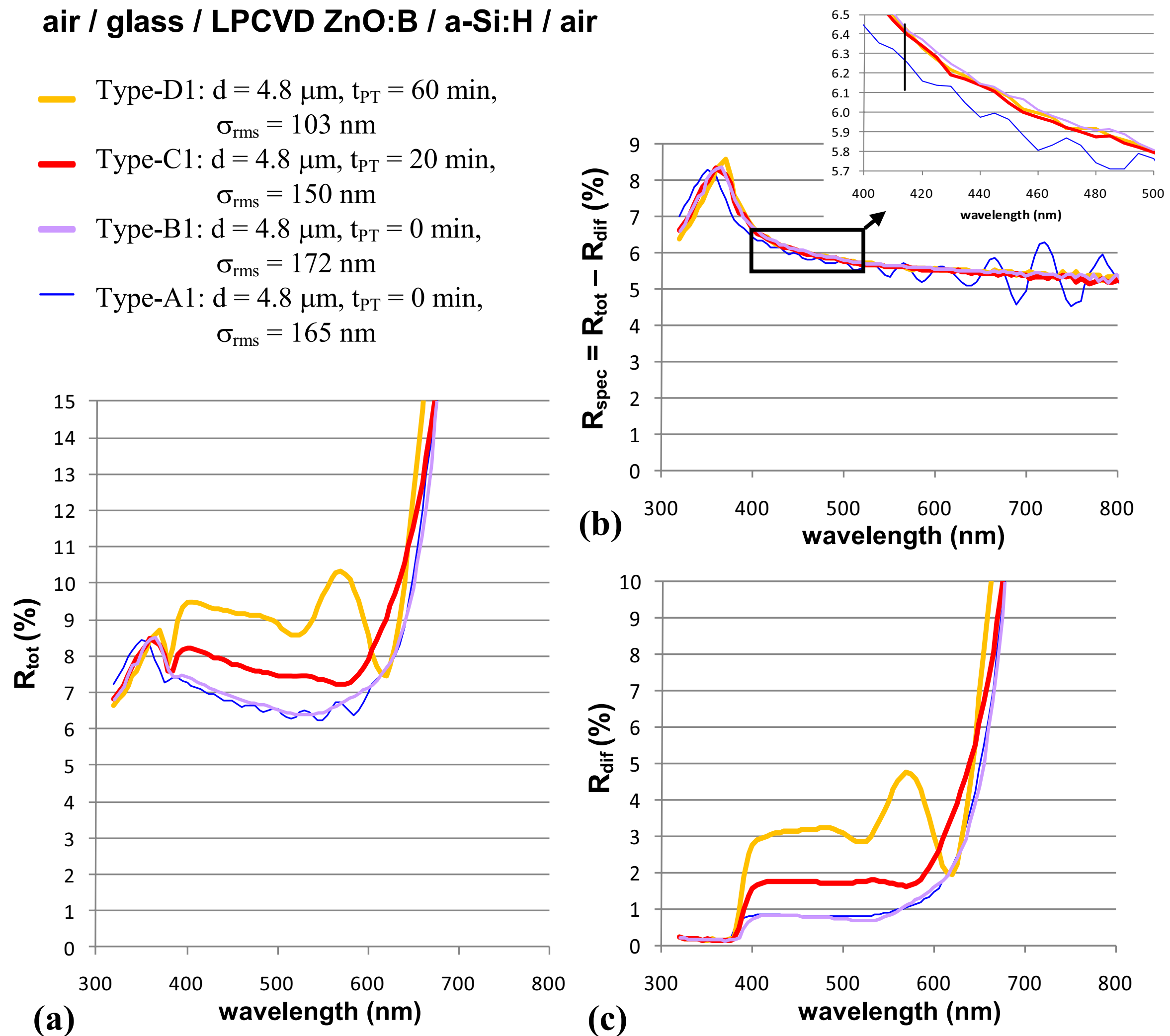

Fig. 8.1: Reflectance spectra of the structure glass/ZnO/a-Si:H, measured in air when light is incident to the glass side; with the ZnO layers of different thickness d and rms surface roughness σ_{rms} listed in Table 8.1 (Type-A1 to -D1). The specular reflectance (R_{spec}) in (b) is calculated from the measured spectra of total reflectance (R_{tot}) in (a) and diffuse reflectance (R_{dif}) in (c). The inset in (b) is an enlargement of R_{spec} in the range of wavelengths from 400 nm to 500 nm.

In view of the marginal role of refractive index grading effects in decreasing the reflectance of our nanotextured ZnO/Si interfaces, it is interesting to note that researchers devote much attention to EMA when studying reflectance of silicon thin-film solar cells (see e.g. [Hagemann 2008]). In our case, this is again the *angular distribution*, but this of the back-scattered light, that gives the major contribution in the reduction of reflectance of the rough ZnO/a-Si:H interface. Actually, the special role of a low refractive index film on top of a rough silicon surface in decreasing the reflectance has already been explained in full detail in the somewhat old but fundamental paper of Yablonovitch [Yablonovitch 1982]

where he states: "*The antireflection coating that we have been describing combines synergistically both the index matching and the texturing to take advantage of a new mechanism, namely, light trapping by total internal reflection in the thin plastic film*." In other words: the diffuse part of the primary reflection at the ZnO/a-Si:H interface can escape the sample only through the escape cone of angular width $2\theta_c = 2\cdot\text{asin}(1/n_{ZnO}) \approx 2\cdot 30°$ (see chapter 6) and is therefore preferentially reflected back into silicon, as schematically shown in Fig. 8.2.

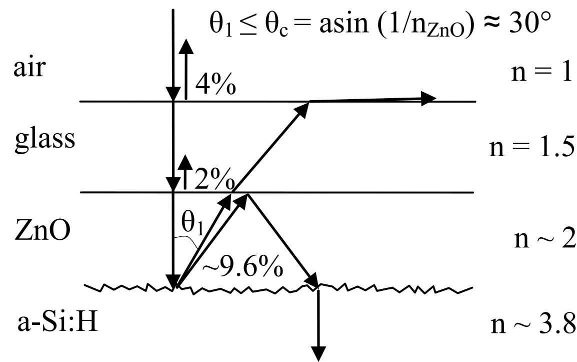

Fig. 8.2: Primary reflectances in the structure glass/ZnO/a-Si:H discussed in this section. For the interfaces air/glass, glass/ZnO and ZnO/a-Si:H, the Fresnel coefficients in normal incidence are 4%, 2% and 9.6% respectively. Simple geometrical optics considerations explain how light trapping by total internal reflection reduces the primary reflectance of the rough a-Si:H/ZnO interface. For light in ZnO, the opening angle of the escape cone is $2\cdot\theta_c = 2\cdot 30°$, where θ_c is the critical angle of total internal reflection for ZnO in air.

Thank to the internal reflection in ZnO (see Fig. 8. 2), the reflectance of ~9.6% at the ZnO/a-Si:H interface is reduced, according to Fig. 8.1(c), in an effective reflectance of ~3% for the layer with the longest post-treatment (Type-D1) and ~0.8% for the layers with no post-treatment (Type-A1 and -B1). For those two layers, this very low effective reflectance is obtained thank to their unmodified as-grown surface texture. The angular distribution of the reflected light at the internal interface (of course, not accessible experimentally) is most probably broader for the Type-A1 and Type-B1 ZnO layers. This provides an explanation for their better anti-reflection effect.

The bump of reflectance noted in (4) is produced by the a-Si:H film, which behaves as a half-wavelength plate (it is indeed surrounded by air and ZnO, with lower refractive indexes). We already discussed this effect in chapter 7 where the bump was produced by the top cell of a micromorph device with intermediate reflector. The important thing to realize here is that, *an interferential effect seems to be possible with diffuse light*. There is a dramatic narrowing of the angular distribution for light transmitted through the ZnO layer with the longest post-treatment time of its surface (see Fig. 6.9 in chapter 6). We suggest here that the light scattered by this surface is indeed diffuse but still coherent. The

diffusion takes place with a narrow angular distribution, the most probable scattering angle in a-Si:H being smaller than 10°.

8.2.2 Front ZnO layer: effects of light trapping and FCA absorption

For comparison of pairs of the front TCO layers listed in Table 8.2, pairs of EQE curves (top cell, bottom cell and sum) of co-deposited micromorph devices with intermediate reflector are plotted in Figs. 8.3(a) to (d). The corresponding pairs of curves ($1 - R_{tot}$) are also plotted in these figures as well as the predicted curve EQE'', calculated from eq. (8.2), as should be observed in case the EQE change is linked to light trapping enhancement only and not to a change in TCO absorption (circles in Figs. 8.3(a) to (d)). We observe that, when the difference between the TCO layers is only the duration of the plasma post-treatment t_{PT} (Figs. 8.3(a) and (b)), the predicted EQE'' for the device deposited on the TCO with short post-treatment nicely fits the actual EQE. The discrepancy for short wavelengths indicates an increased absorption in the p-type Si layer and/or the front ZnO layer, when long post-treatment is used. In the long wavelength region, the similarity between the experimental and calculated (EQE'') curves means that the change of EQEs are mainly due to changes of light trapping capability (70% and 94% of the gain in current from one sample to the other, in Figs. 8.3(a) and (b), respectively) and not to changes of absorption. However, when the front TCO are differently doped (Figs. 8.3(c) and (d)) the major part of the improvement of EQE is due to the reduction of FCA. Indeed, only 32% and 19% of the gain in current density can be attributed to an enhancement of light trapping by the larger grain features in Fig. 8.3(c) and (d), respectively. A large increase of FCA is also manifested in the curves ($1 - R_{tot}$) where we see that the reflectance for $\lambda > 1000$ nm is smaller with the highly doped front TCO. Therefore, we conclude that more than 50% of the benefit of the thick, large grain, lightly-doped Type-C front ZnO layers is due to its decreased FCA and that the large features are not the dominant factor helping the current gain, as could be intuitively thought.

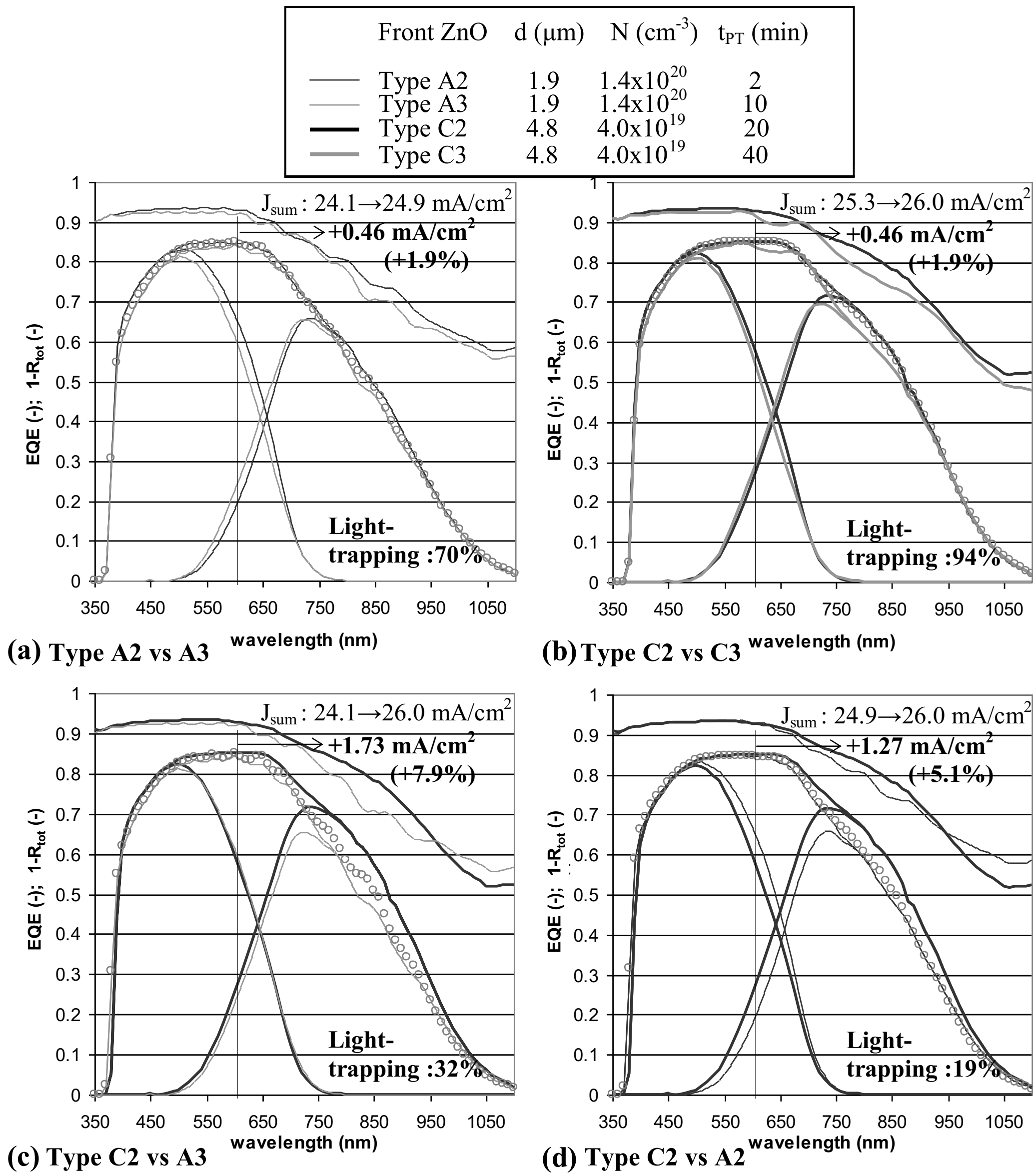

Fig. 8.3: (a)-(d) Pairs of EQE curves (top cell, bottom cell and sum) of micromorph cells with intermediate reflector co-deposited on different pairs of the front ZnO layers described in Table 6.2. The corresponding pairs of total absorbance curves ($1-R_{tot}$) are also plotted in these figures. The circles in (a) to (d) indicate the predicted EQE'', calculated with eq. (8.2), from the EQE of the first cell of the pair and the total reflectance spectra of both cells. Those EQE'' curves correspond to the expected EQE for a cell deposited on a layer with the morphology of the second ZnO layer of the pair but with the free carrier absorption (FCA) of the first one. Therefore they give the expected EQE if only light trapping enhancement was provided by the second ZnO layer of the pair. In (a) the two thin Type-A2 and Type-A3 ZnO layers (thin curves) with two different durations t_{PT} of plasma post-treatment are compared. In (b) the comparison concerns the two thick lightly-doped Type-B2 and Type-B3 ZnO layers (thick curves) with two different t_{PT}. In (c) the thin Type-A3 ZnO layer with the long (10 min) t_{PT} is compared with the thick Type-C2 layer. Finally, in (d) the thin Type-A2 with the short (2 min) t_{PT} is compared to the thick Type-C2 ZnO layer. For each pair of micromorph cell the following information is indicated: the change of total photo-current density (J_{sum}) in the top and bottom cells of the tandem; the absolute and relative contributions of the wavelengths ranging from 600 nm to 1100 nm to the increase of J_{sum}; and the relative contribution of light trapping deduced from EQE''. The vertical lines indicate the wavelength (λ = 600 nm) from which integration with the photon flux of AM1.5g spectrum has been carried out to calculate the increase of J_{sum}.

Another way to distinguish FCA from light trapping is to correct the EQE with eq. (8.7). This gives, in a first approximation, the value that the EQE would take if there were no absorption at all in the TCO layers. Fig. 8.4 shows that, as expected, the increase of the surface post-treatment induces a reduction of the light scattering capability (corrected curves for C2 and C3) in the range of 650 to 950 nm. In the same range, after the correction, the curves for A2 and C3 become closer. This indicates that Type-A ZnO layers with small pyramids and short (or no) post-treatment and providing a broader angular distribution of the scattered light (see chapter 6, Figure 6.9), even though showing a lower haze, can be as efficient as large but smoothened features at scattering light. For this series of samples, if all the absorption losses are canceled, the better light scattering capability in the range 700-900 nm is obtained with a thick, large grain ZnO films with the 20 minutes of surface post-treatment. Surprisingly, we notice that above 980 nm all corrected curves are similar. This would indicate that in the case of a “true” weak absorption limit (absorption length in µc-Si > 100 µm) most of our samples behave similarly in terms of light trapping and light path enhancement.

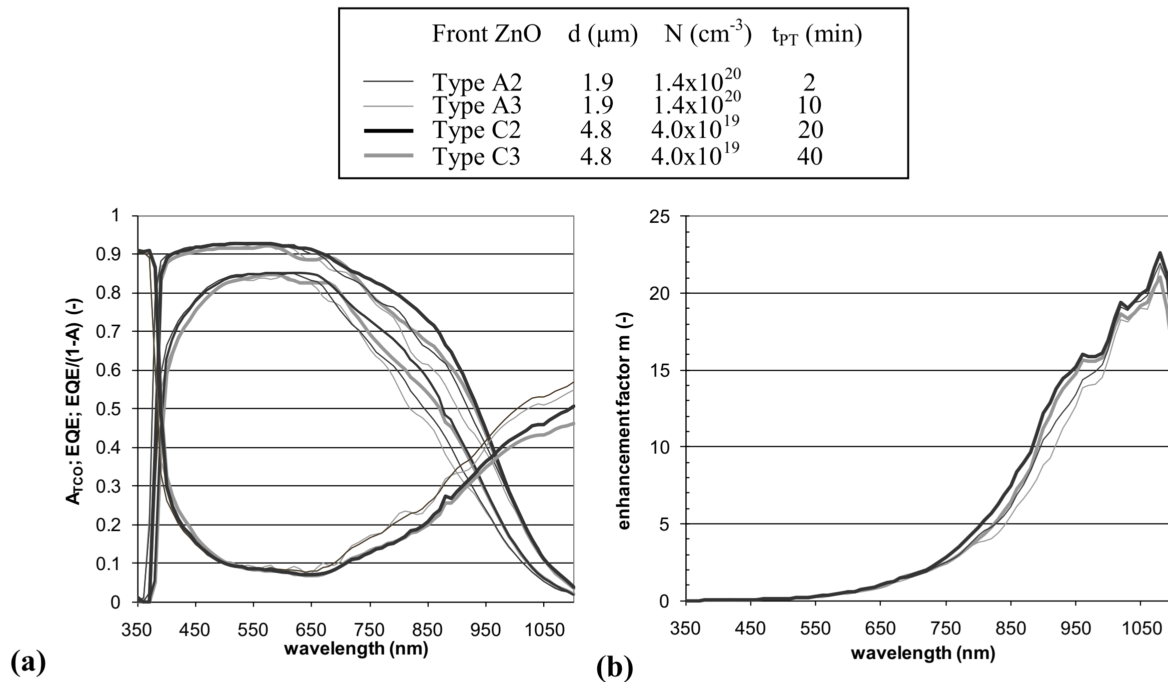

Fig. 8.4: (a) Absorbance losses A_{TCO}, EQE (sum) and $EQE_{cor} = EQE/(1-A_{TCO})$ for the micromorph cells co-deposited on the ZnO layers presented in Table 6.2 (same cells as in Fig. 8.3). (b) Effective light path enhancement calculated with eq. (8.6) for these micromorph cells.

Table 8.3: For micromorph cells deposited on the ZnO layers listed in Table 8.2, current densities J corresponding to EQE and $EQE_{cor} = EQE/(1-A_{TCO})$ for the full wavelength range (300 nm to 1100 nm) and for the light trapping wavelengths range comprised between 600 and 1100 nm, with the corresponding relative increase of J.

Type of front ZnO	A2	A3	C2	C3
J_{EQE} (mA/cm^2)	24.9	24.1	26.0	25.3
J_{EQEcor} (mA/cm^2)	29.9	29.2	30.6	29.7
$J_{EQE,\,600}$ (mA/cm^2)	15.2	14.7	16.5	15.9
$J_{EQEcor,\,600}$ (mA/cm^2)	18.8	18.2	19.6	18.9
$(J_{EQEcor,600} - J_{EQE,600})/J_{EQE,600}$ (%)	+23.5	+23.8	+18.8	+18.9

The current densities deduced from the EQE in Fig. 8.4(a) are listed in Table 8.3. We see in this Table that, when the effect of FCA is removed, the increase of J_{sc} in the light trapping wavelengths range (600 to 1100 nm) is raised by about 24% for the thin and highly-doped ZnO layers against about 19% for the thick and lightly-doped ones. This leads to the same conclusion as the first comparison method: when the free carrier absorption is "removed", smaller difference in the J_{sc} remains (i.e. the difference goes down from 1.8 to 1.4 mA/cm^2 between 600 and 1100 nm, see Table 8.3).

If totally free-FCA ZnO layers also having a wider bandgap (i.e. free of band to band absorption at low wavelength) were achievable, the potential for the higher current would be 30.6 mA/cm^2 for the thick Type-C2 ZnO layer. This is 2.3% better than for the thin Type-A2 ZnO layer (29.9 mA/cm^2).

Also from the plots of the effective optical path enhancement in Fig. 8.4(b), we can directly deduce the effective light path enhancement calculated with eq. (8.6). The enhancement factor rises when the wavelength increases, to reach a maximum of 21 to 23 paths at λ = 1080 nm. Therefore, in the best cases, this factor is still ~2.5 times smaller than the ideal Yablonovitch's limit of $4 \cdot n_{Si}^2$, with n_{Si}~3.8. This illustrates the further potential of light trapping structures if perfect Lambertian scattering could be achieved. Here also, for a given thickness of the ZnO layer, the longer the post-treatment the smaller the light trapping capability in the range of 700 to 980 nm. Larger enhancement factors are obtained for the thick ZnO layers. At 950 nm, the enhancement factor m increases from 13.4 for the thin Type-A3 ZnO layer, with the 10 min plasma post-treatment, to 15.2 for the thick layer with a 20 min plasma post-treatment.

Finally we should point out that, if µc-Si:H had a low absorption coefficient satisfying $\alpha d \ll 1$ over a larger spectral range, we would expect to see a decrease of m with the wavelength (chapter 6). This indeed could explain the apparent fall of m above 1000 nm (even though this would have to be confirmed). The rising m factor up to 1000 nm is not trivial to understand and this is primarily linked to the fact that the assumption of weak absorption limit ($m \cdot d < 1/\alpha$) is no longer fulfilled. Hence the too strong absorption coupled to the reflection losses will lead to a reduction of m which can even become

lower than unity. Besides, other effects can play a role: this includes eq. (8.4) for the absorption of the TCO, the fact to neglect the primary reflection losses in the definition of m in eq. (8.5) (which becomes sensitive to offset of the EQE) and the absorption in doped layers. Berginski *et al*. obtained similar features in the plot of the enhancement factor versus the wavelength for μc-Si:H solar cells deposited on sputtered-etched ZnO:Al layers [Berginski 2007].

8.3 Conclusions

In this chapter, we have shown that for our LPCVD ZnO:B layers, the angular distribution of light reflected at the internal ZnO/a-Si:H interface, coupled with internal total reflection in the ZnO layer, is the major contributor to anti-reflective effect of this rough interface. Its effective reflectance is reduced down to ~0.8% if the surface of the as-grown LPCVD ZnO layer is not modified by the plasma post-treatment. In this case, the benefit of small pyramids (lateral size of 400 nm compared to 900 nm, typically) to decrease the reflectance by means of refractive index grading is almost negligible.

When comparing the relative benefit of using our new thick, large grain, lightly-doped ZnO layer we observe that more than 50% of the gain in the total cell current density is produced by the decrease of free carrier absorption. Typically 20% to 30% of the gain in current density is due to an improvement of light scattering capability of thick Type-C ZnO layers when compared to thin, highly-doped Type-A.

When comparing the potential of totally free-FCA ZnO layers, we observe that the thick layers with short treatment time offer a better light trapping capability, with a current density 2.3% larger, than in the case of the thin layer with a short plasma post-treatment of its surface.

Finally, we obtain a maximum factor of 21 to 23 for the effective light path enhancement produced by our ZnO layers. This is still ~2.5 times smaller than the ideal Yablonovitch's limit of $4 \cdot n_{Si}^2$. This illustrates the further potential if perfect Lambertian scattering would be achieved in our solar cell devices. We point out that further work is definitely required to achieve a full understanding of all the effects in the EQE curves as described in Figs. 8.3 and 8.4.

9 Conclusions and perspectives

We draw a summary of the conclusions reported in this thesis. Then, perspectives for further studies and device efficiency improvement are briefly discussed.

9.1 Final conclusions

9.1.1 Device optimization

The object of the present work was to demonstrate high efficiency micromorph solar cells outside of industrial cost requirements. We therefore explored the potential of increasing the thickness of the bottom cell absorber, introducing an intermediate reflector (IRL) to achieve current matching, and using novel types of front transparent conductive oxide (TCO) layers. Following this strategy the best initial conversion efficiency (η) is 13.3% for a 1.2 cm^2 cell with a broadband anti-reflection (AR) coating on the front side of the glass. The best stabilized efficiency is 11.1% with a 1.2 cm^2 micromorph cell without AR coating. Table 9.1 gives an overview of the main results obtained during this work, with the corresponding top/bottom cell thicknesses and types of intermediate reflector and front TCO layers.

Table 9.1: Micromorph solar cell results obtained with Type-A or Type-C front ZnO layer (Type-A stands for the LPVCD ZnO:B layer with small feature sizes optimized for single junction a-Si:H solar cells; Type-C stands for thick, large grain, lightly doped ZnO layers and with different post-treatment on their surface); different intermediate reflector layers (IRL): ZnO (ZIR) or silicon oxide based (SOIR); and different top/bottom cell thicknesses.

Front ZnO	ARC	IRL	d_{top} (nm)	d_{bot} (µm)	J_{sum}	$J_{sc,top}$ (mA/cm^2)	$J_{sc,bot}$	J_{sc} (mA/cm^2)	Voc (V)	FF (-)	η (%)	Remark
Type-A	no	ZIR	180	1.8	24.5	12.4	12.1	12.1	1.315	0.732	11.6	initial, ~0.25 cm^2 (see 7.3.2)
Type-C	no	ZIR	290	3.0	26.0	13.2	12.8	12.8	1.315	0.702	11.8	initial, ~1 cm^2 (see 7.3.2)
Type-A	no	SOIR	290	3.0	25.0	13.5	11.5					initial, 1.2 cm^2 (see 7.5.2)
Type-C	no	SOIR	290	3.0	26.8	13.0	13.8					initial, 1.2 cm^2 (see 7.5.2)
Type-C	no	SOIR	290	3.0	26.8	13.0	13.8					initial, 1.2 cm^2 (see 7.5.2)
Type-C	no	SOIR	300	3.0	26.0	13.3	12.7	12.7	1.38	0.722	12.6	initial, 1.2 cm^2 (see 7.5.2)
					25.3	12.8	12.5	12.5	1.32	0.672	**11.1**	**degraded**
Type-C	**yes**	SOIR	340	3.5	27.7	13.8	13.9	13.8	1.38	0.708	13.3	initial, 1.2 cm^2 (see 7.6.2)
					26.7	13.2	13.5	13.4	1.29	0.629	**10.7**	**degraded**

This strategy focuses on the increase of the short-circuit current density (J_{sc}). The best J_{sc} in Table 9.1 is 13.8 mA/cm^2, the sum of current densities J_{sum} of the top and bottom cells of the corresponding micromorph device is 27.7 mA/cm^2. This remarkably high current density shows that our concept could most probably yields a J_{sc} of 14 mA/cm^2 which is a prerequisite to reach the threshold of 14% initial efficiency.

9.1.2 Study of the optoelectronic properties of the device: electronic

In chapter 3 we showed that the radii of curvature at steep V-shaped valleys between the pyramid-like objects on the surface of our zinc oxide layers can be increased by means of different plasma post-treatments. In chapter 4 we showed that, the harmful effects of these V-shaped valleys on the open-circuit voltage (V_{oc}) and fill-factor (FF) of μc-Si:H solar cells can be removed if the plasma treatment applied to the surface of the ZnO layer is long enough. In chapter 5 we obtained some evidences, with different scanning electric probe microscopy techniques, that the clusters of μc-Si:H material present on the top of each pyramid of the ZnO layer can be thought as independent nanodiodes connected in parallel by the front and back TCO layers. We proposed that the electrical characteristics of these nanodiodes are mainly influenced by the quality of the μc-Si:H material forming the boundaries between these clusters. In chapter 7 we explained with a simple network model that the fill-factor (FF) of the micromorph cell changes asymmetrically when the balance of current matching between the top and bottom cells changes: a shift towards bottom-limitation produces a larger increase of FF than towards top limitation. Therefore a strong link exists between electrical performances and the optical properties of the device which influence the current balance in the tandem. Also in chapter 7, we observed the negative impact on V_{oc} and FF of large in-plane conductivities of the IRL. We showed that this can be solved by using a silicon oxide based IRL (SOIR) or a dedicated ZnO layer with low conductivity.

9.1.3 Study of the optoelectronic properties of the device: optics

In chapter 6 we used the Beckmann-Kirchhoff scattering theory modified by Harvey to calculate the angular distribution of scattered light when it is transmitted through different surface-textured ZnO layers. As the agreement with experiment is good we used this method to gain insights into light scattering at the internal ZnO/Si interface of our devices. We also showed experimentally that for a same haze in transmission, if the angular distribution of the light transmitted through the TCO is narrow, then the current density in the bottom cell of the micromorph device decreases. However, no clear rule was deduced for the top cell. In chapter 7 we experimentally demonstrated that when an IRL of thickness d_{IRL} is introduced in the device, the gain in current density of the top cell ($J_{sc,top}$) increases linearly with d_{IRL} and saturates when d_{IRL} reaches a value comparable to the surface roughness of the interfaces. We explained that the IRL actually promotes the light trapping capability of the front TCO layer in the 550-700 nm spectral range. Therefore, the better is this capability; the better is the effectiveness of the IRL in

increasing $J_{sc,top}$. The Type-C ZnO (thick, lightly doped, large grain layer, optimized for μc-Si:H cells) was found to be less favorable for the top cell than the Type-A ZnO (small features sizes, optimized for a-Si:H cells) due to a decrease of the effectiveness of the IRL. This is because Type-C ZnO (with large texture sizes) requires long post-treatment of its surface and therefore provides light scattering with a narrow angular distribution. In chapter 8 we showed that more than 50% of the improvement of current density obtained in the bottom cell when this Type-C ZnO is used is due the reduced free carrier absorption (FCA) of this thick but lightly doped layer. In chapter 8 we also showed that for our ZnO layers, the anti-reflective effect of the ZnO/Si interface in the device is not due to refractive index grading but to light trapping in the ZnO layer with total internal reflection at the ZnO/glass interface.

In summary, compared to the status at the beginning of this thesis, with micromorph cells in the range of 10-10.5%, by working on fully different structures we were able to achieve higher established and initial efficiency. Also we could bring in new insights into the various mechanisms leading both to increase (or decrease) of light scattering at nano-textured interfaces and of light trapping in the silicon top and bottom absorbers of the micromorph solar cell, as well as leading to improvement or degradation of its electrical properties.

9.2 Perspectives

The IMT's state-of-the-art value for stable conversion efficiency is 11.1% with a SOIR. This result is obtained without AR coating and a problem of degradation of the V_{oc} when a SOIR is used occurred. We think that this problem is likely to be solved (see (a) below). Thus, perspectives for further improvement are excellent and many interesting topics concerning the micromorph solar cell are left to be studied in more details. In the author's opinion the most pressing topic are therefore:

(a) Studying if nanocracks through the p/i interface, such as the cracks inferred in chapter 5 from Figure 5.6(b), induces selective contaminations by in-diffusion during deposition of the intrinsic μc-Si:H absorber. This may provide an explanation for the degradation of V_{oc} observed in micromorph cells incorporating a silicon oxide based intermediate reflector (SOIR). The new NanoSIMS analysis technique [Lozano-Perez 2008] should be an adequate tool for this study.

(b) Identifying a limit for the maximum allowable thickness for the bottom μc-Si:H absorber. Indeed, up to now, an excellent collection of carriers is achieved within the μc-Si:H absorber, even with 3.5-μm-thick layers (verified in single junction devices). This study is actually less trivial as it appears, because the limit of the maximum thickness is tightly linked, via the electric-field in the intrinsic layer, to the quality of the vacuum in the deposition chamber and to the purity of the gas feed: any deviation due to

the history of the reactor may lead to a shift of the Fermi level in the intrinsic layer and therefore to a weakening of the electric-field. At the moment, the bottleneck for the current density of the micromorph tandem is the top cell. However, this point (b) could give room for current density in the bottom cell (if made thicker than 3.5 μm) and allow for the deposition of the device on a Type-A front ZnO layer, favorable to a high current density in the top cell.

(c) Developing a layer with the surface roughness of Type-A and the low FCA of Type-C should allow increasing the current densities of both the top and the bottom cells. Indeed, FCA reduction gives the main contribution to the improvement of the current density when a micromorph cell is deposited on a Type-C ZnO layer, compared to a Type-A; whereas, effectiveness of the intermediate reflector is improved with Type-A. Further experimental verification could be obtained by growing suitable layers.

(d) Further validating the ability of scalar scattering theory to handle the problem of light scattering by the rough TCO layers used in thin-film PV. Multiple internal reflections of light trapped in the silicon layer could easily be added to the model. This would make possible a confrontation of calculation results with absorbance measurements with glass/ZnO/Si samples. This would also allow the identification of a minimum thickness for the silicon layer, for which this approach is still valid, and below which a rigorous near-field calculation must be used.

(e) Finally, limiting further the apparition of cracks in the μc-Si:H materials. We note indeed that cracks appearing at various places in the devices (also after the amorphous top cells) are strongly detrimental. Even though the Type-C ZnO layers with long post-treatment of their surface allows to some extent a limitation of the apparition of the cracks in the μc-Si:H materials, further work is needed:

- to improve the shape and features of the front TCO

- to improve the processes e.g. by growing “flatter” a-Si layers, or by growing μc-Si:H layers less prone to develop cracks. For instance higher deposition temperature was shown [Python 2009b] to lead to a strong reduction of crack density for μc-Si layers. This is particularly interesting for nip structures, but possibly could also be implemented in pin devices.

References

[Bailat 2003] J. Bailat, E. Vallat-Sauvain, L. Feitknecht, C. Droz and A. Shah, *Microstructure and open-circuit voltage of n-i-p microcrystalline silicon solar cells,* J. Appl. Phys. **93** (2003) 5727-5731.

[Bailat 2004] J. Bailat, *Growth, microstructure and electrical performances of thin film microcrystalline silicon solar cells*, PhD Thesis (2004), Université de Neuchâtel.

[Bailat 2005] J. Bailat, V. Terrazzoni-Daudrix, J. Guillet, F. Freitas, X. Niquille, A. Shah, C. Baillif, T. Sharf, R. Morf, A. Hansen, D. Fischer, Y. Ziegler and A. Closset, *Recent Development of Solar Cells on Low-Cost Plastic Substrates*, Proc. of the 20th EU-PVSEC, Barcelone, 2005, pp. 1529-1532.

[Bailat 2006] J. Bailat, D. Dominé, R. Schlüchter, J. Steinhauser, S. Faÿ, F. Freitas, C. Bücher, L. Feitknecht, X. Niquille, T. Tschaner and A. Shah, *High-efficiency P-I-N microcrystalline and micromorph thin film silicon solar cells deposited on LPCVD ZnO coated glass substrates,* Proc. of the 4th WCPEC, Hawai, 2006, pp. 1533-1536.

[Ballif 2000] C. Ballif, H. R. Moutinho, F. S. Hasoon, R. G. Dhere and M. M. Al-Jassim, *Cross-sectional atomic force microscopy imaging of polycrystalline thin films,* Ultramicroscopy **85** (2000) 61-71.

[Ballif 2001] C. Ballif, H. R. Moutinho and M. M. Al-Jassim, *Cross-sectional electrostatic force microscopy of thin-film solar cells,* J. Appl. Phys. **89** (2001) 1418-1424.

[Beck 1997] N. Beck, *Optical and electrical properties of hydrogenated amorphous and microcrystalline silicon for solar cell applications,* PhD Thesis (1997), Université de Neuchâtel.

[Beckmann 1963] P. Beckmann, A. Spizzichino, *The Scattering of Electromagnetic Waves from Rough Surfaces,* Pergamon Press New York (1963).

[Benedict 1992] J. Benedict, R. Andersen and S. J. Kepeis, Mat. Res. Soc. Sym. Proc. **254** (1992) 121-140.

[Berginski 2007] M. Berginski, J. Hüpkes, M. Schulte, G. Schöpe, H. Stiebig, B. Rech and M. Wuttig, *The Effect of Front ZnO:Al Surface Texture and Optical Transparency on Efficient Light Trapping in Silicon Thin-Film Solar Cells*, J. Appl. Phys. **101** (2007) 074903.1-11.

[Beyer 2007] W. Beyer, J. Hüpkes and H. Stiebig, *Transparent conducting oxide films for thin film silicon photovoltaics*, Thin Solid Films **516** (2007) 2/4, 147-154.

[Bieberícher 2004] A. C. W. Biebericher, A. R. Burgers, C. Devilee and W. J. Soppe, *Effects of plasma conditions on density of microcrystalline silicon*, Proc. of the 19th EU-PVSEC, Paris, 2004.

[Breymesser 2001] A. Breymesser, V. Schlosser, D. Peiro, C. Voz, J. Bertomeu, J. Andreu and J. Summhammer, *Kelvin Probe Measurements of Microcrystalline Silicon on a Nanometer Scale Using SFM*, Sol. Energy Mater. Sol. Cells **66** (2001) 171-177.

[Bruggeman 1935] D. A. G. Bruggeman, Ann. Phys. **24** (1935) 637.

[Bücher 1991] K. Bücher, A. Schönecker, *Spectral Response Measurements of Multi-Junction Solar Cells with a Grating Monochromator and a Fourier-Spectrometer,* proc. of the 10th EC-PVSEC, Lisbon, 1991, pp. 107-110.

[Buehlmann 2007] P. Buehlmann, J. Bailat, D. Dominé, A. Billet, F. Meillaud, A. Feltrin and C. Ballif, *In situ silicon oxide based intermediate reflector for thin-film silicon micromorph solar cells,* Appl. Phys. Lett. **91** (2007) 143505.1-3

[Buehlmann 2007] P. Buehlmann, A. Billet, J. Bailat and C. Ballif, *Anti-reflection layer at the TCO/Si interface for high efficiency thin-film solar cells deposited on rough LP-CVD front ZnO*, Proc. of the 22nd EU-PVSEC, Milan, 2007, p. 2182.

[Buehlmann 2008] P. Buehlmann, J. Bailat, A. Feltrin and C. Ballif, *Conducting two-phase silicon oxide layers for thin-film silicon solar cells*, Mat. Res. Soc. Symp., fall meeting Boston, 2008.

[Burdick 1986] J. Burdick, Troy Glatfelter, *Spectral response and I-V Measurements of Tandem Amorphous-Silicon Alloy Solar Cells*, Solar Cells, **18** (1986) pp301-314.

[Burstein 1954] E. Burstein, *Anomalous Optical Absorption Limit in InSb*, Phys. Rev. Lett. **93** (1954) 632-633.

[Carniglia 1979] C. K. Carniglia, *Scalar Scattering Theory for Multilayer Optical Coatings,* Opt. Eng. **18** (1979) 104.

[Cavallini 2007] A. Cavallini, D. Cavalcoli, M. Rossi, A. Tomasi, S. Pizzini, D. Chrastina and G. Isella, *Defect analysis of hydrogenated nanocrystalline Si thin films,* Physica B **401–402** (2007) 519–522.

[Chang 2005] M. N. Chang, C. Y. Chen, W. J. Huang and T. C. Cheng, *Approach to nonphotoperturbed differential capacitance measurements: A front-wing cantilever*, Appl. Phys. Lett. **87** (2005) 023102 1-3.

[Curtins 1987] H. Curtins, N. Wyrsch, M. Favre and A. Shah, Plasma Chem. Plasma Process. **7** (1987) 367.

[Delli Veneri 2007] P. Delli Veneri, L. V. Mercaldo, P. Aliberti, P. Ciani, I. Usati, and C. Privato, *Micromorph tandem solar cells: influence of microcrystalline silicon bottom cell on device performance*, Proc. of the 22nd EU-PVSEC Milan, 2007 pp. 1814-1818.

[Dominé 2005] D. Dominé, J. Steinhauser, L. Feitknecht, A. Shah and C. Ballif, *Effect of ZnO layer as intermediate reflector in micromorph solar cells*, Proc. of the 20th EU-PVSEC, Barcelona, 2005, pp. 1600-1603.

[Dominé 2006] D. Dominé, J. Bailat, J. Steinhauser, A. Shah, and C. Ballif, *Micromorph solar cell optimization using a ZnO layer as intermediate reflector*, Proc. of the 4th WCPEC, Hawaii, 2006, pp. 1465-1468.

[Dominé 2007] D. Dominé, J. Bailat, M. Python, N. Wyrsch, and C. Ballif, H. R. Moutinho, C.-S. Jiang, and M. M. Al-Jassim, *Investigation of the electric-field profile in microcrystalline silicon p-i-n solar cells by cross-sectional scanning Kelvin-probe microscopy*, Proc. of the 22nd EU-PVSEC, Milan, 2007, pp. 2203-2207.

[Dominé 2008a] D. Dominé, P. Buehlmann, J. Bailat, A. Billet, A. Feltrin, and Christophe Ballif, *Optical management in high-efficiency thin-film silicon micromorph solar cells with a silicon oxide based intermediate reflector*, phys. stat. sol. (RRL) **2** (2008) 163–165.

[Dominé 2008b] D. Dominé, P. Buehlmann, J. Bailat, A. Billet, A. Feltrin, and C. Ballif, *High-efficiency micromorph silicon solar cells with in-situ intermediate reflector deposited on various rough LPCVD ZnO,* Proc. of the 23rd EU-PVSEC, Valencia, 2008, pp. 2091–2095.

[Duparré 2006] A. Duparré, Light Scattering *Techniques for Inspection of Microcomponents and Microstructures,* Optical Methods for the Inspection of Microsystems (2006) 103-119.

[Elson 1979] J. M. Elson and J. M. Bennett, *Vector Scattering Theory*, Opt. Eng. **18** (1979) 116-124.

[Elson 1980] J.M. Elson, J. P. Rahn, J. M. Bennett, *Light scattering from multilayer optics: comparison of theory and experiment*, Appl.Opt. **19** (1980) 669-679.

[Fay 2000] S. Faÿ, S. Dubail, U. Kroll, J. Meier, Y. Ziegler and A. Shah, *Light Trapping Enhancement for Thin-Film Silicon Solar Cells by Roughness Improvement of the ZnO Front TCO*, Proc. of the 16th EU-PVSEC, Glasgow, 2000, pp. 361-364.

[Fay 2003] S. Faÿ, *L'oxyde de zinc par dépôt chimique en phase vapeur comme contact électrique transparent et diffuseur de lumière pour les cellules solaires,* PhD Thesis (2003), Ecole Polytechnique Fédérale de Lausanne.

[Feitknecht2005] L. Feitknecht, J. Steinhauser, R. Schlüchter, S. Faÿ, D. Dominé, E. Vallat-Sauvin, F. Meillaud, C. Ballif and A. Shah, *Investigations on Fill-Factor drop of microcrystalline silicon p-i-n solar cells deposited onto highly surface-textured ZnO substrates*, Proc. of the 15th I-PVSEC, Shanghai, 2005, pp. 473-474.

[Finger 2005] F. Finger, R. Carius, T. Dylla, S. Klein, S. Okura, M. Günesa, *Istability Phenomena in Microcrystalline Silicon Films*, Journal of Optoelectronics and Advanced Materials **7** (2005) 83-90.

[Finger 2007] F. Finger, Y. Mai, S. Klein and R. Carius, *High efficiency microcrystalline silicon solar cells with Hot-Wire CVD buffer layer,* Thin Solid Films **516** (2008) 10.1016.

[Fischer 1994] D. Fischer and A. Shah, *Compensation of the dangling-bond space charge in amorphous silicon solar cells by graded low-level doping in the intrinsic layer*, Appl. Phys. Lett. **8** (1994) 986-988.

[Fisher 1996] D. Fischer, S. Dubail, J. A. Anna Selvan, N. Pellaton Vaucher, R. Platz, Ch. Hof, U. Kroll, J. Meier, P. Torres, H. Keppner, N. Wyrsch, M. Goetz, A. Shah, K.-D.Ufert, *The Micromorph Solar Cell: Extending a-Si:H Technology towards Thin Film Crystalline Silicon*, Proceedings of the 25th IEEE Photovoltaic Specialists Conference, Washington D.C., 1996, pp. 1053-1056.

[Gee 2002] J. M. Gee, *Optically enhanced absorption in thin silicon layers using photonic crystals,* Photovoltaic Specialists Conference Record of the 29th IEEE Photovoltaic Specialists Conference, New Orleans, 2002 pp 150-153.

[Goetzberger 1981] A. Goetzberger, Proceedings of the 15th IEEE Photovoltaic Specialists Conference Orlando, 1981, p 867.

[Goodman 1968] J. W. Goodman, *Introduction to FourierOptics*, McGraw-Hill, San Francisco, 1968.

[Goodman 1985] J. W. Goodman, *Statistical Optics*, Wiley, New York, 1985.

[Green 2009] M.A. Green et al. *Solar Cell Efficiency Tables*, Prog. Photovolt: Res. Appl. **17** (2009) 85–94.

[Haase 2007] C. Haase and H. Stiebig, *Thin-film silicon solar cells with efficient periodic light trapping texture,* Appl. Phys. Lett. **91** (2007) 061116.1-3.

[Hagemann 2008] V. Hagemann, S. Reichel, S. Bauer and P. Lechner, *Quantifying the Antireflection Properties of Internal Interfaces of Solar Cells on Rough TCO*, Proc. of the 23rd EU-PVSEC, Valencia, 2008, p.p 2400- 2402.

[Harvey 1979] J. E. Harvey, *A Fourier Treatment of Near-field Scalar Diffraction Theory*, Am. J. Phys. **47** (1979) 974-980.

[Harvey 1989] J. E. Harvey, *Surface Scatter Phenomena: A Linear, Shift-invariant Process*, in Scatter from Optical Components, J. C. Stover, ed., Proc. SPIE 1165, 1989, pp. 87-99.

[Harvey 1999] J. E. Harvey, C. L. Vernold, A. Krywonos and P. L. Thompson, *Diffracted radiance: a fundamental quantity in nonparaxial scalar diffraction theory,* Appl. Opt. **38** (1999) 6469-6481.

[Harvey 2002] J. E. Harvey and A. Krywonos, *Axial irradiance distribution throughout the whole space behind an annular aperture,* Appl. Opt. **41** (2002) 3790-3795.

[Harvey 2003] J. E. Harvey and A. Krywonos, *Axial Irradiance Distribution Throughout the Whole Space Behind an Annular Aperture: Reply to Comments*, Appl. Opt. **42** (2003) 3792-3794.

[Harvey 2007] J. E. Harvey, A. Krywonos, and C. L. Vernold, *Modified Beckmann-Kirchhoff scattering model for rough surfaces with large incident and scattering angles*, Opt. Eng. **46** (2007) 078002.

[Haug 2008a] F.-J. Haug, T. Söderström, O. Cubero, V. Terrazzoni-Daudrix, X. Niquille, S. Perregeaux and C. Ballif, *Periodic textures for enhanced current in thin film silicon solar cells,* Presented at the MRS Spring Meeting, San Francisco, 2008.

[Haug 2008b] F.-J. Haug, T. Söderström, O. Cubero, V. Terrazzoni-Daudrix and C. Ballif, *Plasmonic absorption in textured silver back reflectors of thin film solar cells,* J. Appl. Phys. **104** (2008) 064509.

[Heine 1995] C. Heine and R. H. Morf, *Submicrometer gratings for solar energy applications*, Applied Optics **34** (1995)2476-2482.

[Hof 1999] C. Hof, *Thin Film Solar Cells of Amorphous Silicon: Influence of i-Layer Material on Cell Efficiency,* PhD Thesis (1999), Université de Neuchâtel.

[Hopkins 1985] H. H. Hopkins, *Image formation by a general optical system. I: General theory* , Applied optic **24** (1985) 2491-2505.

[Hopkins 1991] H. H. Hopkins, *The Nature of the Paraxial Approximation I: Systems of Uniform Refractive Index*, Journal of Modern Optics **38** (1991) 427-445.

[Huang 2008] Y. Huang, T. Chen, A. Gordjin, A. Dasgupta, F. Finger, and R. Carius, *Preparation of microcrystalline silicon solar cells on microcrystalline silicon carbide window layers grown with HWCVD at low temperature,* Journal of Non-Crystalline Solids **354** (2008) 2430-2434.

[Hubin 1995] J. Hubin, A. Shah, *Effect of the recombination function on the collection in a p-i-n solar cell*, Phil. Mag. **72** (1995) 589-599.

[Isabella 2008] O. Isabella, A. Campa, M. C. R. Heijna, W. Soppe, R. van Erven, R. H. Franken, H. Borg, M. Zeman, *Diffraction Gratings for Light Trapping in Thin-Film Silicon Solar Cells*, Proc. of the 23rd EU-PVSEC, Valencia, 2008, pp. 2320-2324.

[IEC 2005] International standard IEC 60904-3, *Measurement principles for terrestrial photovoltaic (PV) solar devices with reference spectral irradiance data*, 2005.

[Isakovitch 1952] M. A. Isakovich, *Wave Scattering from a Statistically Rough Surface*, Zh. Eksp. Teor. Fiz. **23** (1952) 305-314.

[Jiang 2004] C.-S. Jiang, H. R. Moutinho, Q. Wang, M. M. Al-Jassim, B. Yan, J. Yang and S. Guha, *Measurement of the Electric Potential on Amorphous Silicon and Amorphous Silicon Germanium Alloy Thin-Film Solar Cells by Scanning Kelvin Probe Microscopy,* Mat. Res. Soc. Symp. Proc. **808** (2004) A9.42.1-6.

[Jiang 2005] C.-S. Jiang, H. R. Moutinho, M. J. Romero, M. M. Al-Jassim, Y. Q. Xu, and Q. Wang, *Distribution of the electrical potential in hydrogenated amorphous silicon solar cells,* Thin Solid Films **472** (2005) 203–207.

[Kadam 2008] A. Kadam, L. Li, S. Sheng, T. K. Won, J. Su, Y. K. Chae, D. Tanner, C. Eberspacher, S. Y. Choi and J. M. White, *Development of Highly Efficient a-Si:H/μc-*

	Si:H Tandem Thin Film Solar Cells on 5.7m² Size Glass Substrates, Proc. of the 23rd EU-PVSEC, Valencia, 2008, pp. 2062-2064.
[Kleider 2001]	J. P. Kleider, C. Longeaud, R. Brüggemann and F. Houzé, *Electronic and Topographic Properties of Amorphous and Microcrystalline Silicon thin Films,* Thin Solid Films **383** (2001) 57-60.
[Klein 2008]	S. Klein, M. Rohde, T. Stolley, K. Schwanitz, S. Buschbaum, *a-Si/μc-Si Tandem Module Development on 1.4m2 Substrate Size,* Proc. of the 23rd EU-PVSEC, Valencia, 2008, p.p 2088- 2090.
[Kocka 2006]	J. Kocka, T. Mates, H. Stuchlıkova, J. Stuchlık and A. Fejfar, *Characterization of Grain Growth, Nature and Role of Grain Boundaries in Microcrystalline Silicon—Review of Typical Features,* Thin Solid Films **501** (2006) 107– 112.
[Krc 2002]	J. Krc, M. Zeman, F. Smole and M. Topic, *Optical Modeling of a-Si:H Solar cells Deposited on Textured Glass/SnO2 Substrates,* J. Appl. Phys. **92** (2002) 749-755.
[Krc 2003]	J. Krc, F. Smole and M. Topic, *Analysis of Light Scattering in Amorphous Si:H Solar Cells by a One-Dimensional Semi-coherent Optical Model,* Prog. Photovolt: Res. Appl. **11** (2003) 1115–1126.
[Krc 2006]	J. Krc, K. Brecl, F. Smole and M. Topic, *The Effects of Enhanced Light Trapping in Tandem Micromorph Silicon Solar Cells*, Solar Energy Materials & Solar Cells **90** (2006) 3339–3344.
[Kroll 2007]	U. Kroll, J. Meier, S. Benagli, D. Borrello, J. Hötzel, J. Spitznagel, B. Dehbozorgi, H. Schmidt, G .Monteduro, O. Kluth, R. Kravets, M. Kupich, C. Ellert, S. Bakehe, H. Goldbach, M. Keller, T. Roschek, L. Schmid, W. Burkhardt, B. Gilles, J. Springer, D. Zimin, G. Buechel, A. Hügli, A. Zindel, T. Kratzla and D. Koch-Ospelt, *Status of thin Film Silicon PV Developments at Oerlikon Solar*, Proc. of the 22nd EU-PVSEC, Milan, 2007, pp. 1795-1800.
[Lambertz 2007]	A. Lambertz, A Dasgupta, W. Reetz, A. Gordijn, R. Carius and F.Finger, *Microcrystalline Silicon Oxide as Intermediate Reflector for Thin Film Silicon Solar Cells*, Proc. of the 22th EU-PVSEC, Milan, 2007, pp. 1839-1842.
[Landauer 1952]	R. Landauer, *The Electrical Resistance of Binary Metallic Mixtures*, J. Appl. Phys. **23** (1952) 779-784.
[Li 2009]	H. B. T. Li, R. H. Franken, J. K. Rath, R. E. I. Schropp*, Structural defects caused by a rough substrate and their influence on the performance of hydrogenated nano-crystalline silicon n–i–p solar cells,* Solar Energy Materials and Solar Cells **93** (2009) 338-349.
[Lozano-Perez 2008]	S. Lozano-Perez, M. Schröder, T. Yamada, T. Terachi, C. A. English and C. R. M. Grovenor, *Using NanoSIMS to map trace elements in stainless steels from nuclear reactors,* Applied Surface Science **255** (2008) 1541-1543.
[Mahan 1991]	A. H. Mahan, J. Carapella, B. P. Nelson, R. S. Crandall and I. Balberg, *Deposition of device quality, low H content amorphous silicon*, J. Appl. Phys. **69** (1991) 6728-6730.
[Meier 1994]	J. Meier, R. Flückiger, H. Keppner and A. Shah, *Complete microcrystalline p-i-n solar cell-Crystalline or amorphous behavior?,* Appl. Phys. Lett. **65** (1994) 860-862.
[Meier 1996]	J. Meier, P. Torres, R. Platz, S. Dubail, U. Kroll, J. A. Anna Selvan, N. Pellaton Vaucher, Ch. Hof, D. Fisher, H. Keppner, A. Shah, K.-D. Ufert, P. Giannoulès and, J. Koehler, *On the way towards high efficiency thin film silicon solar cells by the "micromorph" concept* , Mat. Res. Soc. Symp. Proc., Spring Meeting, San Francisco 1996, pp. 3-14.

[Meier 2002] J. Meier, J. Spitznagel, S. Faÿ, C. Bucher, U. Graf, U. Kroll, S. Dubail and A. Shah, *Enhanced Light-Trapping for Micromorph Tandem Solar Cells by LP-CVD ZnO,* 29th IEEE Photovoltaic Specialists Conference, New Orleans, 2002, pp.1118-1121.

[Meier 2003] J. Meier, J. Spitznagel, U. Kroll, C. Bucher, S. Faÿ, T. Moriarty and A. Shah, *High-Efficiency Amorphous and"Micromorph"Silicon Solar Cells,* Proc. of 3rd World Conf. Osaka, 2003, pp.2801- 2805.

[Meier 2005] J. Meier, U. Kroll, J. Spitznagel, S. Benagli, T. Roschek, G. Pfanner, C. Ellert, G. Androutsopoulos, A. Hügli, M. Nagel, C. Bucher, L. Feitknecht, G. Büchel, A. Büchel, *Progress in Up-Scaling of Thin Film Silicon Solar Cells by Large-Area PECVD Kai Systems*, 31st IEEE PVSC, 2005, pp. 1464-1467.

[Meier 2008] J. Meier, U. Kroll, S. Benagli, D. Borrello, J. Hötzel, J. Spitznagel, B.Dehbozorgi, E. Vallat-Sauvain, H. Schmidt, O. Kluth, R. Kravets, M. Kupich, C. Ellert, S. Bakehe, H. Goldbach, M. Keller,T. Roschek, W. Burkhardt, B. Gilles, D. Zimin, G. Buechel, A. Hügli, A. Zindel and D. Koch-Ospelt, *Latest R&D Developments of Thin Film Silicon PV at Oerlikon Solar*, Proc. of the 23rdEU-PVSEC, Valencia, 2008, pp. 2057-2061.

[Meillaud 2005] F. Meillaud, E. Vallat-Sauvain, X. Niquille, M.Dubey, J. Bailat, A. Shah, and C. Ballif, *Light- induced Degradation of thin Film Amorphous and Microcrystalline Silicon Solar Cells,* Proc. of the 31th IEEE Photovoltaic Specialist Conference, Lake Buena Vista, FL, 2005, pp. 1412-1415.

[Meillaud 2006] F. Meillaud, A. Shah, C. Droz, E. Vallat-Sauvain and C. Miazza**,** *Efficiency limits for single-junction and tandem solar cells,* Solar Energy Materials and Solar Cells **90** (2006) 2952-2959.

[Merten 1998] J. Merten, J. M. Asensi, C. Voz, A. Shah, R. Platz and J. Andreu, *Improved Equivalent Circuit and Analytical Model for Amorphous Silicon Solar Cells and Modules,* IEEE Transactions on Electron Devices **45** (1998) 423-429.

[Mizuhashi 1988] M. Mizuhashi, Y. Gotog and K. Adachi, *Texture morphology of SnO2:F films and cell reflectance*, Jpn. J. Appl. Phys **27** (1988) 2053-206.

[Myong 2007] S. Y. Myong, K. Sriprapha, S. Miyajima, A. Yamad and M. Konagai, *High efficiency protocrystalline silicon/microcrystalline silicon tandem cell with zinc oxide intermediate layer*, Appl. Phys. Lett. **90** (2007) 263509.1-3

[Nakajima 2004] A. Nakajima, M. Ichikawa, T. Sawada, M. Yoshimi and K. Yamamoto, *Spectral Characteristics of Thin-Film Stacked-Tandem Solar Modules*, Jpn. J. Appl. Phys. **43** (2004) 7296-7302.

[Nasuno 2001] Y. Nasuno, M. Kondo and A. Matsuda, *Effects of Substrate Surface Morphology on Microcrystalline Silicon Solar Cells*, Jpn. J. Appl. Phys. **40** (2001) L303-305.

[Nasuno 2002] Y. Nasuno, M. Kondo , A. Matsuda, H. Fukuhori and Y. Kanemitsu, *Formation of interface defects by enhanced impurity diffusion in microcrystalline silicon solar cells,* Appl. Phys. Lett. **17** (2002) 3155-3157.

[Nath 1988] P. Nath, K. Hoffmann, C. Vogeli and S. R. Ovshinski, *Conversion Process for Passivating Current Shunting Paths in Amorphous Silicon alloy Solar Cells,* Appl. Phys. Lett. **53** (1998) 986-988.

[Nonnenmacher 1991] M. Nonnenmacher, M. P. Oboyle and H. K. Wickramasinghe, *Kelvin probe force microscopy,* Appl. Phys. Lett. **58** (1991) 2921–3.

[Nikolaeva-Dimitrova 2007] M. Nikolaeva-Dimitrova, M. Pravettoni, R. P. Kenny, E. D. Dunlop**,** *Comparison of the Long Term Performance of Silicon Based Thin Film and Crystalline Modules*, proc. of the 22nd EU-PVSEC, Milan, 2007, p.2782.

[O'Donnel 1987] K. A. O'Donnell and E. R. Mendez, *Experimental Study of Scattering from Characterized Random Surfaces*, J. Opt. Soc. Am. A **4** (1987) 1194-1205.

[Okada 2003] N. Okada, *Stacked Photovoltaic Element*, United States Patent Application Publication, n° US 2003/0217769 A1, Nov. 27, 2003.

[Okada 2007] N. Okada and T. Kariya, *Stacked Photovoltaic Device*, United States Patent n° US 7,189,917 B2, Mar. 13, 2007.

[Pellaton 1998a] N. Pellaton Vaucher, *Cellules solaires en silicium amorphe et microcristallin: Optimalisation électrique et optique de la structure tandem*, Ph.D thesis (1998), Université de Neuchâtel.

[Pellaton 1998b] N. Pellaton Vaucher, J.-L. Nagel, R. Platz, D. Fischer, A. Shah, *Light Management in Tandem Cells by an Intermediate Reflector Layer,* Proc. of the 2nd WCPEC, Vienna, 1998, Vol I, pp. 729-731.

[Platz 1997a] R. Platz, D Fischer, S. Dubail and A Shah, *a-Si:H/a-Si:H Stacked Cell from VHF-Deposition in a Single Chamber Reactor with 9% Stabilized Efficiency*, Solar Energy Materials and Solar Cells **46** (1997) 157-172.

[Platz 1997b] R. Platz, J. Meier, D. Fischer, S. Dubail and A. Shah, *The Problem of the Top Cell for the Micromorph Tandem*, Proceedings of the MRS Symp., Spring Meeting, San Francisco, 1997, Vol 467, pp. 699-704.

[Platz 1998] R. Platz, C. Hof, D. Fischer, J. Meier and A. Shah, *High-T_s Amorphous Top Cells for Increased Top Cell Currents in Micromorph Tandem Cells*, Solar Energy Materials and Solar Cells **53** (1998) 1-13.

[Poruba 2000] A. Poruba, A. Fejfar, Z. Remes, J. Springer, M. Vanecek, J. Kocka, J. Meier, P. Torres and A. Shah, *Optical Absorption and Light Scattering in Microcrystalline Silicon thin Films and Solar Cells,* J. Appl. Phys. **88** (2000) 148-160.

[Poruba 2008] A. Poruba, P. Klapetek, J. Holovsky, A. Purkrt and M. Vanecek, *Experimental Limits of Light Capture in Thin Film Silicon Devices*, Mater. Res. Soc. Symp. Proc. 1101, KK02-03.

[Python 2008] M. Python , E. Vallat-Sauvain, J. Bailat, D. Dominé, L. Fesquet, A. Shah and C. Ballif, *Relation between substrate surface morphology and microcrystalline silicon solar cell performance,* Journal of Non-Crystalline Solids **354** (2008) 2258-2262.

[Python 2009a] M. Python, D. Dominé, F. Meillaud and C. Ballif, *Microcrystalline silicon solar cells: effect of substrate temperature on cracks quantified by a new method*, to be published.

[Python 2009b] M. Python, *Microcrystalline silicon: growth and deffects*, PhD Thesis (2009), Université de Neuchâtel.

[Raether 1988] H. Raether, *Surface Plasmons*, Springer Tracts on Modern Physics. **111** (Springer-Verlag, Berlin, 1988)**.**

[Redfield 1974] D. Redfield, Appl. Phys. Lett. **25** (1974) 647.

[Repmann 2003] T. Repmann, J. Kirchhoff, W. Reetz, F. Birmans, J. Müller and B. Rech, *Investigations on the Current Matching of Highly Efficient Tandem Solar Cells Based on Amorphous and Microcrystalline Silicon,* Proceedings of 3rd WCPEC Osaka 2003 pp.1843 –1846.

[Rice 1951] S. O. Rice, *Reflection of Electromagnetic Waves from Slightly Rough Surfaces*, Commun. Pure Appl. Math. **4** (1951) 351.

[Rockstuhl 2007] C. Rockstuhl, F. Lederer, K. Bittkau and R. Carius, *Light localization at randomly textured surfaces for solar-cell applications*, Appl. Phys. Lett. **91** (2007) 171104.1-3.

[Rockstuhl 2008] C. Rockstuhl, S. Fahr, F. Lederer, K. Bittkau, T. Beckers and R. Carius, *Local versus global absorption in thin-film solar cells with randomly textured surfaces*, Appl. Phys. Lett. **93** (2008) 061105.1-3.

[St John 1965] E. St. John, *Multiple internal reflection structure in a silicon detector which is obtained by sandblasting*, U.S. Patent No. 3,487,223 (1969).

[Sakai 1990] H. Sakai, T. Yoshida, T. Hama and Y. Ichikawa, *Effects of Surface Morphology of Transparent Electrode on the Open-Circuit Voltage in a-Si:H Solar Cells*, Jpn. J. Appl. Phys. **29** (1990) 630.

[Sarkozy 1981] R. F. Sarkozy, CVD *Silicon Oxide below 100°C Utilizing Photochemical Combustion of SiH_4 and O_2,* Digest of Technical Papers, Symposium on VLSI Technology, 1981, pp. 68-69.

[Schulte 2007] M. Schulte, S. Jorke, C. Zahren, J. Hüpkes and H. Stiebig, *Analysis of the Scattering Properties of Textured TCO Structures for Thin Film Silicon Solar Cells,* Proc. of the 22nd EU-PVSEC, Milan, 2007, p. 2190.

[Schwarzenbach 1995] W. Schwarzenbach, A. Howling, M. Fivaz, S. Brunner and Ch. Hollenstein, *Sheath Impedance Effects in Very High Frequency Plasma Experiments,* J. Vac. Sci. Technol. **14** (1996) 132-138.

[Sculati-Meillaud 2006]. F. Sculati-Meillaud, *Microcrystalline Silicon Solar Cells: Theory, Diagnosis and Stability*, PhD Thesis (2006), Université de Neuchâtel.

[Shah 2006] A. Shah, J. Meier, A. Buechel, U. Kroll, J. Steinhauser, F. Meillaud, H. Schade and D.Dominé, *Towards very low-cost mass production of thin-film silicon photovoltaic (PV) solar modules on glass*,Thin Solid Films **502** (2006) 292-299.

[Shen 2007] Z. Shen, T. Gotoh, M. Egughi, N. Yoshida, T. Itoh and S. Nonomura, *Study of Nano-Scale Electrical Properties of Hydrogenated Microcrystalline Silicon Solar Cells by Conductive Atomic Force Microscope,* J. Appl. Phys. **46** (2007) 2858-2864.

[Springer 2004] J. Springer, A. Poruba and M. Vanecek, *Improved three-dimensional optical model for thin-film silicon solar cells,* J. Appl. Phys. **96** (2004) 5329-5337.

[Staebler 1977] D. L. Staebler and C. R. Wronski, *Reversible conductivity changes in discharge-produced amorphous Si,* Appl. Phys. Lett. **31** (1977) 292-294.

[Steinhauser 2005] J. Steinhauser, L. Feitknecht, S. Faÿ, R. Schlüchter, J. Springer, A. Shah and C. Ballif, *Effect of Rough ZnO Layers in Improving Performances of Microcrystalline Silicon Solar* Cell, Proc. of the 20th EU-PVSEC, Barcelona, 2005, pp. 1608-1611.

[Steinhauser 2007] J. Steinhauser, S. Faÿ, N. Oliveira, E. Vallat-Sauvain and C. Ballif, *Transition between grain boundary and intragrain scattering transport mechanisms in boron-doped zinc oxide thin films,* Appl. Phys. Lett. **90** (2007) 142107 1-3.

[Steinhauser 2008a] J. Steinhauser, S. Faÿ, N. Oliveira, E. Vallat-Sauvain, D. Zimin, U. Kroll, and C. Ballif, *Electrical transport in boron-doped polycrystalline zinc oxide thin films,* phys. stat. sol. (a) **205** (2008) 1983-1987.

[Steinhauser 2008b] J. Steinhauser, *Low Pressure Chemical Vapor Deposited Zinc Oxide for Silicon Thin Film Solar Cells Optical and Electrical Properties,* PhD Thesis (2008), Université de Neuchâtel.

[Stiebig 2000] H. Stiebig, T. Brammer, T. Repmann, O. Kluth, N. Senoussaoui, A. Lambertz and H. Wagner, *Light scattering in microcrystalline silicon thin-film solar cells*, Proc. of the 16th EU-PVSEC, Glasgow, 2000, pp. 549–552.

[Stutzmann 1985] M. Stutzmann, W.B. Jackson and C.C. Tsai, *Light-induced metastable defects in hydrogenated amorphous silicon: A systematic study*, Phys. Rev. B **32** (1985) 23-47.

[Taneda 2007] N. Taneda, T. Oyama and K. Sato, *Light Scattering Effects of Highly Textured Transparent Conductive Oxides* Films, Proc. of the I-PVSEC-17, Fukuoka, 2007, pp. 309-312.

[Terrazoni 2006] V. Terrazzoni Daudrix, J. Guillet, F. Freitas, A. Shah, C. Ballif, P. Winkler, M. Ferreloc, S. Benagli, X. Niquille, D. Fischer and R. Morf, *Characterisation of Rough*

Reflecting Substrates Incorporated Into thin-Film Silicon Solar Cells, Progress in photovoltaics: Research and application **14** (2006) 485-498.

[Tinga 1973] W.R. Tinga, W.A.G. Voss and D. F. Blossey, *Generalized Approach to Multiphase Dielectric Mixture Theory,* J. Appl. Phys. **44** (1973) 3897-3902.

[Torres 1998] P. Torres, *Hydrogenated Microcrystalline Silicon Deposited by VHF-GD for Thin-Film Solar Cells*, PhD Thesis (1998), Université de Neuchâtel.

[Vanecek 2003] M. Vanecek, J. Springer, A. Poruba, O. Kluth, T. Repmann, B. Rech, N. Wyrsch, J. Meier and A. Shah*, Light Trapping and Optical Losses in Microcrystalline Si and Micromorph Solar Cells*, Proceedings of the 3rd WCPEC, Osaka, 2003, pp. 1527-1532.

[Vepreck 1968] S. Vepreck and V. Marececk, Solid State Communications **11** (1968) 683.

[Wang 2005] Z. L. Wang, F. Xu, Y. Q. Jin and H- Ogura, *A double Kirchhoff approximation for very rough surface scattering using the stochastic functional approach,* Radio Sci. **40** (2005) RS4011, doi:10.1029/2004RS003079.

[Wood 1902] R. W. Wood, *On a remarkable case of uneven distribution of light in a diffraction grating spectrum,* Philos. Mag **4** (1902) 396-402.

[Wyrsch 1998a] N. Wyrsch, P. Torres, J. Meier and A. Shah, *Microcrystalline p–i–n cells: a drift-controlled device?,* J. Non-Cryst. Solids **227–230** (1998) 1272–1276.

[Wyrsch 1998b] N. Wyrsch, N. Beck, J. Meier, P. Torres and A. Shah, *Electric field profile in µc-Si:H p-i-n devices***,** Mat. Res. Soc. Symp**. 507** (1998) 181.

[Yablonovitch 1982] E. Yablonovitch, *Statistical ray optics*, J. Opt. Soc. Amer **72** (1982) 899-907.

[Yamamoto 1998] K. Yamamoto, M. Toshimi, T. Suzuki, Y. Tawada, T. Okamoto and A. Nakajima, *Thin film poly-Si solar cell on glass substrate fabricated at low temperature,* MRS Spring Meeting, San Francisco, April 1998.

[Yamamoto 2000] K. Yamamoto, M. Yoshimi, Y. Tawada, Y. Okamoto and A. Nakajima, *Thin Film Si Solar Cell Fabricated at Low Temperature,* J. Non-Cryst. Solids **266-269** (2000) 1082-1087.

[Yamamoto 2003] K.Yamamoto, A. Nakajima, M. Yoshimi, T. Sawada, S. Fukuda, T. Suezaki, M. Ichikawa, Y. Koi, M. Goto, H. Takata, T. Sasaki and Y. Tawada*, Novel hybrid thin film silicon solar cell and module***,** proc. of the 3rd WCPEC, Osaka, 2003 paper S20B903.

[Yamamoto 2004] K. Yamamoto, A. Nakajima, M. Yoshimi, T. Sawada, S. Fukuda, T. Suezaki, M. Ichikawa, Y. Koi, M. Goto, T. Meguro, T. Matsuda, M. Kondo, T. Sasaki and Y. Tawada, *A high efficiency thin film silicon solar cell and module*, Solar Energy **77** (2004) 939–949.

[Yamamoto 2005] K. Yamamoto, A Nakajima, M. Yoshimi, T. Sawada, S. Fukuda, T. Suezaki, M. Ichikawa, Y. Koi, M. Goto, T. Meguro, T. Matsuda, M. Kondo, T. Sasaki and Y. Tawada, *A Thin-film Silicon Solar Cell and Module,* Prog. Photovolt Res. Appl. **13** (2005) 489–494.

[Yan 2006] B. Yan, G. Yue, M. Owens, J. Yang and S. Guha , *Over 15% Efficient Hydrogenated Amorphous Silicon Based Triple-Junction Solar Cells Incorporating Nanocrystalline Silicon*, Photovoltaic Energy Conversion, Conference Record IEEE 4thWCPEC, 2006, pp.1477-1480.

[Yoshimi 2003] M. Yoshimi, T. Sasaki, T. Sawada, T. Suezaki, T. Meguro, T. Matsuda, K. Santo, K. Wadano, M. Ichikawa, A. Nakajima, K. Yamamoto, *High efficiency thin film silicon hybrid solar cell module on 1m^2-class large area substrate,* Conference Record, 3rd WCPEC, Osaka, 2003, pp. 1566–1569.

[Zaidi 2000] S. H. Zaidi, J. M. Gee and D. S. Ruby, *Diffraction grating structures in solar cells,* Conference Record of the Twenty-Eighth IEEE, 2000, pp. 395-398.

[Zeman 1995] M. Zeman, J. A. Willemen, G. Tao and J. W. Metselaar, *Computer modelling of a-Si:H based solar cells*, Applied solar energy **31** (1995) 30-41.

[Zeman 2000] M. Zeman, R. A. C. M. M. van Swaaij, J. W. Metselaar and R. E. I. Schropp, *Optical modeling of a-Si:H solar cells with rough interfaces:Effect of back contact and interface roughness,* J. Appl. Phys, **88** (2000) 6436-6443

[Zisman 1932] W. A. Zisman, *A new method of measuring contact potential differencies in metals*, Rev. Sci. Instrum. **3** (1932) 367.

LIST OF PUBLICATIONS

D. Dominé, P. Buehlmann, J. Bailat, A. Billet, A. Feltrin, and C. Ballif
High-efficiency micromorph silicon solar cells with in-situ intermediate reflector deposited on various rough LPCVD ZnO
Proceedings of the 23rd EU-PVSEC, Valencia, Spain, 2008.

D. Dominé, P. Buehlmann, J. Bailat, A. Billet, A. Feltrin, and C. Ballif
Optical management in high-efficiency thin-film silicon micromorph solar cells with a silicon oxide based intermediate reflector
Physica Status Solidi (Rapid Reasarch Letters), phys. stat. sol. (RRL), Vol 2, pp. 163-165, July, 2008.

D. Dominé, J. Bailat, M. Python, N. Wyrsch, C. Ballif, H. R. Moutinho, C.-S. Jiang, M. M. Al-Jassim
Investigation of the Electric-Field Profile in Microcrystalline Silicon p-i-n Solar Cells by Cross-Sectional Scanning Kelvin Probe Microscopy
Proceedings of the 22nd EU-PVSEC, Milan, Italy, 2007.

D. Dominé, J. Bailat, J. Steinhauser, A.S hah, C. Ballif
Micromorph solar cell optimization using a Zno layer as intermediate reflector
Proceedings of the 4th WCPEC Conference, Kona Island, Hawaii, USA, pp. 1465-1468, 2006.

D. Dominé, L. Feitknecht, A. Shah, C. Ballif
Effect of ZnO Layer as Intermediate Reflector in Micromorph Solar Cells
Proceedings of the 20th EU Photovoltaic Solar Energy Conference, ISBN 3-936338-19-1, Barcelona, Spain, pp. 1600-1603, June, 2005.

M. Python, D. Dominé, F. Meillaud and C. Ballif, *Microcrystalline silicon solar cells: effect of substrate temperature on cracks quantified by a new method*, 2009, to be published.

M. Python, E. Vallat-Sauvain, J. Bailat, D. Dominé, L. Fesquet, A. Shah, C. Ballif
Relation Between Substrate Surface Morphology and Microcrystalline Silicon Solar Cell Performance
Journal of Non-Crystalline Solids, Proceedings of the 22nd ICANS Conference, Breckenridge, Colorado, Vol 354, pp. 2258-2262, 2008.

P. Buehlmann, J. Bailat, D. Dominé, A. Billet, F. Meillaud, A. Feltrin, and C. Ballif
In situ silicon oxide based intermediate reflector for thin-film silicon micromorph solar cells
Applied Physics Letters, 143505, Vol 91 , 2007.

J. Bailat, D. Dominé, R. Schlüchter, J. Steinhauser, S. Faÿ, F. Freitas, C. Bücher, L. Feitknecht, X. Niquille, T. Tscharner, A. Shah, C. Ballif
High-efficiency p-i-n microcrystalline and micromorph thin film silicon solar cells deposited on LPCVD ZnO coated glass substrates
Proceedings of the 4th WCPEC Conference, Kona Island, Hawaii, USA , pp. 1533-1536, 2006.

F. Meillaud, A. Shah, J. Bailat, E. Vallat-Sauvain, T. Roschek, B. Rech, D. Dominé, T. Söderström, M. Python, C. Ballif
Microcrystalline silicon solar cells: Theory and diagnostic tools
Proceedings of the 4th WCPEC Conference, Kona Island, Hawaii, USA, pp. 1572 -1575, 2006.

C. Ballif, J. Bailat, D. Dominé, J. Steinhauser, S. Faÿ, M. Python, L. Feitknecht
Fabrication of High Efficiency Microcrystalline and Micromorph Thin Film Solar Cells on LPCVD Zno Coated Glass Substrates
p. 1552, Proceedings of the 21th EU PVSEC, Dresden, Germany, 2006.

F. Meillaud, E. Vallat-Sauvain, X. Niquille, D. Dominé, A. Shah, C. Ballif
Annealing behaviour and nature of defects of light-soaked microcrystalline silicon solar cells
to be published in the Proc. of the 21st EU PV Conference, Dresden, Germany, proc. of the 21st EU PV, pp. 1729-1732, 2006.

L. Feitknecht, J. Steinhauser, R. Schlüchter, S. Faÿ, D. Dominé, E. Vallat-Sauvin, F. Meillaud, C. Ballif, A. Shah
Investigations on Fill-Factor drop of microcrystalline silicon p-i-n solar cells deposited onto highly surface-textured ZnO substrates
Technical digest of the 15th International Photovoltaic Science and Engineering Conference, Shanghai, China, October 2005, Vol 1, pp. 473-474, 2005.

PATENTS

D. Dominé, P. Buehlmann, J. Bailat

Dispositif photoélectrique a jonctions multiples et son procédé de réalisation

Office Européen des brevets, N° 08169424.2-1528, date de dépôt 19.11.08.

J. Bailat, C. Ballif, D. Dominé

Couche conductrice transparente et texturée et son procede de réalisation

Office Européen des brevets, N° 07704549.0-1235, date de dépôt 13.02.07.

Acknowledgments

First I would like to thank Prof. Christophe Ballif for giving me the opportunity to accomplish my thesis in the motivating field of photovoltaics in a high level and enthusiastic research group.

I thank greatly the referees Dr. Johannes Meier, Prof. Hans-Peter Herzig, and Prof. Marko Topic that they accepted to join the examination board and devoted time to the reading of this thesis.

A special thank goes to the successive project leaders of the high efficiency p-i-n group Dr. Luc Feitknecht, Dr. Julien Bailat, and Dr. Andrea Feltrin, who gave me so many inputs and led our team with much talents. A second special thank to Andrea and Christophe who adviced and supported me widely, during the final writing period, for the achievement of this thesis.

I would like to gratefully thank Prof. Arvind Shah for having giving me the opportunity to join his laboratory and to work in the field of thin film silicon devices previously from this thesis.

Warm thanks go to all the colleagues of the p-i-n group, Adrian Billet, Peter Bühlmann, also for the good atmosphere in our office, and Gregory Bugnon, Dr. Fanny Sculati-Meillaud, Dr. Gaetano Parascandolo, and Dr. Matthieu Despeisse.

Warm thanks for discussions, superstrates and friendship to the colleagues and former colleagues of the ZnO group, Dr. Sylvie Fäy, Dr. Jérôme Steinhauser, Stefan Meier, Marlène Schwab, Dr. Sylvain Nicolay, Romain Schlüchter, and Nuno Oliveira.

Special thanks to the members and former members of the reciprocal nip-space group for enlightments from the other side, Dr. Franz-Josef Haug, Dr. Vanessa Terrazzoni, Thomas Söderström, Xavier Niquille, Dr. Oscar Cubero, Céline Denizot, Fanny Perregaux, Frédéric Freitas, and Dr. Joëlle Guillet.

Warm thanks also to the collegues involved with characterization, with TFT and detectors, and with wafers, Dr. Evelyne Vallat-Sauvin, Dr. Fanny Sculati-Meillaud, and Martin Python, Dr. Nicolas Wyrsch, Sylvain Dunand, and Grégory Choong, Dr. Sara Olibet, Luc Fesquet, and Dr. Jérôme Damon Lacoste. Their friendship and the numerous scientific discussions we shared together contributed to greatly extend my motivation during this work. I would like to thank all my colleagues and friends at the Institute for their constant help during this work. In particular, Dr. Julien Bailat, Peter Bühlmann, Adrian Billet, Dr. Jérôme Steinhauser, Dr. Andrea Feltrin.

I thank greatly Dr. Mowafak Al-Hassim, Dr. Helio Mountinho, and all the team of the group of Analytical Microscopy at NREL for the warm welcome, scientific inputs and support during my exciting stay in Colorado.

Special thanks also to Martin Python and Mathieu Charrière for TEM pictures and to Ruben De Araujo for the complete and good optical characterizations he did, they were very fruitfull for this thesis. Very special thanks also to Reto Tscharner, Cédric Bucher, Fabrice Jeanneret (SR analyzer!), Jean-Luc Kumin, and Hassan Laaroussi for technical support; Brigitte Khan, Joëlle Benjac, Sandrine Piffaretti, and Martial Racine for administrative support.

Finally, I would like to thank Floriane Membrez for her constant support and for the huge amount of chocolotate and love she gave me during the writing of this thesis.